Titre: Title:	A Fully Lagrangian Model Using DEM-WCMPS to Simulate Solid Objects in Free-surface Flow With Applications to River Ice Dynamics
Auteur: Author:	Andréa Mellado Cusicahua
Date:	2021
Type:	Mémoire ou thèse / Dissertation or Thesis
Référence: Citation:	Mellado Cusicahua, A. (2021). A Fully Lagrangian Model Using DEM-WCMPS to Simulate Solid Objects in Free-surface Flow With Applications to River Ice Dynamics [Mémoire de maîtrise, Polytechnique Montréal]. PolyPublie. https://publications.polymtl.ca/6598/

POLYTECHNIQUE MONTRÉAL

affiliée à l'Université de Montréal

A fully Lagrangian model using DEM-WCMPS to simulate solid objects in free-surface flow with applications to river ice dynamics

ANDREA MELLADO CUSICAHUA

Département de Génie civil, géologique et des mines

Mémoire présenté en vue de l'obtention du diplôme de *Maîtrise en sciences appliquées*

Génie Civil

Mai 2021

POLYTECHNIQUE MONTRÉAL

affiliée à l'Université de Montréal

Ce mémoire intitulé:

A fully Lagrangian model using DEM-WCMPS to simulate solid objects in free-surface flow with applications to river ice dynamics

présenté par **Andrea MELLADO CUSICAHUA**

en vue de l'obtention du diplôme de Maîtrise en sciences appliquées

a été dûment accepté par le jury d'examen constitué de :

Musandji FUAMBA, président
Ahmad SHAKIBAEINIA, membre et directeur de recherche
Elmira HASSANZADEH, membre

DEDICATION

À ma famille, qui a été et qui est une grande source d'inspiration et de soutien.

À mon superviseur, professeur Ahmad Shakibaeinia, pour son dévouement à partager ses compétences.

À tous mes ami(e)s et collègues qui m'ont appuyée tout au long de ce parcours.

À Étienne Bélanger pour son aide précieuse lors de la réalisation des expériences au laboratoire.

ACKNOWLEDGEMENTS

I wish to express my deepest and most sincere gratitude and appreciation to my supervisor, Professor Ahmad Shakibaeinia. I was privileged with his knowledge, good guidance, support, and enjoyable company throughout my masters. Thank you also for your valuable feedback on this thesis.

I would like to acknowledge the financial support from the Natural Sciences and Engineering Research Council of Canada (NSERC) and from la Bourse d'Excellence Hydro-Québec.

I would also like to thank the laboratory technician, Etienne Bélanger, for all his help during the experimental process. Thank you for sharing your experience with me and giving me all the resources required to accomplish my tasks.

Many thanks Mojtaba Jandaghian and Rubens Amaro, for their help and for always being ready to answer my questions. Thank you for your time and knowledge, without which, the output would not be the same.

I am also grateful to many friends whose friendship was very important to me: Abdelkader, Abdellah, Ali, Amanda, Andrew, Baptiste, Claudio, Faezeh, Faroogh and all my other colleagues, Jennie A., Khalil, Lisa, Maryam, Mohamad P., Professor Elmirah Hassanzadeh and to all my professors at École Polytechnique, Professor René Kahawita, Professor Susan Gaskin and to all my professors at McGill University, Rosie and Melanie, Sara, Sarah-Claude, Sr. Louise and all the sisters and friends from the Villa Sainte-Marcelline, Ying and all my McGill friends, and to all my other friends.

Most importantly, I would like to extend my gratitude to my parents, Hercilia and Andres, and to my beloved sister, Elodie, for their unconditional love, patience, and prolonged support. Thank you for always being there for me and for helping me pursue my dreams.

RÉSUMÉ

Les processus des glaces fluviales, tels que la rupture, le transport, le blocage et le dégagement des parcelles de glace, jouent un rôle de restriction dans les processus hydrodynamiques, morphodynamiques et de transport dans les rivières des régions froides. Par exemple, les embâcles de glace, qui se forme lorsqu'il y a une accumulation de frasil ou de glace fragmentée, bloquent l'écoulement de la rivière et peuvent occasionner des inondations, un des plus grands dangers liés aux glaces fluviales. Les embâcles de glace peuvent endommager les résidences et les infrastructures ainsi qu'engendrer des risques pour les populations riveraines, tels que le délogement et même la perte de vie. Afin de réduire ces risques et conséquences, la dynamique des embâcles fluviaux a besoin d'être comprise et prédite. De nos jours, à cause du changement climatique, il est encore plus important de se fier à des outils de prédiction à haute précision afin d'atténuer les impacts des inondations causées par les embâcles de glace. À cause de la complexité de l'interaction entre l'eau et la glace présente dans les embâcles fluviaux, ce phénomène est resté largement imprévisible.

L'objectif principal de ce mémoire est d'aider à la compréhension de ce phénomène en fournissant des cas servant de critère de comparaison ayant des caractéristiques comparables à une rupture d'embâcle et en développant un modèle numérique capable de reproduire le comportement complexe et dynamique de l'interaction solide-liquide (glace-eau).

Des expériences à petite échelle ont été effectuées au Laboratoire Hydraulique de l'École Polytechnique de Montréal où des ruptures d'embâcles ont été reproduites pour un lit en aval sec et mouillé avec des objets flottants (représentant la glace) pour fournir des données de qualité qui seront utiles pour la validation des modèles numériques des embâcles de glace.

De plus, une nouvelle génération de méthode numérique, connue sous le nom de méthodes Lagrangiennes ou méthodes sans maillage, a été utilisée dans ce mémoire pour prédire le comportement hautement dynamique des embâcles fluviaux. Ces méthodes numériques utilisent des particules discrètes possédant chacune des propriétés du système telles que la vitesse, la pression et la position. Les méthodes sans maillage sont ainsi plus efficaces pour reproduire les caractéristiques complexes présentes dans l'interaction entre l'eau et la glace et pour fournir une solution fiable au phénomène des embâcles. La glace solide est modélisée par le *Discrete Element*

Method (DEM) où la glace est représentée par un groupe de particules ayant une position relative entre elles constante (*multisphere*) et dont le mouvement est déterminé par les forces qui y sont appliquées. La force lors de la collision, connue sous le nom de force de contact, est calculée en utilisant un modèle dynamique de contact Hertzien où une combinaison de modèles à ressort et d'amortisseur est implémentée. Les forces hydrodynamiques appliquées sur les particules solides sont calculées en utilisant la méthode de *Moving Particle Semi-Implicit* (MPS).

Le modèle DEM est validé tout d'abord sans la présence de la phase liquide en 2D et en 3D. Par la suite, ce modèle est jumelé à un code MPS existant connu sous le nom de MPARS qui a été développé par le groupe de recherche. Le modèle MPS-DEM a aussi été validé en utilisant des cas de référence en 2D.

ABSTRACT

River ice dynamic processes, such as the break-up, transport, jamming, and release of ice parcels, play a curtail role in hydrodynamic, morphodynamic, and transport processes in cold region rivers. For instance, ice jams, caused by an accumulation of frazil or fragmented ice, restrict flow and can trigger ice jam floods, one of the greatest river ice hazards. Ice jam can damage properties and infrastructures as well as cause inconveniences to people, such as dislocation or even loss of life. In order to mitigate these consequences, the dynamic of river ice jams needs to be understood and predicted. Due to the complexities involved in the multiphase ice-water system, this phenomenon has remained largely unpredictable.

This thesis's main objective is to give more insight into this phenomenon by providing benchmark cases mimicking the characteristics of a jam release and developing a numerical model capable of reproducing the complex dynamic behavior of solid (ice) and fluid (water) interactions.

Small-scale and challenging experiments were carried out at the Hydraulic Laboratory of École Polytechnique of Montreal. Dam-break flows were reproduced over dry and wet beds with floating block floes (representing the ice) to provide useful and comprehensive quality data for the validation of ice jam models.

Furthermore, a newer generation of numerical methods, the mesh-free particle (Lagrangian) numerical methods, has been used in this thesis to predict the highly dynamic movements involved in river ice processes. These methods use a set of mobile discrete particles representing and recording the system's position and state and possessing field variables, such as velocity and pressure. The use of particles renders the mesh-free particle methods effective in dealing with the complexities of ice-water systems and providing a reliable solution for simulating the complexities involved in the water-ice interactions. The solid ice phase is modelled using the Discrete Element Method (DEM), where the ice is represented by a group of solid particles whose relative position is constant (multisphere) and whose motion is determined from the forces applied to it. The collision force, mainly known as the contact force, is calculated using a Hertzian contact dynamic model where a combination of spring and dashpot models are implemented. The hydrodynamic forces applied to the solid particles are calculated using the Moving Particle Semi-Implicit (MPS) method.

The DEM model was validated at first without the fluid phase in 2D and 3D, and then it was coupled with an existing MPS code known as MPARS, which was developed by the host research group at Polytechnique. The MPS-DEM coupled model was also validated using 2D benchmark cases.

TABLE OF CONTENTS

DEDICATION III

ACKNOWLEDGEMENTS IV

RÉSUMÉ V

ABSTRACT VII

TABLE OF CONTENTS IX

LIST OF TABLES XII

LIST OF FIGURES XIII

LIST OF SYMBOLS AND ABBREVIATIONS XX

LIST OF APPENDICES XXIII

CHAPTER 1 INTRODUCTION 1

1.1 Context 1

1.2 Literature Review 2

1.3 Problem Statement 7

CHAPTER 2 OBJECTIVES AND ORGANIZATION OF THE WORK 1

2.1 Research objectives 1

2.2 Organization of the work 2

CHAPTER 3 THREE-DIMENSIONAL EXPERIMENTAL DAM BREAK TEST CASES WITH FLOATING BLOCKS 3

3.1 Introduction 3

3.2 Experimental setup 3

3.2.1 Experimental apparatus 3

3.2.2 Experimental material 5

3.2.3 Experimental case scenarios 8

3.2.4 Data acquisition 8
3.2.5 Gate motion 9
3.3 Results and discussion 10
3.3.1 Dam breaking with four blocks 10
3.3.2 Dam breaking with nine blocks 13
3.4 Conclusion 15
CHAPTER 4 DEM MODEL AND VALIDATION 16
4.1 Governing Equations 16
4.2 The Contact Forces 17
4.2.1 The normal contact force 20
4.2.2 The tangential contact force 21
4.3 Multisphere method 23
4.3.1 Two-Dimensional Rotation 24
4.3.2 Three-Dimensional Rotation 26
4.3.3 Quaternions 28
4.4 Global and Local reference frames 31
4.4.1 Two-dimensional Change in Reference frame 32
4.4.2 Three-dimensional Change in Reference frame 33
4.5 DEM Algorithm 34
4.5.1 Reading input values 36
4.5.2 Calculating overlap 37
4.6 DEM Validation 38
4.6.1 2D Single Particle Dropping 38
4.6.2 2D Multisphere validation 44

4.6.3 Demolisher test case used to validate the 3D multisphere model 47
4.7 Conclusion 63
CHAPTER 5 MPS-DEM COUPLING 65
5.1 MPS 65
5.1.1 Governing Equations 65
5.1.2 MPS discretization 65
5.1.3 The Symplectic Time Integrator 69
5.1.4 Boundary conditions 71
5.1.5 Diffusive Term 72
5.1.6 Particle Shifting Technique 73
5.1.7 Linked Cell method 76
5.2 MPS-DEM coupling 77
5.2.1 Algorithm 80
5.3 MPS-DEM Validation 86
5.3.1 2D Water entry of a solid block 86
5.3.2 2D Water entry of a circular cylinder 91
5.4 Conclusion 95
CHAPTER 6 CONCLUSION AND FUTURE WORK 96
6.1 Future Work 98
REFERENCES 99
APPENDICES 109

LIST OF TABLES

Table 3.1 - Masses used to determine the coefficient of friction 7

Table 3.2 - Experimental case conditions - Number of blocks, upstream (H_{up}) and downstream (H_{do}) water height.....8

Table 4.3 - Particle and floor physical properties.....39

Table 4.4 - The percentage difference between the maximum and average values of contact forces obtained from LIGGGHTS and the proposed model.....43

Table 4.5 - Cylinders' Young modulus, Poisson coefficient, friction coefficient, and density used in the proposed model 44

Table 4.6 - Pendulum, blocks, and wall's physical properties.....48

Table 4.7 - Average force comparison between the proposed model and LIGGGHTS for Blocks A, B, and C.....52

Table 4.8 - Average position comparison between the proposed model, LIGGGHTS, and DualSPHysics.....57

Table 4.9 - Percentage difference of the average position between the proposed model, LIGGGHTS, and DualSPHysics.....58

Table 5.10 - Average position comparison between the proposed model, and the numerical models of Robb et al. [76] and Lee et al. [116] 91

Table 5.11 - Percentage difference of average position between the proposed model, and the numerical models of Robb et al. [76] and Lee et al. [116].....91

LIST OF FIGURES

Figure 1.1 - Frazil ice in rivers [1] 1

Figure 2.1 - MPS and DEM representation of water and ice, respectively 2

Figure 3.1 - (a) Prismatic plexiglass tank used in the dam-break experiments. (b) Schematic drawing of the tank, water levels, gate, rigid blocks, pulley-weight mechanism, cameras disposition, and light source. 4

Figure 3.2 - (a) The FASTCAM Mini WX100 placed above the tank. (b) The camera Vixia HF S200 camera placed in front of the tank.....5

Figure 3.3 - The AOS Offboard 150W Led light source.....5

Figure 3.4 - Sets of polypropylene strips and weights 6

Figure 3.5 - Initial arrangement of the cases with (a) 4 blocks and (b) 9 blocks. 9

Figure 3.6 - Time series of the vertical gate motion for all 24 experiments and the median value of gate velocity. 10

Figure 3.7 - Snapshots of the experimental and numerical dam breaking with 4 blocks and dry bed at the instants t = 0.40, 0.80, 1.20, 1.60, 2.00, 2.40 s (front view). 11

Figure 3.8 - Snapshots of the experimental and numerical dam breaking with 4 blocks and wet bed Hdo = 1 cm at the instants t = 0.40, 0.80, 1.20, 1.60, 2.00, 2.40 s (front view). 11

Figure 3.9 - Snapshots of the experimental and numerical dam breaking with 4 blocks and wet bed Hdo = 2.5 cm at the instants t = 0.40, 0.80, 1.20, 1.60, 2.00, 2.40 s (front view). 12

Figure 3.10 - Snapshots of the experimental and numerical dam breaking with 4 blocks and wet bed Hdo = 5 cm at the instants t = 0.40, 0.80, 1.20, 1.60, 2.00, 2.40 s (front view). 12

Figure 3.11 - Snapshots of the experimental and numerical dam breaking with 9 blocks and dry bed at the instants t = 0.40, 0.80, 1.20, 1.60, 2.00, 2.40 s (front view). 13

Figure 3.12 - Snapshots of the experimental and numerical dam breaking with 9 blocks and wet bed Hdo = 1 cm at the instants t = 0.40, 0.80, 1.20, 1.60, 2.00, 2.40 s (front view). 14

Figure 3.13 - Snapshots of the experimental and numerical dam breaking with 9 blocks and wet bed Hdo = 2.5 cm at the instants t = 0.40, 0.80, 1.20, 1.60, 2.00, 2.40 s (front view). 14

Figure 3.14 - Snapshots of the experimental and numerical dam breaking with 9 blocks and wet bed Hdo = 5 cm at the instants t = 0.40, 0.80, 1.20, 1.60, 2.00, 2.40 s (front view). 15

Figure 4.1 - Simple DEM algorithm 18

Figure 4.2 - Contact Plane 19

Figure 4.3 - Hertzian model with the spring and dashpot system 19

Figure 4.4 - Rotation of a multisphere 25

Figure 4.5 - Gimbal lock occurs when a 90-degree rotation around one of the coordinate axes occurs resulting in the alignment of two gimbals 28

Figure 4.6 - Rotation of a 3D object using a single angle rotating around an axis ***p*** can be performed using quaternions.....29

Figure 4.7 – 2D and 3D representation of the Global and Local coordinate systems.....31

Figure 4.8 - Transforming the vector ***v*** from the global to the local coordinate axis.....33

Figure 4.9 - Complete DEM algorithm - The hydrodynamic forces are not included.....35

Figure 4.10 – An example of an InputDEM.txt file 36

Figure 4.11 - Detection of surface particles 37

Figure 4.12 - Time evolution of the particle bouncing off the floor 41

Figure 4.13 - Rebound height comparison between results obtained with the proposed model vs. results obtained with LIGGGHTS.....42

Figure 4.14 - Calibration curve of the rebound height obtained using the proposed model vs. LIGGGHTS 42

Figure 4.15 - Impact force comparison between LIGGGHTS and the proposed model.....43

Figure 4.16 - Representation of a cylinder using multisphere 45

Figure 4.17 - Cylinder collapse at t=0, 0.101, 0.3, and 0.5 s. (Experimental data in the left [109]; simulation results in the right).....46

Figure 4.18 - Variation of the average center of mass for thirty-three cylinders (a) The horizontal variation (b) The vertical variation.....47

Figure 4.19 - Demolisher test case - Pendulum motion and initial blocks set-up.....48

Figure 4.20 - DualSPhysics Pendulum representation.....49

Figure 4.21 - Pendulum velocity simulated by LIGGGHTS vs. a gravity-driven pendulum.....49

Figure 4.22 - Pendulum motion in the x and z direction for the proposed model, LIGGGHTS, and DualSPHysics.....49

Figure 4.23 - Set up of three blocks released from height of 0.3 m.....50

Figure 4.24 - Snapshots of the block position evolution obtained for the proposed model and LIGGGHTS.....51

Figure 4.25 - Comparison of the z-position and the velocity magnitude between the proposed model and LIGGGHTS of Block A.....52

Figure 4.26 - Comparison of the z-position and the velocity magnitude between the proposed model and LIGGGHTS of Block B.....53

Figure 4.27 - Comparison of the z-position and the velocity magnitude between the proposed model and LIGGGHTS of Block C.....53

Figure 4.28 - Snapshots of demolisher results obtained from the proposed model.....54

Figure 4.29 - Snapshots of demolisher results obtained from the LIGGGHTS.....55

Figure 4.30 - Snapshots of demolisher results obtained from the DualSPHysics.....56

Figure 4.31 - Comparison of the average block motion between the proposed model, LIGGGHTS, and DualSPHysics.....57

Figure 4.32 - Comparison of force magnitude between the proposed model and LIGGGHTS for Pendulum.....59

Figure 4.33 - Force comparison between the proposed model and LIGGGHTS for Block 8.....59

Figure 4.34 – Position comparison between the proposed model and LIGGGHTS for Block 8..60

Figure 4.35 - Force comparison between the proposed model and LIGGGHTS for Block 9.....60

Figure 4.36 - Position comparison between the proposed model and LIGGGHTS for Block 9...61

Figure 4.37 - Position comparison between the proposed model and LIGGGHTS for Block 13.62

Figure 4.38 - Position comparison between the proposed model and LIGGGHTS for Block 14.63

Figure 5.1 - The Symplectic time integrator scheme 70

Figure 5.2 - The boundary configuration 72

Figure 5.3 - Particle classification as free-surface ($i \in \mathbb{F}$), near to free-surface ($i \in \mathbb{B}$), external ($i \in \mathbb{E}$), or internal particle ($i \in \mathbb{I}$) 74

Figure 5.4 - Scanning regions R1 and R2 used to determine if the particle *i* is a free-surface particle or not 74

Figure 5.5 - Linked cell method: neighbors of particle *i* are inside the black square 77

Figure 5.6 – A solid rigid body will have at least three layers of ghost particles inside to avoid incomplete kernel support 78

Figure 5.7 - Subcycling method to ensure stability in both MPS and DEM methods 79

Figure 5.8 - MPS-DEM coupling algorithm 82

Figure 5.9 - MPS input file.....83

Figure 5.10 – Direction of normal unit vectors for rectangular and circular shapes.....84

Figure 5.11 - Dimensions and initial block position 87

Figure 5.12 - Snapshots of the block having a density of 500 kg/m^3 falling in the steady tank. The color gradient shows the pressure from 0 kPa (blue) to 4.905 kPa (red). 87

Figure 5.13 - Snapshots of the block having a density of 1000 kg/m3 falling in the steady tank. The color gradient shows the pressure from 0 kPa (blue) to 4.905 kPa (red). 88

Figure 5.14 - Snapshots of the block having a density of 2000 kg/m3 falling in the steady tank. The color gradient shows the pressure from 0 kPa (blue) to 4.905 kPa (red). 89

Figure 5.15 - Block's horizontal and vertical motion for a density of 500 kg/m^3 89

Figure 5.16 - Block's horizontal and vertical motion for a density of 1000 kg/m^3 90

Figure 5.17 - Block's horizontal and vertical motion for a density of 2000 kg/m^3 90

Figure 5.18 – Geometry setup of a cylinder dropped in a steady-state tank filled with water.....92

Figure 5.19 - Snapshots of the cylinder entering the steady-state tank filled with water for the half-buoyant case 93

Figure 5.20 - Snapshots of the cylinder entering the steady-state tank filled with water for the neutrally-buoyant case.....93

Figure 5.21 - Time histories of the depth of penetration of the half-buoyant cylinder of the proposed model compared with experimental results [117], with δ +-SPH [119], and with BEM [118] 94

Figure 5.22 - Time histories of the depth of penetration of the neutrally-buoyant cylinder of the proposed model compared with experimental results [117], with δ +-SPH [119], and with BEM [118].....95

Figure B1 - Dam breaking with 4 blocks and dry bed. Experimental motions along the longitudinal direction of (a) Block A1 (b) A2 (c) B1 (d) B2. 134

Figure B2- Dam breaking with 4 blocks and H_{do}=1cm. Experimental motions along the longitudinal direction of (a) Block A1 (b) A2 (c) B1 (d) B2. 135

Figure B3 - Dam breaking with 4 blocks and Hdo=2.5cm. Experimental motions along the longitudinal direction of (a) Block A1 (b) A2 (c) B1 (d) B2. 136

Figure B4 - Dam breaking with 4 blocks and Hdo=5 cm. Experimental motions of the four blocks along the longitudinal direction of (a) Block A1 (b) A2 (c) B1 (d) B2. 137

Figure B5 - Dam breaking with 4 blocks and dry bed. Experimental motions along the vertical direction of (a) Block B1 (b) B2. 138

Figure B6 - Dam breaking with 4 blocks and H_{do}=1cm. Experimental motions along the vertical direction of (a) Block B1 (b) B2. 138

Figure B7 - Dam breaking with 4 blocks and Hdo=2.5cm. Experimental motions along the vertical direction of (a) Block B1 (b) B2. 139

Figure B8 - Dam breaking with 4 blocks and Hdo=5cm. Experimental motions along the vertical direction of (a) Block B1 (b) B2. 139

Figure B9 - Dam breaking with 9 blocks and dry bed. Experimental motions of block C1 in the (a) longitudinal and (b) vertical direction 140

Figure B10 - Dam breaking with 9 blocks and dry bed. Experimental motions of block C2 in the (a) longitudinal and (b) vertical direction 140

Figure B11 - Dam breaking with 9 blocks and dry bed. Experimental motions of block C3 in the (a) longitudinal and (b) vertical direction 141

Figure B12 - Dam breaking with 9 blocks and H_{do}=1cm. Experimental motions of block C1 in the (a) longitudinal and (b) vertical direction 141

Figure B13 - Dam breaking with 9 blocks and Hdo=1cm. Experimental motions of block C2 in the (a) longitudinal and (b) vertical direction.....142

Figure B14 - Dam breaking with 9 blocks and Hdo=1cm. Experimental motions of block C3 in the (a) longitudinal and (b) vertical direction.....142

Figure B15 - Dam breaking with 9 blocks and H_{do}=2.5 cm. Experimental motions of block C1 in the (a) longitudinal and (b) vertical direction.....143

Figure B16 - Dam breaking with 9 blocks and Hdo=2.5 cm. Experimental motions of block C2 in the (a) longitudinal and (b) vertical direction.....143

Figure B17 - Dam breaking with 9 blocks and Hdo=2.5 cm. Experimental motions of block C3 in the (a) longitudinal and (b) vertical direction.....144

Figure B18 - Dam breaking with 9 blocks and H_{do}=5 cm. Experimental motions of block C1 in the (a) longitudinal and (b) vertical direction 144

Figure B19 - Dam breaking with 9 blocks and Hdo=5 cm. Experimental motions of block C2 in the (a) longitudinal and (b) vertical direction.....145

Figure B20 - Dam breaking with 9 blocks and Hdo =.5 cm. Experimental motions of block C3 in the (a) longitudinal and (b) vertical direction.....145

LIST OF SYMBOLS AND ABBREVIATIONS

c_0 Numerical sound speed

CFL Courant-Friedrichs-Lewy stability

COM Center of Mass

DEM Discrete Element Method

dt Time step

e Coefficient of restitution

$\mathbf{F}_{c,ij}$ Contact force applied on particle *i* from particle *j*

$\mathbf{F}^{c}_{n,ij}$ Contact normal force applied on particle *i* from particle *j*

$\mathbf{F}^{c}_{t,ij}$ Contact tangential force applied on particle *i* from particle *j*

$\mathbf{F}_{g,i}$ Gravitational force applied on particle *i*

$\mathbf{F}_{h,i}$ Hydrodynamic force applied on particle *i*

F_i Fickian diffusion coefficient

H_{do} Water height in the downstream part of the tank

H_{up} Water height in the upstream part of the tank

$\mathbf{I}_i$ Moment of inertia of particle *i*

$k_{n,ij}$ Normal stiffness coefficient

l_0 The average initial spacing between particles

L_{do} Downstream part length of the tank

L_{up} Upstream part length of the tank

Ma Mach number

$\mathbf{M}_{c,ij}$ Contact torque applied on particle *i*

$\mathbf{M}_{h,i}$ Hydrodynamic torque applied on particle *i*

MPS Moving Particle Semi-Implicit

n	The particle number density
n_0	The normalization factor
N_i,N_0	Number of surrounding particles and the maximum initial number of neighbor particles
$\hat{\mathbf{n}}_{ij}$	Normal unit vector between particles *i* and *j*
p	Pressure
$\mathbf{q}$	Quaternion vector
r_e	The smoothing length
R_i, R_j	Radius of particles *i* and *j*, respectively
$\mathbf{R}_m$	Rotation matrix
t_c	Contact time
t_r	Gate time removal
$\mathbf{v}_i$	Velocity vector of particle *i*
$\mathbf{v}_{n,ij}$	Normal relative velocity between particles *i* and *j*
W_{ij}	The weight (kernel) function
$\mathbf{x}_i$	Position vector of particle *i*
Y	Young's modulus
$\gamma_{n,ij}$	Normal damping coefficient
$\delta_{n,ij}$, $\delta_{t,ij}$	Normal and tangential overlap between particles *i* and *j*
Δt_{DEM}	DEM time step
Δt_{MPS}	MPS time step
ε_n	Contact ratio
μ	Dynamic viscosity
μ_f	Kinetic friction coefficient
μ_s	Static friction coefficient

ν Poisson Ratio

ρ_0 Water density

$\boldsymbol{\omega}_i$ Angular velocity of particle *i*

LIST OF APPENDICES

Appendix A CO-AUTHORED ARTICLE PAPER 109

Appendix B EXPERIMENTAL EXTRA RESULTS 134

Figure B1 - Dam breaking with 4 blocks and dry bed. Experimental motions along the longitudinal direction of (a) Block A1 (b) A2 (c) B1 (d) B2. 134

Figure B2- Dam breaking with 4 blocks and H_{do}=1cm. Experimental motions along the longitudinal direction of (a) Block A1 (b) A2 (c) B1 (d) B2. 135

Figure B3 - Dam breaking with 4 blocks and Hdo=2.5cm. Experimental motions along the longitudinal direction of (a) Block A1 (b) A2 (c) B1 (d) B2. 136

Figure B4 - Dam breaking with 4 blocks and Hdo=5 cm. Experimental motions of the four blocks along the longitudinal direction of (a) Block A1 (b) A2 (c) B1 (d) B2. 137

Figure B5 - Dam breaking with 4 blocks and dry bed. Experimental motions along the vertical direction of (a) Block B1 (b) B2. 138

Figure B6 - Dam breaking with 4 blocks and H_{do}=1cm. Experimental motions along the vertical direction of (a) Block B1 (b) B2. 138

Figure B7 - Dam breaking with 4 blocks and Hdo=2.5cm. Experimental motions along the vertical direction of (a) Block B1 (b) B2. 139

Figure B8 - Dam breaking with 4 blocks and Hdo=5cm. Experimental motions along the vertical direction of (a) Block B1 (b) B2. 139

Figure B9 - Dam breaking with 9 blocks and dry bed. Experimental motions of block C1 in the (a) longitudinal and (b) vertical direction 140

Figure B10 - Dam breaking with 9 blocks and dry bed. Experimental motions of block C2 in the (a) longitudinal and (b) vertical direction 140

Figure B11 - Dam breaking with 9 blocks and dry bed. Experimental motions of block C3 in the (a) longitudinal and (b) vertical direction 141

Figure B12 - Dam breaking with 9 blocks and H_{do}=1cm. Experimental motions of block C1 in the (a) longitudinal and (b) vertical direction 141

Figure B13 - Dam breaking with 9 blocks and Hdo=1cm. Experimental motions of block C2 in the (a) longitudinal and (b) vertical direction.....142

Figure B14 - Dam breaking with 9 blocks and Hdo=1cm. Experimental motions of block C3 in the (a) longitudinal and (b) vertical direction.....142

Figure B15 - Dam breaking with 9 blocks and H_{do}=2.5 cm. Experimental motions of block C1 in the (a) longitudinal and (b) vertical direction.....143

Figure B16 - Dam breaking with 9 blocks and Hdo=2.5 cm. Experimental motions of block C2 in the (a) longitudinal and (b) vertical direction.....143

Figure B17 - Dam breaking with 9 blocks and Hdo=2.5 cm. Experimental motions of block C3 in the (a) longitudinal and (b) vertical direction.....144

Figure B18 - Dam breaking with 9 blocks and H_{do}=5 cm. Experimental motions of block C1 in the (a) longitudinal and (b) vertical direction 144

Figure B19 - Dam breaking with 9 blocks and Hdo=5 cm. Experimental motions of block C2 in the (a) longitudinal and (b) vertical direction.....145

Figure B20 - Dam breaking with 9 blocks and Hdo =.5 cm. Experimental motions of block C3 in the (a) longitudinal and (b) vertical direction.....145

CHAPTER 1 INTRODUCTION

1.1 Context

In the northern hemisphere, where rivers and lakes freeze during winter, river ice processes cannot be neglected, especially in transitional seasons when ice floes are formed. When rivers become supercooled at the beginning of winter, small crystals, known as frazil ice, start to form and agglomerate, creating anchor ice, ice floes, and eventually stable ice covers, as depicted in **Figure 1.1**.

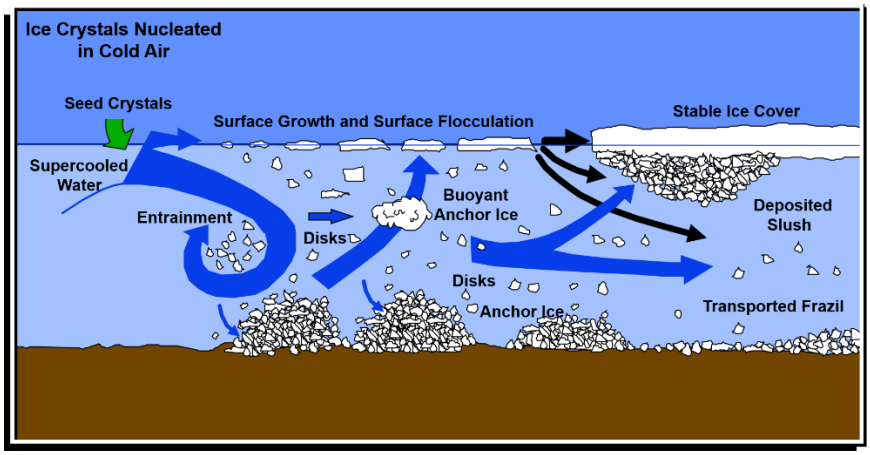

Figure 1.1 - Frazil ice in rivers [1]

Ice floes are also generated at the end of winter, where the ice covers are weakened by the increase of temperature and the flow increase and start to break into ice floes [2].

These ice floes present a hazard to river morphology and the ecosystem when they are carried downstream. They may pose a major threat to riverside communities, hydraulic structures, such as bridges and hydroelectric dams, and infrastructures, such as buildings and roads [3]. Furthermore, they can jam and block the flow if an obstruction is present in the river leading to the rise of the upstream water level. This process is known as ice jam. The resulting upstream flooding can bring some advantages to nearby ecosystems, such as replenishing upstream plains [3]. However, it often happens that houses are already built in these regions, and residents are forced to abandon their homes. The increase in hydraulic pressure on the ice jam due to the increase in water level and an increase in temperature can provoke the ice jam to give way. Consequently, a flash flood might be released, causing the ice floes to be carried downstream, sliding, rolling, and colliding everything

at high speed, damaging infrastructures and bringing forth fish mortality, loss of spawning grounds, and even losses of human lives [3]. Similar high-dynamic ice-wave interaction can also be observed in the dam-break of ice-covered reservoirs and some sea ice processes.

Due to the intrinsic complexities of ice-water interactions, these processes and mechanisms have remained largely unpredictable, especially in the case of river ice. Since the effects of ice floes in rivers are of great impact, it is important to understand the processes and mechanisms involved in the dynamic of river ice to assess their potential impacts, which will promote adequate and reliable management decisions. Due to climate change, river ice jams will be more frequent and more disastrous. Thus, it is even more important to rely on accurate prediction tools nowadays to be able to mitigate ice jam floods impacts.

1.2 Literature Review

Since simplified theoretical models cannot completely describe river ice dynamics or wave-ice interactions due to the intrinsic complexity, field measurements were carried out to study river ice processes [4-10] and sea ice [11-13]. However, field experiment data are scarce, insufficient, and expensive due to the high risk involved in drilling holes on ice (especially during transitional seasons), equipment limitations such as the decrease of efficiency in a cold environment, and resources limitations as financial support and personnel expertise [14]. Thus, to provide more insight on wave-ice interactions, laboratory experiments were conducted and offered many advantages over field measurements such as safety, control of conditions affecting ice formation or deformation, and the possibility of isolating a specific phenomenon for analysis [14-23]. In the literature, reported experiments of wave-ice interaction generally cover two scenarios: one or two ice floes interacting with waves [17-19] and hundreds of ice floes colliding with each other [20, 21].

The last few years have seen an increased interest in applying numerical methods to the subject since they are an economical alternative capable of simulating different scenarios, including future changes such as regulations and climate change [24]. Chen et al. [25] developed a one-dimensional Comprehensive River Ice Simulation System (CRISSP1D) based on an already-existing model, RICE [26], that was applied to many rivers. The CRISSP1D system simulates unsteady flows using a four-point implicit finite difference method and mixed flow conditions using the local partial

inertial (LPI) technique [27]. The system considers the surface and floating ice through a two-layer thermal-ice transport model developed by Shen et al. [23], enabling the simulation of border ice, undercover transport, and frazil jam. However, CRISSP1D does not consider ice dynamics, so it is unable to simulate ice jamming. In 2010, another one-dimensional model, MIKE-ICE, was developed to simulate river ice formation using the thermal balance exchanged between the water, the atmosphere, and the river ice [28]. This model combines many physical processes that have been validated individually, but no validation has yet been performed to verify the capacity to simulate the rapid ice cover change in warm water. A one-dimensional open-source model, RIVICE, was developed by Lindenschmidt [29] to simulate river ice processes that lead to ice jam formation, such as ice transportation and ice cover progression. In RIVICE, an implicit finite difference scheme is used to solve the Saint-Venant equations. A stochastic model for ice jam flood events can be obtained since RIVICE's short computational time allows a Monte-Carlo framework to be embedded. Even though RIVICE was proven to give good estimates of flooding levels, it does not consider flood waters that rise above riverbanks and may have diverted around the ice jam. Since one-dimensional models demand lower computational resources and provide a general picture of the ice processes, which is useful for many applications, they are widely used nowadays for river ice processes in long reaches. However, when dealing with non-uniform water flows and complex geometries, two-dimensional models give a better insight into the complex interaction between water and ice [24, 30].

This is the main reason why the developers of the aforementioned CRISSP1D worked on expanding it to a two-dimensional model CRISSP2D [31]. The latter generalized the DynaRICE model [30] to include thermal-ice processes. DynaRICE is a two-dimensional dynamic river ice model that simulates surface ice transportation and jamming in rivers. In this model, the Eulerian mesh-based finite element method (FEM) is used to simulate the hydrodynamic component, while the Lagrangian particle-based method smoothed particle hydrodynamics (SPH) [32, 33] simulates the ice dynamics. DynaRICE was found useful in determining the maximum load an ice boom can bear before it breaks.

Ensuingly, a range of three-dimensional mesh-based methods has been applied to solve the water-ice interaction problems [34-38]. Nevertheless, free-floating solids in free-surface flows is still a challenge due to the computational complexity involved in the boundary tracking and re-meshing

techniques as well as the splashing, fragmentations, merging, and multiple body interactions present in river ice jams problems.

Instead of simulating ice parcels using a continuum description, where the accuracy depends largely on the ice rheological models, a discrete description can be adopted since it has been proven to describe the underlying physics in detail. The Discrete Element Method (DEM), introduced by Cundall and Strack [39], where an assembly of independent particles is used, has been extensively used to study ice mechanics. For instance, the studies of Hopkins and Hibler [40] and Løset [41], where systems of two-dimensional discs were used to represent ice floe fields, are considered pioneering works on the description of ice behavior using DEM. Furthermore, based on previous DEM studies [42, 43], Hopkins [44] used a two-dimensional polygonal DEM approach to simulate the sea ice floes displacement caused by wind stress and water drag. The ice floes thickness model was based on the work of Ebert and Curry [45], where the ice dynamic incorporates: a lead parameterization that considers a minimum lead fraction, the absorption of solar radiation in and below the leads, the lateral accretion and ablation of the sea ice, and a prescribed sea ice divergence rate. Later, Hopkins and Daly [46] proposed a model in which not only the drag force but also the buoyancy and pressure forces were included. This model combines a three-dimensional DEM with a one-dimensional hydraulic model solved using a four-point implicit discretization scheme whose transverse and vertical geometry and flow data are averaged. Hopkins and Shen [47] and Dai et al. [20] studied pancake-ice dynamics using a three-dimensional DEM model in which the circular floes are formed during ice growth in a wave field. Stockstill et al. [48] took a step forward and combined the three-dimensional DEM with two-dimensional depth-averaged shallow-water equations solved using a finite element (FE) scheme. This model successfully simulated ice transportation and accumulation and the interaction between ice and hydraulic structures. Karulin and Karulina [49] investigated moored tanker’s behaviour in broken ice using the DEM approach. Paavilainen and Tuhkuri [50] coupled the finite element scheme with the DEM method to study the ice rubbling process, where the response of an ice sheet was modeled using the FE scheme, and the contact forces were modeled with DEM. The pressure distributions during selected peak load events were numerically investigated, with special attention on the effects of a loose rubble pile in front of the structure on the pressure distribution. In another study, performed by Ji et al.[51], the influences of ice velocity, ice thickness, and conical angle on ice loads in conical offshore

structures are analyzed using DEM. Ji and Liu [52] took a step forward and used dilated polyhedral elements in DEM based on the Minkowsi sum theory to simulate interactions between ice floes and the floating structure Kulluk, and the results were validated against field data. Herman et al. [53] used DEM to study the ocean waves' energy dissipation due to ice-water drag and ice floe collisions. In Gong et al. [54], a three-dimensional discrete element method was used to study the resistance of a ship in ridges of equal depth but different widths. Extensive reviews on different DEM approaches used to solve ice-related problems are found in Metrikin and Løset [55], Tuhkuri and Polojärvi [56], and Xue et al. [57]. However, in most of the studies mentioned, simplified equations for flow models based on depth-averaged hydraulic models, potential flow theory or finite element solutions, are used. Thus, highly dynamic ice-wave interactions cannot be reproduced accurately.

Several methods exist to represent solid ice in DEM, but among the various representations adopted, two representations are used in several works due to their efficiency and robustness. The first method consists of representing solid ice as individual discrete particles. In such a method, both solid and fluid phases have a similar size. The other method consists of representing solid ice as a collection of particles whose relative positions are fixed. Such a method is known as the multisphere method [58]. The advantage of such a method over the individual discrete particle method is that complex-shaped and large-scale ice bodies can be simulated.

In recent years, the mesh-free particle-based (Lagrangian) methods, such as smoothed particle hydrodynamics (SPH) [32] and moving particle semi-implicit (MPS) [59], opened new perspectives for modeling the fluid-solid interaction problems. The SPH method was developed to solved astrophysical problems with compressible inviscid flows, while MPS was developed for incompressible flows with free surfaces [60]. An artificial viscosity had to be added in SPH to solve free-surface water-flows problems [61]. Originally in MPS, the pressure on each particle is calculated by solving the Poisson equation implicitly. To reduce the computational cost, Shakibaeinia and Jin [62] suggested an explicit formulation where an Equation of State is used instead to determine the pressure. The main difference between the MPS and SPH methods lies in the spatial discretization formulation. In SPH, a superposition of kernels is used, while in MPS, the weighted average of differences is employed [60]. Due to their ability to deal with large deformations and fragmentations in the continuum, these methods are widely used for many fluid

flow problems. In these methods, each particle containing a set of continuum field variables such as mass and momentum moves in the Lagrangian system and satisfies the equations of mass, momentum, and energy conservation [62]. Although these methods have several advantages, they also have some drawbacks, such as being susceptible to unphysical pressure fluctuations, particle clustering [63-66], and momentum conservation violations [67]. In recent years, enhancement techniques to improve accuracy and stability were developed, such as particle stabilizing and regularization techniques [59, 63-68] and momentum conservation frameworks [69-73].

In a fully-Lagrangian framework, fluid-solid interactions can be modeled by a multiphase continuum-discrete system, in which the fluid phase is based on SPH or MPS, while the motion of the solid phase is solved using the DEM. Different engineering-based studies used the SPH/MPS-DEM approach, such as the fluid-solid interaction in a cylindrical tank [74], particle sedimentation [75], river ice dynamics [76], sediment transport in the swash zones [77], and non-Newtonian solid-liquid interaction with the presence of free-surface flow [78]. Concerning the latter representation, some works proposed the numerical approach combining SPH/MPS and DEM mainly for the simulation of rigid bodies transport under free-surface flow [52, 79-82]. Kawano and Ohashi [83] conducted numerical simulations of water-ice interaction by using particle agglomeration with MPS. They reproduced the process of growth and accumulation of crystal nuclei and the formation process of the layer of fine crystals. The sea ice crystal growth from the sea surface was simulated by the Voronoi dynamics technique [84]. However, only calm sea condition was considered, and collisions between solids were not modeled. Besides this work, few recent studies on ice dynamics and ice-wave interactions are using DEM-SPH/MPS particle-based methods and, to the author's knowledge, are limited to Zhang et al. [85] and Robb et al. [76]. In Zhang et al. [86], an ice floe subjected to surge, heave, and displacement caused by regular waves was simulated. In the model proposed by Robb et al. [76], circular (2D) and spherical (3D) particles were used when contact is important, i.e., when high concentrations of ice are considered. The contact forces are calculated using a soft-sphere method, which is used in this thesis and is explained in more detail in Section 4.2. On the other hand, when instantaneous collisions are assumed, Robb et al. [76] used arbitrarily shaped objects to represent solids using a hard-sphere model (see Section 4.2 for more details on the hard-sphere model).

1.3 Problem Statement

As mentioned in Section 1.2, reported wave-ice interaction experiments generally deals with two scenarios:

1. one or two ice floes interacting with waves [17-19];
2. hundreds of ice floes colliding with each other and subjected to waves [20, 21] and towing carriage [22, 23]

There is a gap between these two situations. While using one or two ice floes is a good start for model validation, it cannot reproduce the general highly dynamic characteristics of river ice processes. On the other hand, using an experimental test case involving hundreds of ice floes colliding with each other for validation would be very computationally demanding. Thus, simplified experimental tests with a reduced number of ice floes and capable of reproducing the highly dynamic nature of river ice processes for numerical validation are missing.

Furthermore, as stated in Section 1.2, few numerical models using Lagrangian methods were developed and used to simulate river ice processes. Zhang et al. [85] studied the velocity of a single ice floe and did not consider collision with other ice floes. Robb et al. [76] considered arbitrarily shaped objects only when the collision between particles is almost non-existent. However, in river ice, there are usually several collisions between the solids. In the case of a high number of collisions, Robb et al. [76] were only able to simulate individual spherical particles. Thus, there is still no numerical model available for simulating river ice processes involving a different number of ice floes of different shapes and sizes and capable of dealing with the highly dynamic water and ice interaction.

CHAPTER 2 OBJECTIVES AND ORGANIZATION OF THE WORK

2.1 Research objectives

The overall goal of this research is to provide reliable tools for the prediction of the dynamics of ice. The two specific objectives of this study are to:

1. perform experimental benchmark cases capable of reproducing the main characteristics of an ice jam release for validation of any multi-body motion models with applications for ice-wave interaction problems.
2. develop a model capable of simulating ice-water interactions using the Lagrangian methods.

Lagrangian methods are used in this research because they offer several advantages over the conventional mesh-based methods [87]. Lagrangian methods, also known as mesh-free particle methods, have been developed in recent years to solve computational fluid dynamic problems and use particle positions to determine the motion of the flow [88]. Besides being more robust and accurate than Eulerian methods, these methods are easier to implement computationally. They do not need to track the free surface or use mesh treatments, and they are capable of simulating phenomena with high fragmentations and deformation [88]. These characteristics make these models ideal for simulating highly-dynamic multi-physics problems such as the release of a river ice jam. In the Lagrangian model, particles containing a set of field variables such as mass and momentum move in the Lagrangian system and satisfy the equations of mass, momentum, and energy conservation [88]. In this research, the two Lagrangian methods used are the Moving Particle Semi-Implicit (MPS) method and the Discrete Element Method (DEM). The MPS method simulates the water flow, while the DEM model is used to simulate the solid ice phase, as shown in **Figure 2.1**.

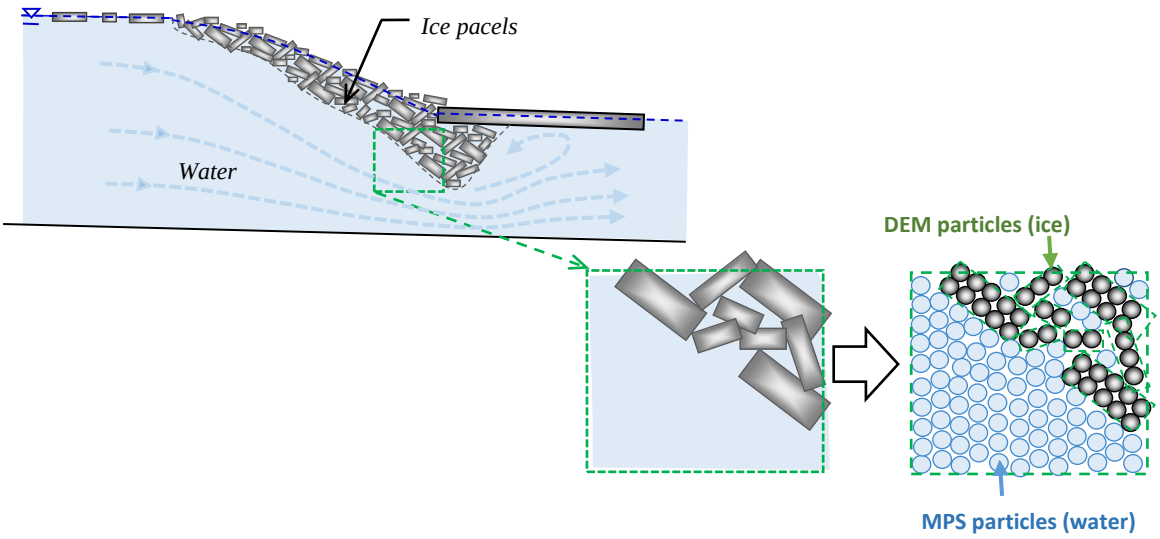

Figure 2.1 - MPS and DEM representation of water and ice, respectively

2.2 Organization of the work

In Chapter 3, the setup and results of the experimental test cases are explained and presented. In Chapter 4, the DEM theory and discretization are described. Also, the model is validated in 2D and 3D with experimental results and with numerical results obtained from widely used open-source models. In Chapter 5, the MPS model is explained, and some enhancement techniques are presented. Moreover, the MPS-DEM coupling is described, and a 2D benchmark numerical test case is presented to validate the proposed model. Finally, the concluding remarks are provided in Chapter 6 as well as some recommendations for future work.

CHAPTER 3 THREE-DIMENSIONAL EXPERIMENTAL DAM BREAK TEST CASES WITH FLOATING BLOCKS

3.1 Introduction

Useful and comprehensive experimental benchmark cases for the investigation of the river ice jams are scarce in the literature. Hence, the author of this thesis performed some experiments that mimic the characteristics of this highly nonlinear phenomenon in the Hydraulic Laboratory of École Polytechnique of Montreal. Although this experiment is a simplification of a real jam release, it provides the basic solid-wave interactions needed as a benchmark for validation as used in the article found in Appendix A, which this thesis' author co-authored. The imagery data from two high-speed cameras have been analyzed and used to track the highly dynamic motion of the blocks and water surface profiles.

3.2 Experimental setup

Characteristics of jam releases and breaches of ice-covered reservoirs, such as having high magnitude waves with floating ice parcels, were recreated by a series of dam-break case scenarios with floating blocks. The present test cases were selected based on their high-dynamic nature, simple geometry, reduced number of ice floes, and valuable data for numerical validation.

3.2.1 Experimental apparatus

The experiments, conducted at the hydraulic laboratory of the École Polytechnique of Montreal, were performed using a prismatic plexiglass tank having interior dimensions of 70 cm length, 15 cm width, and 30 cm height, as shown in **Figure 3.1** (a). The tank is divided into two parts by a removable gate of 0.5 cm thickness. The upstream part has a length of L_{up} = 15 cm and water height of H_{up} = 15 cm, while the downstream part has a length of L_{do} = 55 cm and variable water heights H_{do}, respectively, as depicted in **Figure 3.1** (b). Blocks made of artificial ice material are placed on the surface of the upstream reservoir. A reference frame having the origin at point A has been adopted for analysis purposes. The gate was lifted through a pulley-weight mechanism to release the water column and replicate the dam-break event, as shown in **Figure 3.1** (b). The gate's sides

were sealed with flat and flexible vinyl strips and high-vacuum grease to ensure the reservoir's water tightness.

As depicted in **Figure 3.1** (b), two cameras were used to track each block's horizontal (x-axis) and vertical (y-axis) motions. **Figure 3.2**A high-speed camera (FASTCAM Mini WX100), capable of taking 1080 frames per second (fps) with a 2048 × 2048 resolution, was placed on top of the tank, and another one (Sony DSC-RX100M5A) with 480 fps and 1292 × 436 resolution was placed at the front of the tank. As shown in **Figure 3.3**, an AOS Offboard 150W Led light source, having a high-frequency to eliminate flicker issues, was used.

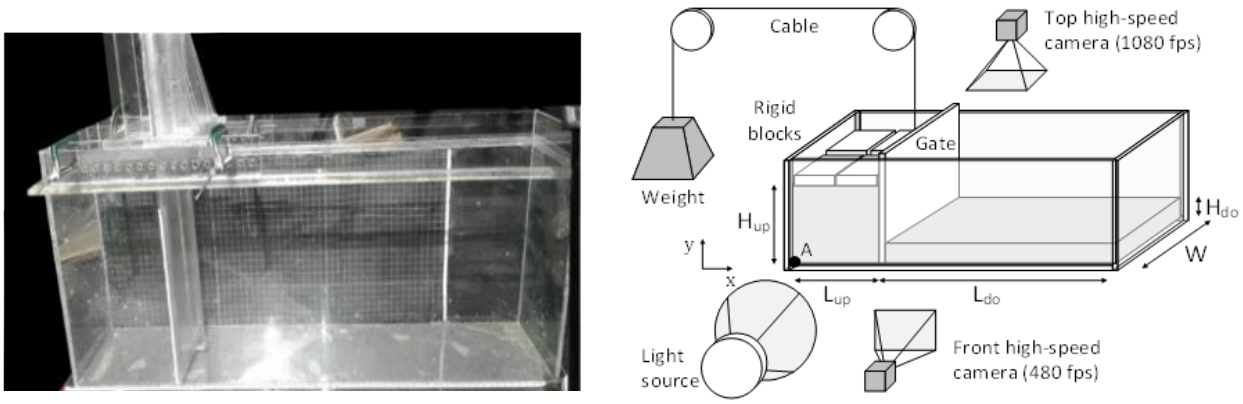

(a) (b)

Figure 3.1 - (a) Prismatic plexiglass tank used in the dam-break experiments. (b) Schematic drawing of the tank, water levels, gate, rigid blocks, pulley-weight mechanism, cameras disposition, and light source.

(a) (b)

Figure 3.2 - (a) The FASTCAM Mini WX100 placed above the tank. (b) The camera Vixia HF S200 camera placed in front of the tank

Figure 3.3 - The AOS Offboard 150W Led light source

3.2.2 Experimental material

Blocks of white polypropylene, having a density of approximately 868 kg/m^3, were used as the artificial ice floes. However, a higher density of around 0.92 kg/m^3 can better estimate river ice floes density. The static friction coefficient between each block was found experimentally using the setup shown in **Figure 3.4**.

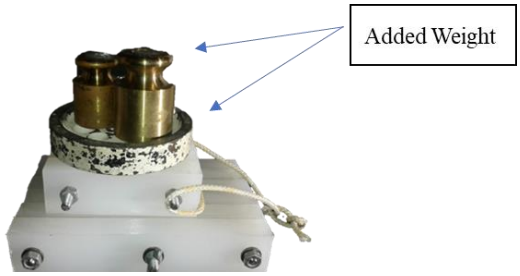

Figure 3.4 - Sets of polypropylene strips and weights

Two sets of polypropylene strips were used, where the top set was free to move, and the bottom one was fixed to the table. Knowing that the blocks are wet during the experiment, the two sets were soaked wet before applying a horizontal force. The normal force was defined by putting additional weight above the top set, and the shear force was obtained by measuring the force required to move the block horizontally with a dynamometer. The different masses put on top of the sets, the average measured shear force, and the corresponding friction coefficients calculated as the ratio of the shear force to the normal force are shown in **Table 3.1**.

Table 3.1 - Masses used to determine the coefficient of friction

Tries	*Mass (g)*	*Shear force (g)*	*Coefficient of Friction*	*Tries*	*Mass (g)*	*Shear force (g)*	*Coefficient of Friction*
1	1702	675	0.397	*10*	2135	900	0.422
2	1702	700	0.411	*11*	2135	900	0.422
3	1702	675	0.397	*12*	2135	850	0.398
4	1702	650	0.382	*13*	2135	925	0.433
5	1702	750	0.441	*14*	2668	1050	0.394
6	2002.5	750	0.375	*15*	2668	1150	0.431
7	2002.5	825	0.412	*16*	2668	1225	0.459
8	2002.5	850	0.424	*17*	2668	1025	0.384
9	2002.5	900	0.449	*18*	2668	1100	0.412
	Average				0.413		
	Median				0.412		
	Standard deviation				0.023		

The median static friction coefficient found for the wet blocks used in the article in Appendix A [89] was $\mu_s=0.412\pm0.050$. The present test did not consider the effect of sliding speed, temperature, and surface tension on the friction coefficient. Furthermore, the kinetic friction coefficient should be used in the simulation instead of the static friction coefficient. However, this set of tests is useful to provide a reference value for the material's kinetic friction coefficient since a wide range of values [0.1, 0.6] given by a function of the velocity of the interaction, has been used in previous papers for the actual ice-ice friction coefficient [90, 91]. Furthermore, in the dam-break case scenarios, the friction forces are relatively small compared to the other solid collision forces.

3.2.3 Experimental case scenarios

Eight case scenarios, summarized in **Table 3.2,** were carried out where a different number of polypropylene blocks and downstream water heights have been used. In the first four cases, four equal-size polypropylene blocks were used. Each block has dimensions (width x length x thickness) 7.25 x 7.25 x 1.95 ± 0.06 cm and a mass of 0.089 ± 0.001 kg. The other four cases used nine polypropylene blocks of 4.80 x 4.80 x 1.95 ± 0.06 cm, each having a mass of 0.039 ± 0.001 kg. Four downstream water heights, i.e., H_{do} = 0, 1.0, 2.5 and 5.0 cm, were tested. Each case was repeated at least three times to ensure reliability, and the three repeated experiments of each case are denominated EXP1, EXP2, and EXP3.

Table 3.2 - Experimental case conditions - Number of blocks, upstream (H_{up}) and downstream (H_{do}) water height.

Cases	Number of blocks	H_{up} (cm)	H_{do} (cm)
1	4	15	0.0
2			1.0
3			2.5
4			5.0
5	9		0.0
6			1.0
7			2.5
8			5.0

3.2.4 Data acquisition

The water surface profile evolution and displacement of ice blocks were determined by processing high-speed imagery data from the top and front cameras. The blocks' displacements in x and y directions were determined by tracking the center of mass (CM), shown in **Figure 3.5**, of each

block using a free video analysis software called Tracker [92]. Furthermore, the water surface profile was obtained by digitizing images extracted from the videos taken by the front camera. The results were then used to validate the numerical model in [89] (see Appendix A).

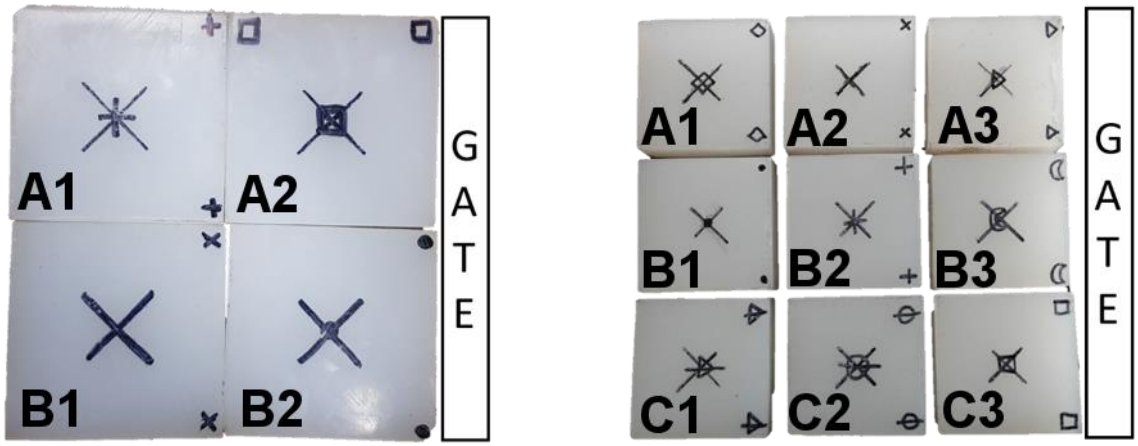

(a) (b)

Figure 3.5 - Initial arrangement of the cases with (a) 4 blocks and (b) 9 blocks.

3.2.5 Gate motion

The vertical gate motion's time series for the 24 experiments are presented in **Figure 3.6**. A sudden dam break can be assumed if the removal, t_r, is less than $\sqrt{2H_{up}/g}$ [93]. In the present experiments, the gate removal duration, estimated as the time required for the gate's lower edge to reach the dam filling height, was around 0.40 s and did not satisfy the criterion

$t_r < \sqrt{2 \times 0.15/9.81} \rightarrow t_r < 0.175$ s. Thus, sudden dam breaks cannot be assumed in the present test cases. Numerical models must include the gate motion since its presence significantly influences the water collapse process and the blocks' motions.

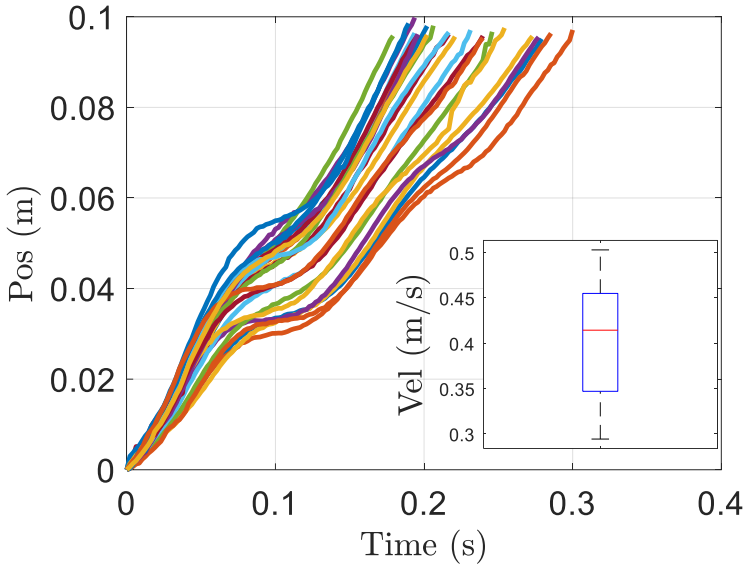

Figure 3.6 - Time series of the vertical gate motion for all 24 experiments and the median value of gate velocity.

3.3 Results and discussion

3.3.1 Dam breaking with four blocks

Figures 3.7 to **3.10** show the water surface profile and the four blocks' motion evolution with time. These figures show only one of the three runs performed. The dry-bed test case is shown in **Figure 3.7**, while the wet-bed having H_{do}=1cm is shown in **Figure 3.8**, H_{do}=2.5cm in **Figure 3.9**, and H_{do}=5cm in **Figure 3.10**. As seen from the figures, after the wave impacts the downstream wall, a backward wave is generated, and the blocks are pushed in the upstream direction. If we compare **Figures 3.7 (b)** to **3.10 (b)**, the effect of the downstream water level can be observed. As the downstream water level increases, the blocks' positions are more restricted in the upstream region. Thus, the downstream water level affects the gravity-driven flow. Indeed, in **Figure 3.10**, the blocks are maintained in the upstream end until t=1.60 s because the downstream height is higher. On the other hand, in **Figure 3.7**, where a dry bed is used, the blocks A2 and B2 have almost reached the downstream end at t = 1.20 s. Furthermore, a mushroom-like jet is generated when a downstream fluid layer is present, as previously reported by Stansby et al. [94] and Jánosi et al. [95]. As the downstream water height increases, the mushroom size increases. This mushroom jet

also affects the blocks' motion, and as its size increases, the blocks' motion is less chaotic. Also, the presence of this jet reduces splashing when the wave impacts the downstream wall. For instance, if we compare **Figures 3.7 (c)** to **3.10 (c)**, it can be observed that as the downstream water level increases, the splashing of water is reduced.

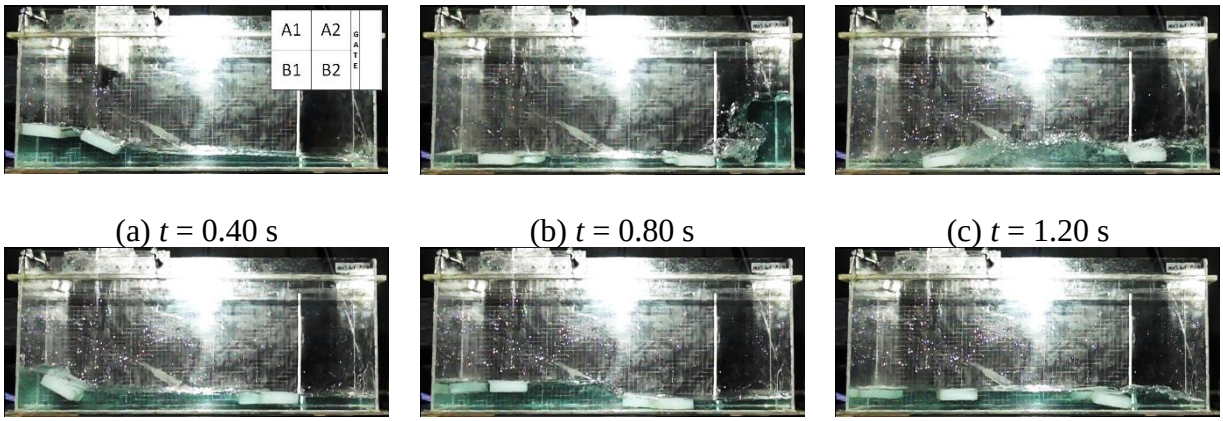

(a) t = 0.40 s (b) t = 0.80 s (c) t = 1.20 s

(d) t = 1.60 s (e) t = 2.00 s (f) t = 2.40 s

Figure 3.7 - Snapshots of the experimental and numerical dam breaking with 4 blocks and dry bed at the instants t = 0.40, 0.80, 1.20, 1.60, 2.00, 2.40 s (front view).

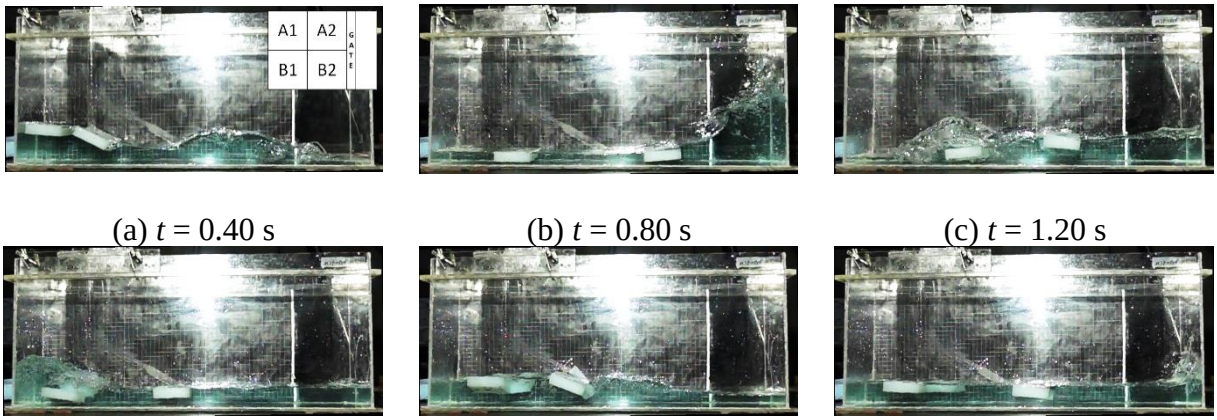

(a) t = 0.40 s (b) t = 0.80 s (c) t = 1.20 s

(d) t = 1.60 s (e) t = 2.00 s (f) t = 2.40 s

Figure 3.8 - Snapshots of the experimental and numerical dam breaking with 4 blocks and wet bed Hdo = 1 cm at the instants t = 0.40, 0.80, 1.20, 1.60, 2.00, 2.40 s (front view).

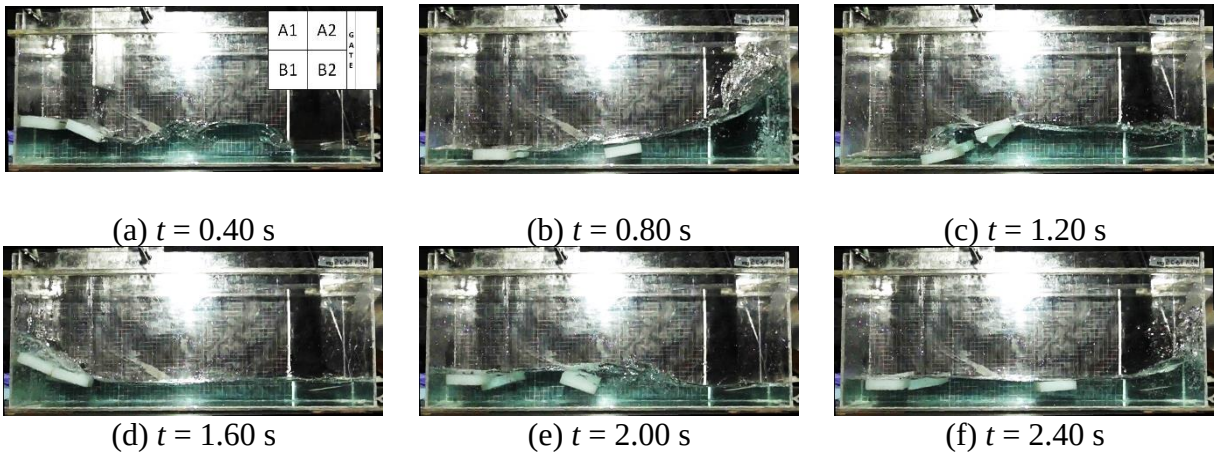

(a) t = 0.40 s (b) t = 0.80 s (c) t = 1.20 s

(d) t = 1.60 s (e) t = 2.00 s (f) t = 2.40 s

Figure 3.9 - Snapshots of the experimental and numerical dam breaking with 4 blocks and wet bed Hdo = 2.5 cm at the instants t = 0.40, 0.80, 1.20, 1.60, 2.00, 2.40 s (front view).

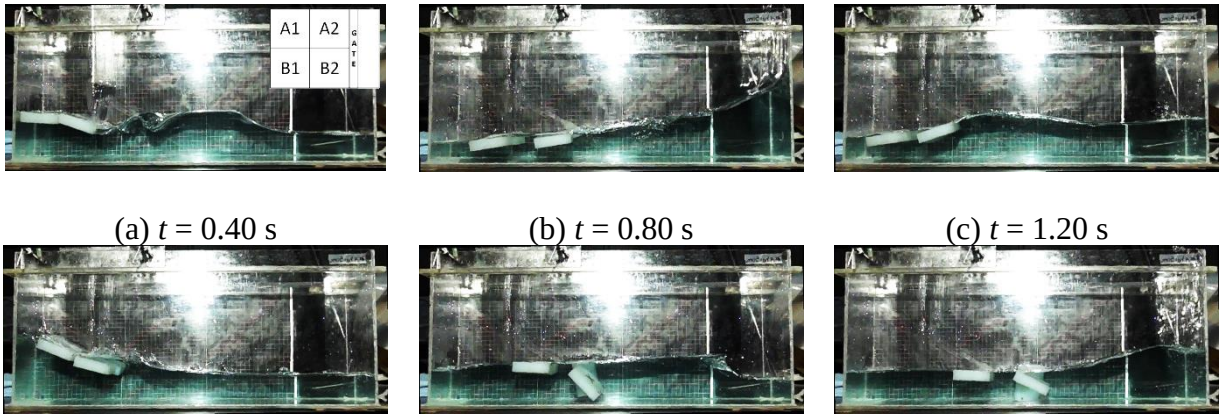

(a) t = 0.40 s (b) t = 0.80 s (c) t = 1.20 s

(d) t = 1.60 s (e) t = 2.00 s (f) t = 2.40 s

Figure 3.10 - Snapshots of the experimental and numerical dam breaking with 4 blocks and wet bed Hdo = 5 cm at the instants t = 0.40, 0.80, 1.20, 1.60, 2.00, 2.40 s (front view).

The blocks' center of mass were tracked for the three trials EXP1, EXP2, and EXP3 and were plotted in **Figures B1** to **B8** in Appendix B. **Figures B1** to **B4** show the longitudinal motion of all four blocks for dry bed and water bed with H_{do} = 1cm, 2.5 cm, and 5cm. **Figures B5** to **B8** show the vertical motion of blocks B1 and B2 for dry bed and water bed with H_{do} = 1cm, 2.5 cm, and 5cm. It can be seen from the figures that the blocks have similar motion until t = 1.5 s, after which the blocks exhibit chaotic behaviors due to the backwater wave.

3.3.2 Dam breaking with nine blocks

Snapshots of the water surface profile and the blocks' motion evolution in time are depicted in **Figures 3.11** to **3.14**. Once more, these figures show only one of the three total runs performed. The dry-bed test case is shown in **Figure 3.11**, while the wed-bed having H_{do}=1cm is shown in **Figure 3.12**, H_{do}=2.5cm in **Figure 3.13**, and H_{do}=5cm in **Figure 3.14**. As seen in the four-block test cases, the blocks are pushed in the upstream direction by the backwater wave, a mushroom-like jet is generated when a downstream fluid layer is present, and as the downstream water level increases, the splashing is reduced. In the nine-block test cases, a more chaotic motion of the solids is generated due to the blocks having smaller dimensions.

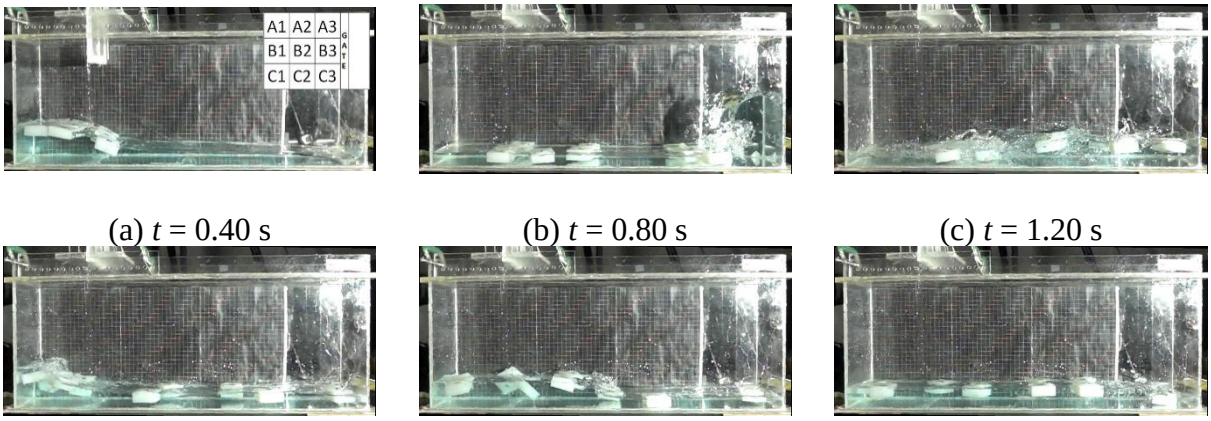

(a) t = 0.40 s (b) t = 0.80 s (c) t = 1.20 s

(d) t = 1.60 s (e) t = 2.00 s (f) t = 2.40 s

Figure 3.11 - Snapshots of the experimental and numerical dam breaking with 9 blocks and dry bed at the instants t = 0.40, 0.80, 1.20, 1.60, 2.00, 2.40 s (front view).

(a) t = 0.40 s (b) t = 0.80 s (c) t = 1.20 s

(d) t = 1.60 s (e) t = 2.00 s (f) t = 2.40 s

Figure 3.12 - Snapshots of the experimental and numerical dam breaking with 9 blocks and wet bed Hdo = 1 cm at the instants t = 0.40, 0.80, 1.20, 1.60, 2.00, 2.40 s (front view).

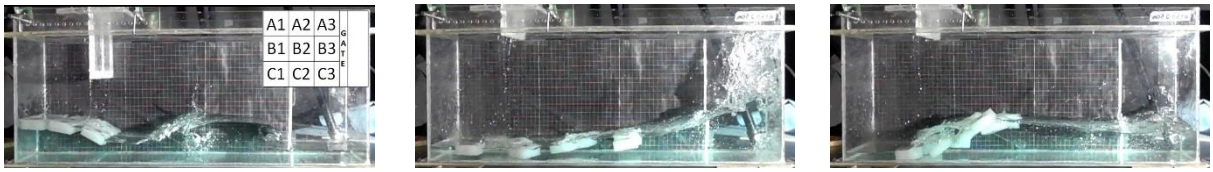

(a) t = 0.40 s (b) t = 0.80 s (c) t = 1.20 s

(d) t = 1.60 s (e) t = 2.00 s (f) t = 2.40 s

Figure 3.13 - Snapshots of the experimental and numerical dam breaking with 9 blocks and wet bed Hdo = 2.5 cm at the instants t = 0.40, 0.80, 1.20, 1.60, 2.00, 2.40 s (front view).

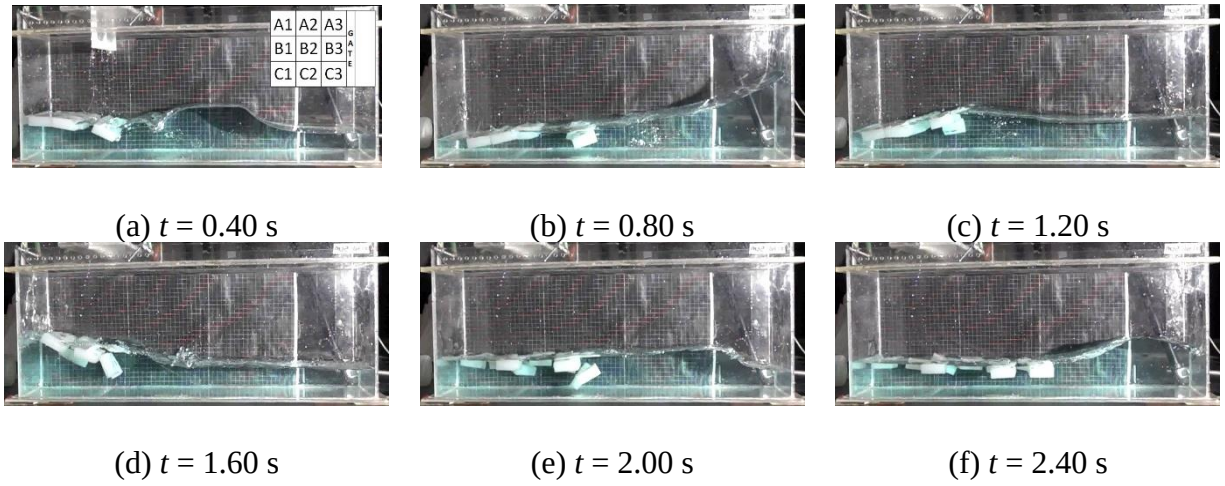

(a) t = 0.40 s (b) t = 0.80 s (c) t = 1.20 s

(d) t = 1.60 s (e) t = 2.00 s (f) t = 2.40 s

Figure 3.14 - Snapshots of the experimental and numerical dam breaking with 9 blocks and wet bed Hdo = 5 cm at the instants t = 0.40, 0.80, 1.20, 1.60, 2.00, 2.40 s (front view).

Figures B9 to **B20** in the Appendix B provide the experimental longitudinal and vertical motions of blocks C1, C2, and C3 for the dry-bed and wet-bed test cases.

3.4 Conclusion

In conclusion, this chapter presents a series of experimental cases performed by this thesis' author, which can be employed as simple 3D benchmark cases to validate river ice models, as used in the paper [89] (see in Appendix A). Such benchmark cases are scarce in the literature. Eight case scenarios were carried out in total. In the first four cases, four equal-size polypropylene blocks were used, and in the next four cases, nine polypropylene blocks were used. For each case, four downstream water heights, i.e., H_{do} = 0, 1.0, 2.5, and 5.0 cm, were adopted. Also, each case was repeated at least three times to ensure reliability. It was observed that a backward wave is generated after the wave impacts the downstream wall. This wave pushed back upstream the blocks in a chaotic behavior. Furthermore, when a downstream fluid layer is present, a mushroom-like jet is generated, as previously observed by Stansby et al. [94] and Jánosi et al. [95]. As the downstream water height increases, the mushroom increases in size, and the blocks' downstream motion is reduced. By tracking each block's center of mass, it was observed that although all blocks follow a similar trend, they exhibit different behavior between each trial. Such disparities are explained by the intrinsic complexity and non-linearity nature of this experiment.

CHAPTER 4 DEM MODEL AND VALIDATION

In this Chapter, a DEM model is developed and validated. The discrete element method (DEM) is a Lagrangian numerical method proposed by Cundall and Strack [39] originally used to model and investigate granular flows at the microscopic level with discrete independent particles whose motion is defined by the interparticle interactions. This method was subsequently applied to a wide range of fields ranging from mechanical engineering to chemical engineering [96] and modified to simulate particles with different shapes.

In DEM, a particle's change in position and velocity is determined explicitly by integrating Newton's Second Law of motion at each time step. Within a time step, each particle's physical properties, such as position, angular and translational velocity, and contact forces, are assumed to be constant [96].

4.1 Governing Equations

The translation and rotational change in position and velocity of particle *i* are determined by explicitly integrating the following equations:

$$\mathbf{v}_i = \frac{d\mathbf{x}_i}{dt} \tag{4.1}$$

$$m_i \frac{d\mathbf{v}_i}{dt} = \mathbf{F}_{g,i} + \mathbf{F}_{h,i} + \sum_j \mathbf{F}_{c,ij} \tag{4.2}$$

$$\mathbf{I}_i \cdot \dot{\boldsymbol{\omega}}_i + \boldsymbol{\omega}_i \times (\mathbf{I}_i \cdot \boldsymbol{\omega}_i) = \mathbf{M}_{h,i} + \sum_j \mathbf{M}_{c,ij} \tag{4.3}$$

where **x**, **v,** **ω**, and **I** are the position, the velocity, the angular velocity, and the inertia matrix of the particle, respectively. $\mathbf{F}_g$ is the gravitational force, and $\mathbf{F}_h$ is the hydrodynamic force, which is non-zero when water is present. The calculation of $\mathbf{F}_h$ is described in Section 5.2 $\mathbf{F}_{c,ij}$ is the contact force generated by the collision between particles *i* and *j* and is the core of DEM. This force is zero

if there is no collision. Similarly, $\mathbf{M}_{c,ij}$ and $\mathbf{M}_h$ are, respectively, the contact and hydrodynamic torques applied to the particle *i* defined as:

$$\mathbf{M}_{h,i} + \mathbf{M}_{c,ij} = (\mathbf{r}_i - \mathbf{r}_{COM,i}) \times (\mathbf{F}_{h,i} + \mathbf{F}_{c,ij}) \tag{4.4}$$

where $\mathbf{r}_i$ and $\mathbf{r}_{COM,i}$ are the position of the particle and its center of mass.

When simulating individual spherical particles, the center of mass coincides with the particles' position and Equation (4.4) drops to zero.

4.2 The Contact Forces

There exist two approaches for modelling the collision of rigid particles and calculating the contact force between them: the hard-sphere contact model and the soft-sphere contact model. In the hard-sphere contact model, the contact between two particles is considered instantaneous and governed by the restitution coefficient, which is defined as the ratio of the approaching relative velocity to the separating relative velocity. In this method, the particles' motion is not determined by the interparticle force, but the after-collision velocity is calculated using the restitution coefficient [76]. One of the hard-sphere model's drawback is that it is only valid when the particles are in motion. When the particles' velocities approach zero, for instance, when equilibrium is reached, this method is no longer valid [76, 97]. In the soft-sphere model, particles are allowed to have a slight overlap, whose amount is used to calculate the contact (normal and tangential) between particles. Hertzian model [76] are widely used approaches for calculating this contact force, based on elastic and plastic deformations as well as frictional forces. The soft-sphere model is the most widely used because it is efficient in special situations such as in dense regimes where there are multiple contacts and in the presence of additional forces such as hydrodynamic forces [97]. For all these reasons, this method is used in this thesis.

Figure 4.1 shows a simplified DEM algorithm that starts by detecting collision and calculates the total force that includes the contact force and the external forces, such as gravity and the hydrodynamic forces. In this chapter, the DEM governing equations and the numerical implementations are discussed.

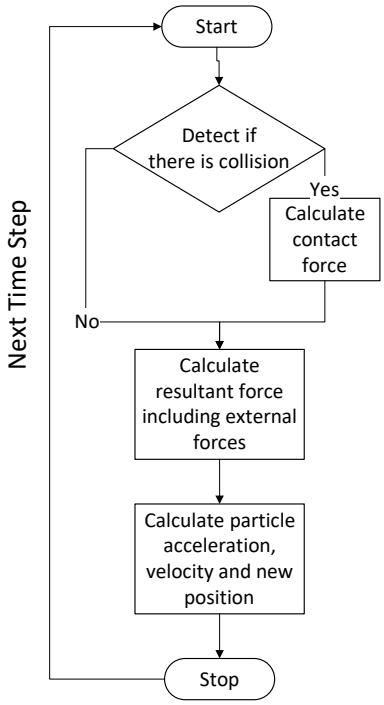

Figure 4.1 - Simple DEM algorithm

In the soft-sphere method, when two particles overlap each other, a collision is detected. The repulsion force between the particles is known as the contact force in DEM. The contact force is proportional to the overlap and the particles' diameter. This force also depends on the material properties such as the Young's Modulus, the Poisson ratio, the friction coefficient, and the restitution coefficient [98].

In 3D, the overlap is represented by a contact plane. As depicted in **Figure 4.2**, the contact plane can be decomposed in a normal, $\mathbf{n}_{ij}$, and tangential, $\mathbf{t}_{ij}$ unit vector. When there is a collision, the normal overlap is positive and is defined as:

$$\delta_{n,ij} = \left(R_i + R_j\right) - \left\|\mathbf{r}_j - \mathbf{r}_i\right\| \tag{4.5}$$

The position vectors of particles i and j are $\mathbf{r}_i$ and $\mathbf{r}_j$, respectively, and R_i and R_j are the particles' radii.

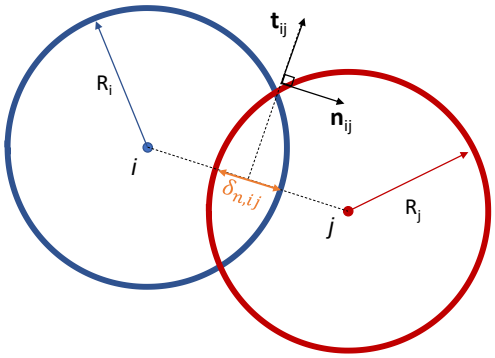

Figure 4.2 - Contact Plane

The contact force is defined as the sum of the normal and tangential contact forces:

$$\mathbf{F}_{c,ij} = \mathbf{F}^{c}_{n,ij} + \mathbf{F}^{c}_{t,ij} \tag{4.6}$$

The normal and tangential contact forces are found using the Hertzian model shown in **Figure 4.3**, where a spring (elastic) and dashpot (dissipative) system are implemented. These forces are explained in detail in Sections 4.2.1 and 4.2.2.

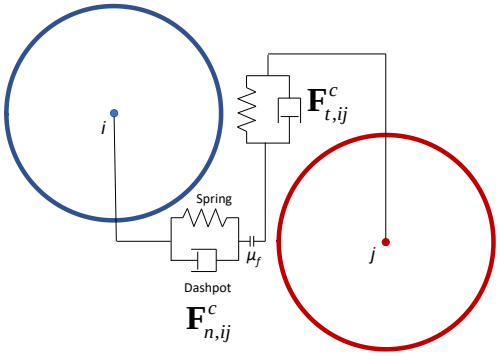

Figure 4.3 - Hertzian model with the spring and dashpot system

4.2.1 The normal contact force

The elastic and dissipative components of the normal contact force are defined as:

$$\mathbf{F}_{n,ij}^{c} = \mathbf{F}_{n,ij}^{e} + \mathbf{F}_{n,ij}^{d} = \underbrace{-k_{n,ij}\delta_{n,ij}\hat{\mathbf{n}}_{ij}}_{\substack{Normal\ elastic \\ force}} + \underbrace{\gamma_{n,ij}\mathbf{v}_{n,ij}}_{\substack{Normal\ dissipative \\ force}} \tag{4.7}$$

where $k_{n,ij}$ and $\gamma_{n,ij}$ are the normal stiffness and damping coefficients, respectively, and $\mathbf{n}_{ij}$ is the normal unit vector defined in Equation (4.8). $\mathbf{v}_{n,ij}$ is the normal relative velocity between particles *i* and *j* defined in Equation (4.9), where $\mathbf{v}_i$ and $\mathbf{v}_j$ are the velocity vectors of particles *i* and *j*, respectively.

$$\hat{\mathbf{n}}_{ij} = \frac{\mathbf{r}_j - \mathbf{r}_i}{\left\|\mathbf{r}_j - \mathbf{r}_i\right\|} \tag{4.8}$$

$$\mathbf{v}_{n,ij} = ((\mathbf{v}_j - \mathbf{v}_i)\cdot\hat{\mathbf{n}}_{ij})\hat{\mathbf{n}}_{ij} \tag{4.9}$$

The normal stiffness and damping coefficients are calculated as [79]:

$$k_{n,ij} = \frac{4}{3}Y^{*}\sqrt{R^{*}\delta_{n,ij}} \tag{4.10}$$

$$\gamma_{n,ij} = \varepsilon_n\sqrt{6m^{*}Y^{*}\sqrt{R^{*}\delta_{n,ij}}} \tag{4.11}$$

where ε_n, a calibration parameter, is the contact ratio. The other parameters, $Y^{*}, m^{*},$ and R^{*}, are given as:

$$\frac{1}{Y^{*}} = \frac{1-\nu_i^2}{Y_i} + \frac{1-\nu_j^2}{Y_j} \tag{4.12}$$

$$R^{*} = \frac{R_i R_j}{R_i + R_j} \tag{4.13}$$

$$m^* = \frac{m_i m_j}{m_i + m_j} \tag{4.14}$$

where Y is Young's modulus, ν is the Poisson ratio, and R and m are the particle's radius and mass, respectively. If a particle collides with the boundary walls, the same equations are used, but the boundary's radius and mass are treated as infinite values and $R^* = R_i$ and $m^* = m_i$.

4.2.2 The tangential contact force

Unlike the normal contact force, the tangential contact force obtained from the Hertzian model is limited by Coulomb's friction force ($\mathbf{F}_{CF}$) [79]:

$$\mathbf{F}_{t,ij}^{c} = \min(\mathbf{F}_{t,ij}^{e} + \mathbf{F}_{t,ij}^{d}, \mathbf{F}_{CF}) \tag{4.15}$$

According to Coulomb's friction law, the friction force can be obtained by multiplying the normal force by a friction coefficient, μ [99]:

$$\mathbf{F}_t = \mu \mathbf{F}_n \tag{4.16}$$

Since we are interested in particles in motion where the static friction has been overcome, the kinetic coefficient of friction will be used. Furthermore, a continuous sigmoidal function is implemented to avoid the instability caused by the friction force discontinuity at zero velocity [99]. Thus, Equation (4.16) becomes:

$$\mathbf{F}_{CF} = \mu_{f,ij} \left\| \mathbf{F}_{n,ij}^{c} \right\| \tanh(8\dot{\delta}_{t,ij}) \hat{\mathbf{t}}_{ij} \tag{4.17}$$

where $\mu_{f,ij}$ is the average kinetic friction coefficient defined as:

$$\mu_{f,ij} = \frac{\mu_{f,i} + \mu_{f,j}}{2} \tag{4.18}$$

The tangential unit vector to the contact plane, $\mathbf{t}_{ij}$, and the tangential deformation rate, $\dot{\delta}_{t,ij}$, depend on the relative tangential velocity found using the relative and normal relative velocity. Knowing

that the particles' relative velocity can be decomposed in a tangential and normal relative velocity, the tangential relative velocity can be calculated as:

$$\mathbf{v}_{t,ij} = \mathbf{v}_{ij} - \mathbf{v}_{n,ij} \tag{4.19}$$

Since the tangential relative velocity is in the tangential contact plane's direction, the tangential unit vector is obtained by dividing the tangential relative velocity by its magnitude:

$$\hat{\mathbf{t}}_{ij} = \frac{\mathbf{v}_{t,ij}}{\| \mathbf{v}_{t,ij} \|} \tag{4.20}$$

The tangential deformation rate is the projection of the relative tangential velocity in the direction of the tangential unit vector:

$$\dot{\delta}_{t,ij} = \mathbf{v}_{t,ij} \cdot \hat{\mathbf{t}}_{ij} \tag{4.21}$$

The tangential contact force obtained from the Hertzian model is determined similarly to the normal contact force:

$$\mathbf{F}^{e}_{t,ij} + \mathbf{F}^{d}_{t,ij} = k_{t,ij}\delta_{t,ij}\hat{\mathbf{t}}_{ij} + \gamma_{t,ij}\dot{\delta}_{t.ij}\hat{\mathbf{t}}_{ij} \tag{4.22}$$

where

$$k_{t,ij} = \frac{8}{21} Y^{*} \sqrt{R^{*}} \tag{4.23}$$

$$\gamma_{t,ij} = \frac{2}{7} \varepsilon_n \sqrt{6 m^{*} Y^{*} \sqrt{R^{*}}} \tag{4.24}$$

$$\delta_{t,ij} = \dot{\delta}_{t,ij} \Delta t_{DEM} \tag{4.25}$$

The time step, Δt_{DEM}, must be chosen small enough to satisfy the stability of this explicit scheme. In DEM, to evaluate the contact behavior accurately, the time step must be smaller than the contact duration, t_c, which, as can be seen in Equation (4.26), depends on the material properties and the

particles' relative incoming velocities [97]. By maintaining a time step smaller than t_c, the contacts are evaluated several times within a collision. In general, the contact is evaluated from 50 to 100 times within a time step. Thus, in this project, $\Delta t_{DEM} = \frac{t_c}{100}$ [81].

$$t_c = 2.87 \frac{m^{*2}}{R^* Y^{*2} \left\| \mathbf{v}_j - \mathbf{v}_i \right\|} \tag{4.26}$$

4.3 Multisphere method

When simulating individual particles, the particles' motions are relatively easy to obtain once all the forces are calculated. Equations (4.1) and (4.2) are integrated using the linear approximation as:

$$\Delta \mathbf{x}_{t,i} = \mathbf{v}_{t,i} \Delta t_{DEM} \tag{4.27}$$

and

$$\mathbf{v}_{t+\Delta t_{DEM},i} = \mathbf{v}_{t,i} + \Delta t_{DEM} \frac{\mathbf{F}_{tot,i}}{m_i} \tag{4.28}$$

No angular velocity is implemented when dealing with single particles since, as mentioned previously, their position coincides with their centroid, and thus, the torque and angular velocity are zero. When simulating individual particles, spheres are the simplest and easiest shape to implement. However, spheres are not representative of real ice floes, and thus, it is necessary to simulate rigid bodies of various shapes. One way to do so is to change each particle's shape, but the contact detection algorithm gets complicated with non-linear equations. Also, only pre-defined shapes such as ellipsoids and superquadric bodies were successfully simulated [100]. If arbitrary shapes are to be implemented in the future, a different approach must be implemented. Thus, another way of simulating different shapes in DEM is to set a group of particles whose relative positions are constant and that will act as a single rigid body. With this method, not only is contact detection simple, but the body can have any arbitrary shape. This method is known as the multisphere method and is used in this project.

The normal and tangential contact forces of the particles constituting the multisphere are calculated as explained in Sections 4.2.1 and 4.2.2. The only difference is that Equation (4.14) now uses the mass of the colliding bodies and not of the individual particles. The forces are then added together to find the total force acting on the rigid body. The only particles likely to collide with other particles are the ones on the surface of the multisphere. Thus, only the surface particles are included in the calculation, and the translational motion is obtained by modifying Equation (4.2) to:

$$m_B \frac{d\mathbf{v}_B}{dt} = \mathbf{F}_{g,B} + \sum_{i \epsilon \Omega_B} (\mathbf{F}_{h,i} + \mathbf{F}_{c,ij}) \tag{4.29}$$

where $m_B, \mathbf{v}_B$, and $\mathbf{F}_{\mathrm{g,B}}$ are the mass, velocity, and gravity force of the solid rigid body *B*. The contact and hydrodynamic forces calculated on the surface particles of the rigid body *B* are added together to get the net force on the multisphere.

The rotational motion is determined similarly and Equations (4.3) and (4.4) become:

$$\mathbf{I}_B \cdot \dot{\boldsymbol{\omega}}_B + \boldsymbol{\omega}_B \times (\mathbf{I}_B \cdot \boldsymbol{\omega}_B) = \mathbf{M}_{h,B} + \mathbf{M}_{c,B} \tag{4.30}$$

$$\mathbf{M}_{h,B} + \mathbf{M}_{c,B} = \sum_{i \epsilon \Omega_B} (\mathbf{r}_i - \mathbf{r}_{COM,B}) \times (\mathbf{F}_{h,i} + \mathbf{F}_{c,ij}) \tag{4.31}$$

where the parameters of Equations (4.30) and (4.31) are applied to the rigid body *B*.

4.3.1 Two-Dimensional Rotation

When a multisphere undergoes a rotation, all the particles move around the center of mass, as shown in **Figure 4.4**, where the multisphere rotates counterclockwise by θ. The relative position of the particles with respect to the center of mass remains constant if $\|\mathbf{r}\| = \|\mathbf{r}'\|$.

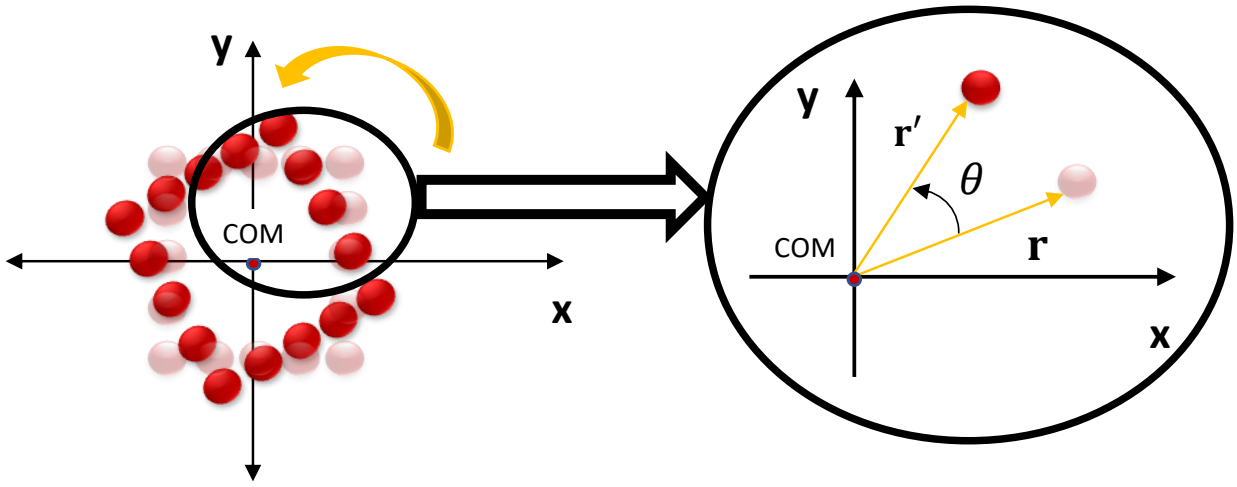

Figure 4.4 - Rotation of a multisphere

The angle θ is determined from the angular velocity, which in 2D is a scalar in one direction:

$$\boldsymbol{\omega} = \begin{bmatrix} 0 \\ 0 \\ \omega_z \end{bmatrix} \tag{4.32}$$

A scalar is also used for the moment of inertia I_z and Equation (4.30) becomes:

$$I_z \dot{\omega}_z \hat{\mathbf{k}} = (M_{h,B} + M_{c,B})\hat{\mathbf{k}} \tag{4.33}$$

where $\hat{\mathbf{k}}$ is the unit vector in the z-direction.

From Equation (4.33), the angular acceleration is obtained and used to update the angular velocity, ω_z, and the angle of rotation θ at each time step:

$$\begin{aligned} \dot{\omega}_z &= \frac{(M_{h,B} + M_{c,B})}{I_z} \\ \omega_z^{t+\Delta t_{DEM}} &= \omega_z^t + \dot{\omega}_z \Delta t_{DEM} \\ \theta^{t+\Delta t_{DEM}} &= \omega^{t+\Delta t_{DEM}} \Delta t_{DEM} \end{aligned} \tag{4.34}$$

The counterclockwise rotation of a particle around a point, as depicted in **Figure 4.4**, is performed by multiplying the current particle's position, $\mathbf{r}$, by a rotation matrix, $\boldsymbol{R}_m$, as:

$$\mathbf{r}' = \mathbf{R}_m \cdot \mathbf{r} \tag{4.35}$$

where $\mathbf{R}_m$ is defined as [101]:

$$\mathbf{R}_m = \begin{bmatrix} r_{11} & r_{12} \\ r_{21} & r_{11} \end{bmatrix} = \begin{bmatrix} \cos(\theta) & -\sin(\theta) \\ \sin(\theta) & \cos(\theta) \end{bmatrix} \tag{4.36}$$

Since $\det(\mathbf{R}_m) = 1$, Equation (4.35) will not change the magnitude of the vector **r**. Combining Equations (4.35) and (4.36), the components of the new position are calculated as:

$$\begin{aligned} r'_x &= r_x \cos(\theta) - r_y \sin(\theta) \\ r'_y &= r_x \sin(\theta) + r_y \cos(\theta) \end{aligned} \tag{4.37}$$

4.3.2 Three-Dimensional Rotation

In 3D, the angular velocity is no longer a scalar, but a three-dimensional vector:

$$\boldsymbol{\omega} = \begin{bmatrix} \omega_x \\ \omega_y \\ \omega_z \end{bmatrix} \tag{4.38}$$

Likewise, the moment of inertia in 3D is a 3-by-3 matrix:

$$\mathbf{I} = \begin{bmatrix} I_{xx} & I_{xy} & I_{xz} \\ I_{yx} & I_{yy} & I_{yz} \\ I_{zx} & I_{zy} & I_{zz} \end{bmatrix} \tag{4.39}$$

where:

$$I_{xx} = \int_{\text{vol}} (y^2 + z^2)\rho \mathrm{d}V \tag{4.40}$$

$$I_{yy} = \int_{\text{vol}} (z^2 + x^2)\rho \mathrm{d}V \tag{4.41}$$

$$I_{zz} = \int_{\text{vol}} (x^2 + y^2)\rho \mathrm{d}V \tag{4.42}$$

$$I_{xy} = I_{yx} = -\int_{\text{vol}} (xy)\rho \mathrm{d}V \tag{4.43}$$

$$I_{yz} = I_{zy} = -\int_{\text{vol}} (yz)\rho \mathrm{d}V \tag{4.44}$$

$$I_{xz} = I_{zx} = -\int_{\text{vol}} (xz)\rho \mathrm{d}V \tag{4.45}$$

If the coordinate axes coincide with the object's principal axes, then the inertia tensor is simplified to:

$$\mathbf{I} = \begin{bmatrix} I_{xx} & 0 & 0 \\ 0 & I_{yy} & 0 \\ 0 & 0 & I_{zz} \end{bmatrix} = \begin{bmatrix} I_x & 0 & 0 \\ 0 & I_y & 0 \\ 0 & 0 & I_z \end{bmatrix} \tag{4.46}$$

Using Equation (4.46), Equation (4.30) becomes:

$$\begin{bmatrix} I_x\dot{\omega}_x + (I_z - I_y)\omega_y\omega_z \\ I_y\dot{\omega}_y + (I_x - I_z)\omega_x\omega_z \\ I_z\dot{\omega}_z + (I_y - I_x)\omega_x\omega_y \end{bmatrix} = \begin{bmatrix} M_{totB,x} \\ M_{totB,y} \\ M_{totB,z} \end{bmatrix} \tag{4.47}$$

It is important to note that the angular velocity and acceleration of Equation (4.47) are around the body's principal axes. Thus, it is important to define a reference frame parallel to the principal axes, and more on that is explained in Section 4.4.

The angular acceleration around the rigid body's principal axes is thus determined from Equation (4.47) as:

$$\dot{\boldsymbol{\omega}}_B^{t+\Delta t_{DEM}} = \begin{bmatrix} \dfrac{M_{totB,x}^t - (I_z - I_y)\omega_y^t \omega_z^t}{I_x} \\ \dfrac{M_{totB,y}^t - (I_x - I_z)\omega_x^t \omega_z^t}{I_y} \\ \dfrac{M_{totB,z}^t - (I_y - I_x)\omega_x^t \omega_y^t}{I_z} \end{bmatrix} \tag{4.48}$$

The rotation of a rigid body in 3D could be performed using the Euler angles method, an extension of the method explained in Section 4.3.1, which consists of defining a second and third rotation angle ϕ and ψ that will rotate around the other two axes. However, this method's side-effect is that, sometimes, one of the independent angles rotates at a 90 degrees angle, resulting in a loss of a degree of freedom [102, 103]. This problem is known as a Gimbal lock. An example is represented in **Figure 4.5**, where a rotation of 90 degrees in the x-axis causes the alignment of the x and z gimbals. As a result, there is no way of distinguishing between the x and z gimbals.

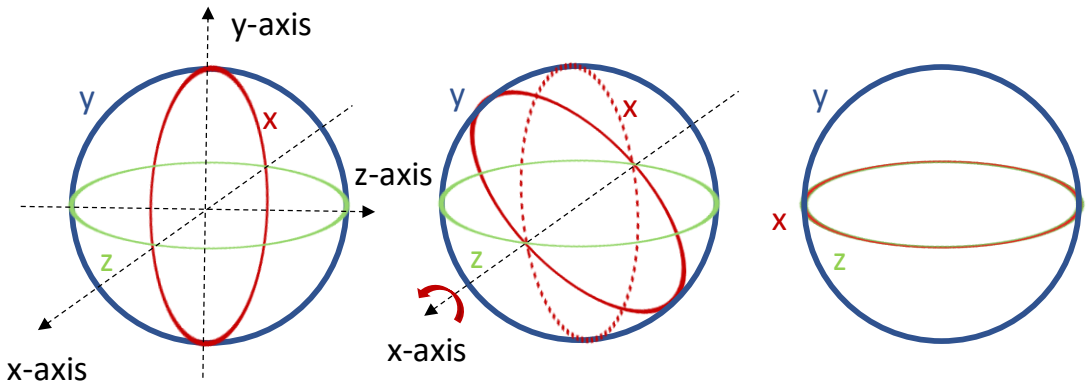

Figure 4.5 - Gimbal lock occurs when a 90-degree rotation around one of the coordinate axes occurs resulting in the alignment of two gimbals

4.3.3 Quaternions

Quaternions offer many advantages over the Euler angles method, such as avoiding the Gimbal lock problem. Also, instead of using three independent rotating angles in three directions, only one angle and an axis of rotation can be used to represent any 3D rotation as depicted in **Figure 4.6** [102].

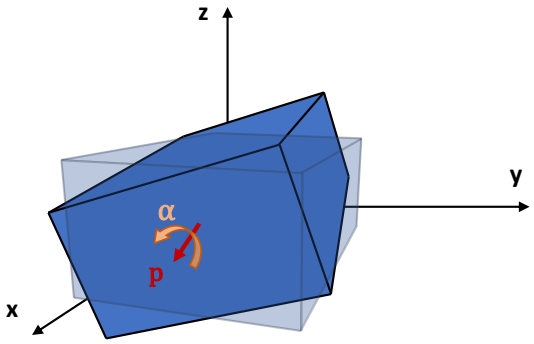

Figure 4.6 - Rotation of a 3D object using a single angle rotating around an axis ***p*** can be performed using quaternions

In the mid 19th century, quaternions were discovered by William Rowan Hamilton, an Irish mathematician who strived to extend the complex numbers from two to three dimensions. Due to its simplicity and ability to represent an object's rotation in 3D, quaternions were applied to various domains, such as classical and quantum mechanics and the theory of relativity [102, 103].

A quaternion is a four-dimensional vector consisting of a scalar q_0 and a vector $\mathbf{p} = (p_x, p_y, p_z)$:

$$\mathbf{q} = (q_0, \mathbf{p}) = (q_0, p_x, p_y, p_z) \tag{4.49}$$

The vector **p** is the axis of rotation around which the object will rotate at an angle α from whence the quaternion can be calculated as [102]:

$$\mathbf{q} = \left(\cos\left(\frac{\alpha}{2}\right), p_x \sin\left(\frac{\alpha}{2}\right), p_y \sin\left(\frac{\alpha}{2}\right), p_z \sin\left(\frac{\alpha}{2}\right) \right) \tag{4.50}$$

Any vector **v** can be rotated using the quaternions as [102]:

$$L_q(\mathbf{v}) = \mathbf{q}\mathbf{v}\mathbf{q}^* \tag{4.51}$$

where $L_q()$ is the quaternion rotation operator and $\mathbf{q}^*$is the conjugate quaternion calculated as:

$$\mathbf{q}^* = (q_0, -\mathbf{p}) = (q_0, -p_x, -p_y, -p_z) \tag{4.52}$$

Since the quaternion will be used to perform the rotation of a vector, the magnitude of the vector will remain constant only if the quaternion is a unit quaternion, $\|\mathbf{q}\| = 1$. At each iteration, the quaternion's magnitude is maintained to 1 by:

$$\mathbf{q} = \frac{\mathbf{q}}{\|\mathbf{q}\|} \tag{4.53}$$

The angular velocity will be modified to be a four-dimensional vector, as the quaternion, and will become:

$$\boldsymbol{\omega} = \begin{bmatrix} 0 \\ \omega_x \\ \omega_y \\ \omega_z \end{bmatrix} \tag{4.54}$$

Using the angular velocity, the variation of quaternion can be determined as:

$$\mathbf{dq} = \frac{1}{2}\boldsymbol{\omega} \otimes \mathbf{q}^t \Delta t_{DEM} \tag{4.55}$$

However, from Equation (4.554.554.55), $\mathbf{dq} \ll 1$, and since it is no longer a unit quaternion, it cannot be used to update the quaternion. This problem is solved by finding a corresponding unit quaternion variation as [104]:

$$\mathbf{q} + \mathbf{dq} = \mathbf{q} \otimes \mathbf{q}_\delta \tag{4.56}$$

where $\mathbf{q}_\delta$ is the unit rotation quaternion, and is determined as:

$$\begin{gathered} \mathbf{q} \otimes (\mathbf{q} + \mathbf{dq}) = \mathbf{q} \otimes (\mathbf{q} \otimes \mathbf{q}_\delta) \\ \underbrace{\mathbf{q}^* \otimes \mathbf{q}}_{\mathbf{q_I}} + \mathbf{q}^* \otimes \mathbf{dq} = \underbrace{\mathbf{q}^* \otimes \mathbf{q}}_{\mathbf{q_I}} \otimes \mathbf{q}_\delta \\ \mathbf{q}_\delta = \mathbf{q_I} + \mathbf{q}^* \otimes \mathbf{dq} \end{gathered} \tag{4.57}$$

where the $\mathbf{q_I} = (1,0,0,0)$ is the identity quaternion.

This unit rotation quaternion is used to update the quaternion as:

$$\mathbf{q}^{t+\Delta t_{DEM}} = \mathbf{q}^{t} + \mathbf{q}_{\delta} \tag{4.58}$$

where the initial quaternion is the identity quaternion, $\mathbf{q}^{t_0} = \mathbf{q_I}$.

There is no need to compute the angle, α, or the axis of rotation, $\mathbf{p}$, directly because they are indirectly obtained when the quaternion is calculated [105].

4.4 Global and Local reference frames

In DEM, when the multisphere method is implemented, two reference frames must be implemented: the global and local reference frames. The global reference frame does not change throughout the simulation, while the local reference frame rotates with the body. This frame is called the local frame, and its unit vectors are parallel to the principal axes of inertia of the solid [106]. A 2D and 3D representation of these frames are shown in **Figure 4.7**.

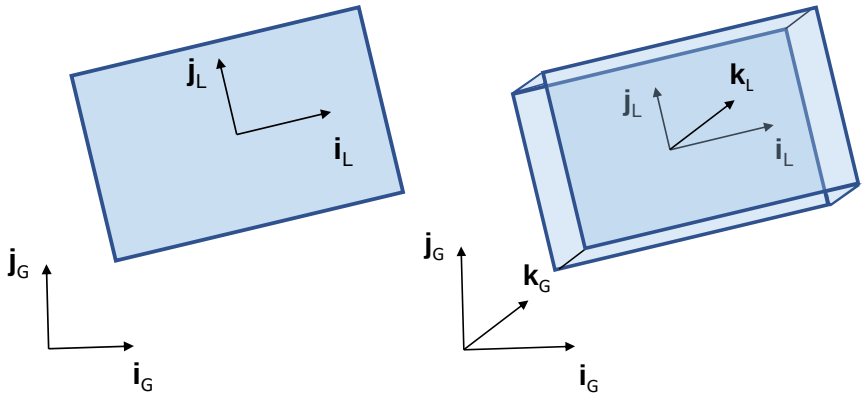

Figure 4.7 – 2D and 3D representation of the Global and Local coordinate systems

By definition, the gravitational force and the contact forces are given in the global coordinate system, while the hydrodynamic forces are given in the local coordinate system. To be added together, all the forces must be defined in the same coordinate system. Thus, the gravitational force is converted from the global coordinate system to the local coordinate system before adding it to the contact and hydrodynamic forces. Subsequently, the velocity and position obtained are in the local coordinate system.

$$\Delta \mathbf{x}_t^L = \mathbf{v}_t^L \Delta t_{DEM} \tag{4.59}$$

and

$$\mathbf{v}_{t+\Delta t_{DEM}}^L = \mathbf{v}_t^L + \Delta t_{DEM} \frac{\mathbf{F}_{tot}^L}{m_i} \tag{4.60}$$

Once $\Delta \mathbf{x}^L$ and $\mathbf{v}_{t+\Delta t_{DEM}}^L$ are obtained, they are converted back to the global coordinate system $\Delta \mathbf{x}^G$ and $\mathbf{v}_{t+\Delta t_{DEM}}^G$ and used to update the particles' positions.

4.4.1 Two-dimensional Change in Reference frame

In 2D, the rotation matrix, $\mathbf{R}_m$, defined in Section 4.3.1 and its transpose, $\mathbf{R}_m^T$, can be used to convert any vector **v** from one coordinate system to the other as [103]:

$$\mathbf{v}^G = \mathbf{R}_m \cdot \mathbf{v}^L \tag{4.61}$$

$$\mathbf{v}^L = \mathbf{R}_m^T \cdot \mathbf{v}^G \tag{4.62}$$

Combining Equations (4.36), (4.61), and (4.62), the components of the vector **v** in the local coordinate axis from the global coordinates (and vice versa) are obtained as:

$$\begin{aligned} \mathrm{v}_x^G &= \mathrm{v}_x^L \cos(\theta) - \mathrm{v}_y^L \sin(\theta) \\ \mathrm{v}_y^G &= \mathrm{v}_x^L \sin(\theta) + \mathrm{v}_y^L \cos(\theta) \end{aligned} \tag{4.63}$$

$$\begin{aligned} \mathrm{v}_x^L &= \mathrm{v}_x^G \cos(\theta) + \mathrm{v}_y^G \sin(\theta) \\ \mathrm{v}_y^L &= -\mathrm{v}_x^G \sin(\theta) + \mathrm{v}_y^G \cos(\theta) \end{aligned} \tag{4.64}$$

where the angle of rotation θ is the angle at which the solid object has rotated and, consequently, at which the local coordinate axis has also rotated. **Figure 4.8** shows the vector **v** projected in both coordinate systems.

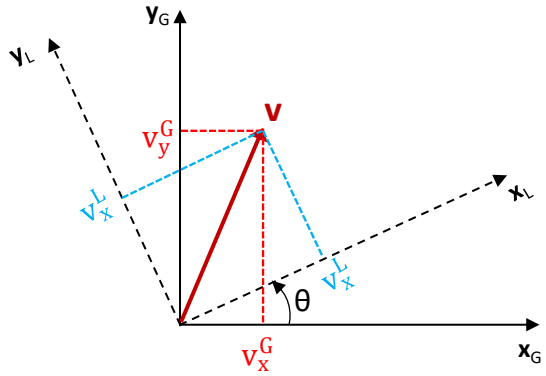

Figure 4.8 - Transforming the vector ***v*** from the global to the local coordinate axis

4.4.2 Three-dimensional Change in Reference frame

The conversion from the global to local (or vice versa) coordinate axes is performed as explained in Section 4.3.3, where quaternions are used in 3D. The following operation must be performed to convert a vector **v** from the local to the global coordinate system:

$$\mathbf{v}^G = \mathbf{q} \cdot \mathbf{v}^L \cdot \mathbf{q}^* \tag{4.65}$$

Similarly, the following must be done to convert back the vector from the global to the local coordinate system:

$$\mathbf{v}^L = \mathbf{q}^* \cdot \mathbf{v}^G \cdot \mathbf{q} \tag{4.66}$$

It must be noted that the angular velocity used to update the quaternion must be defined in the local coordinate system:

$$\boldsymbol{\omega} = \begin{bmatrix} 0 \\ \omega_{Lx} \\ \omega_{Ly} \\ \omega_{Lz} \end{bmatrix} \tag{4.67}$$

4.5 DEM Algorithm

This Section explains the algorithm present in **Figure 4.9** on DEM alone. It is assumed that the hydrodynamic forces are yet not included, and only contact forces with other solids are present.

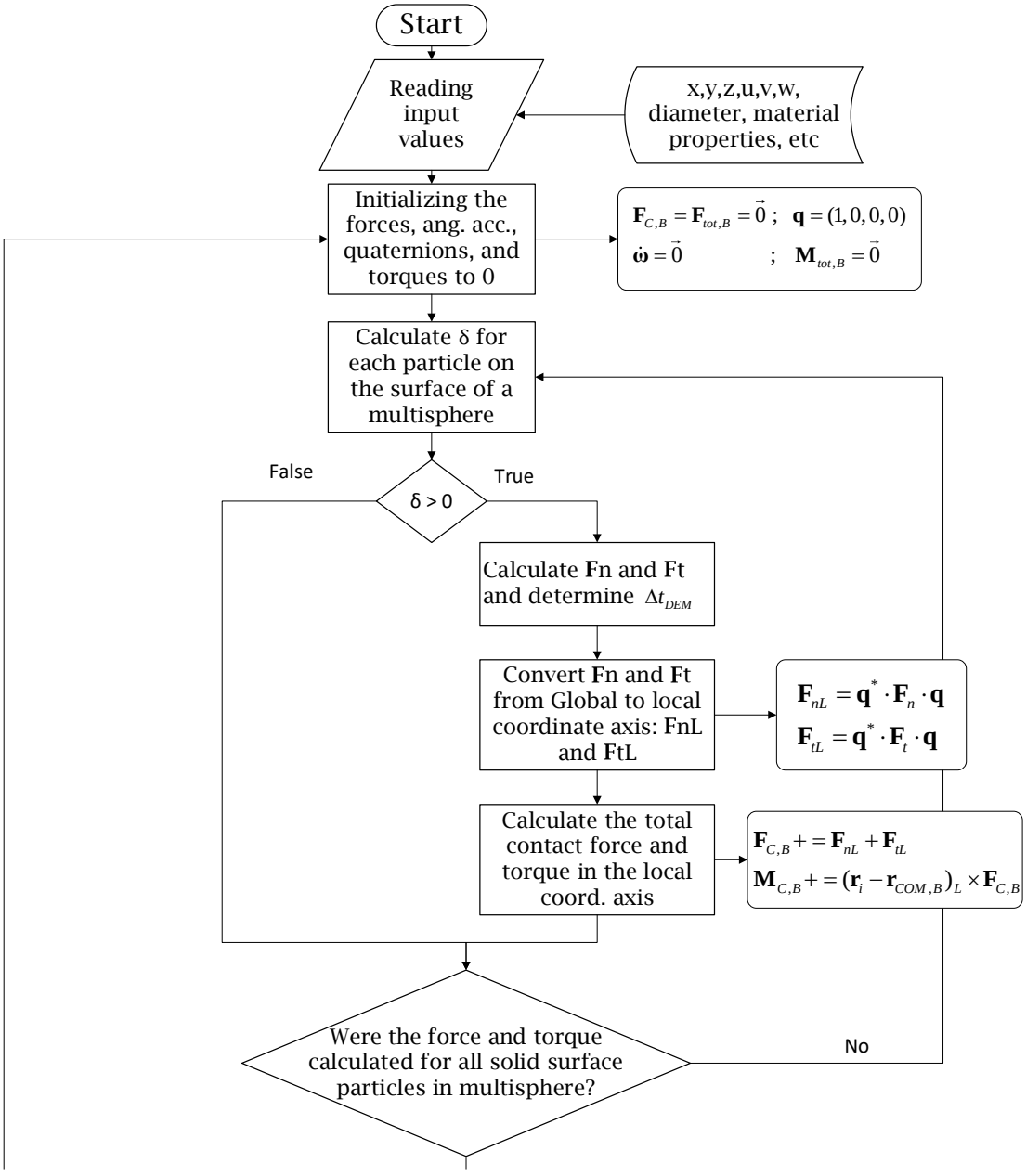

Figure 4.9 - Complete DEM algorithm - The hydrodynamic forces are not included

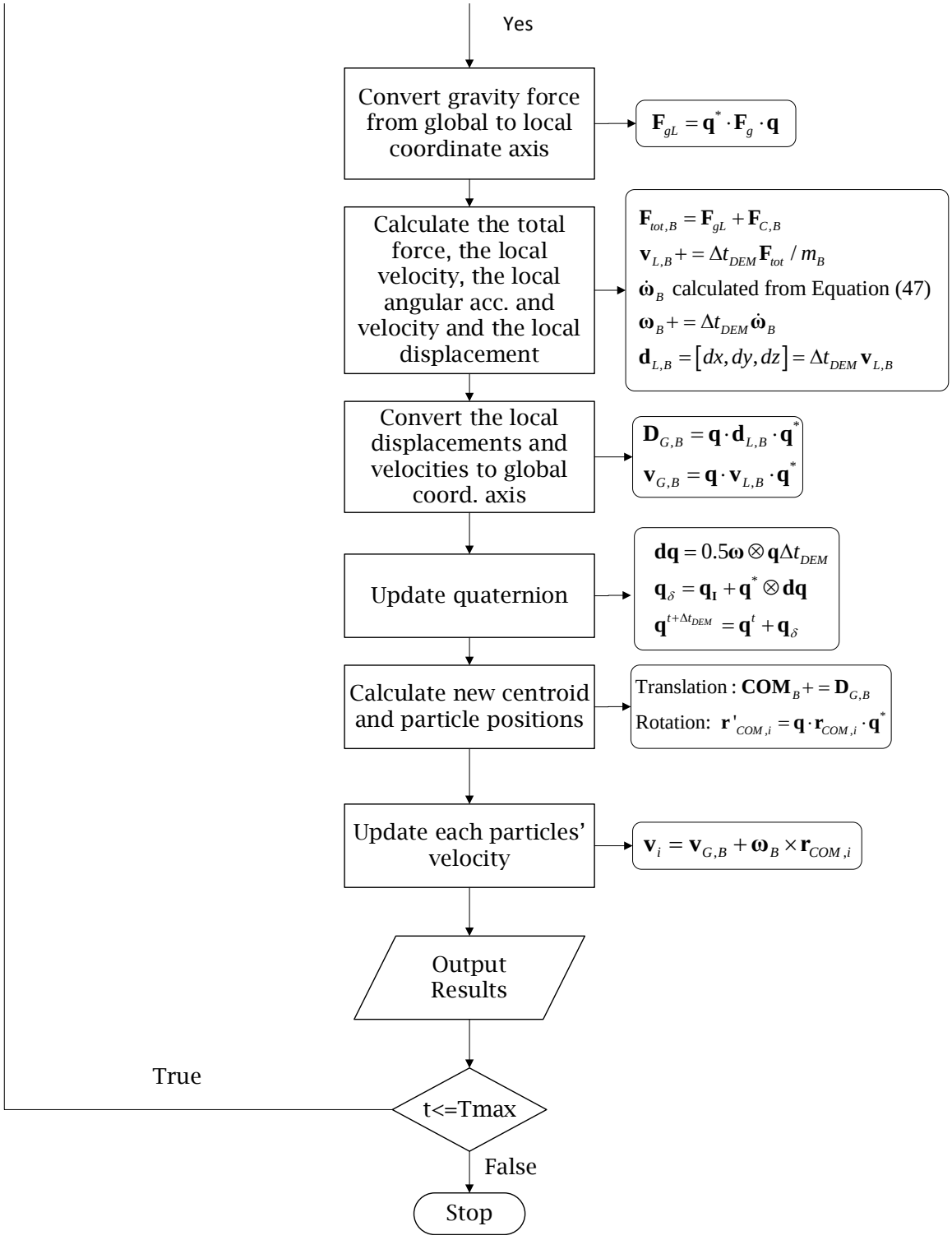

Figure 4.9 - Complete DEM algorithm - The hydrodynamic forces are not included (cont'd)

4.5.1 Reading input values

The required initial values and parameters such as position, diameter, and material properties are read in the simulation through an input file named InputDEM.txt. This input file is separated into two parts: the first part contains the parameters of the multisphere, such as the center of mass of the body, and the second part contains the individual particles' properties. An example of an input DEM file is shown in **Figure 4.10**.

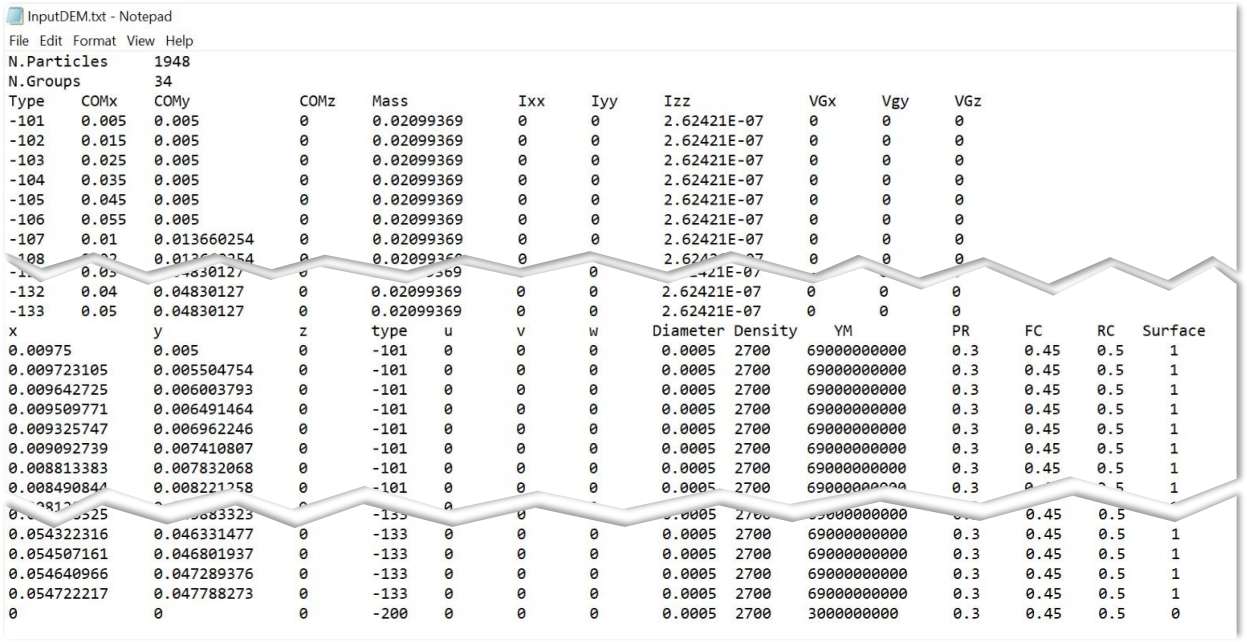

InputDEM.txt - Notepad

File Edit Format View Help

```
N.Particles     1948
N.Groups        34
Type    COMx    COMy            COMz    Mass            Ixx     Iyy     Izz             VGx     Vgy     VGz
-101    0.005   0.005           0       0.02099369      0       0       2.62421E-07     0       0       0
-102    0.015   0.005           0       0.02099369      0       0       2.62421E-07     0       0       0
-103    0.025   0.005           0       0.02099369      0       0       2.62421E-07     0       0       0
-104    0.035   0.005           0       0.02099369      0       0       2.62421E-07     0       0       0
-105    0.045   0.005           0       0.02099369      0       0       2.62421E-07     0       0       0
-106    0.055   0.005           0       0.02099369      0       0       2.62421E-07     0       0       0
-107    0.01    0.013660254     0       0.02099369      0       0       2.62421E-07     0       0       0
-108    0.03    0.013660254     0       0.02099369      0       0       2.62421E-07     0       0       0
-131    0.03    0.04830127      0       0.02099369      0       0       2.62421E-07     0       0       0
-132    0.04    0.04830127      0       0.02099369      0       0       2.62421E-07     0       0       0
-133    0.05    0.04830127      0       0.02099369      0       0       2.62421E-07     0       0       0
x               y               z       type    u       v       w       Diameter Density    YM              PR      FC      RC      Surface
0.00975         0.005           0       -101    0       0       0       0.0005  2700    69000000000     0.3     0.45    0.5     1
0.009723105     0.005504754     0       -101    0       0       0       0.0005  2700    69000000000     0.3     0.45    0.5     1
0.009642725     0.006003793     0       -101    0       0       0       0.0005  2700    69000000000     0.3     0.45    0.5     1
0.009509771     0.006491464     0       -101    0       0       0       0.0005  2700    69000000000     0.3     0.45    0.5     1
0.009325747     0.006962246     0       -101    0       0       0       0.0005  2700    69000000000     0.3     0.45    0.5     1
0.009092739     0.007410807     0       -101    0       0       0       0.0005  2700    69000000000     0.3     0.45    0.5     1
0.008813383     0.007832068     0       -101    0       0       0       0.0005  2700    69000000000     0.3     0.45    0.5     1
0.008490844     0.008221258     0       -101    0       0       0       0.0005  2700    69000000000     0.3     0.45    0.5     1
0.054322316     0.046331477     0       -133    0       0       0       0.0005  2700    69000000000     0.3     0.45    0.5     1
0.054507161     0.046801937     0       -133    0       0       0       0.0005  2700    69000000000     0.3     0.45    0.5     1
0.054640966     0.047289376     0       -133    0       0       0       0.0005  2700    69000000000     0.3     0.45    0.5     1
0.054722217     0.047788273     0       -133    0       0       0       0.0005  2700    69000000000     0.3     0.45    0.5     1
0               0               0       -200    0       0       0       0.0005  2700    3000000000      0.3     0.45    0.5     0
```

Figure 4.10 – An example of an InputDEM.txt file

The first part of the file implements the type, center of mass, mass, the moment of inertia, and velocity of the multisphere. The *type* variable is a tag for each rigid body and will be useful to gather the individual particles in the same group. In the example depicted in **Figure 4.10**, 33 rigid bodies are being simulated. However, a value of 34 is shown next to the variable *N.Groups* in the second line. This is explained by the fact that the boundary is included in the last line to define the essential physical parameters of the boundary walls. Likewise, 1947 particles are simulated in total, but *N.Particles* is given a value of 1948 because the boundary is included.

The second part of the input file implements the parameters of each particle. The parameters include the position, type, velocity, diameter, density, Young's Modulus, Poisson Ratio, friction coefficient, and restitution coefficient. The last column *Surface* will determine if the particle is a

particle located on the rigid body's surface. In other words, if it is a particle likely to get into contact with other particles. Using this variable will reduce computational time if particles are present inside the multisphere, as shown in **Figure 4.11**.

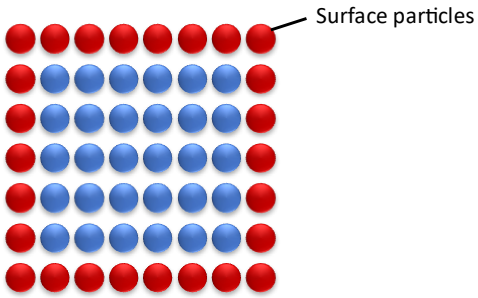

Figure 4.11 - Detection of surface particles

4.5.2 Calculating overlap

The next step consists of initializing all the total forces, torques, and angular acceleration to 0. These variables are calculated at each time step and are cumulative only within the time step. An arbitrary time step Δt can be used as long as it is smaller than Δt_{DEM}.

The overlap is then calculated using Equation (4.5), and if the delta is positive, then there is contact between two particles. The normal and tangential contact forces are calculated using the equations stated in Sections 4.2.1 and 4.2.2, transformed in the local coordinate system using the theory of quaternions, and added to find the total contact force, $\mathbf{F}_{C,B}$. The contact forces due to a collision between a particle and a boundary wall are calculated similarly, but the mass and radius are considered infinite.

Since there is contact, the Δt_{DEM} can also be calculated and compared to the implemented time step Δt. If the implemented time step is bigger than Δt_{DEM}, then Δt_{DEM} must be used. If not, either Δt or Δt_{DEM} can be used. When coupling DEM with MPS, a subcycling algorithm must be used since MPS has a different time step than DEM. More details about that are found in Section 5.2.5.2.1

Once the contact forces are known, the torque can be determined using Equation (4.31). Since the contact forces and the angular acceleration are in the local coordinate system, the relative position between the particle and the center of mass of the multisphere used in Equation (4.31),

$\mathbf{r}_i - \mathbf{r}_{COM,B}$, must be transformed from the global to the local coordinate system as well. The angular acceleration in the local coordinate system can then be obtained using Equation (4.48). All the steps of this paragraph will be repeated for all the particles on the surface of the multisphere.

Next, the gravity force will be converted from the global to the local coordinate system and added to the total local force of the multisphere. If water is included, the hydrodynamic forces must be included in this part. More details on that are found in Section 5.2.

The local velocity, angular velocity, and displacement are calculated using the total force and angular acceleration. While the angular velocity is maintained in the local coordinate system, the displacement and velocity are transformed back into the global reference frame. The quaternion is updated using the angular velocity by making sure that unit quaternions are used at each step.

The rigid body's translation motion is obtained by updating each particle's position and the center of mass using the global displacements, $\mathbf{D}_{G,B}$,. The particles are then rotated around the center of mass using the updated quaternion.

Finally, each particle's velocity is updated as:

$$\mathbf{v}_i = \mathbf{v}_{G,B} + \boldsymbol{\omega}_B \times \mathbf{r}_{COM,i} \tag{4.68}$$

Once all these calculations are performed, they are repeated until the maximum simulation time is reached.

4.6 DEM Validation

4.6.1 2D Single Particle Dropping

In this test case, the simplest case scenario is considered where a particle having a diameter of 0.1 m is dropped from a given height onto a floor. **Table 4.3** shows the parameters used for this test case.

Table 4.3 - Particle and floor physical properties

Properties	*Particle*	*Floor*
Density ρ (kg/m³)	1200	∞
Young's modulus Y (GPa)	0.07	210
Poisson's ratio ν	0.1	0.3
Friction Coefficient μ	0.75	0.45
Restitution coefficient	0.5	0.8

The particle is released at the height of 2 m, and this height decreases after each rebound. The rebound height and contact force with the floor are compared with the results obtained from one of the most widely used open-source software, LIGGGHTS [107].

LIGGGHTS also uses DEM to model solid objects, and the equations are similar to the equations presented in Section 4.2. In LIGGGHTS, the contact force is calculated as [108]:

$$\mathbf{F}_{c,ij} = \underbrace{k_{n,ij}\delta_{n,ij}\hat{\mathbf{n}}_{ij} - \gamma_{n,ij}\mathbf{v}_{n,ij}}_{Normal\ Force} + \underbrace{k_{t,ij}\delta_{t,ij}\hat{\mathbf{t}}_{ij} - \gamma_{t,ij}\mathbf{v}_{t,ij}}_{Tangential\ Force} \tag{4.69}$$

where $k_{n,ij}$ is defined as in Equation (4.10). The sign difference between the LIGGGHTS Equation and the Equations defined in Sections 4.2.1 and 4.2.2 is caused by the difference in the relative vector definition:

$$\hat{\mathbf{n}}_{ij} = \frac{\mathbf{r}_i - \mathbf{r}_j}{\left\|\mathbf{r}_i - \mathbf{r}_j\right\|} \tag{4.70}$$

$$\mathbf{v}_{n,ij} = \left(\left(\mathbf{v}_i - \mathbf{v}_j\right) \cdot \hat{\mathbf{n}}_{ij}\right)\hat{\mathbf{n}}_{ij} \tag{4.71}$$

In LIGGGHTS, the damping coefficient is calculated as:

$$\gamma_n = -2\sqrt{\frac{5}{6}}\beta\sqrt{S_n m^*} \tag{4.72}$$

where

$$\beta = \frac{\ln (e)}{\sqrt{\ln^2(e) + \pi^2}} \tag{4.73}$$

$$S_n = 2Y^* \sqrt{R^* \delta_n} \tag{4.74}$$

The Y^*, R^*, and m^* parameters are determined similarly as in Equations (4.12), (4.13), and (4.14), and e is the coefficient of restitution.

The tangential elastic coefficient is defined as:

$$k_t = 8G^* \sqrt{R^* \delta_n} \tag{4.75}$$

where

$$\frac{1}{G^*} = \frac{2(2 - \nu_i)(1 + \nu_i)}{Y_i} + \frac{2(2 - \nu_j)(1 + \nu_j)}{Y_j} \tag{4.76}$$

The tangential elastic coefficient is defined as:

$$\gamma_t = -2\sqrt{\frac{5}{6}} \beta \sqrt{S_t m^*} \tag{4.77}$$

where

$$S_t = 2G^* \sqrt{R^* \delta_n} \tag{4.78}$$

One of the differences between the model proposed by LIGGGHTS and the one presented in this project is that in LIGGGHTS, all parameters are analytically calculated from the solid's physical properties, and no parameter can be calibrated. Having no such parameter restrains the flexibility of adjusting the contact force to obtain a realistic behavior since the parameters used in the equations are only estimates of the real physical properties.

Figure 4.12 shows the particle position variation with time when a contact ratio of 0.14 is used. The height evolution is compared to results obtained by LIGGGHTS and is compared in **Figures 4.13** and **4.14**.

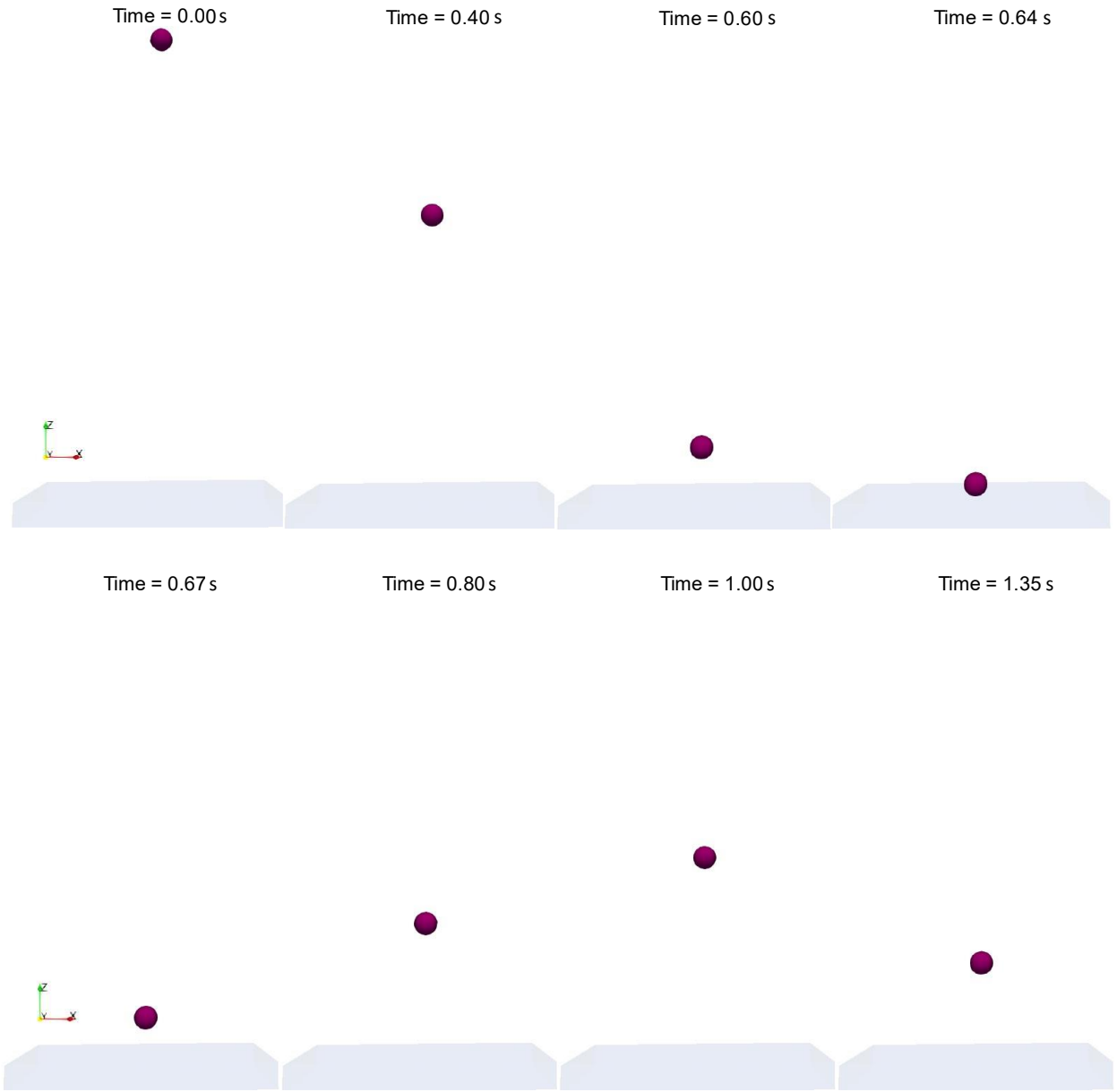

Figure 4.12 - Time evolution of the particle bouncing off the floor

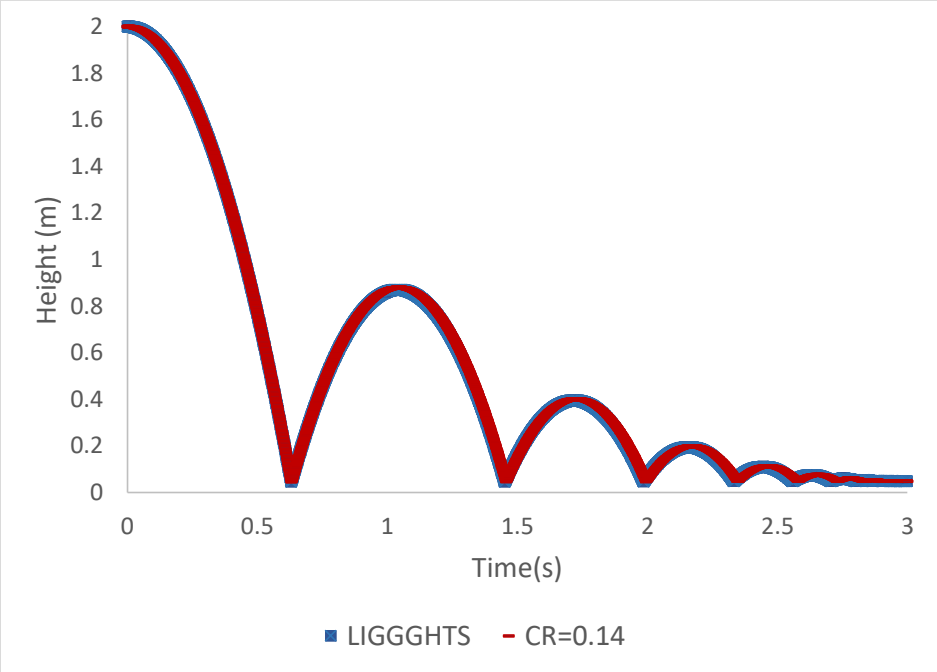

Figure 4.13 - Rebound height comparison between results obtained with the proposed model vs. results obtained with LIGGGHTS

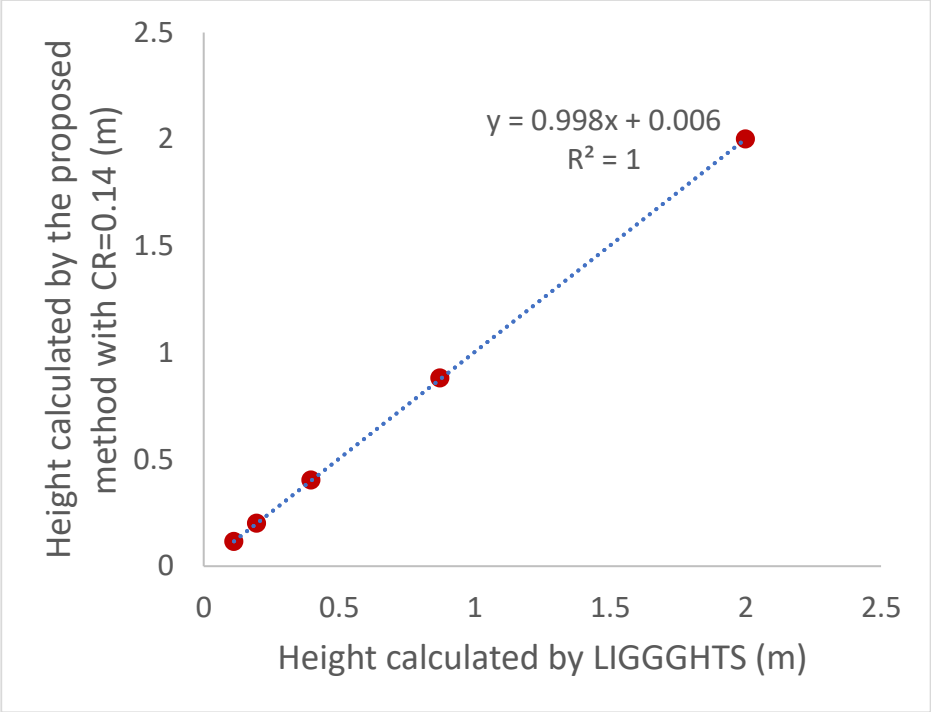

Figure 4.14 - Calibration curve of the rebound height obtained using the proposed model vs. LIGGGHTS

The results obtained from the proposed DEM model are in good agreement with the results obtained by LIGGGHTS since, from **Figure 4.14**, a coefficient of correlation of 1 has been found.

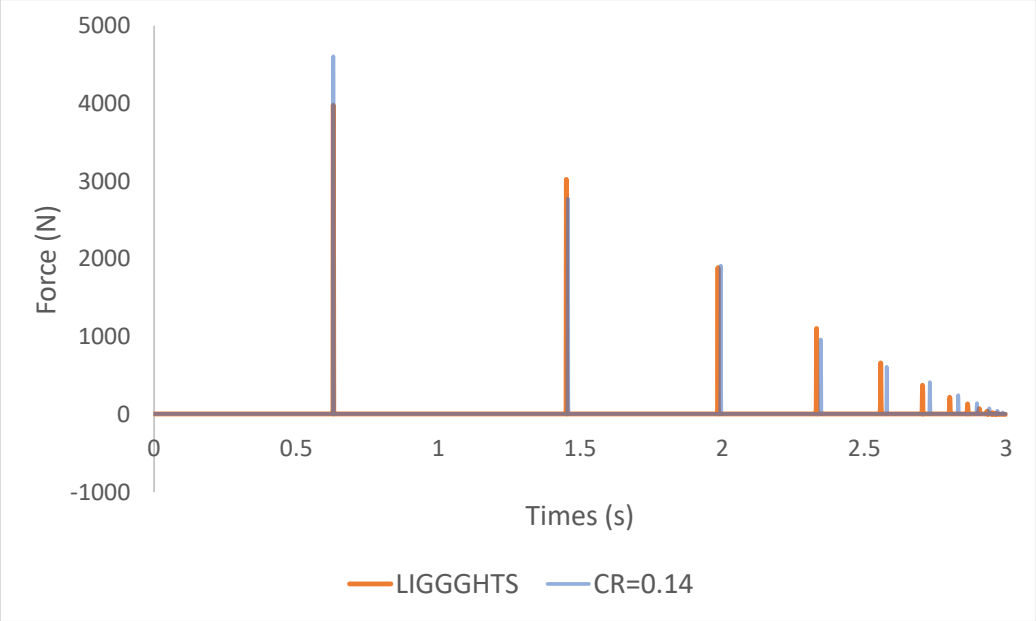

Figure 4.15 - Impact force comparison between LIGGGHTS and the proposed model

Table 4.4 - The percentage difference between the maximum and average values of contact forces obtained from LIGGGHTS and the proposed model

	Present Model	***LIGGGHTS***	***Error(%)***
	Average Forces (N)		
Peak 1	1380.23	1401.02	1.48
Peak 2	453.76	425.87	6.55
Peak 3	202.48	201.67	0.40
Peak 4	98.16	94.46	3.92
Peak 5	49.58	53.21	6.81

The contact forces calculated when the particle bounces off the floor are compared with the contact forces obtained by LIGGGHTS in **Figure 4.15** and **Table 4.4**. It can be seen from **Figure 4.15** that as the rebound height decreases, the discrepancy between the two models increases. This

discrepancy can be explained by the fact that LIGGGHTS has slightly higher damping forces. A small increase in the contact ratio would improve this result. However, the percentage error of the contact force's average value between the two models, shown in **Table 4.4**, is less than 7% for the first five peaks. This small percentage error indicates that even though the forces are sometimes out-of-phase, both models' average contact force is quite similar.

4.6.2 2D Multisphere validation

In order to validate the proposed DEM test case in 2D, the collapse of solid cylinder layers was simulated and compared with experimental results performed by Zhang et al. [109]. Thirty-three cylinders were piled up in an acrylic resin tank having a length of 26 cm, a width of 10 cm, and a height of 26 cm. **Table 4.5** summarizes the physical properties used in this test case.

Table 4.5 - Cylinders' Young modulus, Poisson coefficient, friction coefficient, and density used in the proposed model

	Materials	*Y* $[Nm^{-2}]$	*ν [-]*	μ_f *[-]*	*Density* $[kg/m^3]$
Cylinders	Aluminum	69×10^9	0.3	0.45	2.7×10^3
Tank	PVC	30×10^8	0.3	0.45	∞

Each cylinder has a diameter of 1.0 cm and a length of 9.9 cm. This initial motion is driven by gravity when a vertical gate that was retaining the cylinders is removed.

A calibrated contact ratio of 0.1 was used in the DEM model presented in this thesis, and each particle was assigned a diameter of 0.0005 m. Each cylinder was represented by a set of particles whose relative position remains constant. Furthermore, since the solid surface particles are the only ones likely to collide with other particles, only those were simulated, as shown in **Figure 4.16**.

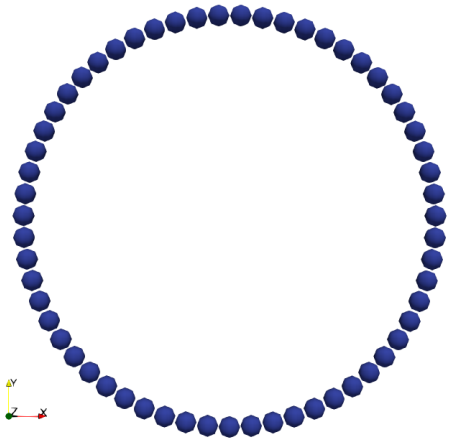

Figure 4.16 - Representation of a cylinder using multisphere

Figure 4.17 shows a qualitative comparison between the experimental and numerical results for thirty-three cylinders piled in six layers. It can be seen that the numerical result agrees well with the collapse behavior of the cylinders obtained experimentally. The average center of mass is used to validate the model quantitatively and is calculated by summing up the center of mass of all the cylinders and diving it by the total number of cylinders, N as:

$$\mathbf{r}_{avg,COM} = \frac{1}{N}\sum_{ci=1}^{N} \mathbf{r}_{ci,COM} \tag{79}$$

where $\mathbf{r}_{avg,COM}$ is the average center of mass and $\mathbf{r}_{ci,COM}$ is the center of mass of each cylinder ci. The transient average center of mass has been normalized and plotted in **Figure 4.18**, where it can be seen that the numerical and experimental results are in good agreement. The experimental results were obtained by averaging the results obtained by five consecutive runs [109].

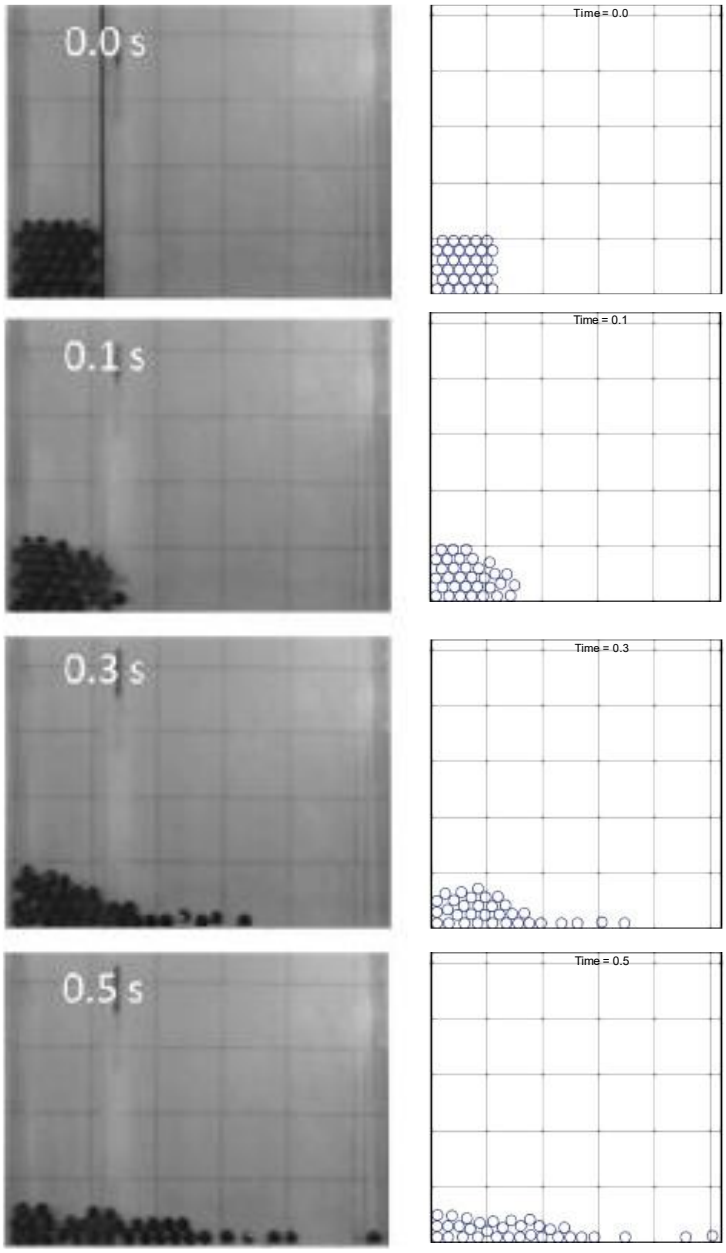

Figure 4.17 - Cylinder collapse at t=0, 0.101, 0.3, and 0.5 s. (Experimental data in the left [109]; simulation results in the right)

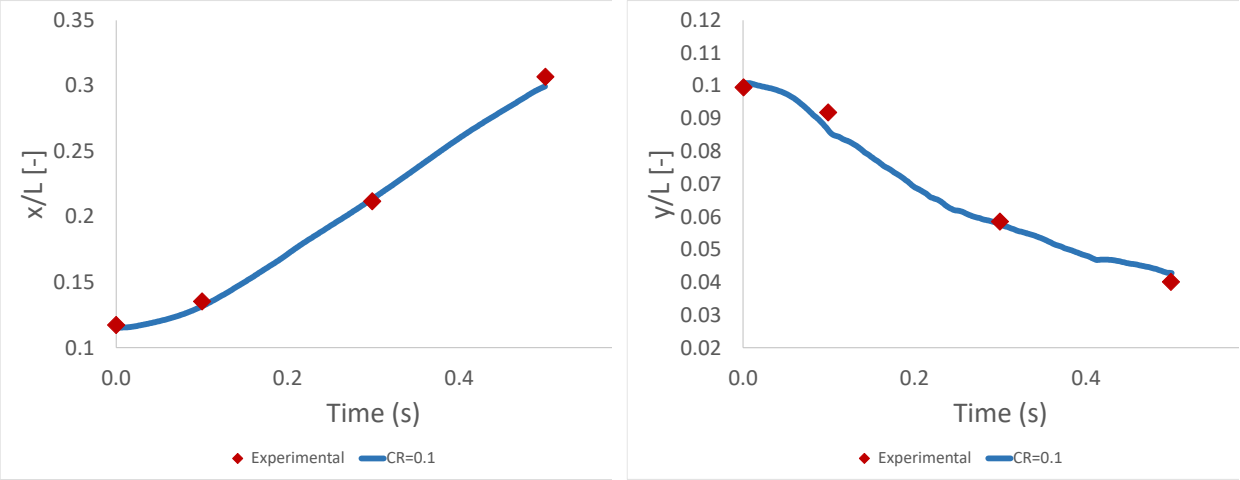

(a) (b)

Figure 4.18 - Variation of the average center of mass for thirty-three cylinders (a) The horizontal variation (b) The vertical variation

4.6.3 Demolisher test case used to validate the 3D multisphere model

No simple experimental-based 3D benchmark cases exist in the literature to validate the DEM model to the author's knowledge. Thus, the model is compared with software widely used industrially to simulate solid-solid interactions. A test case performed by DualSPHysics has been chosen to validate the model. This test case is called the Demolisher test case, where, as shown in **Figure 4.19**, a wrecking ball is released from rest to swing and collapse onto the wall. The tank length (L), width (W), and height (H) are 11 m, 6 m, and 9.5 m, respectively. **Table 4.6** summarizes the block, pendulum, and wall's physical properties. The results obtained by this proposed model are compared once more with the results obtained by LIGGGHTS because LIGGGHTS outputs the position and the contact force while DualSPHysics only outputs the position.

Table 4.6 - Pendulum, blocks, and wall's physical properties

	Materials	*Y [Nm-2]*	*ν[-]*	*μ[-]*	*e*	*Diameters (m)*	*Relative Weight*
Pendulum	Steel	2.1×10^{11}	0.3	0.45	0.8	0.7	2.5
Blocks	Soft-Wood	7×10^{7}	0.1	0.75	0.5	0.05	1.2
Wall	Steel	2.1×10^{11}	0.3	0.45	0.8	inf	2.5

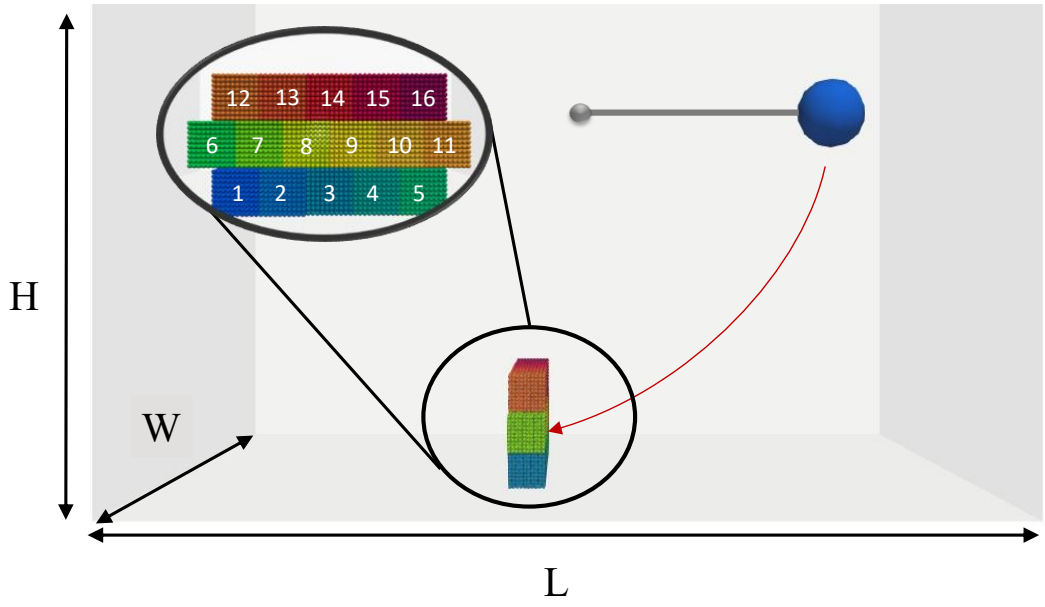

Figure 4.19 - Demolisher test case - Pendulum motion and initial blocks set-up

Each block has dimensions of 0.5 x 0.5 x 0.5 m. In DualSPHysics, the pendulum string is simulated using cylinders attached to each other, as depicted in **Figure 4.20**. Thus, the pendulum motion is gravity-driven, and the length of the string restricts the motion. A first attempt at simulating such a pendulum was performed in the proposed DEM model, but LIGGGHTS does not allow such a motion. A constant velocity for the pendulum motion is the only motion allowed by LIGGGHTS. As a result, a gravity-driven pendulum motion results in a higher velocity at collision, as depicted in **Figure 4.21**. Thus, a pendulum motion similar to LIGGGHTS was simulated to reduce the disparities, as depicted in **Figure 4.22**.

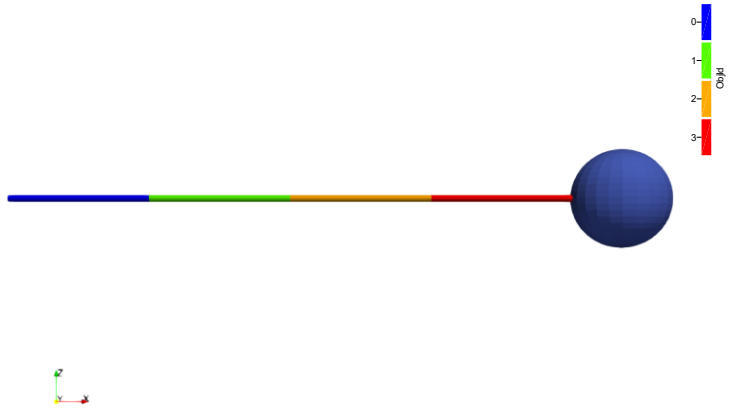

Figure 4.20 - DualSPhysics Pendulum representation

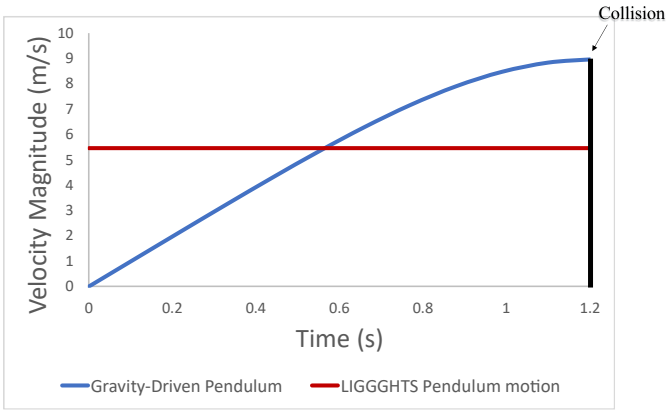

Figure 4.21 - Pendulum velocity simulated by LIGGGHTS vs. a gravity-driven pendulum

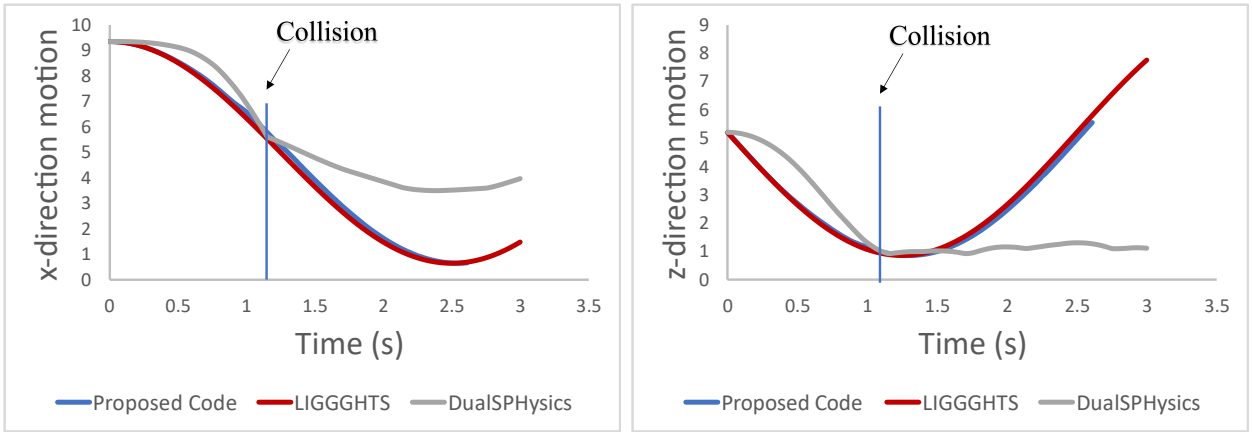

Figure 4.22 - Pendulum motion in the x and z direction for the proposed model, LIGGGHTS, and DualSPHysics

4.6.3.1 Calibration of the contact ratio

A smaller test case, shown in **Figure 4.23**, involving the collision of only three cubes having the same properties and dimensions as in the Demolisher test case, was used to calibrate the contact ratio. The block's position and velocity obtained from the proposed model is in good agreement with the results obtained from LIGGGHTS when a contact ratio of 0.3 is used, as shown in **Figure 4.24**.

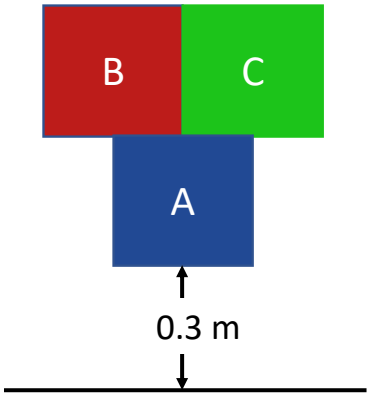

Figure 4.23 - Set up of three blocks released from height of 0.3 m

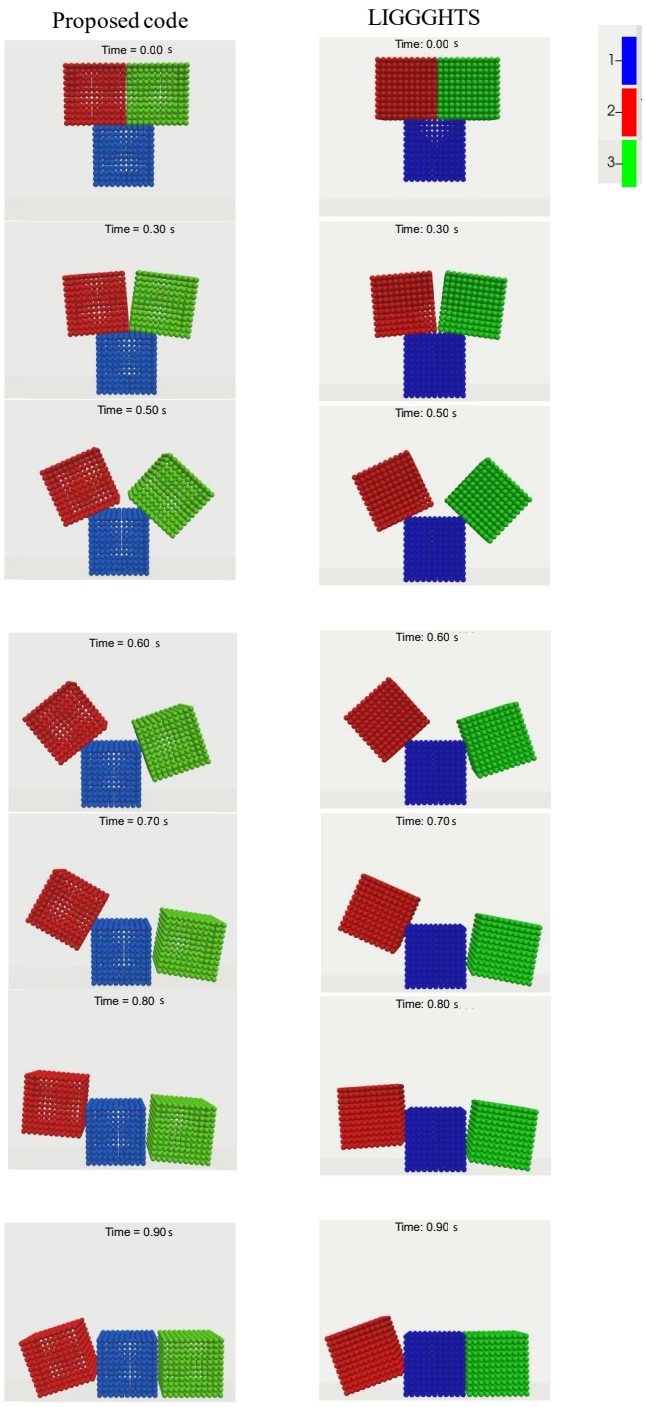

Figure 4.24 - Snapshots of the block position evolution obtained for the proposed model and LIGGGHTS

The average contact force for each block obtained from the proposed model and LIGGGHTS is presented in **Table 4.7**. One of the shortcomings of the LIGGGHTS-public version, which is the one used in this thesis, is that the contact dissipation increases in proportion to the number of spheres used per multisphere, thus rendering the contact force unphysically small [110]. This error is corrected in the LIGGGHTS Premium version, which was not available to the author of this thesis. The contact ratio was adjusted such that despite the contact force being different, similar block behavior is achieved.

The blocks' motion and velocity calculated from the proposed model are in good agreement with those calculated from LIGGGHTS, as shown in **Figures 4.25** to **4.27**.

Table 4.7 - Average force comparison between the proposed model and LIGGGHTS for Blocks A, B, and C

	Average Forces (N)	
	Proposed Model	LIGGGHTS
Block A	754.088	2.389
Block B	1674.66	0.97
Block C	2649.48	1.07

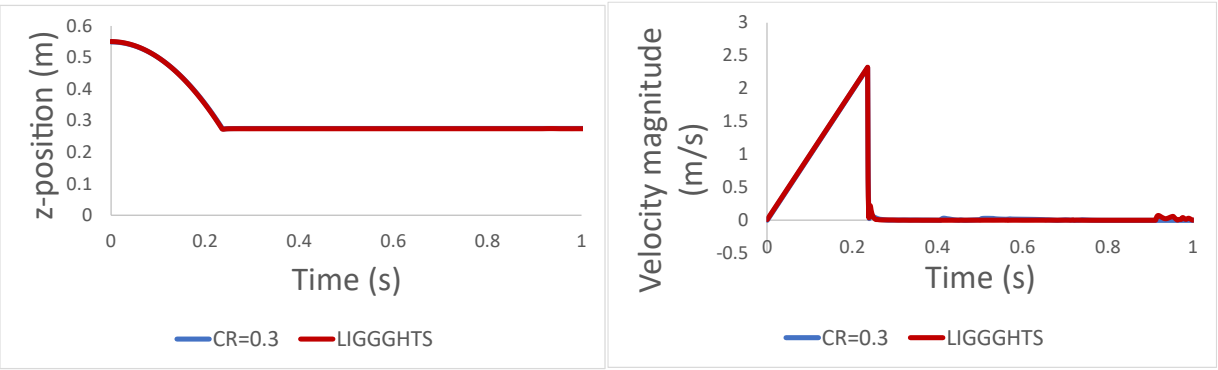

Figure 4.25 - Comparison of the z-position and the velocity magnitude between the proposed model and LIGGGHTS of Block A

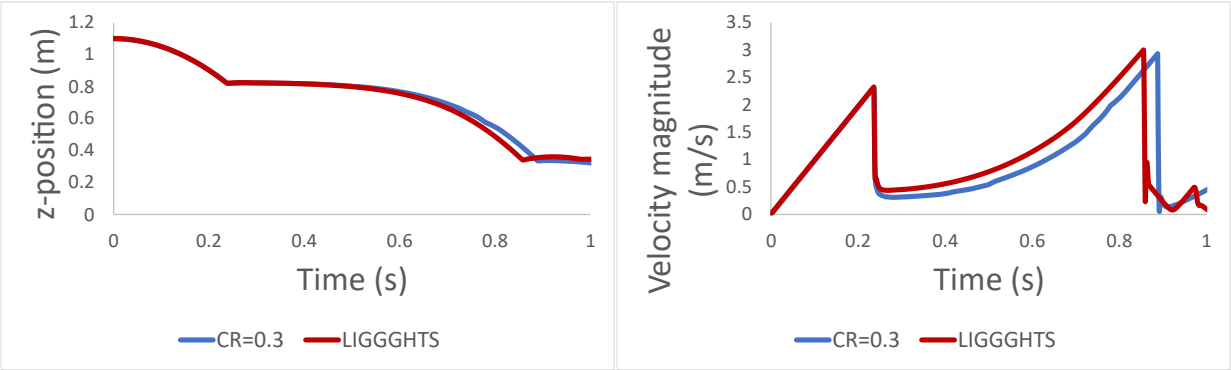

Figure 4.26 - Comparison of the z-position and the velocity magnitude between the proposed model and LIGGGHTS of Block B

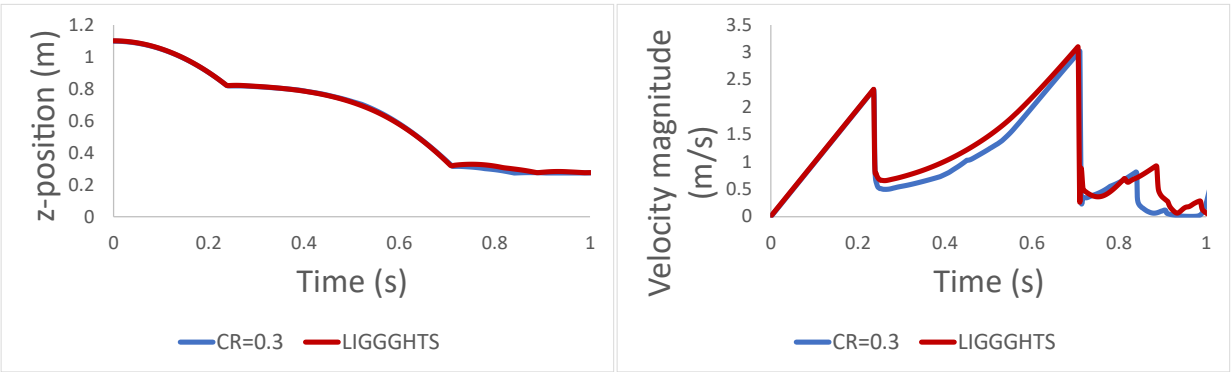

Figure 4.27 - Comparison of the z-position and the velocity magnitude between the proposed model and LIGGGHTS of Block C

4.6.3.2 Demolisher Results

Snapshots of the Demolisher test case obtained from the proposed model, LIGGGHTS, and DualSPHysics, are presented in **Figures 4.28**, **4.29**, and **4.30**, respectively.

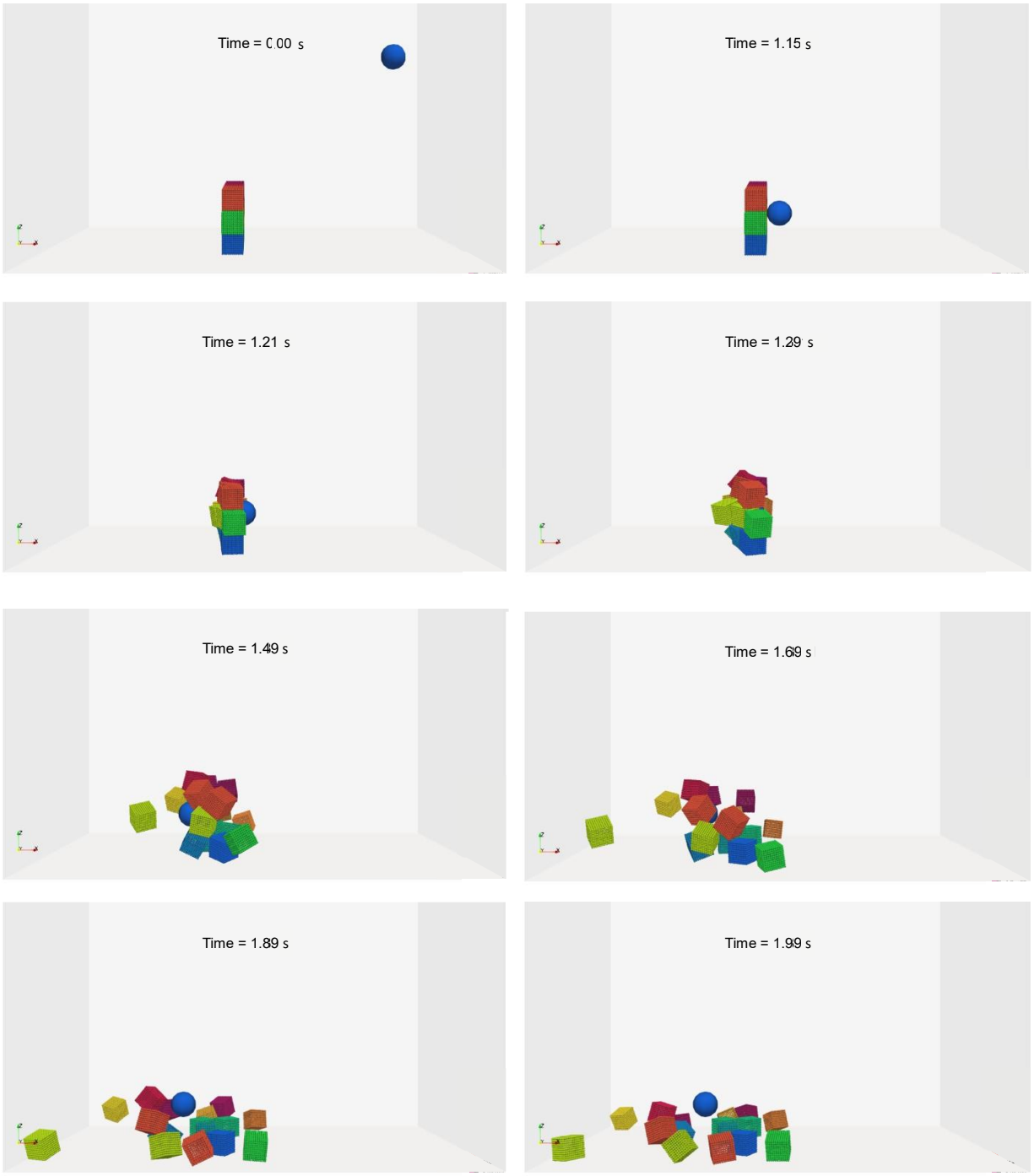

Figure 4.28 - Snapshots of demolisher results obtained from the proposed model

Figure 4.29 - Snapshots of demolisher results obtained from the LIGGGHTS

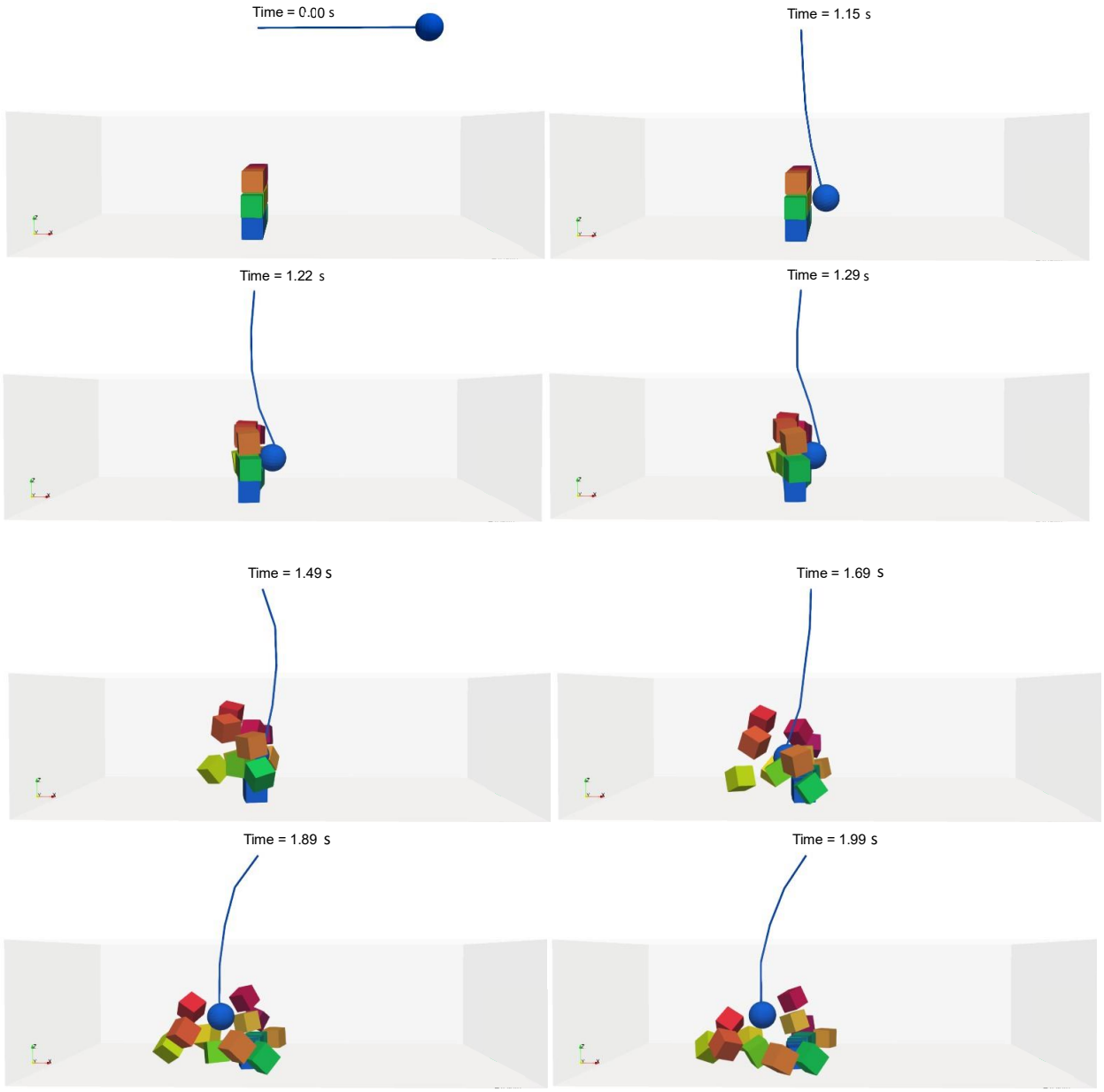

Figure 4.30 - Snapshots of demolisher results obtained from the DualSPHysics

The average block position was calculated as using Equation (79), where N is taken as the number of blocks, $\mathbf{r}_{avg,COM}$ the average center of mass, and $\mathbf{r}_{ci,COM}$ the center of mass of each block. **Figure 4.31** compares the average position in x, y, and z-direction between the proposed model, LIGGGHTS, and DualSPHysics. Overall, the proposed model is in good agreement with the two open-source models.

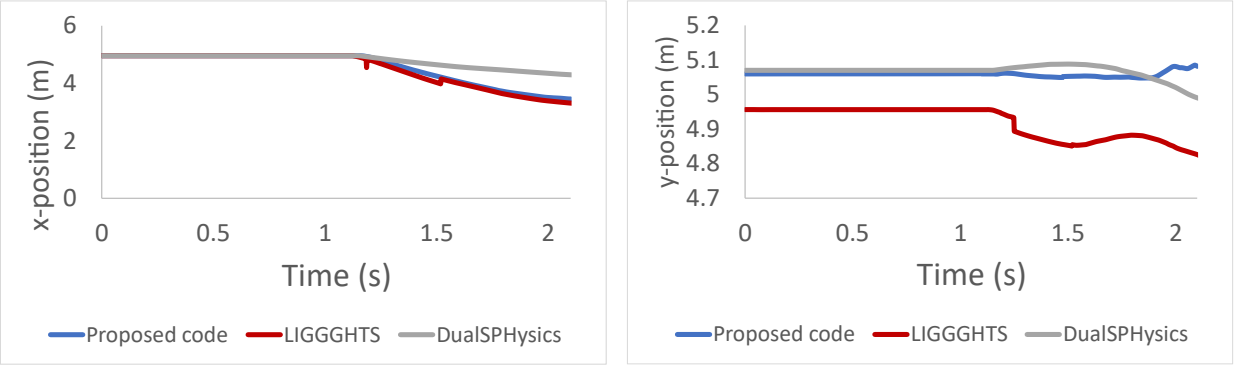

(a)

(b)

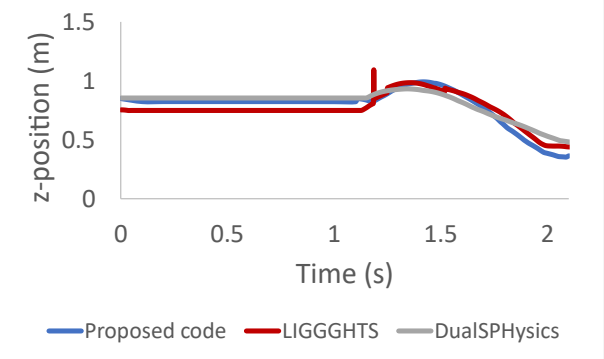

(c)

Figure 4.31 - Comparison of the average block motion between the proposed model, LIGGGHTS, and DualSPHysics

Table 4.8 shows the average of the values obtained in **Figure 4.31**, and **Table 4.9** shows the percentage difference between the proposed model, LIGGGHTS, and DualSPHysics.

Table 4.8 - Average position comparison between the proposed model, LIGGGHTS, and DualSPHysics

	Proposed model	*LIGGGHTS*	*DualSPHysics*
Average x-position	4.53	4.48	4.78
Average y-position	5.06	4.92	5.07
Average z-position	0.79	0.76	0.81

Table 4.9 - Percentage difference of the average position between the proposed model, LIGGGHTS, and DualSPHysics

Percentage difference (%)

	Proposed model and LIGGGHTS	Proposed model and DualSPHysics	LIGGGHTS and DualSPHysics
Average x-position	1.11	5.37	6.48
Average y-position	2.78	0.26	3.03
Average z-position	3.62	2.50	6.12

Since the percentage difference between the proposed model and either LIGGGHTS and DualSPHysics is smaller than the difference between the two open-source codes, the proposed model results are considered acceptable.

4.6.3.3 Pendulum force comparison

The comparison of the contact force evolution of the pendulum is shown in **Figure 4.32**. An average contact force of 319 kN is obtained from the proposed model, while LIGGGHTS calculated 165 kN. When considering a single sphere, the contact forces calculated from the proposed model and LIGGGHTS are of the same order of magnitude, unlike the contact force between multispheres. **Figures 4.33** and **4.35** show the contact forces of blocks 8 and 9 (see **Figure 4.19** for block numbers), where a logarithmic scale is used in the vertical axis to show the difference in magnitude. An average contact force of 16.6 kN was calculated for block 8 in the proposed model, while an average contact force of 0.075 kN was calculated from LIGGGHTS. Similarly, an average contact force of 10.7 kN was obtained from the proposed model, and LIGGGHTS' average contact force was 0.092 kN for block 9. The contact force exerted on blocks 8 and 9 should be of the same order of magnitude as the pendulum's contact force to satisfy Newton's Third Law. However, it is normal to see a bigger contact force exerted on the pendulum because the pendulum enters into contact with blocks 3, 4, 13, and 14 as well. However, while the contact force calculated from the proposed model on blocks 8 and 9 are smaller, they are not as low as the contact force calculated from LIGGGHTS. Once more, the contact forces calculated from LIGGGHTS for multispheres seem to be unphysically small.

This difference in force might explain why in some instances, the z-position obtained from the proposed model is slightly higher than the position calculated from LIGGGHTS, as seen in **Figures 4.34** (c) and **4.36** (c). These two figures show that blocks 8 and 9 from DualSPHysics also have lower heights, but this can be accounted for by the pendulum motion being different. The x and y-position for these blocks are in good agreement with the results from the two open-source codes. Furthermore, the position obtained from the proposed model of the two upper blocks 13 and 14, which also are in contact with the pendulum, are in good agreement with the two other models, as seen from **Figures 4.37**and **4.38**.

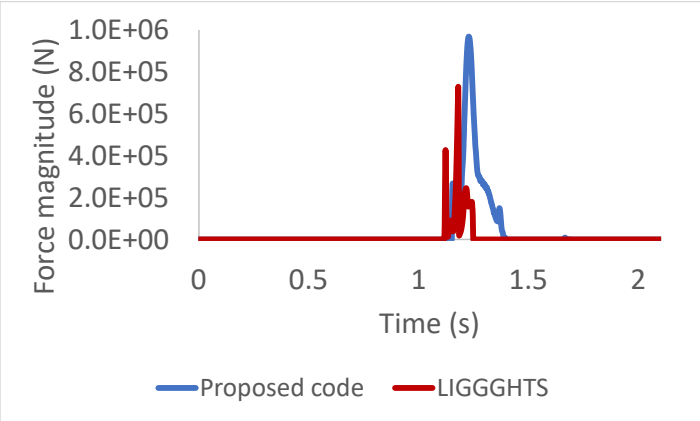

Figure 4.32 - Comparison of force magnitude between the proposed model and LIGGGHTS for Pendulum

4.6.3.4 Block 8 Force and position comparison

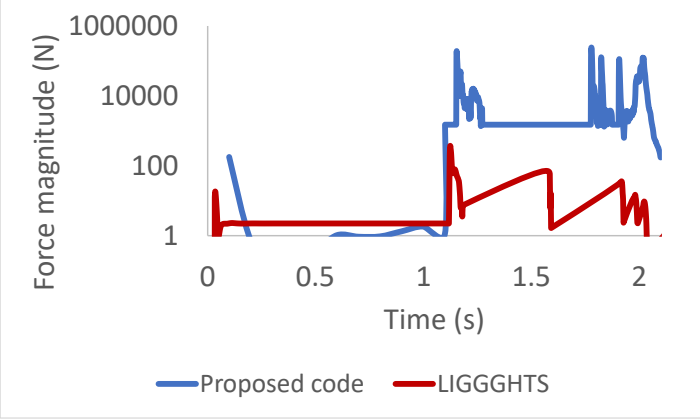

Figure 4.33 - Force comparison between the proposed model and LIGGGHTS for Block 8

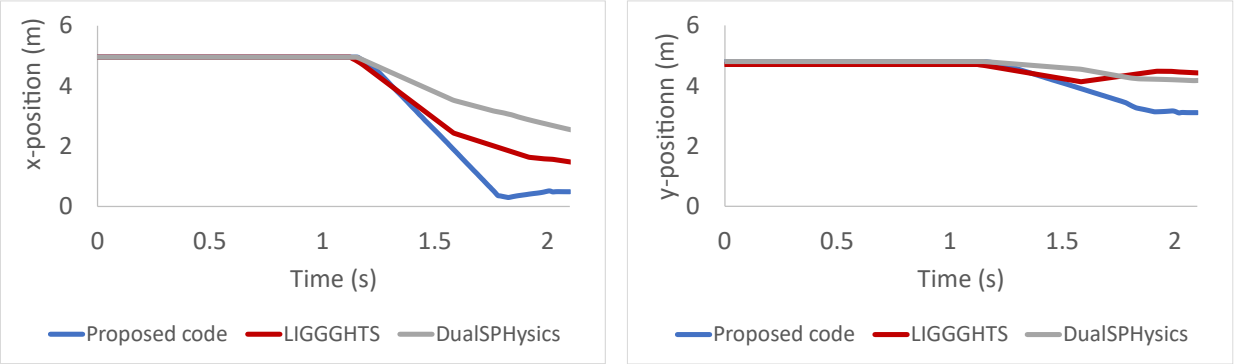

(a) (b)

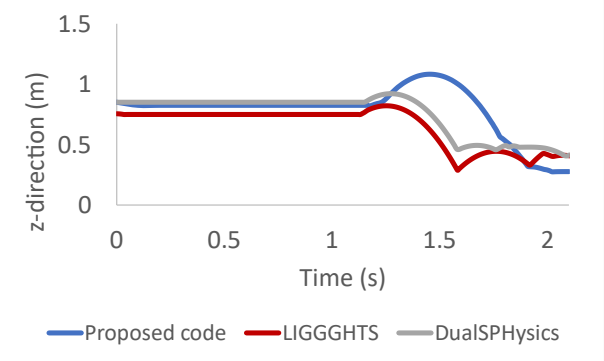

(c)

Figure 4.34 – Position comparison between the proposed model and LIGGGHTS for Block 8

4.6.3.5 Block 9 Force and position comparison

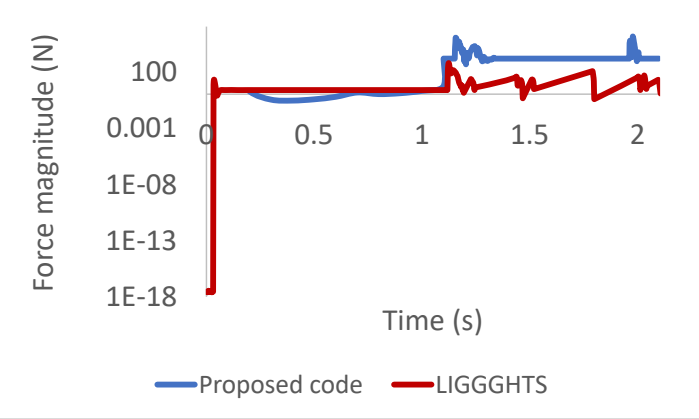

Figure 4.35 - Force comparison between the proposed model and LIGGGHTS for Block 9

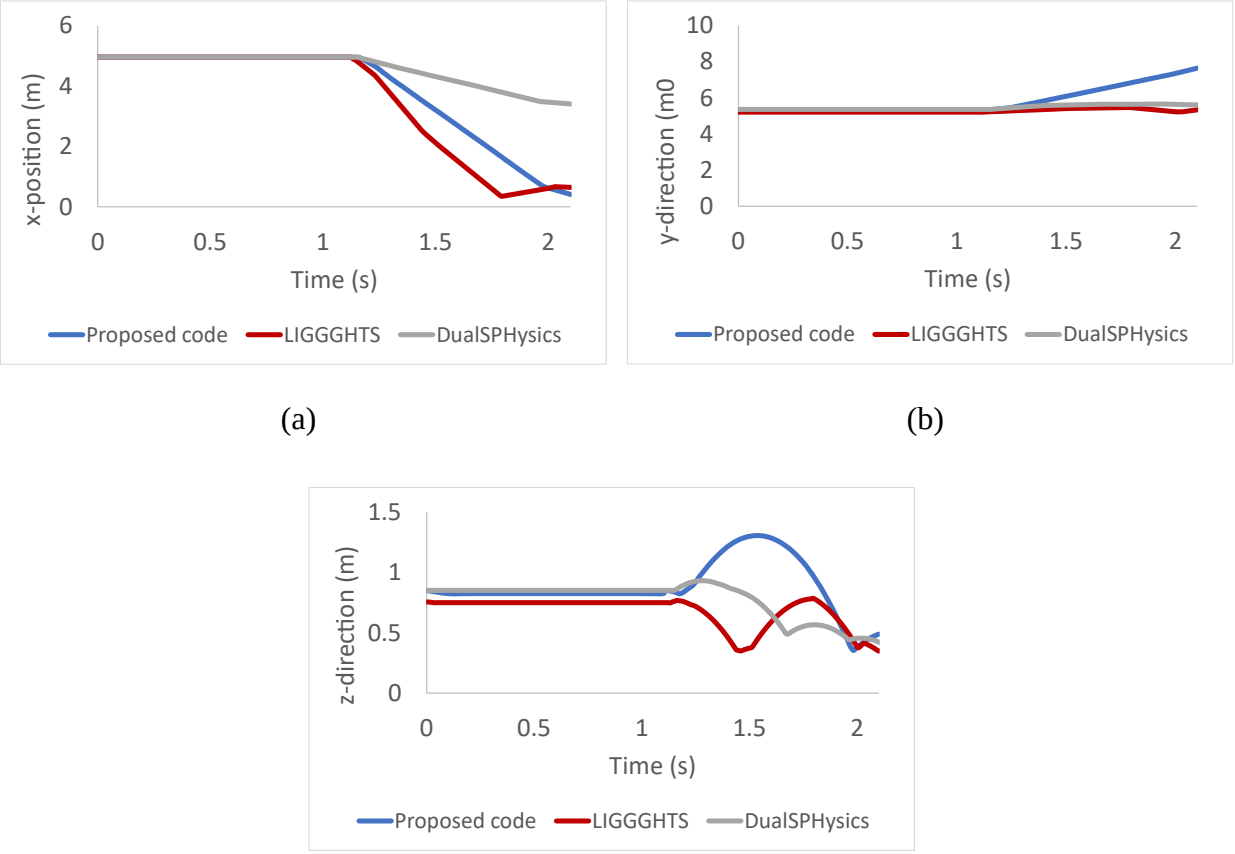

Figure 4.36 - Position comparison between the proposed model and LIGGGHTS for Block 9

4.6.3.6 Block 13 position comparison

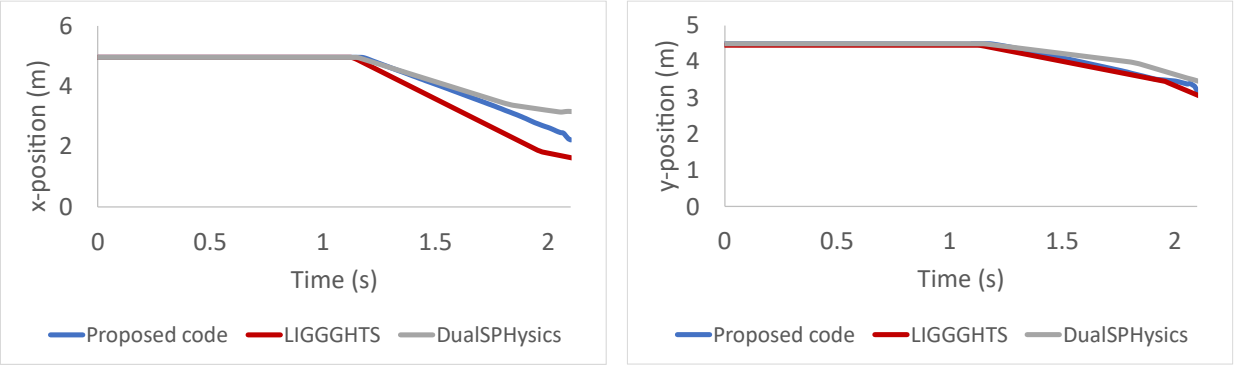

(a) (b)

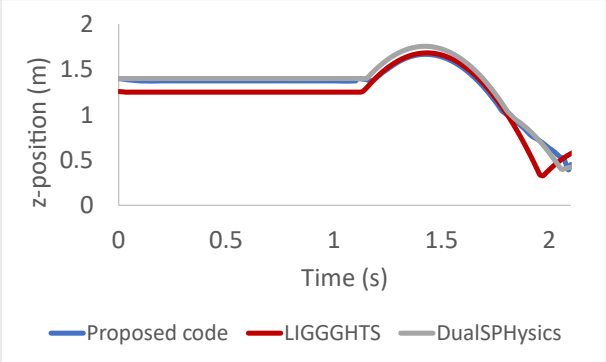

(c)

Figure 4.37 - Position comparison between the proposed model and LIGGGHTS for Block 13

4.6.3.7 Block 14 position comparison

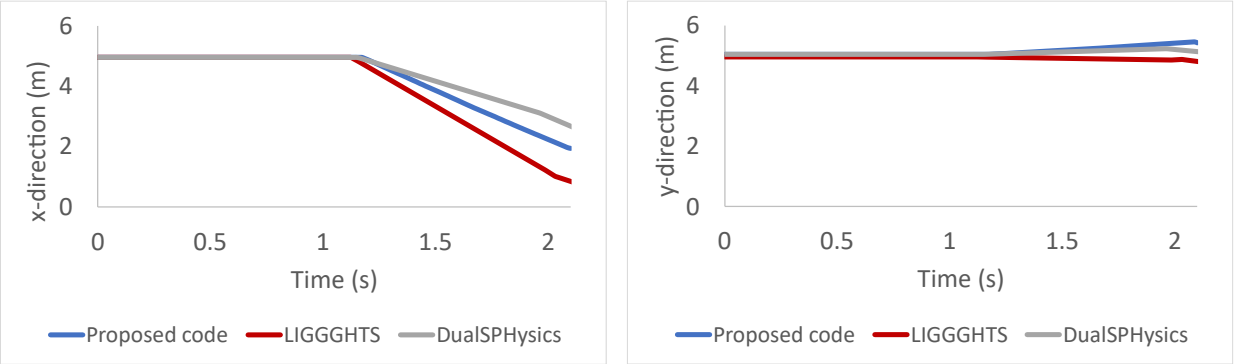

(a)

(b)

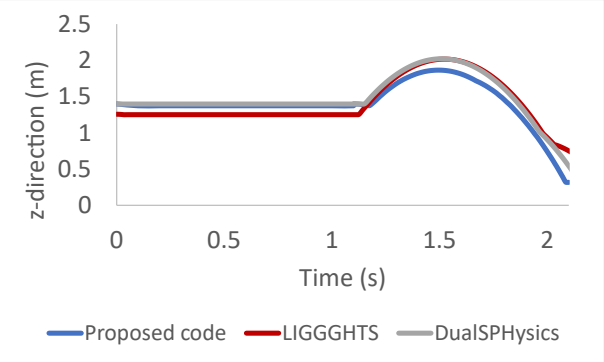

(c)

Figure 4.38 - Position comparison between the proposed model and LIGGGHTS for Block 14

4.7 Conclusion

In this chapter, the DEM model is explained, and the equations used are presented. Next, the DEM model, developed by the author of this thesis, was validated in 2D and 3D using both the single-particle and multisphere methods. The single-particle method was validated by comparing results with a well-known open-source code, LIGGGHTS. A single particle was released from rest, and the contact force with the floor was calculated. A maximum percentage difference of 6.81 % was obtained among the first five peaks of the contact force. The 2D multisphere method was validated using an experimental test case where the numerical results were in good agreement with the experimental test case when a contact ratio of 0.1 was used. The 3D multisphere method was

validated using a Demolisher test case performed by DualSPHysics, which only outputs the position. Thus, the simulation was reproduced in LIGGGHTS, with which the results were mainly compared. A simplified test case was performed to calibrate the contact ratio where three blocks were released from a given height. A contact ratio of 0.3 in the proposed model gave results that were in good agreement with LIGGGHTS. However, it was observed that the contact forces calculated from LIGGGHTS were unphysically small, and, according to LIGGGHTS' website [110], this error is corrected in the Premium version. Nonetheless, the blocks' overall position obtained from the proposed model was in good agreement with both LIGGGHTS and DualSPHysics.

CHAPTER 5 MPS-DEM COUPLING

Here in this research work, the interaction of rigid-solid bodies (i.e., ice) with fluid (i.e., water) is modelled by coupling the DEM method (for solid) with the moving particle semi-implicit (MPS) method (for fluid flow). This chapter is divided into two parts. In the first part, MPS is introduced. The second part explains how MPS is coupled with DEM.

5.1 MPS

5.1.1 Governing Equations

In a Lagrangian frame, the governing equations of fluid flow include the mass and momentum conservation laws, written as:

$$\frac{1}{\rho}\frac{D\rho}{Dt} = -\nabla \cdot \mathbf{v} \tag{5.1}$$

$$\rho\frac{D\mathbf{v}}{Dt} = -\nabla p + \mathbf{F} + \nabla(\mu\nabla \cdot \mathbf{v}) \tag{5.2}$$

$$\frac{D\mathbf{r}}{Dt} = \mathbf{v} \tag{5.3}$$

where ρ is the fluid density, $\mathbf{v}$ is the velocity vector, p is the pressure as a scalar, $\mathbf{F}$ is the body forces per unit volume, μ is the dynamic viscosity, and $\mathbf{r}$ is the position vector.

5.1.2 MPS discretization

In MPS, the fluid domain is represented by discrete particles whose position $\boldsymbol{r}_i$ is updated by Eq. (5.3). The physical quantities, such as velocity $\mathbf{v}$, pressure p, and spatial derivatives on each target particle i, are approximated using a weight-averaging (kernel smoothing) procedure over its neighboring particles, j, situated within a radius r_e, also known as the smoothing length of the approximation procedure. This influence is quantified by a weight (kernel) function $W_{ij} = W(r_{ij}, r_e)$, with $r_{ij} = |\mathbf{r}_j - \mathbf{r}_i|$ being the distance of particle i with its neighbor j.

In this project, the most widely used rational kernel function is adopted:

$$W(r_{ij}, r_e) = \begin{cases} r_e / r_{ij} - 1 & r_{ij} < r_e \\ 0 & r_{ij} \geq r_e \end{cases} \tag{5.4}$$

Also, the smoothing length is defined as $r_e = kl_0$ where k is a constant between 2 and 4 and l_0 is the average initial spacing between particles. In this project, a k value of 3.1 is chosen as it was seen to provide enough stability and accuracy [67]. In MPS, the density of particle *i* is represented by a dimensionless parameter *n* known as particle number density. This parameter is obtained by taking the summation of the kernel functions of the neighboring particles:

$$n_i = \sum_{i \neq j}^{N} W_{ij} \tag{5.5}$$

where $W_{ij} = W(r_{ij}, r_e)$ and N is the total number of neighboring particles *j* around particle *i*. Since the density does not vary for an incompressible fluid, the particle number density should remain constant [111].

A parameter *f* of particle *i*, such as velocity, temperature or pressure, is approximated (interpolated) in MPS using the normalized weighted average, represented by the operator ⟨⟩, of *f* on the neighboring particles *j* as follow:

$$\langle f \rangle_i = \frac{\sum_{i \neq j}^{N} f_j W_{ij}}{\sum_{i \neq j}^{N} W_{ij}} \tag{5.6}$$

The denominator of Equation (5.6) is defined as the normalization factor, n_0, and this equation can be rewritten as:

$$\langle f \rangle_i = \frac{1}{n_0} \sum_{i \neq j}^{N} f_j W_{ij} \tag{5.7}$$

In MPS, the gradient of an arbitrary scalar *f* is estimated by using the weight averaging gradient of *f* between particles *i* and *j*:

$$\langle \nabla f \rangle_i = \frac{d}{n_0} \sum_{i \neq j}^{N} \frac{f_j - f_i}{\|\mathbf{r}_{ij}\|} \mathbf{e}_{ij} W_{ij} \tag{5.8}$$

where d is the number of dimensions (e.g., for 2D, d=2) and $\mathbf{e}_{ij} = \mathbf{r}_{ij} / \|\mathbf{r}_{ij}\|$ is the unit direction vector between particles i and j. In the same way, the divergence of a vector **F** is obtained as:

$$\langle \nabla \cdot \mathbf{F} \rangle_i = \frac{d}{n_0} \sum_{i \neq j}^{N} \frac{\mathbf{F}_j - \mathbf{F}_i}{\|\mathbf{r}_{ij}\|} \cdot \mathbf{e}_{ij} W_{ij} \tag{5.9}$$

Similarly, the divergence of a vector gradient **F**, or the Laplacian of a vector **F**, is obtained as:

$$\langle \nabla^2 \mathbf{F} \rangle_i = \frac{2d}{n_0} \sum_{i \neq j}^{N} \frac{\mathbf{F}_j - \mathbf{F}_i}{\|\mathbf{r}_{ij}\|^2} W_{ij} \tag{5.10}$$

Eq. (5.10) can be rewritten as:

$$\langle \nabla^2 \mathbf{F} \rangle_i = \frac{2d}{\lambda n_0} \sum_{i \neq j}^{N} (\mathbf{F}_j - \mathbf{F}_i) W_{ij} \tag{5.11}$$

where λ is the average of the squared distance between particles i and j [60] and is defined as:

$$\lambda = \frac{\sum_{i \neq j}^{N} \|r_{ij}\|^2 W_{ij}}{\sum_{i \neq j}^{N} W_{ij}} \tag{5.12}$$

Equations (5.8) to (5.11) are used in MPS to discretize the governing equations from equations (5.1) and (5.2), and the parameters are updated using the second-order Symplectic time integrator, explained in more details in Section 5.1.3.

In the original MPS, the pressure and viscous terms of Equation (5.2) are estimated from Eqs. (5.8) and (5.11) as:

$$\left\langle \nabla p \right\rangle_i = \frac{d}{n_0} \sum_{i \neq j}^{N} \frac{p_j - p_i}{\left\| \mathbf{r}_{ij} \right\|} \mathbf{e}_{ij} W_{ij} \tag{5.13}$$

$$\left\langle \nabla (\mu \nabla \cdot \mathbf{u}) \right\rangle_i = \frac{2d\mu}{\lambda n_0} \sum_{i \neq j}^{N} \frac{\mathbf{u}_j - \mathbf{u}_i}{\left\| \mathbf{r}_{ij} \right\|} \mathbf{e}_{ij} W_{ij} \tag{5.14}$$

Nonetheless, Eq. (5.13) is derived for a regular particle distribution, and errors can arise for irregular particle distributions [72]. A corrective matrix has been derived using Taylor series expansion to enhance accuracy [70, 72, 73]. This enhancement's side-effect is that the momentum conservation is not satisfied because the interparticle pressure forces are not antisymmetric [67, 70].

The new formulation proposed by [67] is used in this study:

$$\left\langle \nabla p \right\rangle_i = \frac{d}{n_0} \sum_{i \neq j}^{N} \left(n_i \frac{p_j}{n_j} + n_j \frac{p_i}{n_i} \right) \frac{\mathbf{e}_{ij}}{\left\| \mathbf{r}_{ij} \right\|} W_{ij} \tag{5.15}$$

This discretization complies with the linear and angular momentum conservation law when external and shear forces are not present and do not require additional stabilizing techniques. Unlike non-conservative models, formulas that satisfy momentum conservation can reach a stable condition when a non-uniform particle distribution is defined initially [67].

Jandaghian and Shakibaeinia [67] proposed a new way of estimating the particle number density other than the widely-used formula shown in Eq. (5.5), whose accuracy varies greatly depending on the type of kernel function and the fluctuations of the particle distribution. The new way to calculate n_i, obtained from the continuity equation, limits errors near boundaries such as free-surfaces [67] and is defined as:

$$\frac{1}{n_i} \frac{Dn_i}{Dt} = -\frac{d}{n_0} \sum_{i \neq j}^{N} \left(\frac{n_j}{n_i} \right) \frac{\mathbf{v}_{ij}}{\left\| \mathbf{r}_{ij} \right\|} \mathbf{e}_{ij} W_{ij} \tag{5.16}$$

where $\mathbf{v}_{ij} = \mathbf{v}_j - \mathbf{v}_i$. Using the conjugate form of the gradient and divergence operators through Eqs. (5.15) and (5.16) conserve the total energy of the system without dissipative terms [67].

Unlike the original MPS, where the fluid is considered incompressible and the pressure is calculated implicitly using the Poisson equation [60], a weakly compressible fluid is considered in this paper. Thus, the Equation of State (EOS) proposed by Shakibaeinia and Jin [62], where the pressure is a function of n_i as given in Eq. (5.17)., is explicitly solved to calculate the pressure:

$$p_i = \frac{c_0^2 \rho_0}{\gamma}\left(\left(\frac{n_i}{n_0}\right)^{\gamma} - 1\right), \quad \gamma = 7 \tag{5.17}$$

where c_0 is the numerical sound speed and ρ_0 is the water density. Since the fluid is considered compressible, a speed of sound exists [112]. However, since the time step is related to c_0 as:

$$\Delta t_{MPS} \leq CFL \frac{l_0}{c_0 + \|\mathbf{u}\|_{max}} \tag{5.18}$$

where CFL is the Courant-Friedrichs-Lewy stability condition ($0 < CFL \leq 1$), c_0 cannot be equal to the real sound speed since that would lead to very small time steps and unexpectedly high computational time. Thus, c_0 used in this project is smaller than the real fluid sound speed and is taken to be about ten times the maximum flow velocity, u_{max}. The Mach number is therefore 0.1 ($Ma = u_{max}/c_0 = 0.1$) and the variation of the fluid density is less than 1% [112].

5.1.3 The Symplectic Time Integrator

The second-order symplectic integrator, also known as the Verlet integrator, is used in this project to update the position, velocity, particle number density, and pressure [113]. In this algorithm, the position is updated at each half step, while the velocity is not. However, the velocity at each half step is calculated, as depicted in **Figure 5.1**, to determine the viscosity halfway. If viscosity is zero, then $\mathbf{v}^{t+\frac{1}{2}\Delta t_{MPS}}$ does not need to be calculated [113].

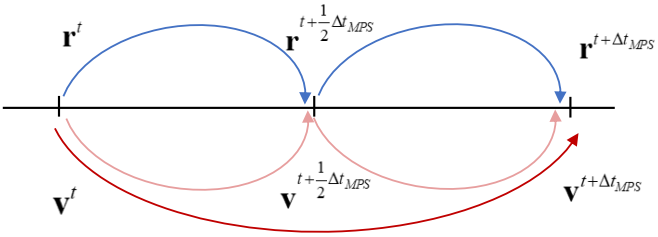

Figure 5.1 - The Symplectic time integrator scheme

For simplicity, Equations (5.2), (5.3), and (5.16) are rewritten as:

$$\frac{\mathrm{D}\mathbf{r}}{\mathrm{D}t} = \mathbf{v} \tag{5.19}$$

$$\rho \frac{\mathrm{D}\mathbf{v}}{\mathrm{D}t} = \boldsymbol{\Gamma} \tag{5.20}$$

$$\frac{1}{n_i}\frac{\mathrm{D}n_i}{\mathrm{D}t} = \mathbf{N} \tag{5.21}$$

where, $\boldsymbol{\Gamma}$ and $\mathbf{N}$ are the LHS of Equations (5.2) and (5.16), respectively. The position, velocity, and particle number density can be defined at half a time step as:

$$\mathbf{r}_i^{t+\frac{1}{2}\Delta t_{MPS}} = \mathbf{r}_i^t + \frac{1}{2}\Delta t_{MPS}\mathbf{v}_i^t \tag{5.22}$$

$$\mathbf{v}_i^{t+\frac{1}{2}\Delta t_{MPS}} = \mathbf{v}_i^t + \frac{1}{2}\Delta t_{MPS}\rho\boldsymbol{\Gamma}_i^t \tag{5.23}$$

$$n_i^{t+\frac{1}{2}\Delta t_{MPS}} = n_i^t\left(1+\frac{1}{2}\Delta t_{MPS}\mathbf{N}_i^t\right) \tag{5.24}$$

Once these values are obtained, the parameter, $\boldsymbol{\Gamma}^{t+\frac{1}{2}\Delta t_{MPS}}$, is determined. Ulteriorly, the particle's position and velocity at the new time step are calculated as:

$$\mathbf{v}_i^{t+\Delta t_{MPS}} = \mathbf{v}_i^t + \Delta t_{MPS}\boldsymbol{\Gamma}_i^{t+\frac{1}{2}\Delta t_{MPS}} \tag{5.25}$$

$$\mathbf{r}_i^{t+\Delta t_{MPS}} = \mathbf{r}_i^{t+\frac{1}{2}\Delta t_{MPS}} + \frac{1}{2}\Delta t_{MPS}\mathbf{v}_i^{t+\Delta t_{MPS}} \tag{5.26}$$

From these values, $\mathbf{N}_i^{t+\Delta t_{MPS}}$ is calculated, and the new particle number density is found as:

$$n_i^{t+\Delta t_{MPS}} = n_i^{t+\frac{1}{2}\Delta t_{MPS}} + \frac{1}{2}\Delta t_{MPS} n_i^{t+\frac{1}{2}\Delta t_{MPS}} \mathbf{N}^{t+\Delta t_{MPS}} \tag{5.27}$$

5.1.4 Boundary conditions

5.1.4.1 Free surface

As a particle approaches the free surface, its particle number density decreases because fewer neighboring particles are detected as there is no particle beyond the free surface. If the particle number density of particle *i* satisfies:

$$n_i \leq \beta_n n_0 \tag{5.28}$$

where β_n is an empirical parameter that varies between 0.8 and 0.99, then particle *i* is considered a free-surface particle [111]. In this study, β_n is set at 0.9 and a Dirichlet boundary condition for pressure is imposed to these particles.

5.1.4.2 Wall Boundary

The wall boundaries are defined by fixed particles divided into two categories: wall and ghost particles. The wall particles are the particles in direct contact with the fluid particles. The ghost particles, placed beyond the wall particles, are used to avoid the kernel truncation of wall particles and fluid particles near the boundary wall. As a result, the presence of ghost particles avoids fluid particles' penetration through the walls. The number of ghost particles required to avoid incomplete kernel support depends on the smoothing length r_e. In this project, since a smoothing length of $r_e = 3.1 l_0$ is chosen, three ghost particles are placed beyond the wall particles. An example of the boundary implementation is shown in Figure 5.2.

The pressure of solid boundary particles is determined using a Neumann boundary condition where a zero pressure gradient is defined [60].

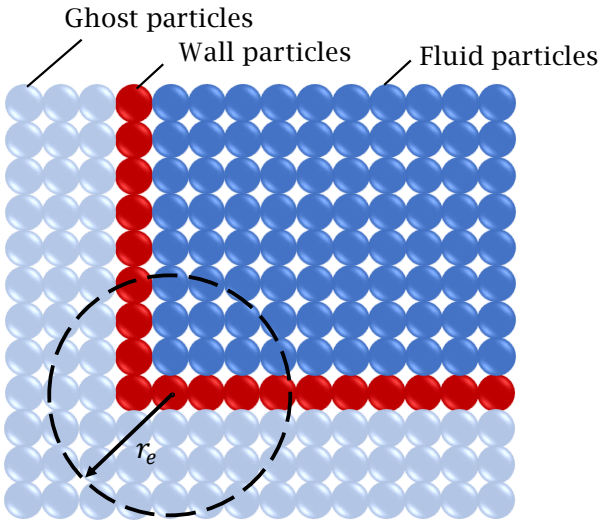

Figure 5.2 - The boundary configuration

A slip boundary can be implemented by setting the wall and ghost particles' velocity to be the same as the nearest fluid particle's velocity. Likewise, a non-slip condition is defined by setting the boundary particles' velocity to zero.

5.1.5 Diffusive Term

The shortcoming of considering a weakly compressible model is that some unphysical fluctuations in the density occur. Thus, a diffusive term is added to the continuity equation approximation from Eq. (5.16) to avoid such behavior. The diffusive term defined and adopted by [67] is used in this project:

$$D_i = \delta_{MPS} \frac{c_0^2 \Delta t_{MPS}}{n_0} \left\langle \nabla^2 n \right\rangle_i \tag{5.29}$$

where δ_{MPS} is a calibrated dimensionless coefficient that varies between 0 and 1. Thus, the new continuity equation Eq. (5.16) with the diffusive term becomes:

$$\frac{1}{n_i}\frac{Dn_i}{Dt} = -\frac{d}{n_0}\sum_{i\neq j}^{N}\left(\frac{n_j}{n_i}\right)\frac{\mathbf{v}_{ij}}{\|\mathbf{r}_{ij}\|}\mathbf{e}_{ij}W_{ij} + \left(\frac{\delta_{MPS}\Delta t_{MPS}{c_0}^2}{n_0}\right)\frac{2d}{\lambda n_0}\sum_{i\neq j}^{N} n_{ij}W_{ij} \tag{5.30}$$

where *i* and *j* belong to fluid particles only. It should be noted that the magnitude of the diffusive term decreases when spatial resolution increases [67].

5.1.6 Particle Shifting Technique

Several studies on particle methods have adopted particle shifting techniques to prevent density fluctuations and particle clustering [66, 72, 114, 115]. In this paper, the particle shifting (PS) algorithm proposed by [67] is implemented. This algorithm defines the particle shifting vector based on the "Fick's law of diffusion," similar to what has been applied in SPH [66], as:

$$\delta \mathbf{r}_i = -F_i \nabla C_i \tag{5.31}$$

where C_i is particle i's concentration and F_i is the Fickian diffusion coefficient defined as $F_i = 2l_0^2 CFL \cdot Ma$. Using the MPS approximation, C_i is approximated as:

$$C_i = \frac{\sum_{i \neq j}^{N} W_{ij}}{n_0} \tag{5.32}$$

and the gradient of C_i is:

$$\langle \nabla C \rangle_i = \frac{d}{n_0} \sum_{i \neq j}^{N} \frac{C_i + C_j}{\|\mathbf{r}_{ij}\|} \mathbf{e}_{ij} W_{ij} \tag{5.33}$$

This new concentration gradient equation is conservative and does not have any pairing instability problem found in other concentration gradient equations used in SPH. Nonetheless, if the particle shifting technique is applied to particles near the free surface, these particles would be shifted towards the free surface leading to erroneous behaviors caused by the incomplete kernel support of particles near the free surface. This issue is addressed by implementing an algorithm that identifies the particles near the free surface and prevents them from shifting towards the surface [67]. Therefore, the algorithm defines four categories of particles depicted in **Figure 5.3**:

1. free-surface particle ($i \in \mathbb{F}$)
2. vicinity of a free-surface particle ($i \in \mathbb{B}$)
3. internal particle ($i \in \mathbb{I}$)

4. external/splashed particle ($i \in \mathbb{E}$)

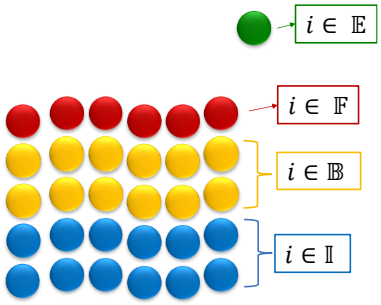

Figure 5.3 - Particle classification as free-surface ($i \in \mathbb{F}$), near to free-surface ($i \in \mathbb{B}$), external ($i \in \mathbb{E}$), or internal particle ($i \in \mathbb{I}$)

The particle's concentration is used to define in which category the fluid particle falls into. If $C_i < \beta_E$, where β_E is a calibrated coefficient set to 0.4, then the particle is considered an external particle ($i \in \mathbb{E}$). If $\beta_E \leq C_i \leq \beta_F$, where β_F is a calibrated coefficient set to 0.9, a region perpendicular to the free-surface is scanned to determine whether the particle is a free-surface particle or not. The region to be scanned is the umbrella-shaped region that comprises regions R1 and R2 shown in **Figure 5.4**.

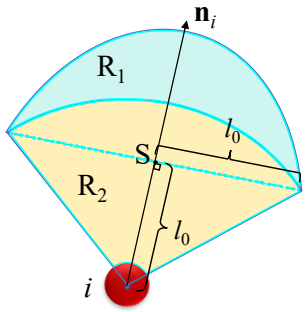

Figure 5.4 - Scanning regions R1 and R2 used to determine if the particle *i* is a free-surface particle or not

If no neighboring particle *j* is found in either region R1 or R2 ($j \notin R1 \cup R2$), then particle *i* is considered a free-surface particle. Another way of defining a free-surface particle is to compare the number of surrounding particles, N_i, to the maximum initial number of neighbors, N_0. If $N_i < \beta_N N_0$, where β_N is a parameter set to 0.75, then particle *i* is also considered a free-surface particle [67].

The particle *j* is located inside region R1 or R2 if it satisfies the following conditions:

$$\begin{cases} \left|\mathbf{r}_{ij}\right| \geq \sqrt{2}l_0 \ \textit{and} \ \left|\mathbf{r}_{jS}\right| < l_0 & j \in \mathrm{R1} \\ \left|\mathbf{r}_{ij}\right| < \sqrt{2}l_0 \ \textit{and} \ \left|\mathbf{n}_i \cdot \mathbf{r}_{jS}\right| + \left|\mathbf{t}_i \cdot \mathbf{r}_{jS}\right| < l_0 & j \in \mathrm{R2} \end{cases} \tag{5.34}$$

where $\mathbf{r}_{jS} = \mathbf{r}_j - \mathbf{r}_S$ and $\mathbf{r}_S = \mathbf{r}_i + l_0\mathbf{n}_i$. The local unit normal and tangential vector to the surface of particle *i* are $\mathbf{n}_i$ and $\mathbf{t}_i$, respectively, and are defined as:

$$\begin{aligned} \mathbf{n}_i &= \frac{\mathbf{N}_i}{\left\|\mathbf{N}_i\right\|}, \qquad \mathbf{N}_i = \sum_{i \neq j}^{N} \mathbf{e}_{ij} W_{ij} \\ \mathbf{t}_i &= \begin{bmatrix} 0 & -1 \\ 1 & 0 \end{bmatrix} \mathbf{n}_i \end{aligned} \tag{5.35}$$

If particle *j* is a free-surface particle ($j \in \mathbb{F}$) and satisfies either condition from Equations (5.34), particle *i* is considered a neighbor to a free-surface particle ($i \in \mathbb{B}$). Particle *i* also belongs to $\mathbb{B}$ if $\beta_F < C_i$ and $\mathbf{r}_{ij} \leq \alpha l_0$, where α is a variable dependent on the smoothing length [67]. A value of $\alpha = 2.1$ is used in this paper. All other particles are classified as internal fluid particles ($i \in \mathbb{I}$).

The particle shifting technique is defined as:

$$\delta\mathbf{r}_i = \begin{cases} -F_i \nabla C_i & \textit{if} \ \ i \in \mathbb{I} \\ -F_i(\mathbf{I} - F_c \hat{\mathbf{n}}_i \otimes \hat{\mathbf{n}}_\mathbf{i})\nabla C_i & \textit{if} \ \ i \in \mathbb{B} \\ -F_i(\mathbf{I} - \mathbf{n}_i \otimes \mathbf{n}_\mathbf{i})\nabla C_i & \textit{if} \ \ i \in \mathbb{F} \\ 0 & \textit{if} \ \ i \in \mathbb{E} \end{cases} \tag{5.36}$$

where $\mathbf{I}$ is the identity matrix and $\hat{\mathbf{n}}_i$ is a non-local unit vector determined as:

$$\mathbf{n}_i = \frac{\mathbf{N}_i}{\left\|\mathbf{N}_i\right\|}, \qquad \mathbf{N}_i = \sum_{j \in \mathbb{F}}^{N} \mathbf{n}_j W_{ij} \tag{5.37}$$

F_c is a factor of correction defined as either 0 or 1. If particle *i* belongs to $\mathbb{B}$ and does not move towards the free-surface ($\hat{\mathbf{n}}_i \cdot \delta\mathbf{r}_i < 0$), then F_c is set to 0 and $\delta\boldsymbol{r}_{i \in \mathbb{B}} = -F_i \nabla C_i$. In other words, if

a particle near the free-surface does not move towards the free-surface, then the particle shifting method is applied as though the particle was an internal particle.

While the particle shifting technique prevents tensile instability in the internal particles, the particles' motion near the free surface is sensitive to negative pressure. Thus, either the negative pressures are set to zero, or a particle collision (PC) method is implemented for particles near the free surface as:

$$\begin{aligned} \tilde{\mathbf{v}}_i &= \mathbf{v}_i - \frac{1+\varepsilon}{2}\mathbf{v}_{ij}^{coll}, \qquad i \in \mathbb{F} \cup \mathbb{B} \\ \tilde{\mathbf{v}}_j &= \mathbf{v}_j + \frac{1+\varepsilon}{2}\mathbf{v}_{ij}^{coll}, \qquad j \in \mathbb{F} \cup \mathbb{B} \end{aligned} \tag{5.38}$$

where ε is the collision ratio set to 0.5, and $\tilde{\mathbf{v}}_i$ and $\tilde{\mathbf{v}}_j$ are the velocity after a collision between particles *i* and *j*, respectively. The collision velocity $\mathbf{v}_{ij}^{coll}$, obtained from Equation (5.39), between particles *i* and *j* is calculated if the particles are close enough ($\|\mathbf{r}_{ij}\| \leq 0.90 l_0$) and they are approaching ($\mathbf{v}_{ij} \cdot \mathbf{r}_{ij} < 0$).

$$\mathbf{v}_{ij}^{coll} = (\mathbf{v}_{ij} \cdot \mathbf{e}_{ij})\mathbf{e}_{ij} \tag{5.39}$$

5.1.7 Linked Cell method

In particle-based methods, the interparticle interactions are used to determine each particle's physical properties. A naïve approach is to let the model calculate the interaction between all the particles in the domain. Nonetheless, with such a method, the computational time is proportional to N^2 where N is the total number of particles in the domain [62]. In MPS, each particle' physical properties are estimated using the particles within a radius r_e. In other words, only the closest particles will affect each other, and there is no need to calculate the interaction between all particles. Thus, an algorithm that will search for the closest, or neighbor, particles can be implemented to reduce computational time. In this project, a linked cell method is implemented to search the neighbor particles, and thus, to reduce the computational time from N^2 to $N\log N$ [62].

In the linked cell method, the computational domain is divided into square cells using a background cartesian grid having a mesh size of $r_e + \delta$. Based on each particle's location, all particles are allocated to a cell. For instance, as shown in **Figure 5.5**, particle i is allocated to cell 18. The particles located in the nearby cells are denoted as neighbor particles of particle i. Thus, from **Figure 5.5**, the particles in dark blue are included in the neighbor list and are the ones that will interact with particle i. In 2D, the eight cells surrounding the cell containing particle i are considered in the neighbour search, while in 3D, the 26 nearby cells are considered. In this project, $\delta = l_0/5$.

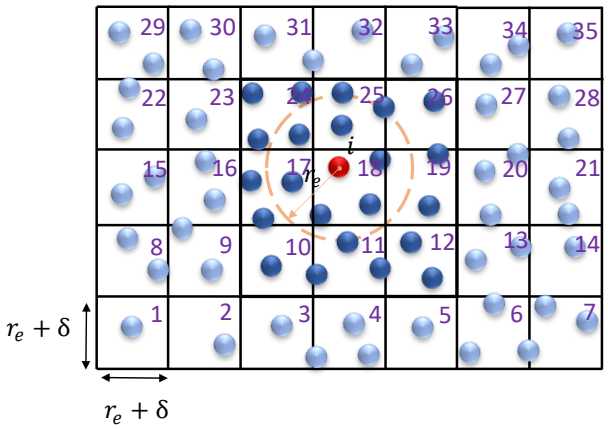

Figure 5.5 - Linked cell method: neighbors of particle *i* are inside the black square

5.2 MPS-DEM coupling

Once MPS and DEM have been developed individually, they can be coupled together to simulate the solid-fluid (ice and water) interactions. MPS will simulate the fluid phase, and DEM will simulate the solid phase. Here, we consider a two-way coupling approach. MPS provides the hydrodynamic force for the DEM, and the DEM provides the solid boundary for MPS.

As mentioned in Chapter 4, the movement of a rigid body is governed by the forces applied to it. The force of fluid (hydrodynamic force) $\mathbf{F}_h$ from Equations (4.29), (4.30), and (4.31) is analyzed in this Section. The hydrodynamic force can be calculated by integrating the fluid stress tensor over the surface of the solid bodies. Here, only the fluid normal force, i.e., the fluid pressure, is considered. In other words. the fluid shear force is ignored. Therefore, $\mathbf{F}_{h,i}$ (the hydrodynamic force applied on particle i on the surface of the solid body) is calculated by multiplying the pressure of

particle i (given by MPS) by the surface area of the object represented by particle i. In this case, particle i refers to the particle on the surface of the solid body, and its pressure is calculated using Equation (5.17). Note that the particles located on the solid surface (or solid surface particles) are considered fluid particles in MPS, for which the pressure is calculated.

When the solid and fluid particles are close enough to be considered neighbor particles, the solid particles must be included in the fluid particles' neighbor list. In this way, the fluid particles will detect the solid particles, and a repulsion force from the solid surface particles will avoid fluid penetration inside the solid. Furthermore, to avoid incomplete kernel support on the solid surface particles, three ghost particles are placed inside the solid, as shown in **Figure 5.6**. These particles are called solid ghost particles. For Equations (5.15) and (5.17), the particle number density of the solid surface particles is calculated using Equation (5.24), while the ghost particles have been assigned a value of $0.8n_0$ for stability.

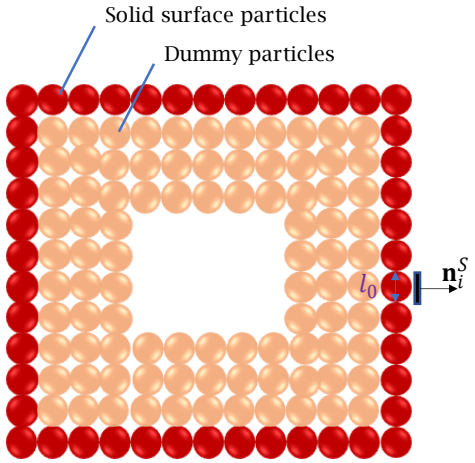

Figure 5.6 – A solid rigid body will have at least three layers of ghost particles inside to avoid incomplete kernel support

The hydrodynamic force on the solid surface particles is calculated as:

$$\mathbf{F}_{h,i} = -p_i A \mathbf{n}_i^S \tag{5.40}$$

where p_i is the pressure on the solid surface particle, $A(= l_0^2)$ is the contact area between the fluid and the solid particles, and $\mathbf{n}_i^S$ is the normal vector on the solid surface, shown in **Figure 5.6**.

This force is updated each time the solid's motion is updated. As mentioned in Section 4.2.2, the solid's positions must be calculated at each Δt_{DEM} to maintain stability. However, the pressure p_i calculated by MPS is updated each Δt_{MPS}. Since the DEM time step is much smaller than the MPS time step, Δt_{DEM} should be taken as the time step for the whole model to maintain stability in both DEM and MPS. However, by doing so, the computational cost is increased significantly because Δt_{DEM} is in general around three orders of magnitude smaller than the Δt_{MPS} [80]. Taking Δt_{MPS} for the whole process would not be a good option either because the DEM model would not converge. To solve this problem, a dynamic sub-cycling algorithm is implemented in this project where the DEM calculations are performed several times using Δt_{DEM} within a single Δt_{MPS} time step, as depicted in **Figure 5.7**.

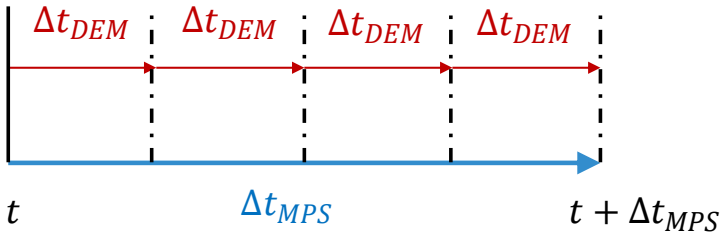

Figure 5.7 - Subcycling method to ensure stability in both MPS and DEM methods

5.2.1 Algorithm

This subsection explains the following flowchart.

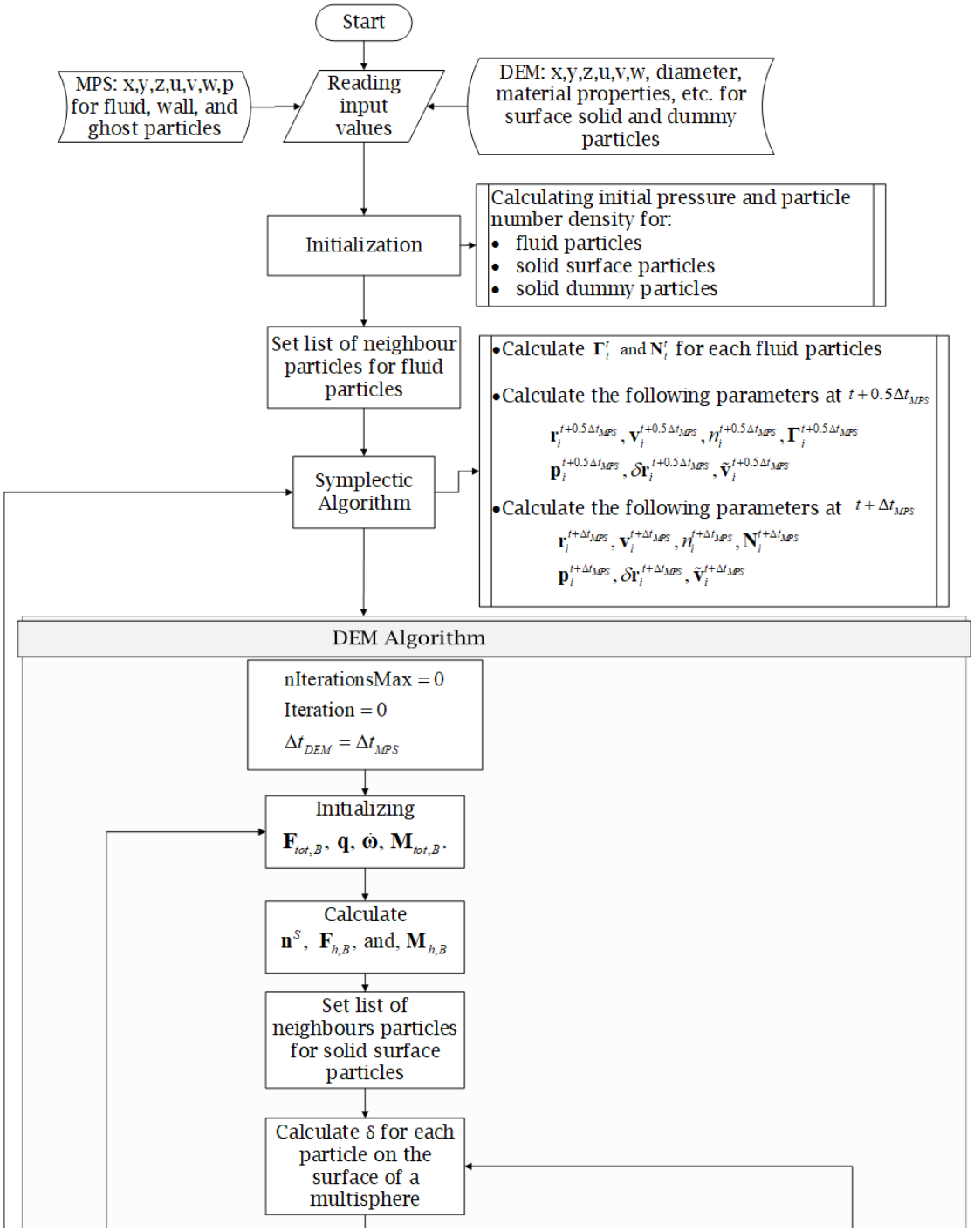

Figure 5.8 - MPS-DEM coupling algorithm

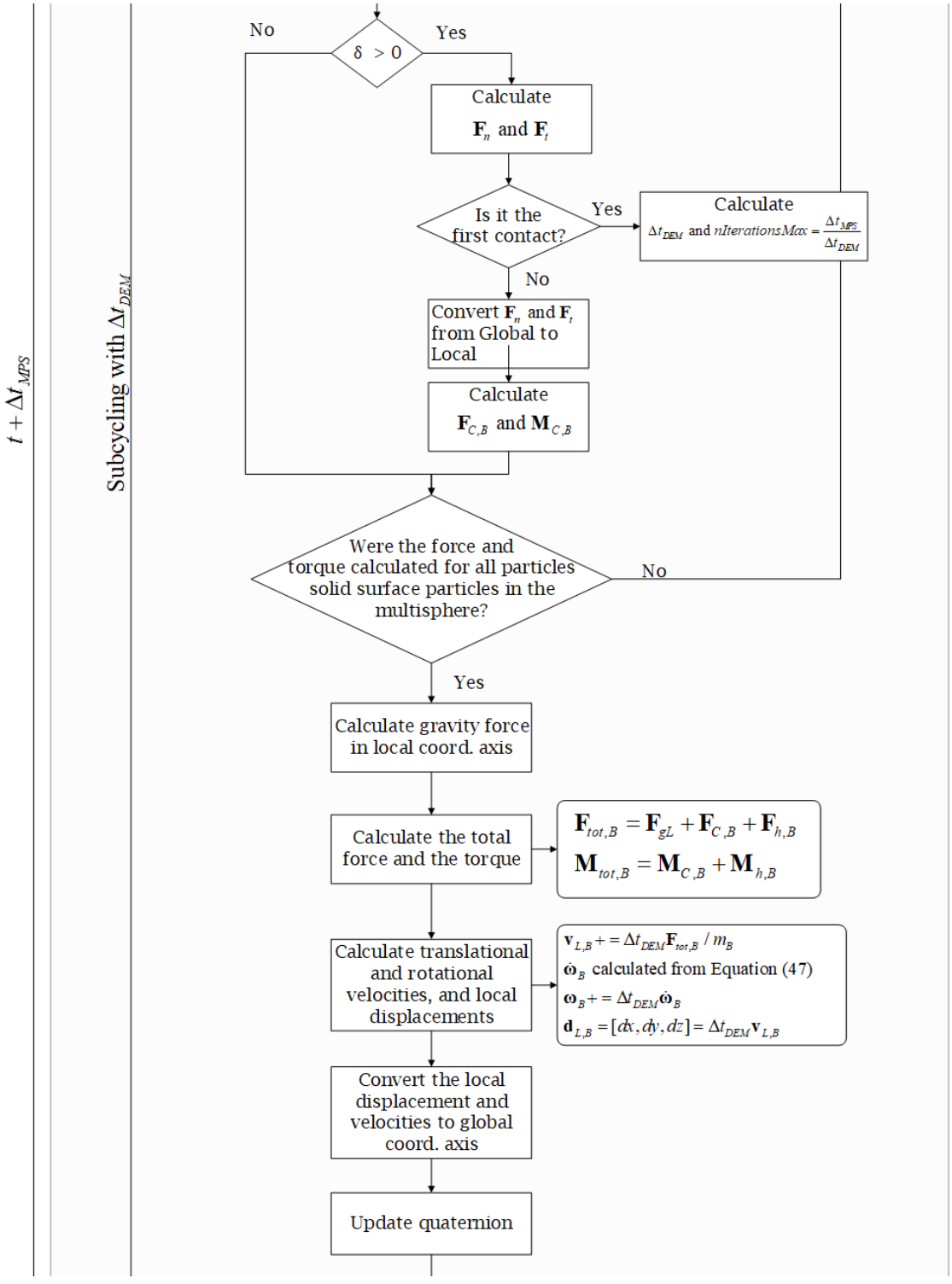

Figure 5.8 - MPS-DEM coupling algorithm (cont'd)

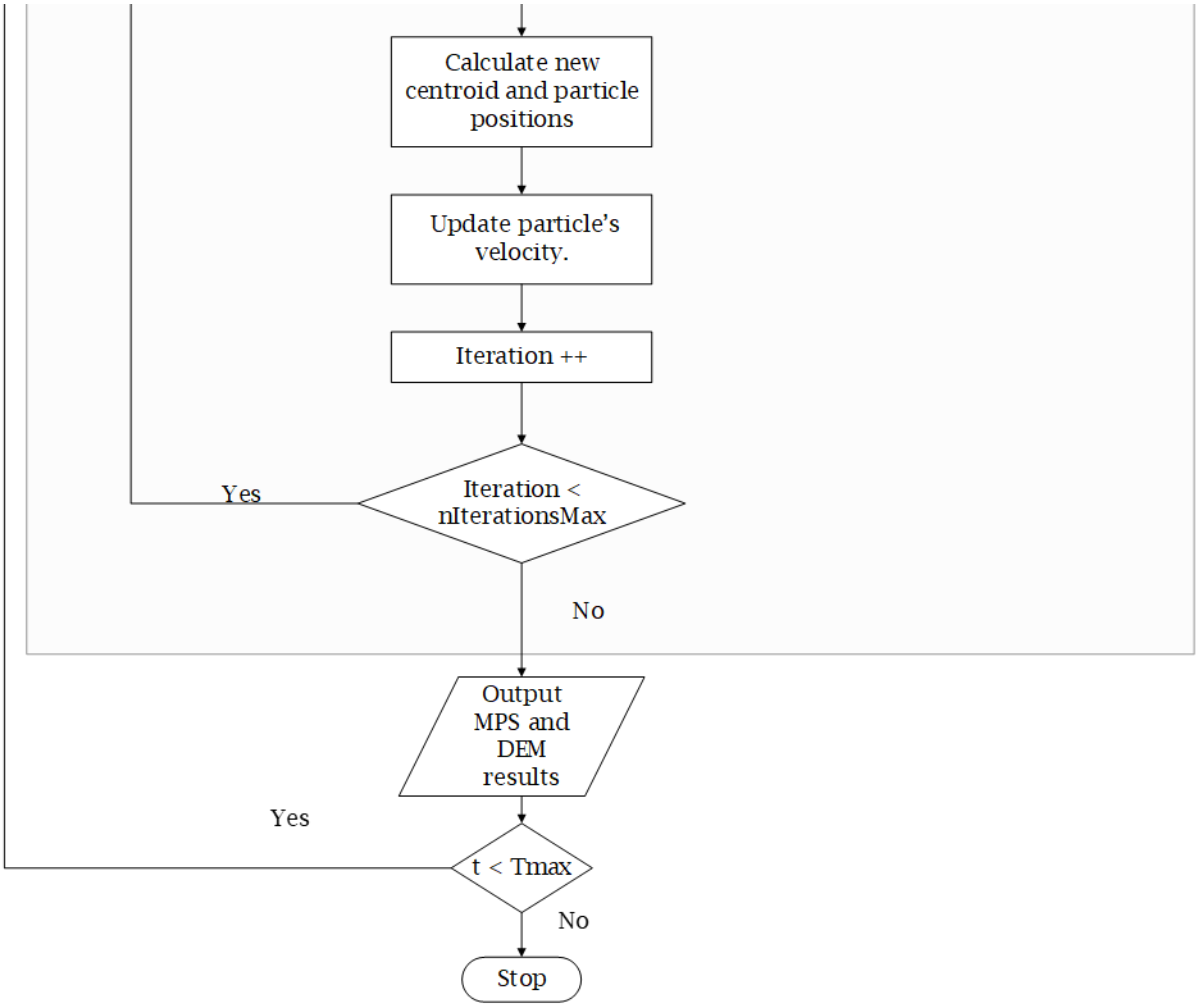

Figure 5.8 - MPS-DEM coupling algorithm (cont'd)

Two input files are required to run the coupled method: the DEM and MPS input files. The DEM input file is the same as the one explained in Section 4.5.1, while an example of the MPS input file, named *input.txt*, is shown in **Figure 5.9**.

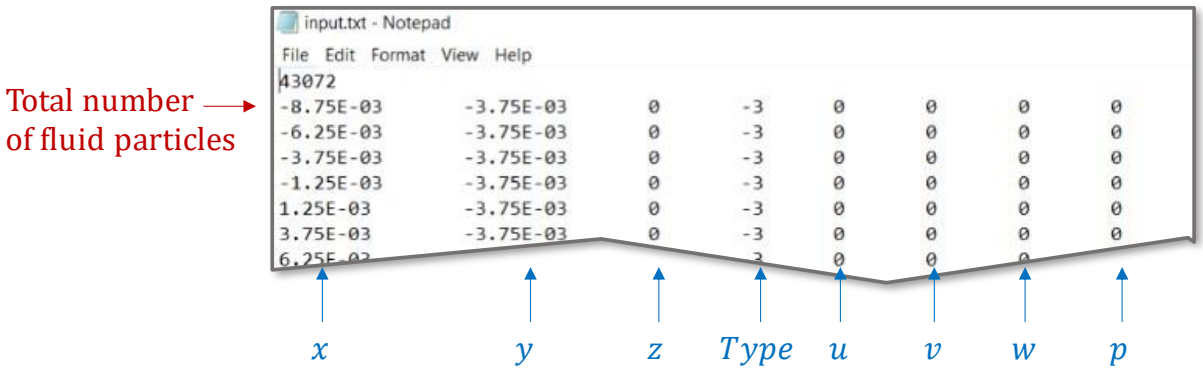

Figure 5.9 - MPS input file

Once all the parameters are assigned, the first step consists of initializing the pressure and particle number density for fluid, solid surface, and solid ghost particles. While the pressure on solid ghost particles is set to 0, the pressure for fluid and solid surface particles is initialized using the hydrostatic equation:

$$p_i = \gamma h_i \tag{5.41}$$

The fluid and solid surface particles' particle number densities are determined from Equation (5.17) by using the pressure p_i found from Equation (5.41):

$$n_i = n_0 \cdot \sqrt[\gamma]{\frac{p_i \gamma}{\rho_0 c_0^2} + 1}\,, \qquad \gamma = 7 \tag{5.42}$$

For the solid ghost particles, $n_i = 0.8\, n_0$.

The next step consists of setting a list of neighbor particles for all the fluid particles. This step is performed using the Linked Cell algorithm mentioned in Section 5.1.7.

The following step involves calculating all the fluid particles' properties using the Symplectic Time Integrator algorithm explained in Section 5.1.3. In this step, only the pressure and particle number density of the solid surface particles are updated.

Next, upon entering the DEM algorithm, two variables, *nIterationsMax* and *Iteration*, are set to 0. These variables are used for the DEM algorithm subcycling, where *nIterationsMax* determines the maximum number of subcycling iterations to be performed, and *Iteration* is the number of

iteration(s) performed. Also, $\Delta t_{DEM} = \Delta t_{MPS}$ at the beginning of the DEM algorithm because if no contact occurs, then the subcycling time step is the same as the model's time step, which is Δt_{MPS}.

Then comes the DEM initialization step, as explained in Section 4.5.2. The subsequent step involves calculating the normal unit vector to the solid surface and the hydrodynamic force and torque. Depending on the implemented geometry, the calculation of the normal unit vector varies. In this project, spheres and rectangular prisms were used (or circles and rectangles in 2D). The normal unit vector to the solid having a rectangular shape is:

$$\mathbf{n}_i^S = \frac{\mathbf{r}_{i\epsilon\Omega_B} - \mathbf{r}_{j\epsilon\mathrm{D}}}{\left\|\mathbf{r}_{i\epsilon\Omega_B} - \mathbf{r}_{j\epsilon\mathrm{D}}\right\|} \tag{5.43}$$

where $\mathbf{r}_{i\epsilon\Omega_B}$ is the position of the solid surface particle *i* while $\mathbf{r}_{j\epsilon D}$ is the position of the closest ghost particle to the solid surface particle, as shown in **Figure 5.10**.

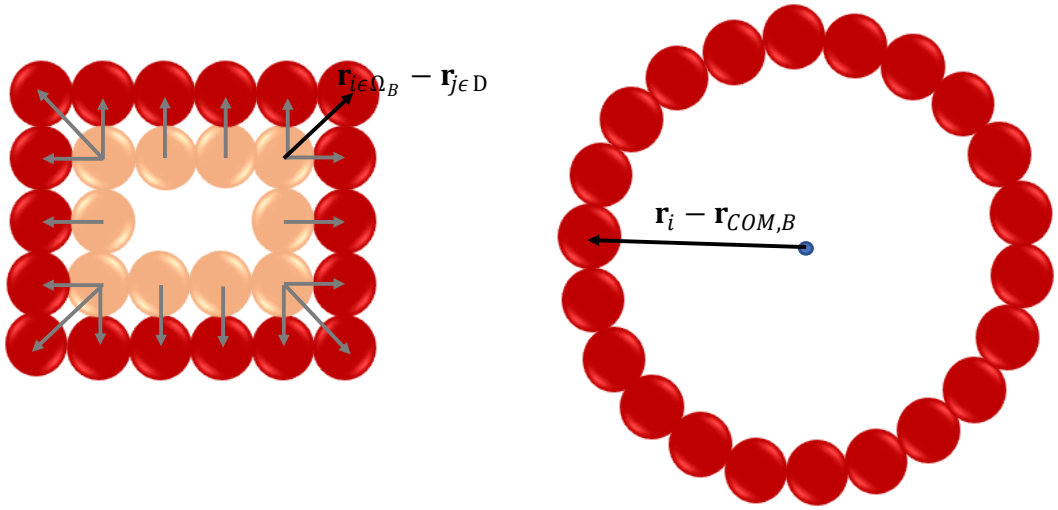

Figure 5.10 – Direction of normal unit vectors for rectangular and circular shapes

The normal unit vector for a circular shape is determined using the vector shown in **Figure 5.10**, $\mathbf{r}_i - \mathbf{r}_{COM,B}$**,** which is the relative position vector between the solid surface particle and the solid's center of mass:

$$\mathbf{n}_i^S = \frac{\mathbf{r}_i - \mathbf{r}_{COM,B}}{\left\|\mathbf{r}_i - \mathbf{r}_{COM,B}\right\|} \tag{5.44}$$

The hydrodynamic force applied to the solid rigid body is calculated by summing up all the hydrodynamic forces applied to the solid surface particles:

$$\mathbf{F}_{h,B} = \sum_{i \epsilon \Omega_B} \mathbf{F}_{h,i} = - \sum_{i \epsilon \Omega_B} p_i l_0^2 \mathbf{n}_i^S \tag{5.45}$$

Likewise, the hydrodynamic torque applied to the solid surface rigid body is determined as:

$$\mathbf{M}_{h,B} = \sum_{i \epsilon \Omega_B} \left(\mathbf{r}_i - \mathbf{r}_{COM,B}\right) \times \mathbf{F}_{h,i} = - \sum_{i \epsilon \Omega_B} \left(\mathbf{r}_i - \mathbf{r}_{COM,B}\right) \times p_i l_0^2 \mathbf{n}_i^S \tag{5.46}$$

For a circular (2D) or spherical (3D) solid shape, the hydrodynamic torque is equal to 0.

In the next step, a linked cell algorithm is implemented once more, but only the solid surface particles are included in the neighboring list.

The following steps are the same as in the DEM algorithm with the only difference that, in the first contact, *nIterationsMax* is calculated as the ratio between Δt_{MPS} and Δt_{DEM} and is assumed constant throughout the subcycling.

Once $\mathbf{F}_{C,B}$ and $\mathbf{M}_{C,B}$ are calculated as explained in the DEM chapter, the total force acting on the rigid body, $\mathbf{F}_{C,B}$, can be calculated by adding the gravity, contact, and hydrodynamic forces together. Similarly, the total torque can be determined by adding the contact and hydrodynamic torques. Then, as detailed in the DEM chapter, the translational and rotational velocities and the displacements of the rigid body are found.

After updating the quaternion, each particle's position and velocity, and the solid's center of mass position, the *Iteration* value is incremented. The DEM loops as long as the *Iteration* value is smaller than *nIterationsMax.* In other words, it loops until enough iterations using Δt_{DEM} have been performed to maintain stability in DEM.

Once the DEM algorithm is exited, the MPS and DEM results are output either in Paraview or in Tecplot.

The whole process is then iterated until the final time is reached.

5.3 MPS-DEM Validation

5.3.1 2D Water entry of a solid block

Once the DEM was validated, it was implemented in the MPS model, and a simple numerical test case, performed by Robb et al. [76] and Lee et al. [116], was used to validate the MPS-DEM model. This case involves the simulation of a solid block released from a height of 0.1 m into a steady-state tank filled with water, where the dimensions are given in **Figure 5.11**. The block's density is modified in each run into 500 kg/m^3, 1000 kg/m^3, and 2000 kg/m^3 to verify if the DEM-MPS model reproduces the buoyancy effect. The solid block, having dimensions of 0.1 m x 0.1 m, is modeled using particles of 0.0025 m at the outer surface and three layers of ghost particles inside. Snapshots of the numerical results obtained from the proposed model are shown in **Figures 5.12**, **5.13**, and **5.14.** As expected, when the density is half the density of water, the block floats on the surface, and when the density is twice the density of water, the block sinks to the bottom. As for the density of 1000 kg/m^3, **Figure 5.13** shows that the block resurfaces at t = 1.2 s. However, from Archimedes' principle, since the block has the same density as water, it should remain in the fluid and not resurface. Before t = 1.0 s, the block attains an equilibrium inside the water as it should. However, due to the weakly-compressible fluid assumption, the density fluctuates and becomes slightly higher than 1000 kg/m^3, thus pushing the block upwards. Further investigation needs to be done to improve this condition. Nonetheless, from Figures **5.15**, **5.16**, and **5.17**, where the block's center of mass is compared with the other two models, [76] and [116], the overall numerical results obtained from the proposed model are in acceptable agreement with them. **Table 5.10** shows the average x and y-position of the three models, and **Table 5.11** shows the percentage difference between the three models. A maximum percentage difference of 14.09 % is found when density is 1000 kg/m^3.

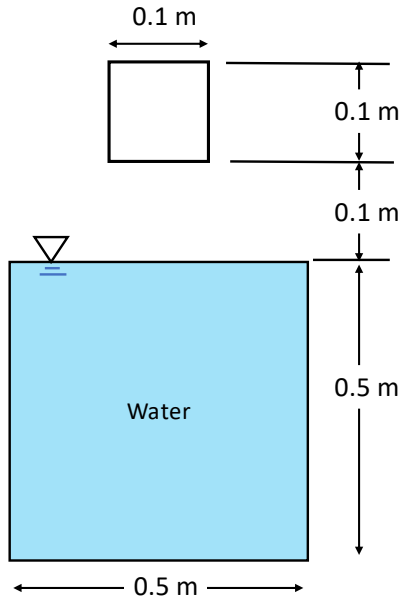

Figure 5.11 - Dimensions and initial block position

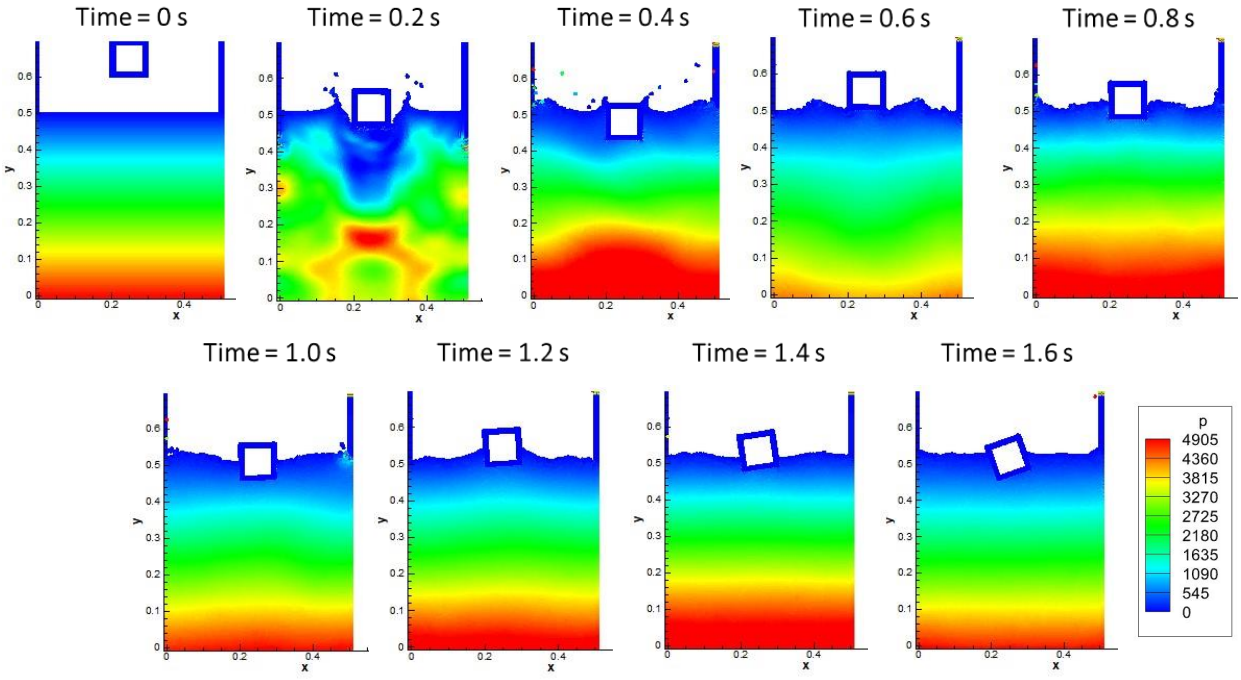

Figure 5.12 - Snapshots of the block having a density of 500 kg/m^3 falling in the steady tank. The color gradient shows the pressure from 0 kPa (blue) to 4.905 kPa (red).

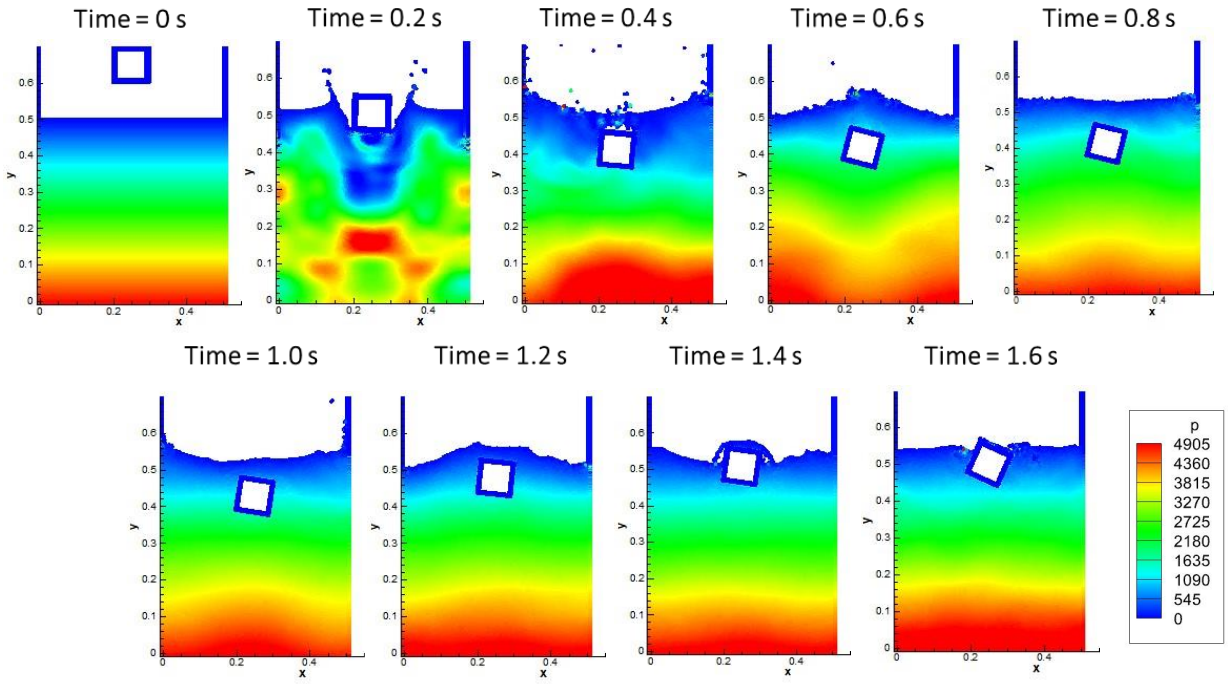

Figure 5.13 - Snapshots of the block having a density of 1000 kg/m3 falling in the steady tank. The color gradient shows the pressure from 0 kPa (blue) to 4.905 kPa (red).

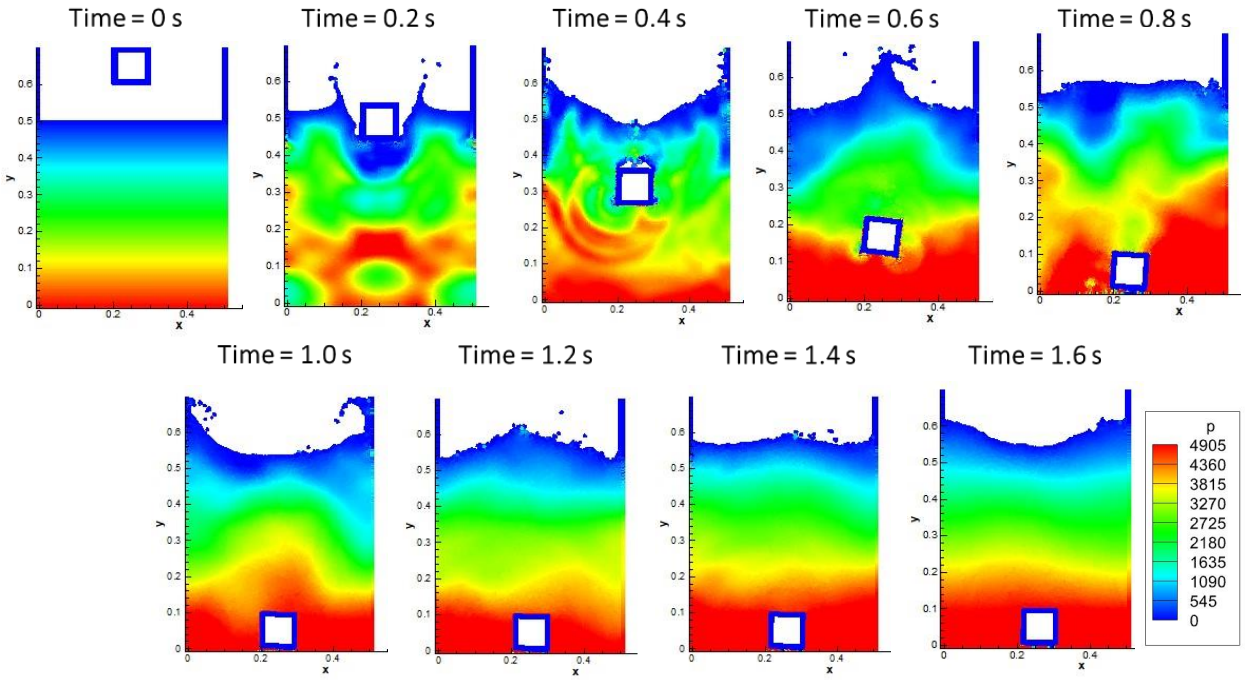

Figure 5.14 - Snapshots of the block having a density of 2000 kg/m3 falling in the steady tank. The color gradient shows the pressure from 0 kPa (blue) to 4.905 kPa (red).

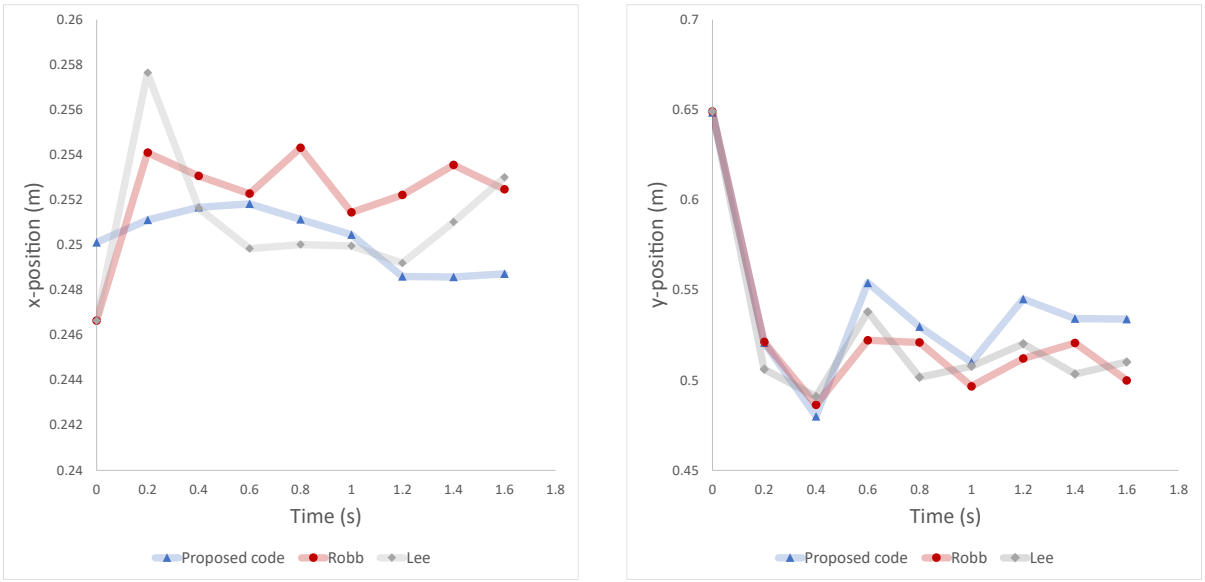

(a) (b)

Figure 5.15 - Block's horizontal and vertical motion for a density of 500 kg/m^3

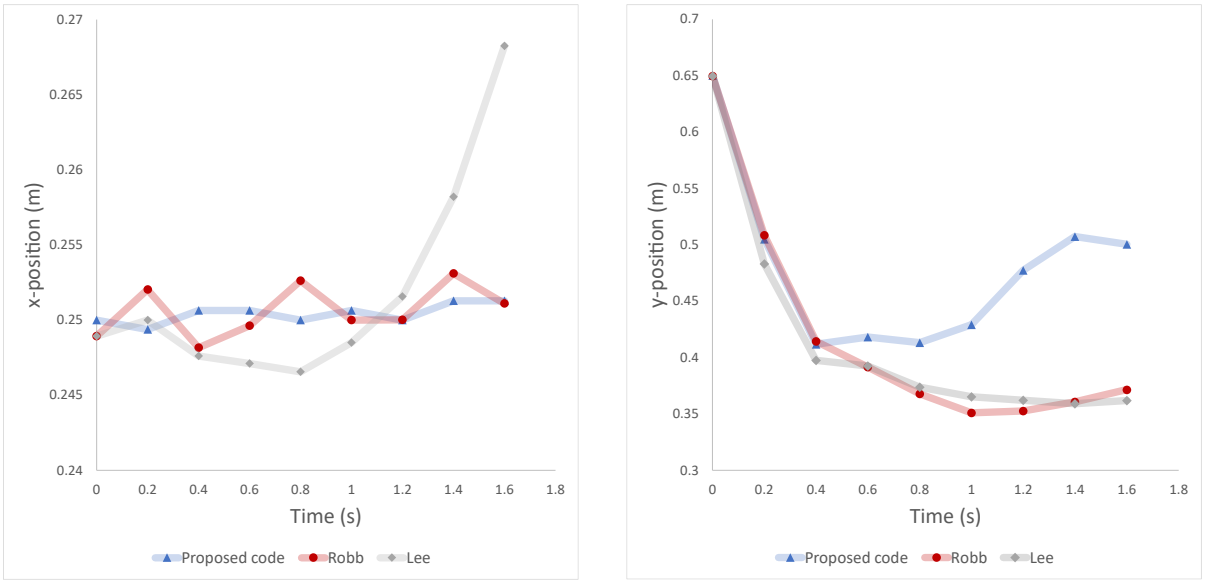

(a) (b)

Figure 5.16 - Block's horizontal and vertical motion for a density of 1000 kg/m^3

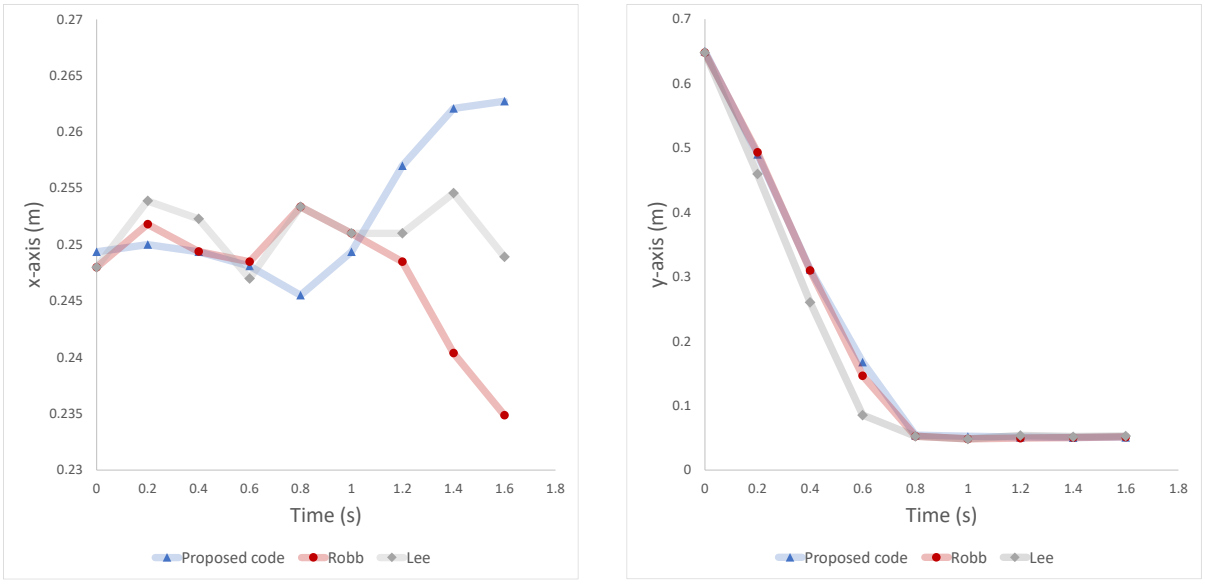

(a) (b)

Figure 5.17 - Block's horizontal and vertical motion for a density of 2000 kg/m^3

Table 5.10 - Average position comparison between the proposed model, and the numerical models of Robb et al. [76] and Lee et al. [116]

Densities (kg/m^3)	*Average*	*Proposed model (m)*	*Robb et al. [76] (m)*	*Lee et al. [116] (m)*
500	x-position	0.2502	0.2522	0.2510
	y-position	0.5396	0.5255	0.5253
1000	x-position	0.2504	0.2506	0.2518
	y-position	0.4792	0.4186	0.4161
2000	x-position	0.2526	0.2473	0.2511
	y-position	0.2088	0.2056	0.1904

Table 5.11 - Percentage difference of average position between the proposed model, and the numerical models of Robb et al. [76] and Lee et al. [116]

Densities (kg/m^3)	*Average*	*Proposed model vs. Robb et al. [76] (%)*	*Proposed model vs. Lee et al. [116] (%)*	*Robb et al. [76] vs. Lee et al. [116] (%)*
500	x-position	0.79	0.30	0.49
	y-position	2.66	2.70	0.04
1000	x-position	0.08	0.57	0.49
	y-position	13.50	14.09	0.59
2000	x-position	2.12	0.60	1.53
	y-position	1.50	9.21	7.72

5.3.2 2D Water entry of a circular cylinder

The proposed model is also validated using a 2D experimental test case performed by Greenhow and Lin [117]. In this test case, a cylinder of diameter D=0.11m is dropped into a steady-state tank

from a height of H=0.5 m, where H is the distance between the cylinder center and the water surface, as shown in **Figure 5.18**.

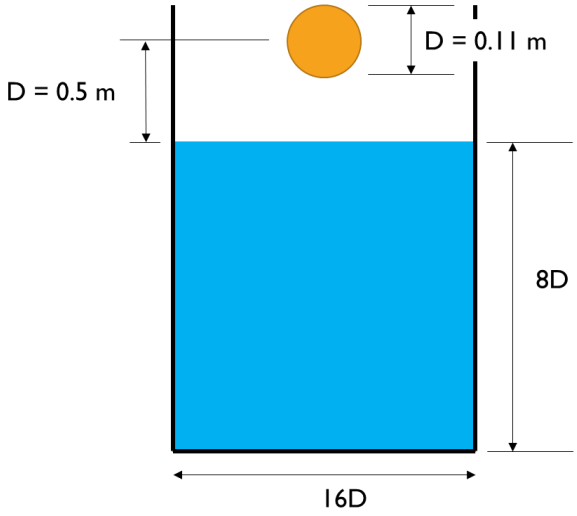

Figure 5.18 – Geometry setup of a cylinder dropped in a steady-state tank filled with water

The water density is $\rho = 1000$ kg/m^3 while the cylinder is tested with two different densities: half-buoyant and neutrally buoyant. In other words, the cylinder's densities are $\rho = 500$ kg/m^3 and $\rho=1000$ kg/m^3, respectively.

The fluid domain has a length of 16D and a depth of 8D, as shown in **Figure 5.18**. The particles used have a diameter of 0.0022 m, and the viscosity is ignored. Snapshots of the results obtained from the proposed model are shown in **Figures 5.19** and **5.20.**

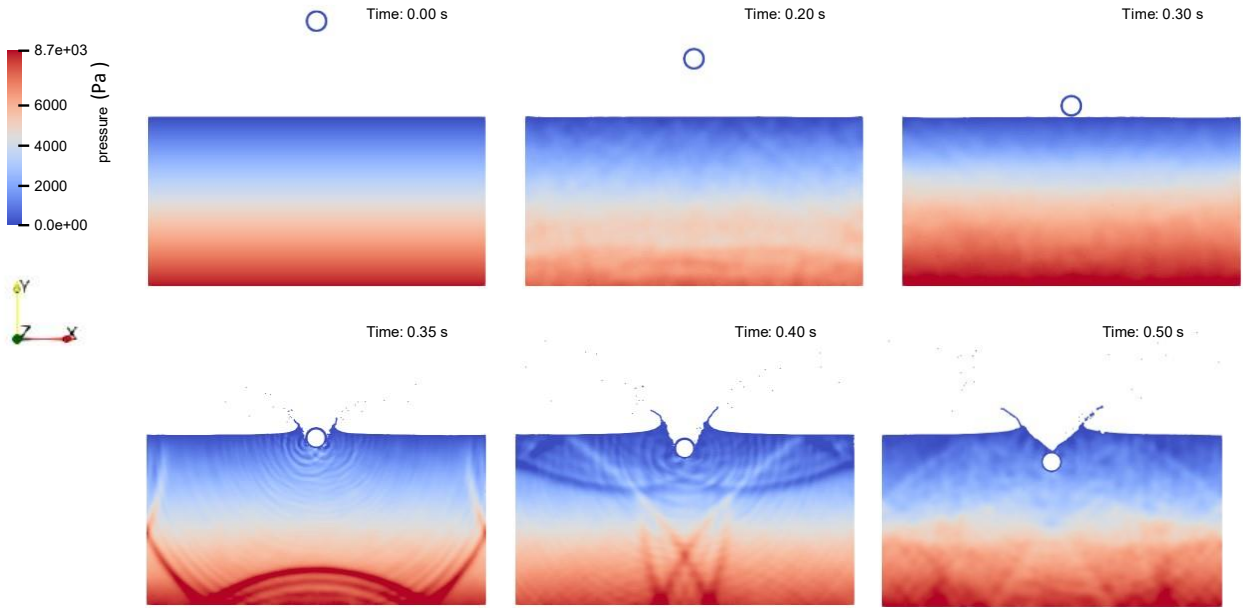

Figure 5.19 - Snapshots of the cylinder entering the steady-state tank filled with water for the half-buoyant case

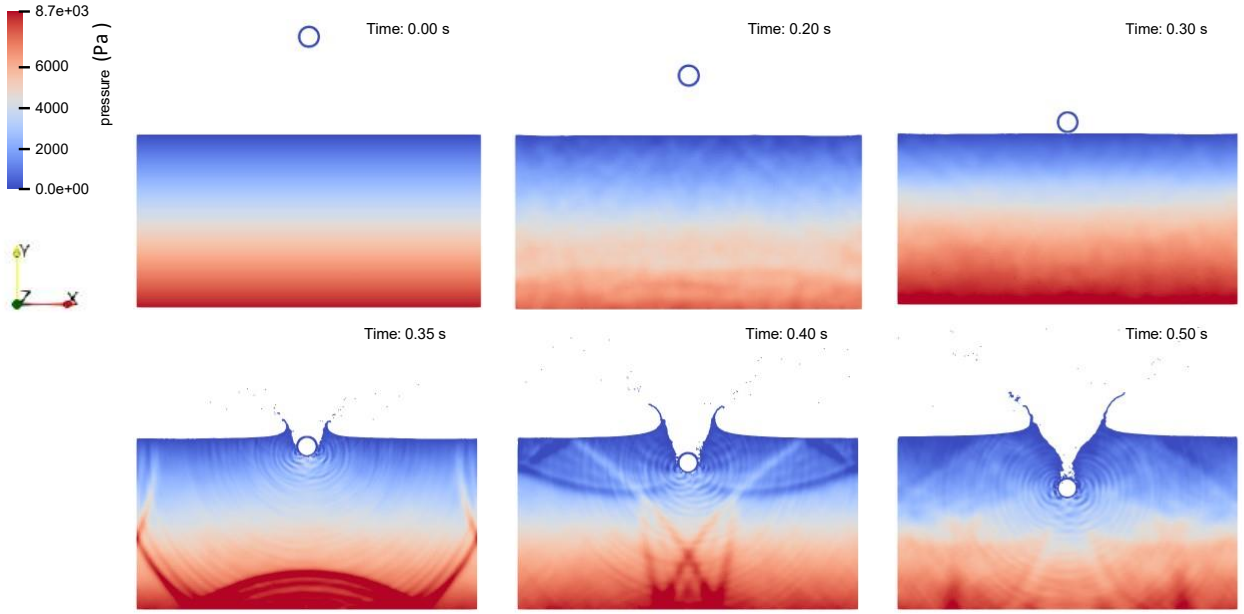

Figure 5.20 - Snapshots of the cylinder entering the steady-state tank filled with water for the neutrally-buoyant case

The penetration depth (in cm) of the cylinder into the steady-tank is compared to the experimental results given by [117] and to two numerical results. The first numerical model, proposed by Sun

and Faltinsen [118], used the two-dimensional boundary element method (BEM) to simulate the water phase. The second numerical model, proposed by Sun et al. [119], used a δ^+-SPH scheme for simulating the water flow. In Sun et al. [119], several resolutions were used to simulate the cylinder's water entry. However, in this thesis, only the resolution of $D/\Delta x_m = 50$ is used to compare the results with the proposed model because this resolution is similar to the one used in this thesis. **Figures 5.21** and **5.22** show the comparison between results for the half-buoyant and neutrally-buoyant cases.

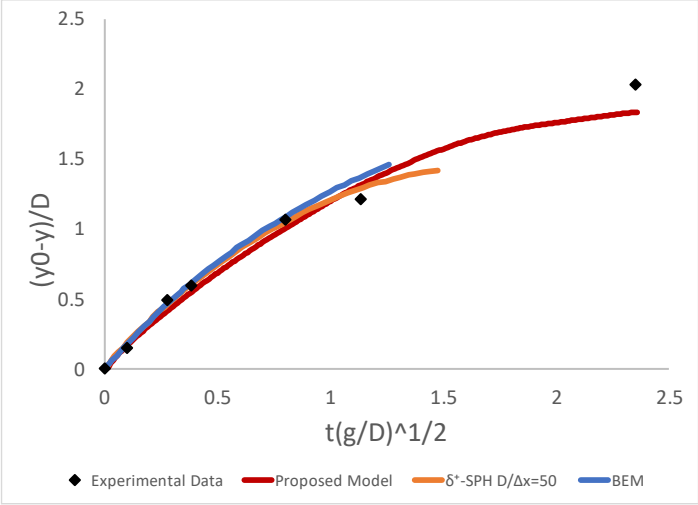

Figure 5.21 - Time histories of the depth of penetration of the half-buoyant cylinder of the proposed model compared with experimental results [117], with δ^+-SPH [119], and with BEM [118]

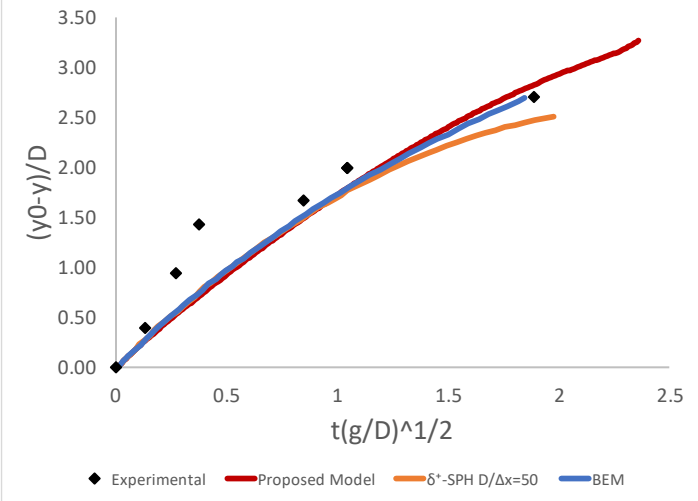

Figure 5.22 - Time histories of the depth of penetration of the neutrally-buoyant cylinder of the proposed model compared with experimental results [117], with δ^+-SPH [119], and with BEM [118]

In these figures, the dimensionless cylindrical penetration is used in the y-axis, where y is the cylinder's position, y_0 is the cylinder's position at the moment it touches the water surface, and D is the diameter of the cylinder. A dimensionless time is used in the x-axis, where the initial time is set at the moment the cylinder touches the water surface. **Figures 5.21** and **5.22** show that the numerical results obtained from the proposed model are in good agreement with both numerical results and fairly good agreement with the experimental results.

5.4 Conclusion

In this Chapter, the MPS governing equations and their discretization are presented. A Symplectic Time Integrator is used to calculate and update the field variables at each half step. The wall boundaries are defined where wall and ghost particles are used to avoid fluid penetration into the walls and where a Neumann boundary condition is used. The Particle Shifting Technique and Particle Collision methods are explained since they are implemented in the proposed model. A linked cell method, widely used in particle-based methods to reduce computational time, is described. Finally, a 2D test case was used to validate the MPS-DEM method, where a block was released from rest into a steady-state tank filled with water. The block's density was changed from 500, 1000, and 2000 kg/m^3 to verify if the buoyancy effect is satisfied. Overall, the results obtained from the proposed DEM-MPS method were in good agreement with the numerical results obtained by [76] and [116]. Still, it was observed that the fluid density fluctuations influenced the block's motion when a density of 1000 kg/m^3 was used. A similar test case was used to validate the MPS-DEM coupled model in 2D. The test case involved a circular cylinder of diameter D=0.11 m dropped from a height H = 0.5 m in a steady-state tank filled with water. The penetration depth of the cylinder entering the water surface obtained from the proposed model was compared with experimental and numerical results. The proposed model provided results which were in good agreement with these results.

CHAPTER 6 CONCLUSION AND FUTURE WORK

Ice jams present a hazard to the ecosystem, hydraulic structures, and riverside communities. The intrinsic complexity of this phenomenon renders it still unpredictable. A better understanding of the processes and mechanisms involved in the river ice dynamic will promote adequate and reliable management decisions. Due to climate change, relying on accurate prediction tools becomes even more important to reduce ice jam floods impacts.

This thesis's main objective was to provide more insight into river ice processes by providing high-quality benchmark data reproducing an ice jam release's overall characteristics and developing a model capable of simulating ice-water interactions with Lagrangian methods.

Experimental benchmark test cases involving the collapse of a water column with floating blocks were performed to provide valuable data that can be used for numerical model validation. These test cases, which involve a series of case scenarios having different numbers and sizes of floating blocks as well as being performed over dry and wet beds, mimics the general characteristics of an ice jam release. It was noted that after the wave impacted the downstream wall, a backward wave was generated. This backward wave pushed the floating blocks back in the upstream direction. Moreover, when a downstream fluid layer was present, a mushroom-like jet was generated, and the size was proportional to the downstream fluid layer.

The center of mass of each block was tracked using a free video analysis software called Tracker, and the water surface profile was digitized using the images extracted from the front camera videos. These results were used to validate the numerical model presented in Amaro et al. [89].

Additionally, solid objects moving in free-surface flow have been simulated using the coupling of the MPS and DEM methods. The solid objects were simulated using the multisphere method, which consists of using a group of particles whose relative position is constant. Newton's Second Law of motion is used to calculate the solids' position at each time step once the total force acting on them is obtained. The total force consists of the gravity force, the hydrodynamic force, and the contact force. The contact force is the core of the DEM and is calculated using an elastic Hertzian model, which involves the implementation of a spring and dashpot system.

The 2D single-sphere DEM method was validated by dropping a particle onto a level surface. The force and position were in good agreement with numerical results obtained from a widely-used

open-source software called LIGGGHTS. The 2D multisphere DEM model was validated using an experimental test case performed by Zhang et al. [109] where thirty-three cylinders were piled up and, after removing the plate that was maintaining them in place, collapsed due to gravity. The numerical results agreed well with the experimental results, as shown by the snapshots of the cylinders' transient behavior. Also, the average center of mass was plotted with time and compared with the experimental results.

A demolisher test case, presented and performed by DualSPHysics, was reproduced to validate the DEM multisphere method in 3D. In the demolisher test case, a wrecking ball was released from rest to swing and collapse onto a sixteen-block wall. This same test case was also simulated using LIGGGHTS. In the proposed DEM model, the contact ratio was calibrated using a simplified test case involving three cubes having the same properties as the demolisher test case. For a contact ratio of 0.3, the block's motion and velocity obtained from the proposed model were in good agreement with the results obtained with LIGGGHTS. The demolisher test case was then simulated with this contact ratio implemented in the proposed model. The average x, y, and z positions of the blocks were compared between the proposed model, LIGGGHTS, and DualSPHysics. It was shown that the percentage difference between the proposed model and either LIGGGHTS and DualSPHysics was smaller than the percentage difference between LIGGGHTS and DualSPHysics. Thus, the proposed model was in good agreement with both codes. However, the force obtained by the proposed model was always higher than the force obtained by LIGGGHTS. This discrepancy was explained by the fact that the contact dissipation in the LIGGGHTS-public version increased proportionally with the number of spheres. This dissipation is corrected in the LIGGGHTS-premium version, which was not available to the author of this thesis.

The MPS-DEM model was validated by simulating the release from rest of a block into a steady-state tank, where the block changed in density. The buoyancy effect was analyzed in this case, and the numerical results were compared with the results obtained by Robb et al. [76] and Lee et al. [116]. Overall, the results obtained by the proposed model were in acceptable agreement with Archimedes' principle. However, when the block was neutrally buoyant, the block rose to the surface instead of remaining inside the fluid. The fluctuation of the fluid density can explain this discrepancy due to the weakly-compressible fluid assumption. Further inquiry is required to improve this condition.

The MPS-DEM model was also validated using a test case involving a circular cylinder dropped in a steady-state tank filled with water. The cylinder's penetration depth in the water surface obtained from the proposed model was compared with experimental [117] and numerical [118, 119] results. The proposed model provided results that were in good agreement with these results.

6.1 Future Work

In this thesis, the author could not apply and validate the developed model to the 3D experimental benchmark cases explained in Chapter 3. This impediment was mainly due to the need for further validations and improved model efficiency (computational time). To accurately replicate river ice jams, high-resolution simulations must be used. However, the models using higher resolution are computationally more demanding since more particles are used. All but one of the test cases presented in this thesis were performed using a serial code and had a very high computational time. The extension of this research will apply for modeling the proposed benchmark experiments as well as the larger scale ice dynamics problems. Implementing parallel programming with CUDA will decrease computational time and render the model more suitable to simulate 3D real-life river ice dynamic cases.

In this project, the solid blocks are assumed to have no change in geometry. However, real ice floes undergo mechanical and thermal breakup. Thus, the simulation of ice floes' breakage and the impact of climate change on river ice jams can be explored in the future.

Furthermore, in this thesis, for calculating the hydrodynamic forces, only the normal stresses were considered. In the future, other forces, such as the shear force, should be considered.

REFERENCES

[1] K. D. White, "Introduction to River Ice," *US Army Cold Regions Research and Engineering Laboratory*, vol. 2021, no. 4/8, p. 6, 1999.https://slideplayer.com/slide/4063588/

[2] S. Beltaos, Pomerleau, and R. A Halliday, *Ice-jam effects on Red River flooding and possible mitigation methods*. 2000.

[3] S. Beltaos, "Assessing Ice-Jam Flood Risk: Methodology and Limitations," in *20th IAHR International Symposium on Ice*, Lahti, Finland, 2010.

[4] J. S. Ford, S. Beltaos, W. J. Moody, and N. K. Madsen, "Remote measurements of ice jam thickness," in *Proceedings of 6th Workshop on River Ice, Canadian Committee on River Ice, CGU-HS*, Ottawa, 1991.

[5] Y. She *et al.*, "Athabasca River ice jam formation and release events in 2006 and 2007," *Cold Regions Science and Technology*, vol. 55, no. 2, pp. 249-261, 2009/02/01/ 2009.http://www.sciencedirect.com/science/article/pii/S0165232X08000426

[6] S. Beltaos, R. Rowsell, and P. Tang, "Remote data collection on ice breakup dynamics: Saint John River case study," *Cold Regions Science and Technology*, vol. 67, no. 3, pp. 135-145, 2011/07/01/ 2011.http://www.sciencedirect.com/science/article/pii/S0165232X11000619

[7] S. Beltaos, "Erosion potential of dynamic ice breakup in Lower Athabasca River. Part II: Field data analysis and interpretation," *Cold Regions Science and Technology*, vol. 148, pp. 77-87, 2018/04/01/ 2018.http://www.sciencedirect.com/science/article/pii/S0165232X17301982

[8] M. Jasek, "Ice jam release surges, ice runs, and breaking fronts: field measurements, physical descriptions, and research needs," *Canadian Journal of Civil Engineering*, vol. 30, no. 1, pp. 113-127, 2003/02/01 2003.https://doi.org/10.1139/l02-072

[9] J. Nafziger, Y. She, and F. Hicks, "Celerities of waves and ice runs from ice jam releases," *Cold Regions Science and Technology*, vol. 123, pp. 71-80, 2016/03/01/ 2016.https://www.sciencedirect.com/science/article/pii/S0165232X15002931

[10] J. Nafziger, Y. She, and F. Hicks, "Dynamic river ice processes in a river delta network," *Cold Regions Science and Technology*, vol. 158, pp. 275-287, 2019/02/01/ 2019.https://www.sciencedirect.com/science/article/pii/S0165232X17305827

[11] V. A. Squire, "Of ocean waves and sea-ice revisited," *Cold Regions Science and Technology*, vol. 49, no. 2, pp. 110-133, 2007/08/01/ 2007.https://www.sciencedirect.com/science/article/pii/S0165232X07000870

[12] V. A. Squire, "A fresh look at how ocean waves and sea ice interact," *Philosophical Transactions of the Royal Society A: Mathematical, Physical and Engineering Sciences*, vol. 376, no. 2129, p. 20170342, 2018/09/28 2018.https://doi.org/10.1098/rsta.2017.0342

[13] V. A. Squire, "Ocean Wave Interactions with Sea Ice: A Reappraisal," *Annual Review of Fluid Mechanics*, vol. 52, no. 1, pp. 37-60, 2020/01/05 2020.https://doi.org/10.1146/annurev-fluid-010719-060301

[14] B. Morse, B. Burrell, A. St. Hilaire, N. Bergeron, D. Messier, and Q. T. Tung, "River Ice Processes in Tidal Rivers: Research needs," in *Proceedings of the 10th Workshop on the Hydraulics of Ice Covered Rivers*, Winnipeg, Manitoba, 1999.

[15] D. Healy and F. Hicks, "Experimental Observations on Ice Jam Shoving," 01/01 2001.

[16] S. Beltaos, "River ice breakup processes: recent advances and future directions," *Canadian Journal of Civil Engineering*, vol. 34, no. 6, pp. 703-716, 2007/06/01 2007.https://doi.org/10.1139/l06-021

[17] L. J. Yiew, L. G. Bennetts, M. H. Meylan, B. J. French, and G. A. Thomas, "Hydrodynamic responses of a thin floating disk to regular waves," *Ocean Modelling*, vol. 97, pp. 52-64, 2016/01/01/ 2016.https://www.sciencedirect.com/science/article/pii/S1463500315002243

[18] L. J. Yiew, L. G. Bennetts, M. H. Meylan, G. A. Thomas, and B. J. French, "Wave-induced collisions of thin floating disks," *Physics of Fluids*, vol. 29, no. 12, p. 127102, 2017/12/01 2017.https://doi.org/10.1063/1.5003310

[19] D. J. McGovern and W. Bai, "Experimental study on kinematics of sea ice floes in regular waves," *Cold Regions Science and Technology*, vol. 103, pp. 15-30, 2014/07/01/ 2014.https://www.sciencedirect.com/science/article/pii/S0165232X14000597

[20] M. Dai, H. H. Shen, M. A. Hopkins, and S. F. Ackley, "Wave rafting and the equilibrium pancake ice cover thickness," *Journal of Geophysical Research: Oceans*, https://doi.org/10.1029/2003JC002192 vol. 109, no. C7, 2004/07/01 2004.https://doi.org/10.1029/2003JC002192

[21] L. G. Bennetts and T. D. Williams, "Water wave transmission by an array of floating discs," *Proceedings of the Royal Society A: Mathematical, Physical and Engineering Sciences*, vol. 471, no. 2173, p. 20140698, 2015/01/08 2015.https://doi.org/10.1098/rspa.2014.0698

[22] J. Hu and L. Zhou, "Experimental and numerical study on ice resistance for icebreaking vessels," *International Journal of Naval Architecture and Ocean Engineering*, vol. 7, no. 3, pp. 626-639, 2015/05/01/ 2015.https://www.sciencedirect.com/science/article/pii/S2092678216300693

[23] W.-Z. Luo, C.-Y. Guo, T.-C. Wu, and Y.-M. Su, "Experimental research on resistance and motion attitude variation of ship–wave–ice interaction in marginal ice zones," *Marine Structures*, vol. 58, pp. 399-415, 2018/03/01/ 2018.https://www.sciencedirect.com/science/article/pii/S0951833917302629

[24] J. Blackburn and Y. She, "A comprehensive public-domain river ice process model and its application to a complex natural river," *Cold Regions Science and Technology*, vol. 163, pp. 44-58, 2019/07/01/ 2019.http://www.sciencedirect.com/science/article/pii/S0165232X18302945

[25] F. Chen, H. Shen, and N. Jayasundara, "A one-dimensional comprehensive river ice model," 01/01 2006.https://www.researchgate.net/publication/237701227_A_one-dimensional_comprehensive_river_ice_model

[26] A. M. W. Lal and T. Shen Hung, "Mathematical Model for River Ice Processes," *Journal of Hydraulic Engineering*, vol. 117, no. 7, pp. 851-867, 1991/07/01 1991.https://doi.org/10.1061/(ASCE)0733-9429(1991)117:7(851)

[27] D. Fread, M. Jin, and J. M. Lewis, "An LPI numerical implicit solution for unsteady mixed-flow simulation," in *North American Water and Environment Congress & Destructive Water*, 1996, pp. 322-327: ASCE.

[28] I. Thériault, J.-P. Saucet, and W. Taha, "Validation of the Mike-Ice model simulating river flows in presence of ice and forecast of changes to the ice regime of the Romaine river due to hydroelectric project," in *Proceedings of the 20th IAHR international symposium on ice, Lahti, Finland*, 2010, pp. 14-17.

[29] K.-E. Lindenschmidt, "RIVICE—A Non-Proprietary, Open-Source, One-Dimensional River-Ice Model," *Water*, vol. 9, no. 5, 2017.

[30] H. T. Shen, J. Su, and L. Liu, "SPH Simulation of River Ice Dynamics," *Journal of Computational Physics*, vol. 165, no. 2, pp. 752-770, 2000/12/10/ 2000.https://www.sciencedirect.com/science/article/pii/S0021999100966397

[31] L. Liu, H. Li, and H. T. Shen, "A two-dimensional comprehensive river ice model," in *Proceedings of the 18th IAHR symposium on river ice, Sapporo, Japan*, 2006, vol. 28.

[32] R. A. Gingold and J. J. Monaghan, "Smoothed particle hydrodynamics: theory and application to non-spherical stars," *Monthly Notices of the Royal Astronomical Society*, vol. 181, no. 3, pp. 375-389, 1977.https://doi.org/10.1093/mnras/181.3.375

[33] L. B. Lucy, "A numerical approach to the testing of the fission hypothesis," *The Astronomical Journal*, vol. 82, p. 1013, December 01, 1977 1977.https://ui.adsabs.harvard.edu/abs/1977AJ.....82.1013L

[34] C. D. Wang and M. H. Meylan, "A higher-order-coupled boundary element and finite element method for the wave forcing of a floating elastic plate," *Journal of Fluids and Structures*, vol. 19, no. 4, pp. 557-572, 2004/05/01/ 2004.http://www.sciencedirect.com/science/article/pii/S0889974604000386

[35] R. E. Gagnon and J. Wang, "Numerical simulations of a tanker collision with a bergy bit incorporating hydrodynamics, a validated ice model and damage to the vessel," *Cold Regions Science and Technology*, vol. 81, pp. 26-35, 2012/09/01/ 2012.http://www.sciencedirect.com/science/article/pii/S0165232X12000870

[36] M. Song, E. Kim, J. Amdahl, J. Ma, and Y. Huang, "A comparative analysis of the fluid-structure interaction method and the constant added mass method for ice-structure collisions," *Marine Structures*, vol. 49, pp. 58-75, 2016/09/01/ 2016.http://www.sciencedirect.com/science/article/pii/S0951833916300739

[37] W. Bai, T. Zhang, and D. J. McGovern, "Response of small sea ice floes in regular waves: A comparison of numerical and experimental results," *Ocean Engineering*, vol. 129, pp. 495-506, 2017/01/01/ 2017.http://www.sciencedirect.com/science/article/pii/S0029801816304875

[38] T. Sayeed, B. Colbourne, and D. Molyneux, "Experimental and numerical investigation of wave induced forces and motions of partially submerged bodies near a fixed structure in irregular waves," *Ocean Engineering*, vol. 163, pp. 451-475, 2018/09/01/ 2018.http://www.sciencedirect.com/science/article/pii/S0029801818310321

[39] P. A. Cundall and O. D. L. Strack, "A discrete numerical model for granular assemblies," *Géotechnique*, vol. 29, no. 1, pp. 47-65, 1979.https://www.icevirtuallibrary.com/doi/abs/10.1680/geot.1979.29.1.47

[40] M. A. Hopkins and W. D. Hibler, "Numerical simulations of a compact convergent system of ice floes," *Annals of Glaciology*, vol. 15, pp. 26-30, 1991.https://www.cambridge.org/core/article/numerical-simulations-of-a-compact-convergent-system-of-ice-floes/C4770F3B33A74299DCC8D50E2E2D495C

[41] S. Løset, "Discrete element modelling of a broken ice field — Part I: model development," *Cold Regions Science and Technology*, vol. 22, no. 4, pp. 339-347, 1994/06/01/ 1994.https://www.sciencedirect.com/science/article/pii/0165232X94900191

[42] S. Daly and M. Hopkins, "Estimating Forces on an Ice Control Structure Using DEM," 01/01 2001.

[43] A. Hopkins Mark and M. Tuthill Andrew, "Ice Boom Simulations and Experiments," *Journal of Cold Regions Engineering*, vol. 16, no. 3, pp. 138-155, 2002/09/01 2002.https://doi.org/10.1061/(ASCE)0887-381X(2002)16:3(138)

[44] M. A. Hopkins, "A discrete element Lagrangian sea ice model," *Engineering Computations*, vol. 21, no. 2/3/4, pp. 409-421, 2004.https://doi.org/10.1108/02644400410519857

[45] E. E. Ebert and J. A. Curry, "An intermediate one-dimensional thermodynamic sea ice model for investigating ice-atmosphere interactions," *Journal of Geophysical Research: Oceans*, https://doi.org/10.1029/93JC00656 vol. 98, no. C6, pp. 10085-10109, 1993/06/15 1993.https://doi.org/10.1029/93JC00656

[46] M. Hopkins and S. Daly, "Recent advances in discrete element modeling of river ice," 07/19 2003.https://www.researchgate.net/publication/229001876_Recent_advances_in_discrete_element_modeling_of_river_ice

[47] M. A. Hopkins and H. H. Shen, "Simulation of pancake-ice dynamics in a wave field," *Annals of Glaciology*, vol. 33, pp. 355-360, 2001.https://www.cambridge.org/core/article/simulation-of-pancakeice-dynamics-in-a-wave-field/E7B7AC8E438ABC3E4AAFC52E3B1C05BA

[48] L. Stockstill Richard, F. Daly Steven, and A. Hopkins Mark, "Modeling Floating Objects at River Structures," *Journal of Hydraulic Engineering*, vol. 135, no. 5, pp. 403-414, 2009/05/01 2009.https://doi.org/10.1061/(ASCE)0733-9429(2009)135:5(403)

[49] E. B. Karulin and M. M. Karulina, "Numerical and physical simulations of moored tanker behaviour," *Ships and Offshore Structures*, vol. 6, no. 3, pp. 179-184, 2011/09/01 2011.https://doi.org/10.1080/17445302.2010.544087

[50] J. Paavilainen and J. Tuhkuri, "Pressure distributions and force chains during simulated ice rubbling against sloped structures," *Cold Regions Science and Technology*, vol. 85, pp. 157-

174, 2013/01/01/ 2013.https://www.sciencedirect.com/science/article/pii/S0165232X12001875

[51] S. Ji, S. Di, and S. Liu, "Analysis of ice load on conical structure with discrete element method," *Engineering Computations*, vol. 32, no. 4, pp. 1121-1134, 2015.https://doi.org/10.1108/EC-04-2014-0090

[52] S. Ji, X. Chen, and L. Liu, "Coupled DEM-SPH Method for Interaction between Dilated Polyhedral Particles and Fluid," *Mathematical Problems in Engineering*, vol. 2019, p. 4987801, 2019/08/21 2019.https://doi.org/10.1155/2019/4987801

[53] A. Herman, S. Cheng, and H. H. J. T. C. Shen, "Wave energy attenuation in fields of colliding ice floes–Part 1: Discrete-element modelling of dissipation due to ice–water drag," vol. 13, no. 11, pp. 2887-2900, 2019.

[54] H. Gong, A. Polojärvi, and J. Tuhkuri, "Discrete element simulation of the resistance of a ship in unconsolidated ridges," *Cold Regions Science and Technology*, vol. 167, p. 102855, 2019/11/01/ 2019.https://www.sciencedirect.com/science/article/pii/S0165232X18304270

[55] I. Metrikin and S. Løset, "Nonsmooth 3D discrete element simulation of a drillship in discontinuous ice," in *Proceedings of the International Conference on Port and Ocean Engineering Under Arctic Conditions*, 2013.

[56] J. Tuhkuri, A. J. P. T. o. t. R. S. A. M. Polojärvi, Physical, and E. Sciences, "A review of discrete element simulation of ice–structure interaction," vol. 376, no. 2129, p. 20170335, 2018.

[57] Y. Xue, R. Liu, Z. Li, and D. J. O. E. Han, "A review for numerical simulation methods of ship–ice interaction," vol. 215, p. 107853, 2020.

[58] J. Favier, M. Abbaspour-Fard, M. Kremmer, and A. J. E. c. Raji, "Shape representation of axi-symmetrical, non-spherical particles in discrete element simulation using multi-element model particles," 1999.

[59] S. Koshizuka and Y. Oka, "Moving-Particle Semi-Implicit Method for Fragmentation of Incompressible Fluid," *Nuclear Science and Engineering*, vol. 123, no. 3, pp. 421-434, 1996/07/01 1996.https://doi.org/10.13182/NSE96-A24205

[60] S. Koshizuka, K. Shibata, M. Kondo, and T. Matsunaga, *Moving particle semi-implicit method: a meshfree particle method for fluid dynamics*. Academic Press, 2018.

[61] J. J. Monaghan, "Simulating Free Surface Flows with SPH," *Journal of Computational Physics*, vol. 110, no. 2, pp. 399-406, 1994/02/01/ 1994.https://www.sciencedirect.com/science/article/pii/S0021999184710345

[62] A. Shakibaeinia and Y.-C. Jin, "A weakly compressible MPS method for modeling of open-boundary free-surface flow," *International Journal for Numerical Methods in Fluids*, vol. 63, no. 10, pp. 1208-1232, 2010/08/10 2010.https://doi.org/10.1002/fld.2132

https://onlinelibrary.wiley.com/doi/pdfdirect/10.1002/fld.2132?download=true

[63] R. Xu, P. Stansby, and D. Laurence, "Accuracy and stability in incompressible SPH (ISPH) based on the projection method and a new approach," *Journal of Computational Physics*,

vol. 228, no. 18, pp. 6703-6725, 2009/10/01/ 2009.https://www.sciencedirect.com/science/article/pii/S0021999109002885

[64] M. S. Shadloo, A. Zainali, and M. Yildiz, "Simulation of single mode Rayleigh–Taylor instability by SPH method," *Computational Mechanics*, vol. 51, no. 5, pp. 699-715, 2013/05/01 2013.https://doi.org/10.1007/s00466-012-0746-2

[65] A. Khayyer, H. Gotoh, and Y. Shimizu, "Comparative study on accuracy and conservation properties of two particle regularization schemes and proposal of an optimized particle shifting scheme in ISPH context," *Journal of Computational Physics*, vol. 332, pp. 236-256, 2017/03/01/ 2017.https://www.sciencedirect.com/science/article/pii/S0021999116306465

[66] S. J. Lind, R. Xu, P. K. Stansby, and B. D. Rogers, "Incompressible smoothed particle hydrodynamics for free-surface flows: A generalised diffusion-based algorithm for stability and validations for impulsive flows and propagating waves," *Journal of Computational Physics*, vol. 231, no. 4, pp. 1499-1523, 2012/02/20/ 2012.http://www.sciencedirect.com/science/article/pii/S0021999111006279

[67] M. Jandaghian and A. Shakibaeinia, "An enhanced weakly-compressible MPS method for free-surface flows," *Computer Methods in Applied Mechanics and Engineering*, vol. 360, p. 112771, 2020/03/01/ 2020.http://www.sciencedirect.com/science/article/pii/S0045782519306632

[68] A. Khayyer and H. Gotoh, "Modified Moving Particle Semi-implicit methods for the prediction of 2D wave impact pressure," *Coastal Engineering*, vol. 56, no. 4, pp. 419-440, 2009/04/01/ 2009.https://www.sciencedirect.com/science/article/pii/S0378383908001646

[69] A. Khayyer and H. Gotoh, "A 3D higher order Laplacian model for enhancement and stabilization of pressure calculation in 3D MPS-based simulations," *Applied Ocean Research*, vol. 37, pp. 120-126, 2012/08/01/ 2012.https://www.sciencedirect.com/science/article/pii/S0141118712000399

[70] A. Khayyer and H. Gotoh, "Enhancement of stability and accuracy of the moving particle semi-implicit method," *Journal of Computational Physics*, vol. 230, no. 8, pp. 3093-3118, 2011/04/20/ 2011.http://www.sciencedirect.com/science/article/pii/S0021999111000271

[71] X. Liu, K. Morita, and S. Zhang, "An advanced moving particle semi-implicit method for accurate and stable simulation of incompressible flows," *Computer Methods in Applied Mechanics and Engineering*, vol. 339, pp. 467-487, 2018/09/01/ 2018.https://www.sciencedirect.com/science/article/pii/S0045782518302408

[72] G. Duan, S. Koshizuka, A. Yamaji, B. Chen, X. Li, and T. Tamai, "An accurate and stable multiphase moving particle semi-implicit method based on a corrective matrix for all particle interaction models," *International Journal for Numerical Methods in Engineering*, https://doi.org/10.1002/nme.5844 vol. 115, no. 10, pp. 1287-1314, 2018/09/07 2018.https://doi.org/10.1002/nme.5844

[73] G. Duan, B. Chen, X. Zhang, and Y. Wang, "A multiphase MPS solver for modeling multi-fluid interaction with free surface and its application in oil spill," *Computer Methods in*

Applied Mechanics and Engineering, vol. 320, pp. 133-161, 2017/06/15/ 2017.http://www.sciencedirect.com/science/article/pii/S0045782516317819

[74] M. Sakai *et al.*, "Lagrangian–Lagrangian modeling for a solid–liquid flow in a cylindrical tank," vol. 200, pp. 663-672, 2012.

[75] M. Robinson, M. Ramaioli, and S. J. I. j. o. m. f. Luding, "Fluid–particle flow simulations using two-way-coupled mesoscale SPH–DEM and validation," vol. 59, pp. 121-134, 2014.

[76] D. M. Robb, S. J. Gaskin, and J.-C. Marongiu, "SPH-DEM model for free-surface flows containing solids applied to river ice jams," *Journal of Hydraulic Research*, vol. 54, no. 1, pp. 27-40, 2016/01/02 2016.https://doi.org/10.1080/00221686.2015.1131203

[77] E. Harada, H. Gotoh, H. Ikari, and A. J. A. i. W. R. Khayyer, "Numerical simulation for sediment transport using MPS-DEM coupling model," vol. 129, pp. 354-364, 2019.

[78] J.-J. Li, L.-C. Qiu, L. Tian, Y.-S. Yang, and Y. J. E. A. w. B. E. Han, "Modeling 3D non-Newtonian solid–liquid flows with a free-surface using DEM-MPS," vol. 105, pp. 70-77, 2019.

[79] R. B. Canelas, A. J. C. Crespo, J. M. Domínguez, R. M. L. Ferreira, and M. Gómez-Gesteira, "SPH–DCDEM model for arbitrary geometries in free surface solid–fluid flows," *Computer Physics Communications*, vol. 202, pp. 131-140, 2016/05/01/ 2016.https://www.sciencedirect.com/science/article/pii/S0010465516000254

[80] G. Kailun, C. Ronghua, L. Yonglin, Q. Suizheng, and G. H. Su, "Numerical investigation of the fluid-solid mixture flow using the FOCUS code," *Progress in Nuclear Energy*, vol. 97, pp. 197-213, 05/ 2017.http://dx.doi.org/10.1016/j.pnucene.2017.01.015

[81] R. A. Amaro Junior, L.-Y. Cheng, and P. H. S. Osello, "An improvement of rigid bodies contact for particle-based non-smooth walls modeling," *Computational Particle Mechanics*, vol. 6, no. 4, pp. 561-580, 2019/10/01 2019.https://doi.org/10.1007/s40571-019-00233-4

[82] Z. Wang, F. Hu, G. Duan, K. Shibata, and S. Koshizuka, "Numerical modeling of floating bodies transport for flooding analysis in nuclear reactor building," *Nuclear Engineering and Design*, vol. 341, pp. 390-405, 2019/01/01/ 2019.https://www.sciencedirect.com/science/article/pii/S0029549318307350

[83] Y. Kawano and T. Ohashi, "Numerical study on c-axis orientations of sea ice surface grown under calm sea conditions using a particle method and Voronoi dynamics," *Cold Regions Science and Technology*, vol. 112, pp. 29-38, 2015.

[84] T. Ohashi, Sasaki, M., & Yoshimura, Y., "A numerical simulation of the development of ice-microstructure," in *19th International Symposiumon Okhotsk Sea & Sea Ice*, 2004, pp. (pp. 180-185).

[85] N. Zhang, X. Zheng, and Q. Ma, "Study on wave-induced kinematic responses and flexures of ice floe by Smoothed Particle Hydrodynamics," *Computers & Fluids*, vol. 189, pp. 46-59, 2019/07/15/ 2019.https://www.sciencedirect.com/science/article/pii/S0045793019301331

[86] C. Zhang, M. Rezavand, and X. Hu, "A multi-resolution SPH method for fluid-structure interactions," *Journal of Computational Physics*, vol. 429, p. 110028, 2021/03/15/ 2021.https://www.sciencedirect.com/science/article/pii/S0021999120308020

[87] A. Damsgaard, A. Adcroft, and O. Sergienko, "Application of Discrete Element Methods to Approximate Sea Ice Dynamics," *Journal of Advances in Modeling Earth Systems*, vol. 10, no. 9, pp. 2228-2244, 2018/09/01 2018.https://doi.org/10.1029/2018MS001299

[88] A. Shakibaeinia and Y.-C. Jin, "A mesh-free particle model for simulation of mobile-bed dam break," *Advances in Water Resources*, vol. 34, no. 6, pp. 794-807, 2011/06/01/ 2011.http://www.sciencedirect.com/science/article/pii/S0309170811000753

[89] R. A. Amaro, A. Mellado-Cusicahua, A. Shakibaeinia, and L.-Y. Cheng, "A fully Lagrangian DEM-MPS mesh-free model for ice-wave dynamics," *Cold Regions Science and Technology*, p. 103266, 2021/03/05/ 2021.https://www.sciencedirect.com/science/article/pii/S0165232X21000471

[90] G. W. Timco and W. F. Weeks, "A review of the engineering properties of sea ice," *Cold Regions Science and Technology*, vol. 60, no. 2, pp. 107-129, 2010/02/01/ 2010.https://www.sciencedirect.com/science/article/pii/S0165232X09001797

[91] M. van den Berg, R. Lubbad, and S. Løset, "The effect of ice floe shape on the load experienced by vertical-sided structures interacting with a broken ice field," *Marine Structures*, vol. 65, pp. 229-248, 2019/05/01/ 2019.https://www.sciencedirect.com/science/article/pii/S0951833918303915

[92] D. Brown, R. Hanson, and W. Christian. (2020, 3/6/2021). *Tracker*. Available: https://physlets.org/tracker/index.html

[93] G. Lauber and W. H. Hager, "Experiments to dambreak wave: Horizontal channel," *Journal of Hydraulic Research*, vol. 36, no. 3, pp. 291-307, 1998/05/01 1998.https://doi.org/10.1080/00221689809498620

[94] P. K. Stansby, A. Chegini, and T. C. D. Barnes, "The initial stages of dam-break flow," *Journal of Fluid Mechanics*, vol. 374, pp. 407-424, 1998.https://www.cambridge.org/core/article/initial-stages-of-dambreak-flow/93BE6179D1B681951D62F3FB0955036E

[95] I. M. Jánosi, D. Jan, K. G. Szabó, and T. Tél, "Turbulent drag reduction in dam-break flows," *Experiments in Fluids*, vol. 37, no. 2, pp. 219-229, 2004/08/01 2004.https://doi.org/10.1007/s00348-004-0804-4

[96] T. Zhao, "Introduction to Discrete Element Method," in *Coupled DEM-CFD Analyses of Landslide-Induced Debris Flows*, T. Zhao, Ed. Singapore: Springer Singapore, 2017, pp. 25-45.

[97] M. A. van der Hoef, M. Ye, M. van Sint Annaland, A. T. Andrews, S. Sundaresan, and J. A. M. Kuipers, "Multiscale Modeling of Gas-Fluidized Beds," in *Advances in Chemical Engineering*, vol. 31, G. B. Marin, Ed.: Academic Press, 2006, pp. 65-149.

[98] B. Blais, D. Vidal, F. Bertrand, G. S. Patience, and J. Chaouki, "Experimental Methods in Chemical Engineering: Discrete Element Method—DEM," *The Canadian Journal of*

Chemical Engineering, https://doi.org/10.1002/cjce.23501 vol. 97, no. 7, pp. 1964-1973, 2019/07/01 2019.https://doi.org/10.1002/cjce.23501

[99] D. Vetsch, *Numerical Simulation of Sediment Transport with Meshfree Methods*. KS Omniscriptum Publishing, 2012.

[100] H. Kruggel-Emden, S. Rickelt, S. Wirtz, and V. Scherer, "A study on the validity of the multi-sphere Discrete Element Method," *Powder Technology*, vol. 188, no. 2, pp. 153-165, 2008/12/20/ 2008.https://www.sciencedirect.com/science/article/pii/S0032591008002143

[101] E. W. Weisstein, "Rotation matrix," *https://mathworld. wolfram. com/*, 2003.

[102] R. Mukundan, "Quaternions: From classical mechanics to computer graphics, and beyond," in *Proceedings of the 7th Asian Technology conference in Mathematics*, 2002, pp. 97-105.

[103] J. Diebel, "Representing attitude: Euler angles, unit quaternions, and rotation vectors," *Matrix*, vol. 58, no. 15-16, pp. 1-35, 2006.

[104] B. Graf, "Quaternions and dynamics," p. arXiv:0811.2889Accessed on: November 01, 2008Available: https://ui.adsabs.harvard.edu/abs/2008arXiv0811.2889G

[105] S. Madgwick, "An efficient orientation filter for inertial and inertial/magnetic sensor arrays," *Report x-io and University of Bristol (UK)*, vol. 25, pp. 113-118, 2010.

[106] A. Munjiza, J. P. Latham, and N. W. M. John, "3D dynamics of discrete element systems comprising irregular discrete elements—integration solution for finite rotations in 3D," *International Journal for Numerical Methods in Engineering*, https://doi.org/10.1002/nme.552 vol. 56, no. 1, pp. 35-55, 2003/01/07 2003.https://doi.org/10.1002/nme.552

[107] CFDEM. (2011). *CFDEM – Open Source CFD, DEM and CFD*. Available: http://www.cfdem.com

[108] R. Tayeb, Y. Mao, and Y. Zhang, *Numerical Investigation of Evaporation Induced Self-Assembly of Sub-Micron Particles Suspended in Water*. 2016, p. V002T07A002.

[109] S. Zhang, S. Kuwabara, T. Suzuki, Y. Kawano, K. Morita, and K. Fukuda, "Simulation of solid–fluid mixture flow using moving particle methods," *Journal of Computational Physics*, vol. 228, no. 7, pp. 2552-2565, 2009/04/20/ 2009.https://www.sciencedirect.com/science/article/pii/S0021999108006499

[110] *Advanced Multi-sphere method: resolved non-spherical particles*. Available: https://www.cfdem.com/advanced-multi-sphere-method-resolved-non-spherical-particles

[111] S. Koshizuka, A. Nobe, and Y. Oka, "Numerical analysis of breaking waves using the moving particle semi-implicit method," *International Journal for Numerical Methods in Fluids*, https://doi.org/10.1002/(SICI)1097-0363(19980415)26:7<751::AID-FLD671>3.0.CO;2-C vol. 26, no. 7, pp. 751-769, 1998/04/15 1998.https://doi.org/10.1002/(SICI)1097-0363(19980415)26:7<751::AID-FLD671>3.0.CO;2-C

[112] R. A. Dalrymple and B. D. Rogers, "Numerical modeling of water waves with the SPH method," *Coastal Engineering*, vol. 53, no. 2, pp. 141-147, 2006/02/01/ 2006.http://www.sciencedirect.com/science/article/pii/S0378383905001304

[113] J. J. Monaghan and A. Rafiee, "A simple SPH algorithm for multi-fluid flow with high density ratios," *International Journal for Numerical Methods in Fluids*, https://doi.org/10.1002/fld.3671 vol. 71, no. 5, pp. 537-561, 2013/02/20 2013.https://doi.org/10.1002/fld.3671

[114] G. Duan, A. Yamaji, and S. Koshizuka, "A novel multiphase MPS algorithm for modeling crust formation by highly viscous fluid for simulating corium spreading," *Nuclear Engineering and Design*, vol. 343, pp. 218-231, 2019/03/01/ 2019.https://www.sciencedirect.com/science/article/pii/S002954931830596X

[115] P. N. Sun, A. Colagrossi, S. Marrone, and A. M. Zhang, "The δplus-SPH model: Simple procedures for a further improvement of the SPH scheme," *Computer Methods in Applied Mechanics and Engineering*, vol. 315, pp. 25-49, 2017/03/01/ 2017.https://www.sciencedirect.com/science/article/pii/S0045782516309112

[116] B. H. Lee, J. C. Park, M. H. Kim, S. J. Jung, M. C. Ryu, and Y. S. Kim, "Numerical simulation of impact loads using a particle method," *Ocean Engineering*, vol. 37, no. 2, pp. 164-173, 2010/02/01/ 2010.https://www.sciencedirect.com/science/article/pii/S0029801809002820

[117] M. Greenhow and W.-M. Lin, "Nonlinear-free surface effects: experiments and theory," Massachusetts Inst Of Tech Cambridge Dept Of Ocean Engineering1983.

[118] H. Sun and O. M. Faltinsen, "Water impact of horizontal circular cylinders and cylindrical shells," *Applied Ocean Research*, vol. 28, no. 5, pp. 299-311, 2006/10/01/ 2006.https://www.sciencedirect.com/science/article/pii/S0141118707000260

[119] P. Sun, A. M. Zhang, S. Marrone, and F. Ming, "An accurate and efficient SPH modeling of the water entry of circular cylinders," *Applied Ocean Research*, vol. 72, pp. 60-75, 2018/03/01/ 2018.https://www.sciencedirect.com/science/article/pii/S0141118717304984

APPENDIX A CO-AUTHORED ARTICLE PAPER

Cold Regions Science and Technology 186 (2021) 103266

Contents lists available at ScienceDirect

Cold Regions Science and Technology

journal homepage: www.elsevier.com/locate/coldregions

A fully Lagrangian DEM-MPS mesh-free model for ice-wave dynamics

Rubens Augusto Amaro Junior [a,b], Andrea Mellado-Cusicahua [a], Ahmad Shakibaeinia [a,c,*], Liang-Yee Cheng [b]

[a] Department of Civil, Geological and Mining Engineering, Polytechnique Montreal, Canada
[b] Department of Construction Engineering, Polytechnic School of the University of São Paulo, Brazil
[c] Canada Research Chair in Computational Hydrosystems, Canada

ARTICLE INFO

Keywords:
Mesh-free particle-based methods
DEM
MPS
Ice-wave interaction

ABSTRACT

This paper develops and evaluates a novel three-dimensional fully-Lagrangian (particle-based) numerical model, based on the hybrid discrete element method (DEM) and moving particle semi-implicit (MPS) mesh-free techniques, for modeling the highly-dynamic ice-wave interactions. Both MPS and DEM belong to mesh-free Lagrangian (particle) techniques. The model considers ice-wave dynamics as a multiphase continuum-discrete system. While the MPS solves the continuum equations of free-surface flow in a Lagrangian particle-based domain, the DEM uses a multi-sphere Hertzian contact dynamic model to simulate the ice floes motion and interaction. The hybrid model predicts the motion and collision of ice floes as well as their interaction with water, boundaries, and any obstacle in their way. Considering the mesh-free Lagrangian nature of both DEM and MPS, the developed model has an inherent ability to predict the free-drift (absence of internal stress) movements of the ice floes, e.g., sliding, rolling, colliding, and piling-up, in violent free-surface flow. A small-scale and challenging experiment based on dam-break flow over dry and wet beds with floating block floes, which mimics the characteristics of an idealized jam release, has been conducted to provide useful and comprehensive quality data for the validation of the proposed model, as well as other numerical models. Experimental and numerical results of the free-surface profile and the position of the blocks are compared. The results show the ability of the model to numerically reproduce and predict the complex three-dimensional dynamic behavior of wave-ice floes interaction. Overall, this study is a first effort toward developing an ice-wave dynamic within a fully Lagrangian framework (i.e. both flow hydrodynamics and ice dynamics in the Lagrangian particle-based system), and its results can be extended to bring an in-depth understanding of the physics of the real-scale ice-wave or river ice dynamic problems in the future.

1. Introduction

River ice processes play an important role in cold-region hydrosystems (e.g., rivers and lakes), especially during the ice formation and breakup seasons. At the beginning of winter, when rivers become supercooled, small crystals known as frazil ice start to form and they agglomerate creating ice floes. At the end of winter, ice floes are formed due to the breakup of the solid ice covers caused by temperature and flow increase (Beltaos et al., 2000). These ice floes are carried downstream and can impact the river morphology and ecosystem and threaten riverside communities and infrastructures (e.g., bridges and hydroelectric dams, buildings, and roads) (Beltaos, 2010). Furthermore, they can jam and block the flow leading to the rise of the upstream water level and flooding. The increase in the forces acting on the jam or cover front can provoke the breakup and release of the ice jam, with a high magnitude flood wave causing the ice floes to be carried downstream while sliding, rolling, and colliding with everything at high-speed damaging infrastructures and threatening human lives (Beltaos, 2010). Similar high dynamic interaction of wave and ice can also be observed in the dam-break of ice-covered reservoirs and in some sea ice processes. Predicting and understanding the processes and mechanisms involved in the dynamics of wave-ice interaction is crucial for assessing and mitigating the potential impacts. Nevertheless, due to the complexities involved in such a highly dynamic multi-physics system, these processes and mechanisms have remained largely unpredictable, especially in the case of river ice.

* Corresponding author at: Department of Civil, Geological and Mining Engineering, Polytechnique Montreal, Canada.
E-mail addresses: rubens.amaro@usp.br (R.A. Amaro), andrea.mellado-cusicahua@polymtl.ca (A. Mellado-Cusicahua), ahmad.shakibaeinia@polymtl.ca (A. Shakibaeinia), cheng.yee@usp.br (L.-Y. Cheng).

https://doi.org/10.1016/j.coldregions.2021.103266
Received 5 April 2020; Received in revised form 22 December 2020; Accepted 1 March 2021
Available online 5 March 2021

Due to the intrinsic complexity, simplified theoretical models of river ice dynamics or wave-ice interactions are unable to describe the complete problem. Field measurements were made to study and understand river ice (Hicks, 2003; She et al., 2009; Beltaos et al., 2011) and wave-ice interaction dynamics in the contexts of ice jam processes (Jasek, 2003; Nafziger et al., 2016) and sea ice (Squire, 2007; Squire, 2018; Squire, 2020), but the data obtained were generally limited, scarce, insufficient, and expensive due to instrumental and accessibility limitations as well as the associated risks. Several past studies have used laboratory experimentation to shed light on the complex dynamics of river ice (Morse et al., 1999; Healy and Hicks, 2001; Beltaos, 2007).

More recent efforts have focused on the numerical methods, which can provide an economical alternative to simulate different scenarios that can include future changes such as regulations and/or climate change, e.g., Blackburn and She (2019). Many past numerical studies on ice dynamics (particularly for river ice) have been based on one-dimensional (1D) models. Though these models have been able to provide a general picture of the ice processes (useful for many applications), they are limited in providing a detailed undelaying physics, especially when the second and third dimension play important roles in the flow structure and ice floe motions (e.g., when dealing with highly-dynamic flows with circulations and complex geometries). In the past, several two-dimensional (2D) models have been successfully applied to simulations of general ice dynamics, including frazil ice, jamming of ice floes, ice jam release and ice cover breakup, as stated in the extensive review of Shen (2010). Subsequently, a range of three-dimensional (3D) numerical formulations using Eulerian mesh-based methods, based on the continuum description of ice, has been applied to solve ice-wave interaction problems (Wang and Meylan, 2004; Bai et al., 2017; Sayeed et al., 2018). Nevertheless, dealing with the free-floating solids in free-surface flows is still a challenge due to the presence of splashing, fragmentations, merging, or multiple body interactions. Furthermore, boundary tracking or re-meshing techniques are required for mesh-based methods, increasing the computational complexity.

Another group of numerical methods are those based are the discrete description of ice floes. While the accuracy of the continuum description largely depends on the accuracy of the ice rheological models, the discrete models have shown to be able to describe the underlying physics in detail. Among discrete techniques, the discrete element method (DEM; Cundall and Strack, 1979), which is the base of currently study, have been extensively used to study ice mechanics. The studies of Hopkins and Hibler (1991) and Løset (1994), in which ice floe fields were considered as systems of 2D discs, are pioneering works on the application of DEM to describe the ice behavior. Hopkins (2004) used a 2D polygonal DEM approach, based on previous DEM work (Daly and Hopkins, 2001; Hopkins and Tuthill, 2002), to simulate the sea ice floes displacement caused by wind stress and water drag. Ice floes thickness were modeled using an algorithm proposed by Ebert and Curry (1993), in which the ice dynamics incorporates a lead parameterization that takes into account a minimum lead fraction, the absorption of solar radiation in and below the leads, the lateral accretion and ablation of the sea ice and a prescribed sea ice divergence rate. Hopkins and Daly (2003) developed a similar DEM model that includes not only the drag force but also the buoyancy and pressure force. This model combines a 3D DEM with a 1D hydraulic model whose transverse and vertical geometry and flow data are averaged. In Hopkins and Shen (2001) and Dai et al. (2004), a 3D DEM model was used to study the dynamics of pancake-ice, i.e., the circular floes formed during ice growth in a wave field. They demonstrated that the final ice cover thickness due to the rafting process is a function of wave amplitude, wavelength and floe diameter. Another model developed by Stockstill et al. (2009) took a step forward and combined the 3D DEM with depth-averaged 2D shallow-water equations solved using a finite element (FE) scheme. The ice rubbling process was simulated by the finite-discrete element method in Paavilainen and Tuhkuri (2013), where an ice sheet and blocks were modeled using a finite element method (FEM), and the ice rubble pile was modeled by a discrete element scheme. Ji et al. (2015) applied the DEM to analyse the influences of ice velocity, ice thickness, and conical angle on ice loads in conical offshore structures. A dilated polyhedral DEM was developed by Liu and Ji (2018), and numerical simulations of the interaction between ice floes and the floating structure Kulluk were validated against field data. Herman et al. (2019) conducted numerical studies on wave attenuation through ice-floe fields, and used DEM to account for the energy dissipation due to ice floe collisions. In Gong et al. (2019), the resistance of a ship in ridges of equal depth but different widths was studied using a 3D DEM. A good review of different types of DEM approaches and their applications on ice-related problems can be found in Metrikin and Løset (2013), Tuhkuri and Polojärvi (2018), and Xue et al. (2020). There are various methods in the DEM to represent solids of different scales or shapes. While some techniques represent each solid parcel with a single particle, the so-called multi-sphere methods (Favier et al., 1999) use a collection of attached particles (with fixed relative positions) to construct the complex shapes. Most of the numerical flow models adopted in these works the flow hydrodynamic and interaction force of fluid (water) on the solid (ice) have been based on simplified depth-averaged hydrodynamics, or potential flow theory. Hence, they are not able to reproduce the highly dynamic ice-wave interactions.

An alternative for simulation of flow hydrodynamics and fluid-solid interactions is the continuum-based particle (Lagrangian) methods, such as Smoothed Particle Hydrodynamics (SPH) (Gingold and Monagham, 1977) and Moving Particle Semi-implicit (MPS) (Koshizuka and Oka, 1996) which are widely used methods for many fluid flow problems. These methods solve the continuum conservation equations over a set of particles, containing the continuum field variables, that move in the Lagrangian system (Shakibaeinia and Jin, 2010). Being mesh-free and Lagrangian giving the flexibility of dealing with any deformations and fragmentations. Combination of these continuum-based particle methods with DEM (i.e. a discrete-based particle method) will create a fully-Lagrangian multiphase-continuum modeling systems (e.g., DEM-SPH or DEM-MPS), ideal for simulation highly dynamics movements in both fluid and solid phases and their interaction. Such fully-Lagrangian framework is the base of current study.

DEM-SPH/MPS approach has been applied to engineering problems such as the interaction between fluid and solid particles in a cylindrical tank (Sakai et al., 2012), particle sedimentation (Robinson et al., 2014), sediment transport in the swash zones (Harada et al., 2019), non-Newtonian solid-liquid interaction with the presence of free-surface flow (Li et al., 2019), among others. Some of the past works combined multi-sphere DEM and SPH/MPS mainly to simulate rigid bodies transport under free-surface flow (Canelas et al., 2016; Amaro Jr et al., 2019). To the author's knowledge, the application of these DEM-SPH/MPS particle based techniques to ice dynamics and ice wave interaction problems, has been limited to a few recent works (e.g., Robb et al., 2016; Kawano and Ohashi, 2015; Zhang et al., 2019). Kawano and Ohashi (2015) used MPS to reproduce the process of growth and accumulation of crystal nuclei and the formation process of the layer of fine crystals. Zhang et al. (2019) used a SPH hydrodynamics to study the kinematic and flexural responses of a single deformable ice floe. Nonetheless, only 2D cases with a single ice floe (no collision model) were simulated.

In this paper, a novel 3D fully-Lagrangian model able to handle ice-wave interaction is proposed, which couples MPS and DEM, for continuum (water) and discrete (ice) phases, respectively. Although DEM has been extensively used in the past for the ice dynamic simulations, this is the first effort toward an efficient fully Lagrangian model that combines DEM with a continuum particle method (e.g., MPS) to make it capable of simulating the highly dynamic 3D ice-wave systems. In the MPS method, the differential operators of the continuum mechanics are replaced by weighted average discrete operators on irregular nodes, and a semi-implicit algorithm is applied to solve the governing equations. Furthermore, MPS is very effective for the simulations of incompressible

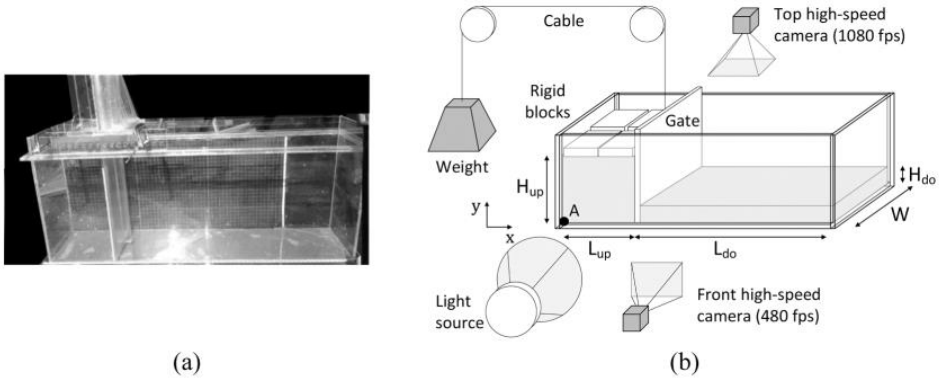

Fig. 1. (a) Prismatic plexiglass tank used in the dam-break experiments. (b) Schematic drawing of the tank, water levels, gate, rigid blocks, pulley-weight mechanism, cameras disposition, and light source.

flow involving large deformation of free surfaces, fragmentation, and merging, or involving complex shaped bodies, large deformation or motion of boundaries, multi-bodies, multi-phase flows, and multi-physic problems. The DEM is coupled with the MPS method and is used to simulate the solid ice phase, here simplified by rigid body. Here the DEM is adopted following the original idea of Koshizuka (1998), the so-called passively moving solid (PMS) model, in which the shell of a rigid body is represented by a cluster of particles whose relative positions remain unchanged, similar to the multi-sphere technique. In order to address numerical instabilities due to non-smooth solid walls modeled by particles, an approach based on the faces of the bodies and contact force computed using the normal vectors of solid walls (Amaro Jr et al., 2019) is adopted here. This study uses a high resolution of particles for both DEM and MPS (e.g., a single ice flow is represented with more than 5000 particles) leading to computationally expensive simulations. Therefore, this study implements the model on a shared-memory parallel code (to use the power of multicore processors) and limits the test cases to simple geometries with a limited number of ice floes simplified by rigid bodies, i.e., internal ice stress and broken ice behavior are neglected, and therefore the dynamics are close to a state of free-drift motions. The physical and mathematical aspects of free-drift motions of ice are well discussed in Leppäranta (2011).

Moreover, considering the currently lacking comprehensive data for the detailed validation of ice-wave interaction dynamics, a small-scale yet challenging experiment based on dam-break flow over dry and wet beds with floating block floes (ice dynamics simplified by dynamics of rigid bodies), which somehow mimics the characteristics of an idealized jam release, has been conducted to provide quality and quantitative data for the validation of the proposed model and investigation of the highly nonlinear phenomenon. Though this experiment is a simplification of a real jam release, it provides the basic solid-wave interactions needed to validate the proposed DEM-MPS simulation. The imagery data from two high-speed cameras have been analyzed and used to track the highly dynamic motion of the blocks and water surface profiles.

Fig. 2. Polypropylene strips and weights used for measuring static friction coefficient.

2. Experimental setup

The experiments consist of a series of dam-break case scenarios with floating blocks that offer similar characteristics to jam releases and breaches of ice-covered reservoirs in terms of having high magnitude waves with floating ice parcels. Reported experiments in the literature of wave-ice interaction generally cover two scenarios:

i.) one or two ice floes interacting with waves (McGovern and Bai, 2014; Yiew et al., 2016, 2017);
ii.) hundreds of ice floes subjected to waves and colliding with each other (Dai et al., 2004; Bennetts and Williams, 2015) and also with towing carriage (Hu and Zhou, 2015; Luo et al., 2018).

In the present work, our goal is to provide an experimental benchmark test to fill the gap between these two situations. In this way, the present test cases were selected based on their high-dynamic nature, simple geometry, reduced number of ice floes, and valuable data that they can provide for the numerical model validation.

2.1. Experimental apparatus

The experiments have been conducted at the hydraulic laboratory of the École Polytechnique of Montreal. A prismatic plexiglass tank having interior dimensions of 70 cm length, 15 cm width, and 30 cm height, was used here, see Fig. 1(a). A removable gate of 0.5 cm thickness divides the tank into two parts. The upstream part has a length of $L_{up} = 15$ cm and water height of $H_{up} = 15$ cm, and the downstream part has a length of $L_{do} = 55$ cm and variable water heights H_{do}, respectively, see Fig. 1(b). Blocks of artificial ice material float on the surface of the upstream reservoir. For analysis purposes, a reference frame, having the origin at point A, has been adopted. To replicate the dam-break event, the gate was removed (lifted) almost instantaneously through a pulley-weight mechanism, as shown in Fig. 1(b). The sides of the gate were sealed with flat and flexible vinyl strips and high-vacuum grease to ensure the reservoir's water tightness. Two high-speed cameras were used to track the longitudinal and vertical motions. A high-speed camera (FASTCAM Mini WX100), capable of taking 1080 frames per second (fps) with a 2048 × 2048 resolution, was placed on top of the tank, and another one (Sony DSC-RX100M5A) with 480 fps and 1292 × 436 resolution was placed at the front of the tank. The light source was a high-frequency AOS Offboard 150 W Led, which eliminates flicker issues.

Table 1
Experimental case conditions. Number of blocks, upstream (H_{up}) and downstream (H_{do}) water height.

Case	Number of blocks	H_{up} (cm)	H_{do} (cm)
1	4	15	0.0
2			1.0
3			2.5
4			5.0
5	9		0.0
6			1.0
7			2.5
8			5.0

2.2. Experimental material

Blocks of white polypropylene, with a density of approximately 868 kg/m^3, were used as the artificial ice floes. However, it shall be mentioned that a higher density around 0.92 kg/m^3, can provide a better estimation for river ice floes, i.e., salinity ~0 ppt (parts per thousand), see Fig. 3 in Timco and Frederking (1996). The friction coefficient required for the numerical simulations was determined experimentally. The static friction coefficient between blocks was measured using the setup shown in Fig. 2. Two sets of polypropylene strips were attached, where the top one was free to move, and the bottom one was fixed to the table. Knowing that the blocks are wet during the experiment, the strips were soaked wet before applying a horizontal force. By putting additional weight above the free set of strips, the normal force was defined, and the shear force was obtained by measuring the force required to move the block horizontally. The different masses put on top of the blocks, the average measured shear force, and the correspondent friction coefficients calculated as the ratio of the shear force to the normal are shown in Appendix A. The median static friction coefficient found for the wet blocks and used in the numerical simulations was $\mu_s = 0.412 \pm 0.050$. It should be mentioned that the present test did not consider the effect of sliding speed, temperature, and surface tension on the friction coefficient. Furthermore, the static friction coefficient might not be the best parameter to use in dynamic simulations, but the relevance of the friction forces seems to be small compared to the other solid collision forces in the present study. Nonetheless, to the authors' knowledge, a wide range of values [0.1, 0.6], given by a function of the velocity of the interaction, has been used for the actual ice-ice friction coefficient (Timco and Weeks, 2010; van den Berg et al., 2019). In this way, we intended to provide a value of reference for the friction coefficient for the material used here, namely polypropylene, with the available laboratory instrumentation in the hydraulic laboratory of the École Polytechnique Montreal.

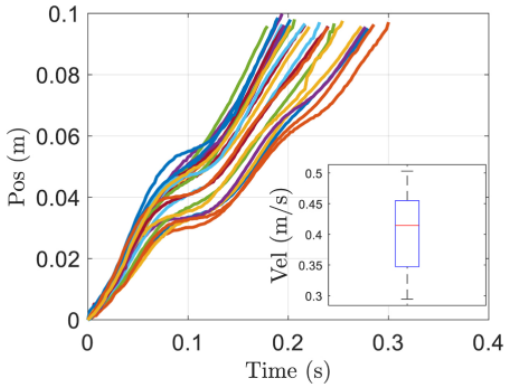

Fig. 4. Time series of the vertical gate motion for all 24 experiments and the median value of gate velocity.

2.3. Experimental case scenarios

Eight case scenarios, which differ in the number of polypropylene blocks and the downstream water heights, were carried out as summarized in Table 1. In the first four cases, 4 equal-size polypropylene blocks were used. Each block has dimensions (width × length × thickness) 7.25 × 7.25 × 1.95 ± 0.06 cm and a mass of 0.089 ± 0.001 kg. The other four cases used 9 polypropylene blocks of 4.80 × 4.80 × 1.95 ± 0.06 cm, each having a mass of 0.039 ± 0.001 kg. Four downstream water heights, i.e., H_{do} = 0, 1.0, 2.5 and 5.0 cm, were tested. Each case was repeated at least three times to check the reliability, and the three repeated experiments of each case are denominated EXP1, EXP2, and EXP3.

2.4. Data acquisition

The evolution of the water surface profile and displacement of ice blocks were determined by processing high-speed imagery data from the top and front cameras. The displacements of the blocks in x and y directions were determined using the high-speed videos obtained from the top and front cameras, respectively. For this purpose, a free video analysis software called Tracker (Brown, 2019) was used to automatically track the center of mass (CM) of each block, as shown in Fig. 3, using a template matching algorithm. The water surface profile was obtained by digitizing images extracted from the videos taken by the front camera.

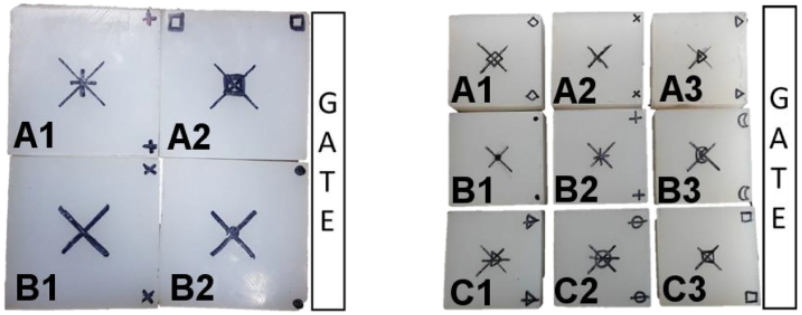

(a) (b)

Fig. 3. Initial arrangement of the cases with (a) 4 blocks and (b) 9 blocks.

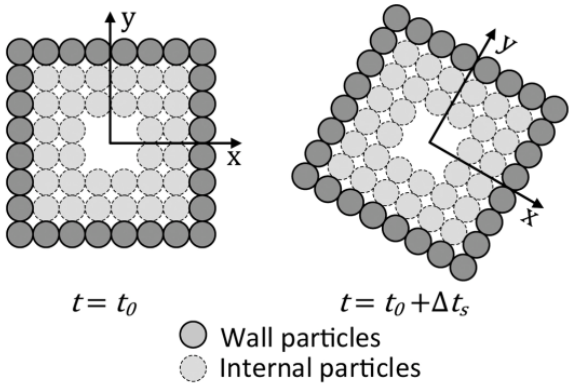

Fig. 5. Rigid body represented by a collection of wall and internal particles in 2D space.

2.5. Gate motion

The time series of the vertical gate motion for the 24 experiments are presented in Fig. 4. According to Lauber and Hager (Lauber and Hager, 1998), the gate motion satisfies the criterion of a sudden removal if the removal period t_r (time required for a fluid particle located at the top of the fluid column to reach the bottom of the tank) is smaller than $\sqrt{2H_{up}/g}$. From the video records, the gate removal duration, i.e., the instant when the gate's lower edge reaches the dam filling height, was around 0.40 s and did not satisfy the criterion $t_r < \sqrt{2 \times 0.15/9.81} \rightarrow t_r < 0.175$ s. Therefore, the present experiments can not be considered as sudden dam breaks. Furthermore, since the gate motion has a significant influence on the water collapse process and dam-break results, it cannot be neglected in the numerical model. Nevertheless, we performed some simulations using: i) the behavior of the vertical gate motion observed in the experiments (see Fig. 4), i.e., a variable vertical velocity; and ii) a constant vertical velocity so that the trajectory of the gate becomes linear. Negligible differences in the wave-profile evolutions as well as the solid motions were observed between the experimentally measured and the numerically computed results when using the varying or constant gate velocity. Thus, the constant gate velocity, which can be easily assigned as a boundary condition in a wider range of numerical solvers, was chosen based on the median of the average gate velocity of the 24 cases ($v_g = 0.4$ m/s) and adopted in the numerical simulations. The median value of gate velocity and the relevant confidence intervals are shown in Fig. 4.

3. Governing equations

The physical system includes the interaction of a continuum phase (water) and a discrete phase (solid ice blocks). The governing equations describing the dynamics of the continuum phase (flow of an incompressible viscous fluid) are expressed by the conservation laws of mass and momentum, which in their Lagrangian form are as follows:

$$\frac{D\rho_f}{Dt} + \rho_f \nabla \cdot \mathbf{u}_f = 0 \tag{1}$$

$$\frac{D\mathbf{u}_f}{Dt} = -\frac{\nabla P}{\rho_f} + \nu_f \nabla^2 \mathbf{u}_f + \mathcal{F}_b \tag{2}$$

where ρ_f is the fluid density, $\mathbf{u}_f$ stands for the fluid velocity vector, P denotes the pressure, ν_f represents the kinematic viscosity and $\mathcal{F}_b$ is the external body force per unit mass vector, namely the gravitational acceleration vector $\mathbf{g}$ in the present work.

For the discrete phase (solid blocks), the governing equations of motion are those of translational and rotational motion given by:

$$m_s \frac{D\mathbf{u}_s}{Dt} = \mathbf{F}_h + \mathbf{F}_g + \mathbf{F}_c = -\iint_{\mathscr{A}} P d\mathbf{a} + m\mathbf{g} + \mathbf{F}_c \tag{3}$$

$$\mathbf{I} \cdot \frac{D\boldsymbol{\omega}_s}{Dt} + \boldsymbol{\omega}_s \times (\mathbf{I} \cdot \boldsymbol{\omega}_s) = \mathbf{T}_h + \mathbf{T}_c = -\iint_{\mathscr{A}} \mathbf{r}_s \times P d\mathbf{a} + \mathbf{T}_c \tag{4}$$

where m_s is the total mass of the rigid body, $\mathbf{u}_s$ represents the velocity vector at the CM of the rigid body, $\mathbf{I}$ is the inertia matrix and $\boldsymbol{\omega}_s$ stands for the angular velocity vector about the principal axes of the rigid body. The hydrodynamic forces on the rigid surface $\mathbf{F}_h$, gravitational force $\mathbf{F}_g$, contact forces between the rigid bodies $\mathbf{F}_c$, hydrodynamic torque $\mathbf{T}_h$ and contact torque $\mathbf{T}_c$ are taken into consideration for the motion of rigid bodies. The vector $\mathbf{r}_s$ denotes the position vector from the CM of the rigid body and $d\mathbf{a}$ is the face vector of the rigid body surface, whose magnitude is the area of the discrete face and direction is normal to the body surface. Focusing the impulsive hydrodynamic loads on the rigid solid, the contribution of fluid shear forces was assumed to be negligible in the present study. It is important to highlight that it is a practical limitation of the present model since shear forces would be very important in ice jam formation and release events.

4. Numerical methods

Here, the moving particle semi-implicit (MPS) method and discrete element method (DEM) are used to solve the governing equation of the continuum-phase (water) and discrete phase (solid ice blocks), respectively.

4.1. Moving Particle Semi-implicit (MPS)

As a particle method, MPS represents the continuum with a set of mobile particles (without any connectivity) over which the flow governing equations are solved. Here, a semi-implicit algorithm, which divides each time step into prediction and correction steps, is used for the temporal integration of the governing equations. At first, predictions of the velocity and position of a fluid particle i are carried out explicitly by using viscosity and external forces terms of the momentum conservation:

Table 2
Physical properties of the fluid (MPS).

Property	Water
Density ρ_f (kg/m^3)	1000
Kinematic viscosity ν_f (m^2/s)	10^{-6}

Table 3
Physical properties of the solids (DEM).

Property	Tank (Plexiglass)	Block (Polypropylene)
Density ρ_S (kg/m^3)	∞	868
Young's modulus E_s (GPa)	1.0	3.3
Poisson's ratio υ_s	0.37	0.40
Static friction μ_s	0.412	0.412

Table 4
Simulation parameters of the fluid (MPS) and solid (DEM) domains.

Parameter	Value	Parameter	Value
Particle distance l^0 (m)	0.002	Collision distance α_1	0.8
Time step (fluid) Δt_f (s)	1.25×10^{-4}	Coefficient of restitution α_2	0.2
Effective radius r_e (m)	$2.1 \times l^0$	Relaxation coefficient γ	0.01
Surface threshold β	0.97	Compressibility α_c (ms^2/kg)	10^{-8}
Surface threshold ϱ	0.2	Damping ratio of the collision ξ_n	0.05
Courant number C_r	0.2		

$$\mathbf{u}_i^* = \mathbf{u}_i^t + \Delta t\left[\nu_f\langle\nabla^2\mathbf{u}\rangle_i + \mathcal{F}_b\right]^t \tag{5}$$

$$\mathbf{r}_i^* = \mathbf{r}_i^t + \Delta t\mathbf{u}_i^* \tag{6}$$

Here, the superscript * refers to the prediction step. The approximation of spatial derivations in MPS is based on the kernel smoothing (weighted averaging) process. The MPS approximation of Laplacian of velocity over neighboring particles Ω_i is given by:

$$\langle\nabla^2\mathbf{u}\rangle_i = \frac{2d}{\lambda_i pnd^0}\sum_{j\in\Omega_i}(\mathbf{u}_j - \mathbf{u}_i)\omega_{ij} \tag{7}$$

where $d = 1$, 2 or 3 is the number of spatial dimensions, pnd^0 stands for the particle number density of a fully compact support with an initial cubic arrangement of particles, ω_{ij} represents a weight (kernel) function and λ_i is a correction parameter by which the variance increase is adjusted to be equal to the analytical solution. Here, the widely used rational weight function (Koshizuka and Oka, 1996) is used:

$$\omega_{ij} = \begin{cases} \dfrac{r_e}{\|\mathbf{r}_{ij}\|} - 1 & \|\mathbf{r}_{ij}\| \le r_e \\ 0 & \|\mathbf{r}_{ij}\| > r_e \end{cases} \tag{8}$$

where r_e is the effective radius that limits the range of influence and $\|\mathbf{r}_{ij}\| = \|\mathbf{r}_j - \mathbf{r}_i\|$ is the distance between the particles i and j. As demonstrated by Koshizuka and Oka (Koshizuka and Oka, 1996), more accurate and stable computations can be achieved with $r_e \in [1.8l^0, 3.1l^0]$ in 3D problems, where l^0 represents the initial distance between two adjacent particles. Therefore, in the present work, $r_e = 2.1l_0$ is adopted for the calculations of particle number density and all differential operators. For an extensive and quantitative study of the influence of r_e on the numerical accuracy, the reader is referred to the work of Duan et al. (Duan et al., 2019). The summation of the weight of all the particles in the neighborhood of particle i is defined as its particle number density

$$pnd_i = \sum_{j\in\Omega_i}\omega_{ij} \tag{9}$$

which is proportional to the fluid density. The correction parameter λ_i is defined as:

$$\lambda_i = \frac{\sum_{j\in\Omega_i}\|\mathbf{r}_{ij}\|^2\omega_{ij}}{\sum_{j\in\Omega_i}\omega_{ij}} \tag{10}$$

After the prediction of velocities and positions of the fluid particles, a collision model is applied to fluid particles located at the free surface or some inner particles with few neighbors to the proper calculation of the discrete differential operators, avoiding clustering of particles, and the contribution $\Delta\mathbf{u}^*$ is added:

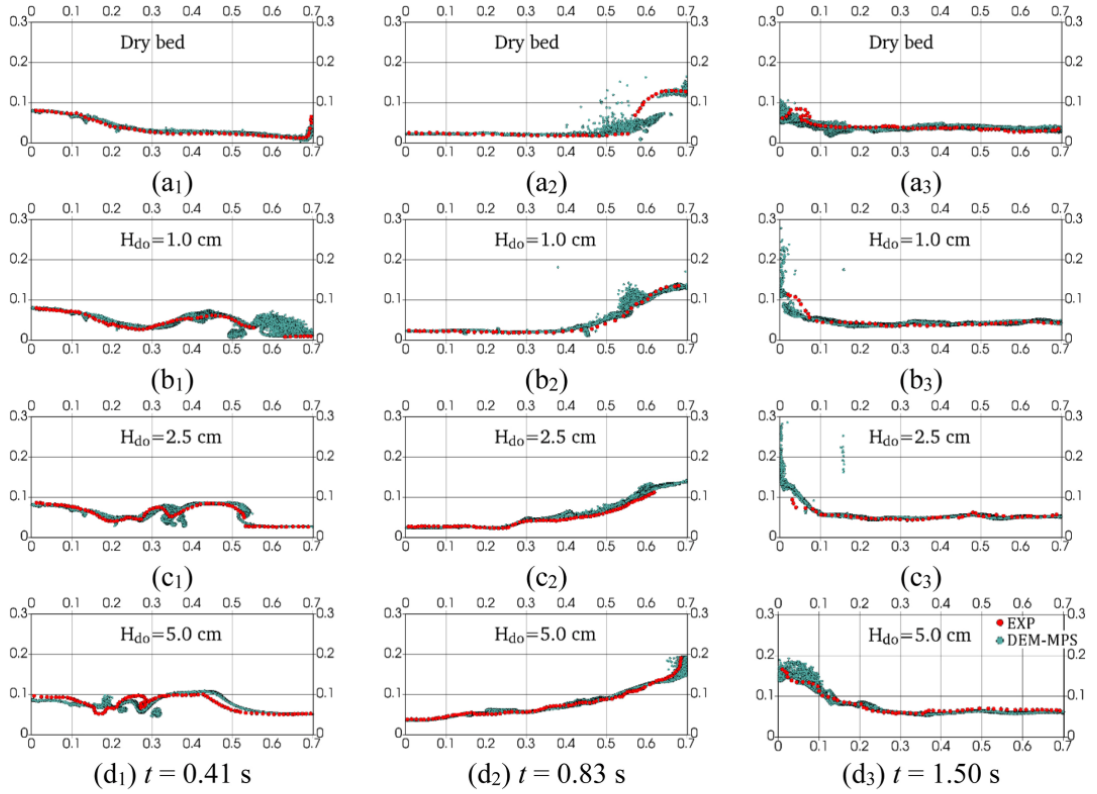

Fig. 6. Evolution of the experimental (red dots) and numerical (turquoise dots) wave profiles for dam breaking with 4 blocks at the instants $t = 0.41$, 0.83, 1.50 s (from left to right). (a_1, a_2, a_3) Dry bed and wet beds H_{do} = (b_1, b_2, b_3) 1.0, (c_1, c_2, c_3) 2.5 and (d_1, d_2, d_3) 5.0 cm. Experimental and numerical results are from the front camera and exclude the splash.

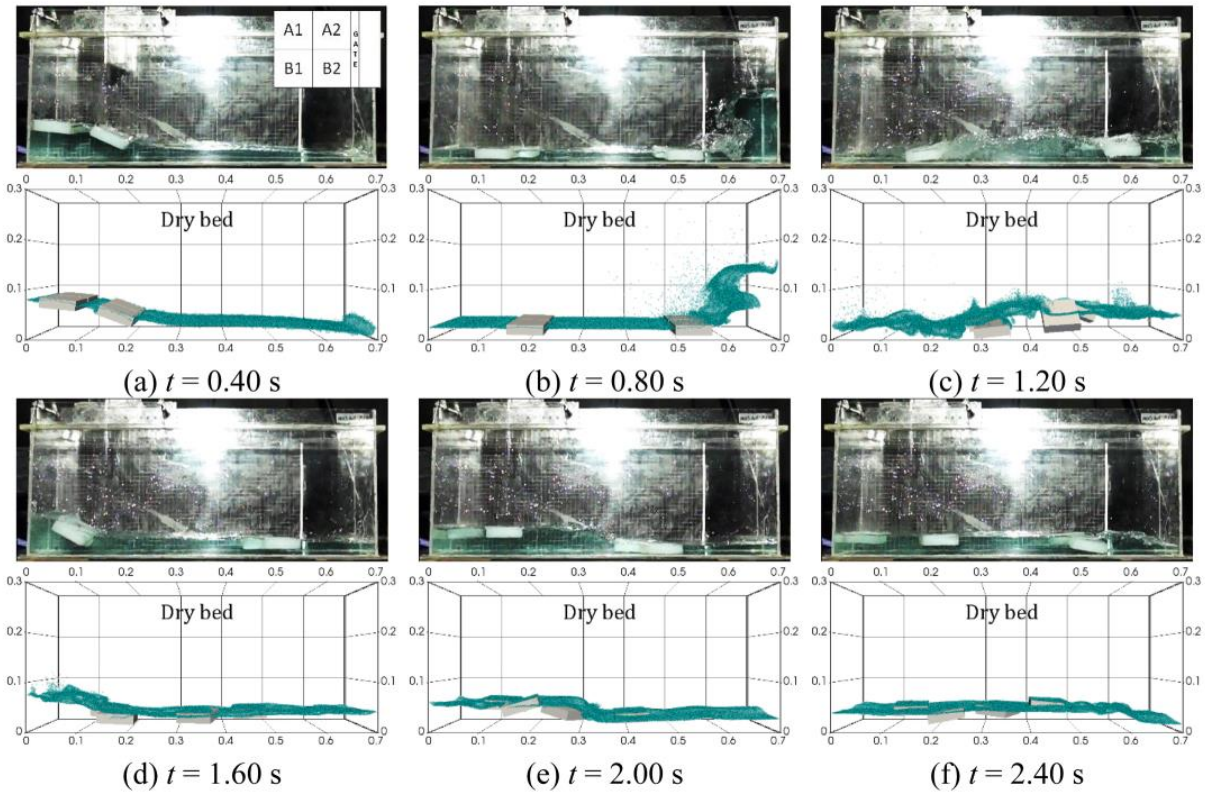

Fig. 7. Snapshots of the experimental and numerical dam breaking with 4 blocks and dry bed at the instants t = 0.40, 0.80, 1.20, 1.60, 2.00, 2.40 s (front view).

$$\mathbf{u}_i^{**} = \mathbf{u}_i^{*} + \Delta\mathbf{u}_i^{*} \tag{11}$$

$$\mathbf{r}_i^{**} = \mathbf{r}_i^{*} + \Delta t\Delta\mathbf{u}_i^{*} \tag{12}$$

where $\Delta\mathbf{u}_i$* can be calculated from:

$$\Delta\mathbf{u}_i^{*} = \begin{cases} \sum_{j\in\Omega_i} \frac{(1+\alpha_2)}{\alpha_3} \frac{\mathbf{r}_{ij}^{*}\cdot\mathbf{u}_{ij}^{*}}{\left\|\mathbf{r}_{ij}^{*}\right\|} \frac{\mathbf{r}_{ij}^{*}}{\left\|\mathbf{r}_{ij}^{*}\right\|} & \left\|\mathbf{r}_{ij}^{*}\right\| \le \alpha_1 l^0 \text{ and } \mathbf{r}_{ij}^{*}\cdot\mathbf{u}_{ij}^{*} < 0 \\ 0 & \text{otherwise} \end{cases} \tag{13}$$

If the neighbor j is a fluid particle, then the coefficient $\alpha_3 = 2$ otherwise $\alpha_3 = 1$. According to Lee et al. (Lee et al., 2011), values of the coefficient that define the collision distance $\alpha_1 \ge 0.8$ and coefficient of restitution $\alpha_2 \le 0.2$ increase the spatial stability in simulations.

Then the pressures of fluid and wall particles are obtained implicitly by solving a linear system of pressure Poisson equation (PPE) (Koshizuka et al., 1999; Ikeda et al., 2001):

$$\left\langle\nabla^2 P\right\rangle_i^{t+\Delta t} - \frac{\rho_f}{\Delta t^2}\alpha_c P_i^{t+\Delta t} = \gamma\frac{\rho_f}{\Delta t^2}\left(\frac{pnd^0 - pnd_i^{**}}{pnd^0}\right) \tag{14}$$

where Δt is the time step, pnd_i** is the particle number density calculated after the prediction and collision processes, α_c is the coefficient of artificial compressibility, and γ is the relaxation coefficient. Both α_c and γ are used to improve the stability of the computation method. Eq. (14) represents a linear system, characterized by a sparse matrix, in which a higher coefficient α_c makes the diagonal elements of the matrix bigger, rending it very useful for computational stabilization. The relaxation coefficient γ is adopted to enforce the incompressibility condition in a robust way while mitigating high-frequency pressure oscillations in the discrete PPE. Nevertheless, both α_c and γ should be chosen appropriately in order to avoid non-physical fluid behavior. Typically, the ranges $\alpha_c \in [10^{-9}, 10^{-8}]$ ms^2/kg and $\gamma \in [0.001, 0.05]$ provide stable simulations (Duan et al., 2019; Shibata et al., 2015; Tsukamoto et al., 2020). The experience of the authors has shown that the coefficients $\alpha_c = 10^{-8}$ ms^2/kg and $\gamma = 0.01$ give satisfactory results, and therefore they were used for all simulations herein.

The Laplacian of pressure is approximated by:

$$\left\langle\nabla^2 P\right\rangle_i = \frac{2d}{\lambda_i pnd^0}\sum_{j\in\Omega_i}(P_j - P_i)\omega_{ij} \tag{15}$$

Finally, the velocity of the fluid particles ($\mathbf{u}_i^{t+\Delta t}$) is updated by using the pressure gradient term of the momentum conservation (see Eq. (2)) and the updated positions $\mathbf{r}_i^{t+\Delta t}$ are obtained:

$$\mathbf{u}_i^{t+\Delta t} = \mathbf{u}_i^{**} - \frac{\Delta t}{\rho_f}\left\langle\nabla P\right\rangle_i^{t+\Delta t} \tag{16}$$

$$\mathbf{r}_i^{t+\Delta t} = \mathbf{r}_i^{**} + \Delta t\left(\mathbf{u}_i^{t+\Delta t} - \mathbf{u}_i^{**}\right) \tag{17}$$

To prevent instability issue induced by attractive pressure and to reduce the effect of nonuniform particle distribution, the first-order pressure gradient was adopted here as (Wang et al., 2017):

$$\left\langle\nabla P\right\rangle_i = \left[\sum_{j\in\Omega_i}\omega_{ij}\frac{\mathbf{r}_{ij}}{\left\|\mathbf{r}_{ij}\right\|}\otimes\frac{\mathbf{r}_{ij}^{T}}{\left\|\mathbf{r}_{ij}\right\|}\right]^{-1}\left[\sum_{j\in\Omega_i}\frac{P_j - \widehat{P}_i}{\left\|\mathbf{r}_{ij}\right\|^2}\mathbf{r}_{ij}\omega_{ij}\right] \tag{18}$$

where $\widehat{P}_i$ is the minimum pressure between the neighborhood of the particle i, i.e., $\widehat{P}_i = \min_{j\in\Omega_i}(P_j, P_i)$.

4.2. Discrete Element Method (DEM)

Here, an approach similar to the multi-sphere DEM technique is used in which the shells of a solid body (here rigid cuboids) are represented by a collection of wall and internal spherical particles whose relative positions remain unchanged, following Koshizuka et al. (Koshizuka, 1998), see Fig. 5.

The overall contact force on the rigid body is calculated by adding the contributions due to the normal $\mathbf{F}_n$ and tangential $\mathbf{F}_t$ contact forces between wall particles belonging to different bodies. Here, subscript n stands for the normal component, and t denotes the tangential component.

The normal forces between the pair of the closest particles k and l belonging to different bodies can be described following a non-linear Hertz's elastic contact theory (Johnson, 1985):

$$\mathbf{F}_{n,kl} = k_{n,kl}\delta_{kl}^{3/2}\mathbf{n}_c + c_{n,kl}\delta_{kl}^{1/4}\dot{\delta}_{kl}\mathbf{n}_c \tag{19}$$

where $k_{n,kl} = 4/3E_{kl}\sqrt{l_{kl}^0}$ is the normal stiffness constant of pair kl, δ_{kl} is the overlap (penetration) between two wall particles belonging to two different bodies, $\dot{\delta}_{kl}$ is the rate of normal penetration, $c_{n,kl} = \xi_n\sqrt{6m_{kl}E_{kl}\sqrt{l_{kl}^0}}$ is the normal damping constant and $\mathbf{n}_c$ is the contact normal vector defined as follows:

1. If particle l is *face*, the normal of l is used as $\mathbf{n}_c$.
2. If particle l is not face, but k is *face*, the reverse of the normal of k is used as $\mathbf{n}_c$.
3. None of the particles are face, the reverse of the distance vector $\mathbf{r}_{kl}/|\mathbf{r}_{kl}|$ is used as $\mathbf{n}_c$.

As the geometry of a cuboid is enough to model all rigid bodies considered herein, the number of neighbor solid particles is used as the criterion to identify if a particle belongs to a face.

The damping ratio ξ_n must be high enough to obtain a non-oscillatory motion of the rigid solids while not too high so that too much energy is dissipated unnaturally during the collision, whereas E_{kl}, m_{kl} and $l_{0,\,kl}$ are obtained as:

$$E_{kl} = \frac{E_kE_l}{(1-\upsilon_l^2)E_k + (1-\upsilon_k^2)E_l}, \quad m_{kl} = \frac{m_km_l}{m_k+m_l}, \quad l_{kl}^0 = \frac{l_k^0 l_l^0}{l_k^0 + l_l^0} \tag{20}$$

where E_k, E_l, υ_k and υ_l are the Young's modulus and the Poisson's ratio of particles k and l, respectively. In the present work, a single spatial resolution is used for all domain, i.e., the initial distance between two adjacent particles l^0 is the same for the particles k and l, thus leading to $l_{kl}^0 = l^0/2$. Moreover, if the l-th particle belongs to a fixed rigid wall, then $m_l \to \infty$, implying that $m_{kl} = m_k$.

Tangential forces can be obtained from the Coulomb friction law given by Eq. (21) and a sigmoidal function is used to make the forces continuous in the origin regarding the tangential relative velocity $\dot{\delta}_{kl}^t$ (Vetsch, 2011). The tangential forces can also be obtained using a linear model of repulsive and damped forces given by Eq. (22).

$$\mathbf{F}_{t,kl}^C = \mu_{kl}\|\mathbf{F}_n\|tanh\left(8\dot{\delta}_{kl}^t\right)\mathbf{t}_c \tag{21}$$

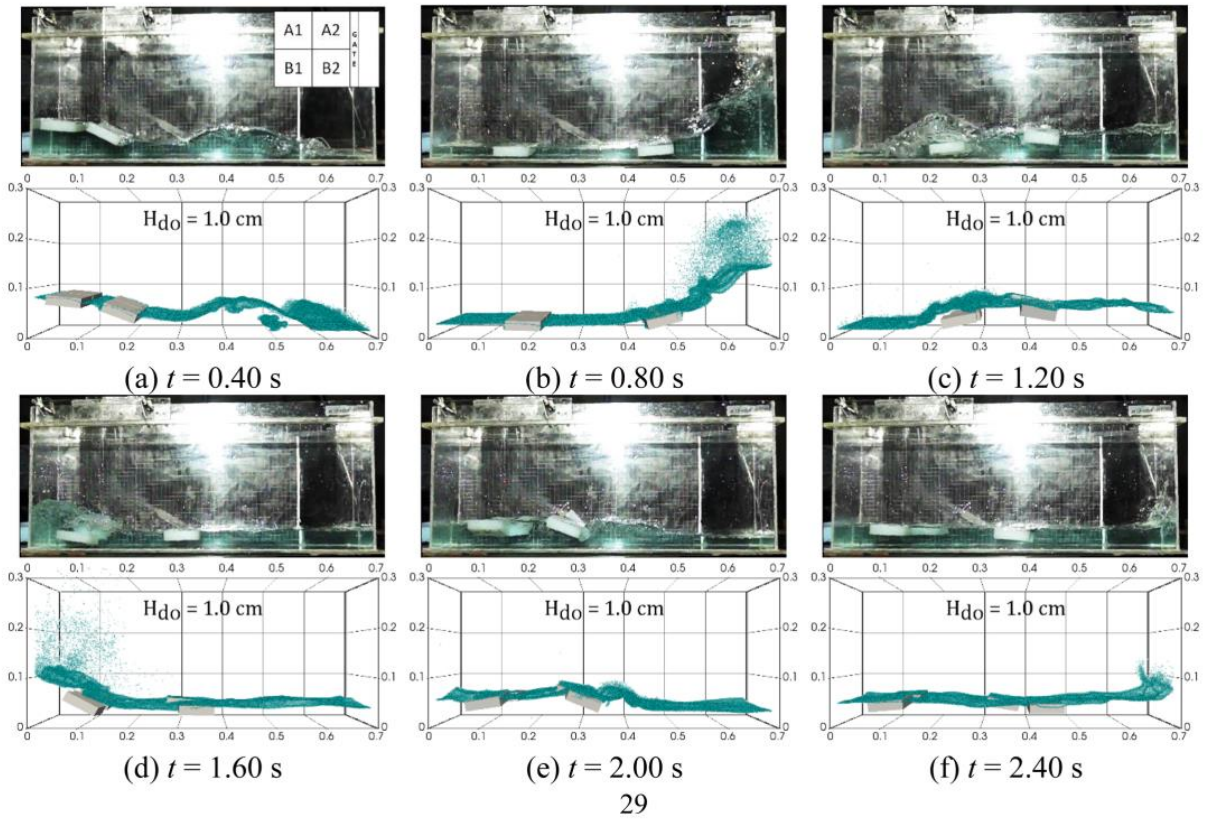

Fig. 8. Snapshots of the experimental and numerical dam breaking with 4 blocks and wet bed H_{do} = 1 cm at the instants t = 0.40, 0.80, 1.20, 1.60, 2.00, 2.40 s (front view).

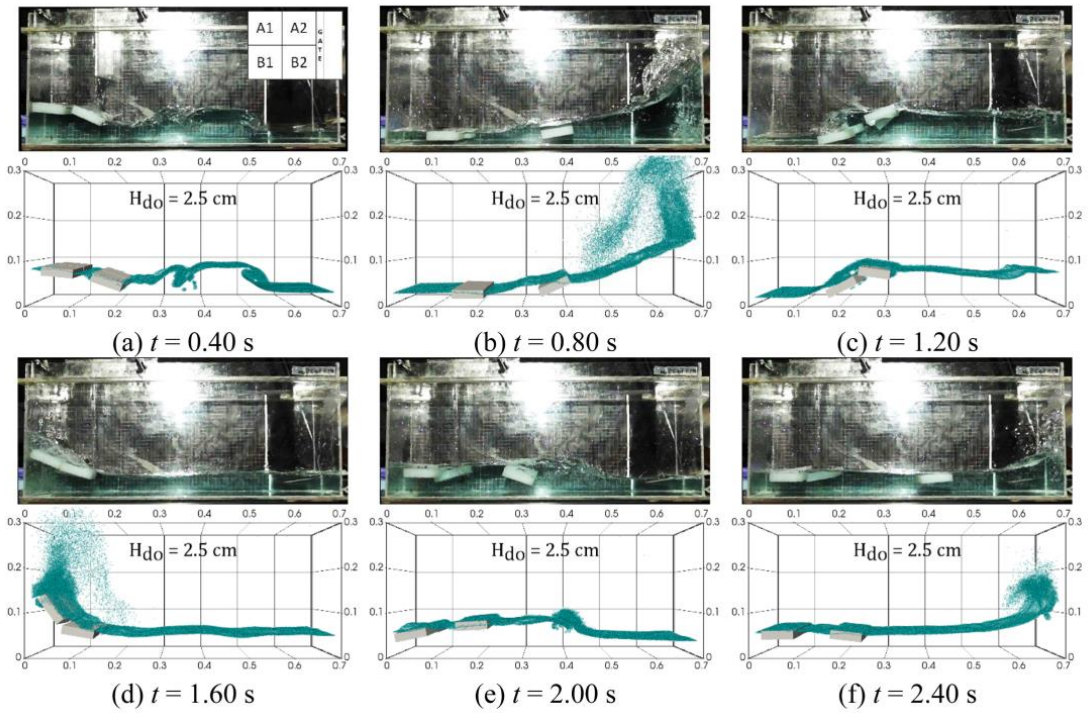

Fig. 9. Snapshots of the experimental and numerical dam breaking with 4 blocks and wet bed H_{do} = 2.5 cm at the instants t = 0.40, 0.80, 1.20, 1.60, 2.00, 2.40 s (front view).

$$\mathbf{F}^{L}_{t,kl} = k_{t,kl}\delta^{t}_{kl}\mathbf{t}_c + c_{t,kl}\dot{\delta}^{t}_{kl}\mathbf{t}_c \tag{22}$$

Here, μ_{kl} is the friction coefficient for the pair of particles k and l, δ^{t}_{kl} is the relative sliding, $\dot{\delta}^{t}_{kl}$ is the tangential relative velocity, $\mathbf{t}_c$ is the tangential contact vector, and $k_{t,kl} = 2/7k_{n,kl}\sqrt{l^0}$ and $c_{t,\,kl} = 2/7c_{n,\,kl}(l^0)^{1/4}$ (Hoomans, 2000) are the spring-damping coefficients. The superscripts C and L correspond to Coulomb and linear forces, respectively.

In the present work, when the neighbor particle l belongs to a forced (prescribed motion) or fixed solid, the friction coefficient μ_l of the neighbor particle l is adopted for μ_{kl}, otherwise μ_{kl} is obtained as the mean value:

$$\mu_{kl} = \left(\frac{\mu^{\theta}_{k} + \mu^{\theta}_{l}}{2}\right)^{\theta} \tag{23}$$

similar to the interaction viscosity between two particles given in Shakibaeinia and Jin (Shakibaeinia and Jin, 2012). In this work, we used the arithmetic mean for all simulations, i.e., $\theta = 1$.

The force with smaller absolute value is used as tangential force during the simulation, i.e.:

$$\mathbf{F}_{t,kl} = \begin{cases} \mathbf{F}^{C}_{t,kl} & \left\|\mathbf{F}^{C}_{t,kl}\right\| \le \left\|\mathbf{F}^{L}_{t,kl}\right\| \\ \mathbf{F}^{L}_{t,kl} & \left\|\mathbf{F}^{C}_{t,kl}\right\| > \left\|\mathbf{F}^{L}_{t,kl}\right\| \end{cases} \tag{24}$$

After calculating all contacts between the pairs of the closest particles belonging to different bodies, e.g., bodies p and q, the resultant contact forces for a rigid body p can be calculated by:

$$\mathbf{F}_{n,p} = \sum_{q\in NB}\left(\sum_{m\in NP}\left(\mathbf{F}_{n,kl}\right)_m\right), \quad \mathbf{F}_{t,p} = \sum_{q\in NB}\left(\sum_{m\in NP}\left(\mathbf{F}_{t,kl}\right)_m\right) \tag{25}$$

where NP is the number of pairs of the closest particles (m) belonging to the shell of the rigid bodies $q \in [1, NB]$, and NB is the number of bodies in contact with body p.

The torque that acts on the CM of the solid generated by the contact forces is evaluated as:

$$\mathbf{T}_{c,kl} = \left(\bar{\mathbf{r}}_{kl} - \mathbf{r}_{CM}\right) \times \left(\mathbf{F}_{n,kl} + \mathbf{F}_{t,kl}\right) \tag{26}$$

where $\bar{\mathbf{r}}_{kl} = (\mathbf{r}_k + \mathbf{r}_l)/2$ represents the average position vector of particle k and l and $\mathbf{r}_{CM}$ symbolizes the position vector of the CM. The average position $\bar{\mathbf{r}}_{kl}$ is used to ensure the conservation of angular moment. Accordingly, after calculating all torques due to contacts between particles, the contact torques for each rigid body p can be obtained by:

$$\mathbf{T}_{c,p} = \sum_{q\in NB}\left(\sum_{m\in NP}\left(\mathbf{T}_{c,kl}\right)_m\right) \tag{27}$$

A detailed description of the solid-solid collision model can be found in the previous work (Amaro Jr et al., 2019).

4.3. Boundary conditions

The rigid boundaries are modeled using three layers of particles. The particles that form the layer in contact with the fluid are denominated wall particles, of which the pressure is computed by solving PPE together with the fluid particles. The particles that form two other layers

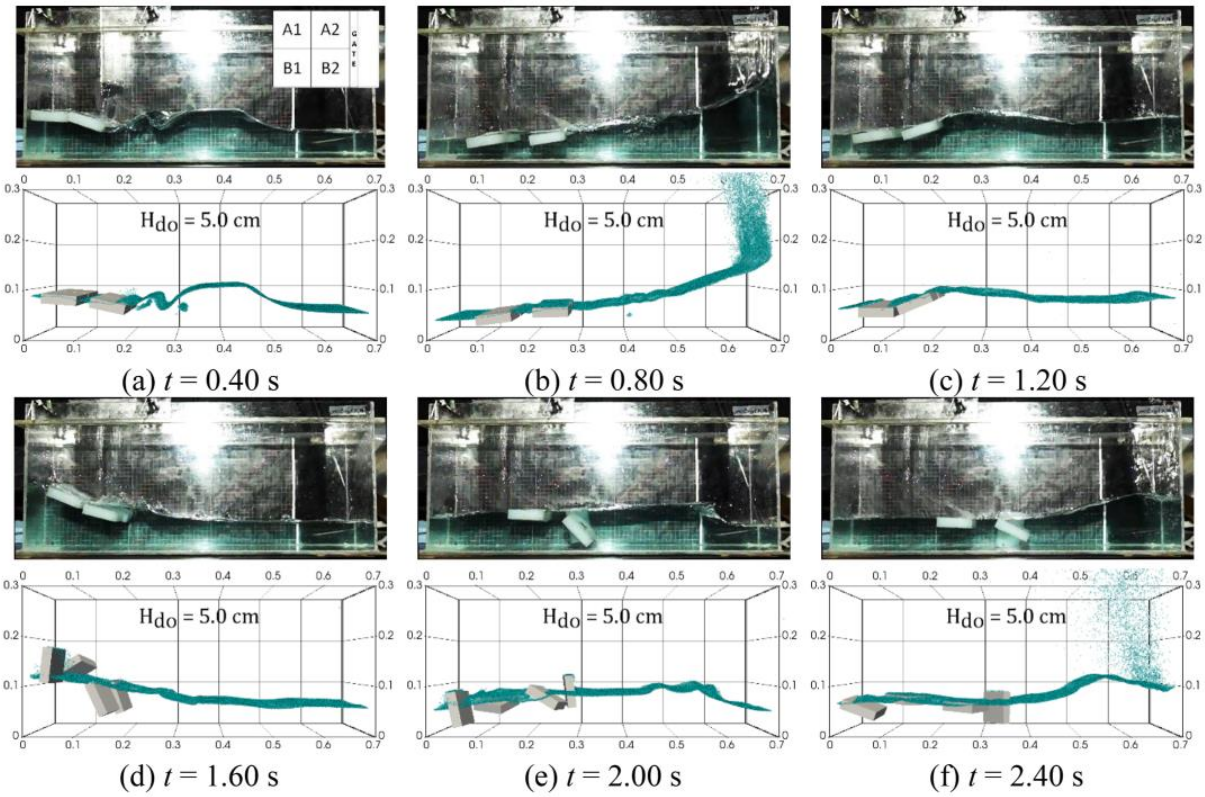

Fig. 10. Snapshots of the experimental and numerical dam breaking with 4 blocks and wet bed H_{do} = 5 cm at the instants t = 0.40, 0.80, 1.20, 1.60, 2.00, 2.40 s (front view).

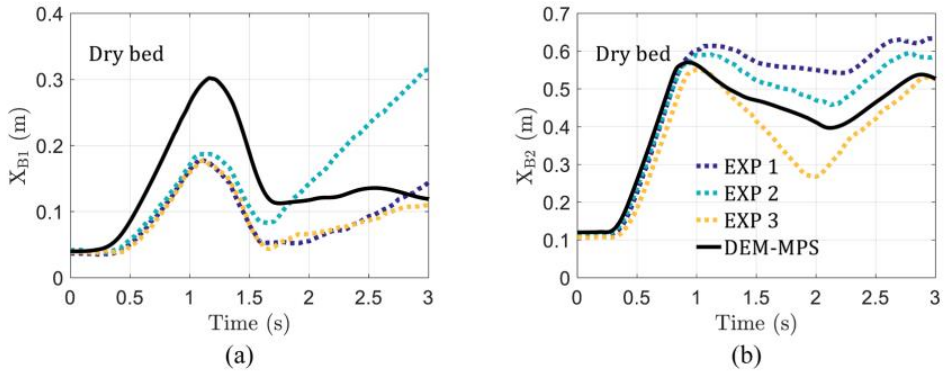

Fig. 11. Dam breaking with 4 blocks and dry bed. Experimental (dotted lines) and numerical (solid line) motions of the (a) block B1 and (b) block B2 along the longitudinal direction.

are called dummy particles in MPS (fixed walls and forced solids) and inner particles in DEM (free solids), which are used to assure the correct particle number density calculation of the wall particles. The pressure is not calculated in the dummy or internal particles. As a boundary condition of rigid walls, the null relative velocity between the fluid and the wall is imposed. The Dirichlet pressure boundary condition is imposed on the particles identified as free-surface ones and is considered during the implicit step of the method. In order to identify the free-surface particles, the neighborhood particles centroid deviation (NPCD) method (Tsukamoto et al., 2016) is adopted here. In the NCPD technique, a particle is defined as free-surface one, and its pressure is set to zero if:

$$\begin{cases} n_i < \beta \cdot n^0 \\ \sigma_i > \varrho \cdot l^0 \end{cases} \tag{28}$$

The deviation σ_i is written as:

$$\sigma_i = \frac{\sqrt{\left(\sum_{j\in\Omega_i}\omega_{ij}x_{ij}\right)^2 + \left(\sum_{j\in\Omega_i}\omega_{ij}y_{ij}\right)^2 + \left(\sum_{j\in\Omega_i}\omega_{ij}z_{ij}\right)^2}}{\sum_{j\in\Omega_i}\omega_{ij}} \tag{29}$$

where $x_{ij} = (x_j - x_i)$, $y_{ij} = (y_j - y_i)$ and $z_{ij} = (z_j - z_i)$

According to Koshizuka and Oka (Koshizuka and Oka, 1996), the constant β should be chosen between 0.80 and 0.99 and Tsukamoto et al. (Tsukamoto et al., 2016) suggests a ϱ higher than 0.2. The NPCD method improves the stability and accuracy of the pressure computation by eliminating spurious oscillations due to misdetection of free-surface particles.

4.4. DEM and MPS coupling

The resultant hydrodynamic force ($\mathbf{F}_h$) and torque ($\mathbf{T}_h$), see Eq. (3), acting on the rigid bodies are calculated by integrating the pressures (P_k), computed by solving the PPE (Eq. (14)), of DEM wall particles k belonging to a rigid body p:

$$\mathbf{F}_h = -\sum_{k\in\Omega_p} P_k \left(l^0\right)^{d-1} \mathbf{n}_k \tag{30}$$

$$\mathbf{T}_h = -\sum_{k\in\Omega_p} P_k \left(l^0\right)^{d-1} \mathbf{r}_{ck} \times \mathbf{n}_k \tag{31}$$

where $\mathbf{n}_k$ represents the normal vector of the wall at the wall particle k, $\mathbf{r}_{ck}$ denotes the position vector between the CM of the rigid body p and the particle k, and Ω_p is the domain with solid wall particles.

The time step of the fluid domain Δt_f should follow the Courant–Friedrichs–Lewy (CFL) condition (Courant et al., 1967):

$$\Delta t_f < \frac{l^0 C_r}{|u_{max}|}, 0 < C_r \leq 1 \tag{32}$$

where u_{max} denotes the maximum velocity and C_r represents the Courant number. Here we adopted the canonical solution of the analytical

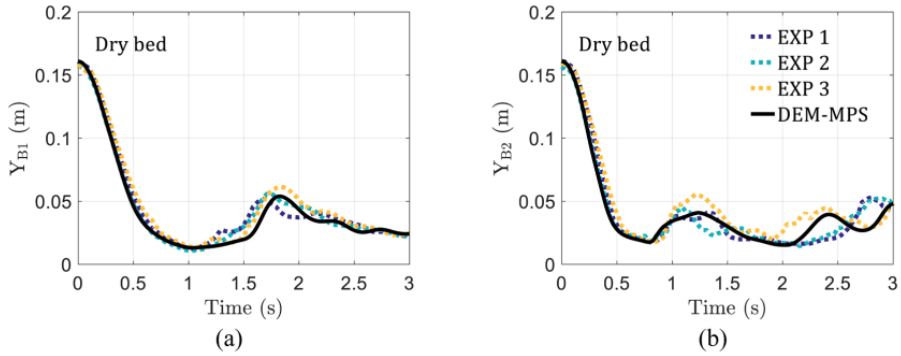

Fig. 12. Dam breaking with 4 blocks and dry bed. Experimental (dotted lines) and numerical (solid line) motions of the (a) block B1 and (b) block B2 along the vertical direction.

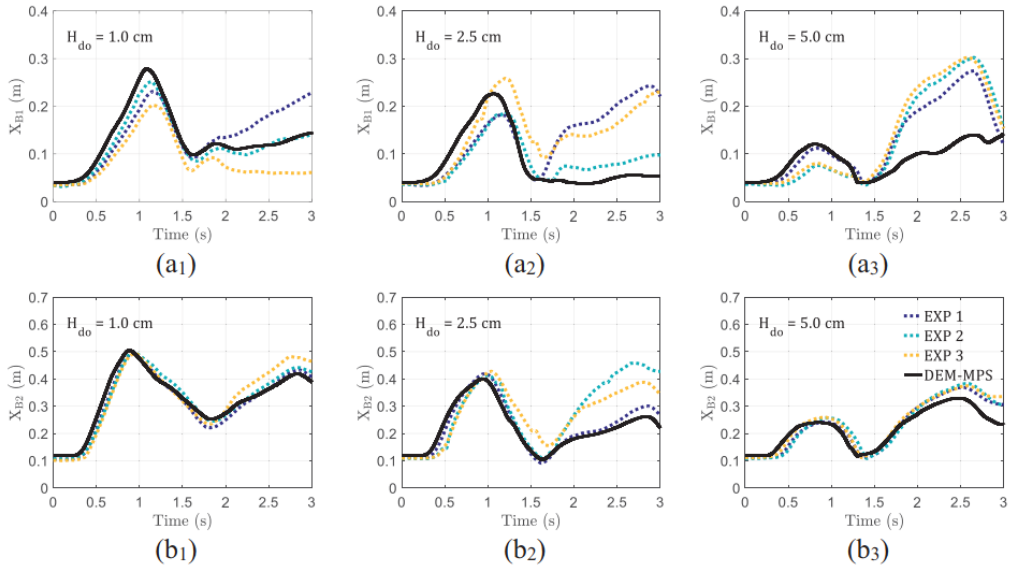

Fig. 13. Dam breaking with 4 blocks and wet beds: H_{do} = 1, 2.5 and 5 cm. Experimental (dotted lines) and numerical (solid line) motions of the (a_1, a_2, a_3) block B1 and (b_1, b_2, b_3) block B2 along the longitudinal direction.

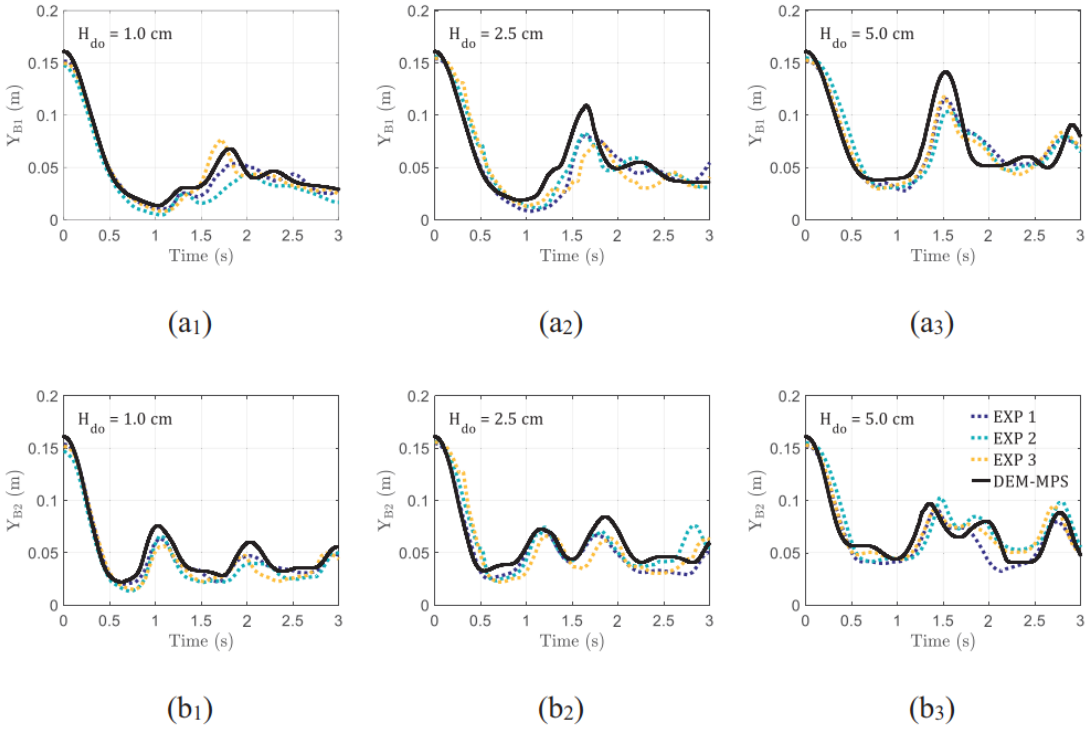

Fig. 14. Dam breaking with 4 blocks and wet beds: H_{do} = 1, 2.5 and 5 cm. Experimental (dotted lines) and numerical (solid line) motions of the (a_1, a_2, a_3) block B1 and (b_1, b_2, b_3) block B2 along the vertical direction.

formulation based on shallow water waves (Ritter, 1892) and assumes the maximum velocity of $|u_{max}| = 2\sqrt{gH_{up}}$. $C_r = 0.2$ is used for all simulations.

Since the transient response for the rigid body contact must be captured in a smaller time step, a dynamic sub-cycling algorithm for rigid bodies is adopted, improving the computational efficiency. Considering that at least one hundred time steps are used during the solid contact, and taken into account the duration t_c of a typical contact among rigid bodies, based on Hertz's contact theory (Johnson, 1985), an adaptive time step for the solid domain is adopted $\Delta t_s = N_{dt}\Delta t_f$, where N_{dt} denotes an integer, since that:

$$\Delta t_s \leq min\left(\frac{t_c}{100}\right) \leq min\left(\frac{2.87}{100}\left[\frac{m_{kl}^2}{l_{kl}^0 E_{kl}^2 \|\mathbf{u}_k - \mathbf{u}_l\|}\right]^{\frac{1}{5}}\right) \tag{33}$$

During one time step Δt_f, the hydrodynamic effects are assumed to be unchanged and the values of $\mathbf{F}_h$, $\mathbf{F}_g$ and $\mathbf{T}_h$ remain constant. The values are used in the governing equations of solid motion (Eqs. (3) and (4)) during the sub-cycling. On the other hand, contact forces and torques, $\mathbf{F}_c$ and $\mathbf{T}_c$, are computed and considered in Eqs. (3) and (4) at each iteration of the sub-cycling, and then the velocity and position of solid are updated.

In the absence of contact between rigid solids, $\Delta t_s = \Delta t_f$, the solid motion is update considering only the influence of $\mathbf{F}_h$, $\mathbf{F}_g$ and $\mathbf{T}_h$, and the DEM calculations are not carried out.

From the viewpoint of the fluid, the new positions of the DEM particles (wall and internal) are used as the boundary conditions of the MPS, completing the coupling between solid and fluid. A schematic diagram of the algorithm implemented is illustrated in Appendix B.

4.5. Computational performance

Particle-based methods suffer from the high computational cost associated with the large number of particles necessary to solve large-scale practical engineering problems. Parallel computing in shared memory systems using OpenMP® 3.0 (Dagum and Menon, 1998) was used to simulate the present cases in reasonable processing time. The numerical simulations with about 1.5 million particles (fluid and solid walls using $\sim 10^6$ particles and free rigid bodies, i.e., ice floes, using $\sim 10^3$ particles) for a physical time of 3.0 s took approximately 30 to 60 h with a central processing unit (CPU) Intel® Xeon® Processor E5 v2 Family, a processor base frequency of 2.80 GHz, 20 cores, and 126 GB of memory.

To overcome the high computational cost involving in the simulations of real-world relevant phenomena like ice jam formation and breakup, our next task will be to include the present DEM-MPS model in the 3D parallelized version of our MPS code based on the message passing interface (MPI) (Gropp et al., 1996) strategy and implemented by Fernandes et al. (Fernandes et al., 2015). By using a high-performance computing (HPC) technique, consisting of a combination of a nongeometric dynamic domain decomposition strategy based on particle renumbering and a distributed parallel sorting algorithm for the particle renumbering, the parallelized code enables hybrid parallel processing of hundreds of millions of particles within reasonable runtime in computer CPU clusters.

5. Results and discussion

In order to illustrate the ability of the proposed model to numerically reproduce the complex dynamic behavior of the ice-wave interaction

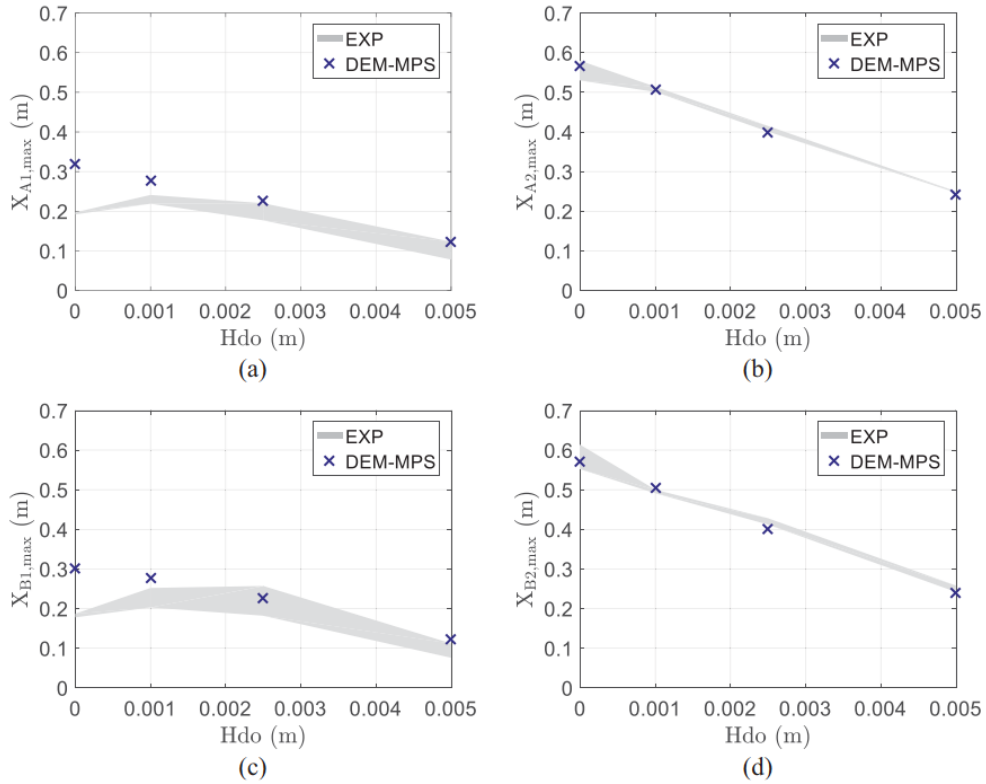

Fig. 15. Dam breaking with 4 blocks over dry and wet beds. Maximum longitudinal displacement of blocks (a) A1, (b) A2, (c) B1 and (d) B2. Experimental and numerical results between the instants $t = 0$ and $t = 1.5$ s.

phenomenon, it was applied to solid-fluid dam-break flow over dry and wet beds, previously detailed in Section 2. For all simulations, we adopted the gravity acceleration $g = 9.81$ m/s^2. According to the experimental results shown in Fig. 4, the constant vertical velocity of $v_g = 0.4$ m/s was assigned to the gate. The physical properties of the fluid and solids are summarized in Table 2 and Table 3, respectively, and simulation parameters are presented in Table 4. Based on experience of the authors and others, some numerical parameters that can provide reliable predictions were adopted, as illustrated in Table 4. The reader interested in the calibration process of such parameters is invited to refer to Koshizuka and Oka (1996) and Duan et al. (2019) for effective radius r_e, Tsukamoto et al. (2016) for surface thresholds β and ϱ, Lee et al. (2011) for the collision distance α_1 and coefficient of restitution α_2, and Tsukamoto et al. (2020) for the relaxation coefficient γ. Adequate damping should be high enough to obtain a non-oscillatory motion of the rigid solids while not too high so that too much energy is dissipated during the collision. Following Amaro Jr et al. (2019), the damping ratio of the collision $\xi_n = 0.05$ provided a good compromise between static response and low energy dissipation for a complex problem of dam break with multiple blocks and was also adopted herein.

5.1. Dam breaking with 4 blocks

The free-surface profile evolution of the present numerical model and experimental results are compared for the cases with 4 blocks in dry (Figs. 6(a_1)-(a_3)) and wet beds with $H_{do} = 1.0$ (Figs. 6(b_1)-(b_3)), 2.5 (Figs. 6(c_1)-(c_3)), and 5.0 (Figs. 6(d_1)-(d_3)) cm. It is worth mentioning that the experimental results are from the front camera and exclude the splash. In this sense, splashed fluid particles are omitted in the numerical results. Also, for a cleaner visualization, the blocks are omitted. At the instant $t = 0.41$ s, the wavefront travels smoothly along the dry bed and hits the downstream wall (Fig. 6(a_1)). However, the behavior of the flow changes remarkably with the presence of the initial downstream fluid layer. As shown in Fig. 6(b_1), (c_1), and (d_1), the downstream fluid remains unaffected by the wave and, consequently, a mushroom-like jet is formed as previously reported by Stansby et al. (1998) and Jánosi et al. (2004). For instance, for $H_{do} = 2.5$ and 5.0 cm a collapse breaker occurs. As the dam-break flow proceeds, at $t = 0.83$ s, a backward wave is generated for the cases of dry bed (Fig. 6(a_2)) and fluid layer of 1 cm depth (Fig. 6(b_2)). At the same time, the wave barely impacts the downstream wall for the downstream fluid depth of 2.5 cm (Fig. 6(c_2)) and the fluid run-up on the downstream wall occurs for the depth of 5 cm (Fig. 6(d_2)). Afterwards, at $t = 1.50$ s, the wave moves downstream after it hits the upstream wall for the dry bed case (Fig. 6(a_3)), the wave impacts the upstream wall and a portion of the flow forms a vertical run-up jet for $H_{do} = 1$ and 2.5 cm (Figs. 6(b_2) and (c_2)), and the wave propagates upstream for the fluid layer of 5 cm (Fig. 6). Moreover, during the progress of the fluid flow, the sequence of events such as wavefront progress, wave impact, and run-up is delayed as the downstream fluid layer increases.

Comparing the free-surface profile between the numerical and the experimental results shows that the present numerical model has successfully reproduced the dam-break flow behavior for all downstream fluid depths. However, Figs. 6(c_1) and (d_1) show small deviations between experimental and numerical wave events computed by the present model. Such discrepancy can be seen in other particle-based simulations (Crespo et al., 2008; Farzin et al., 2019; Soleimani and Ketabdari, 2020; Ye et al., 2020). As stated in Duan et al. (2019),

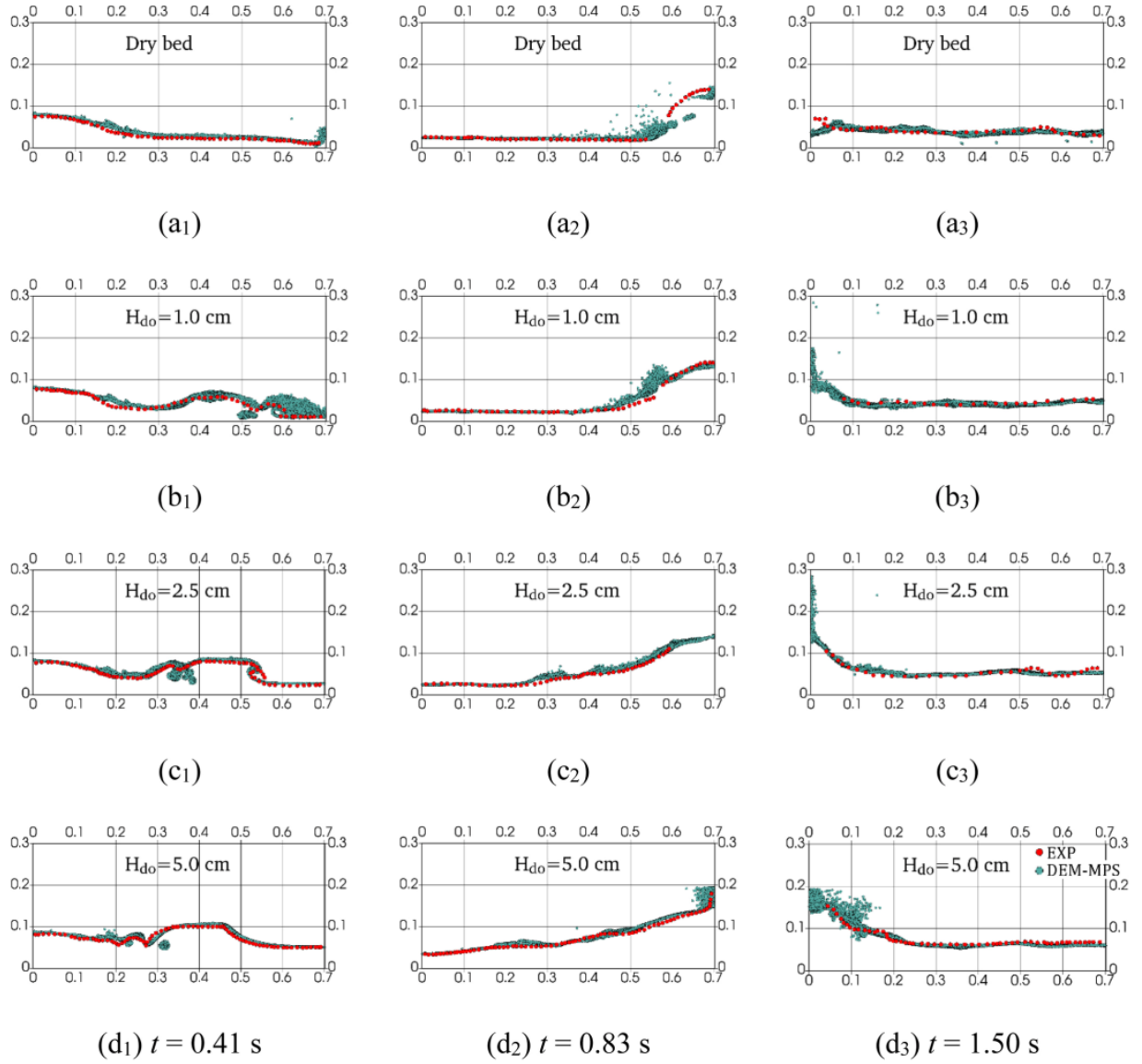

Fig. 16. Evolution of the experimental (red dots) and numerical (turquoise dots) wave profiles for dam breaking with 9 blocks at the instants $t = 0.41$, 0.83, 1.50 s (from left to right). (a_1, a_2, a_3) Dry bed and wet beds H_{do} = (b_1, b_2, b_3) 1, (c_1, c_2, c_3) 2.5 and (d_1, d_2, d_3) 5.0 cm. Experimental and numerical results are from the front camera and exclude the splash.

stabilization adjustments usually adopted by particle-based methods inevitably bring some numerical dissipation. Here, the first-order pressure gradient, see Eq. (18), used to prevent numerical instability, has a particle stabilizing term (PST), i.e., an adjustment technique represented by the adoption of the minimum pressure $\widehat{P}_i$. Therefore, this numerical dissipation associated with variations in the gate removal process might be possible reasons for such discrepancy.

The snapshots of the dam breaking with 4 blocks from the experiments and simulations are presented in Figs. 7-10 (see also Video 1). The top view of the initial position of the 4 blocks is highlighted at the top left. Delaunay triangulation filter of the open-source Paraview (Ahrens et al., 2005) is used to represent the blocks as a mesh of triangle polygons. The dry bed case is shown in Fig. 7. After the gate is released, the blocks are transported downstream. The experimental and numerical results show similar behaviors of blocks, nevertheless, the computed evolution of blocks A1 and B1 are slightly faster than those measured in the experiments until $t = 0.8$ s. After that, a backward wave transports the blocks back upstream until the instant $t = 1.6$ s. The experimentally measured and numerically computed positions of the A2 block are in good agreement, but the remaining blocks' positions show some differences. Such discrepancies are expected considering the challenge of spacing evenly the blocks initially and the chaotic features of the phenomena through time, such as breaking waves, wave-splash, and plunging jet. The blocks are transported downstream after $t = 2.0$ s, and the flow starts to calm down. As we will show later, chaotic flow features after the wave hits the downstream wall may not be completely reproduced in experimental repetitions.

The dam breaking with the 1 cm depth fluid layer is depicted in Fig. 8. During the first 2.4 s, where the blocks were transported by the

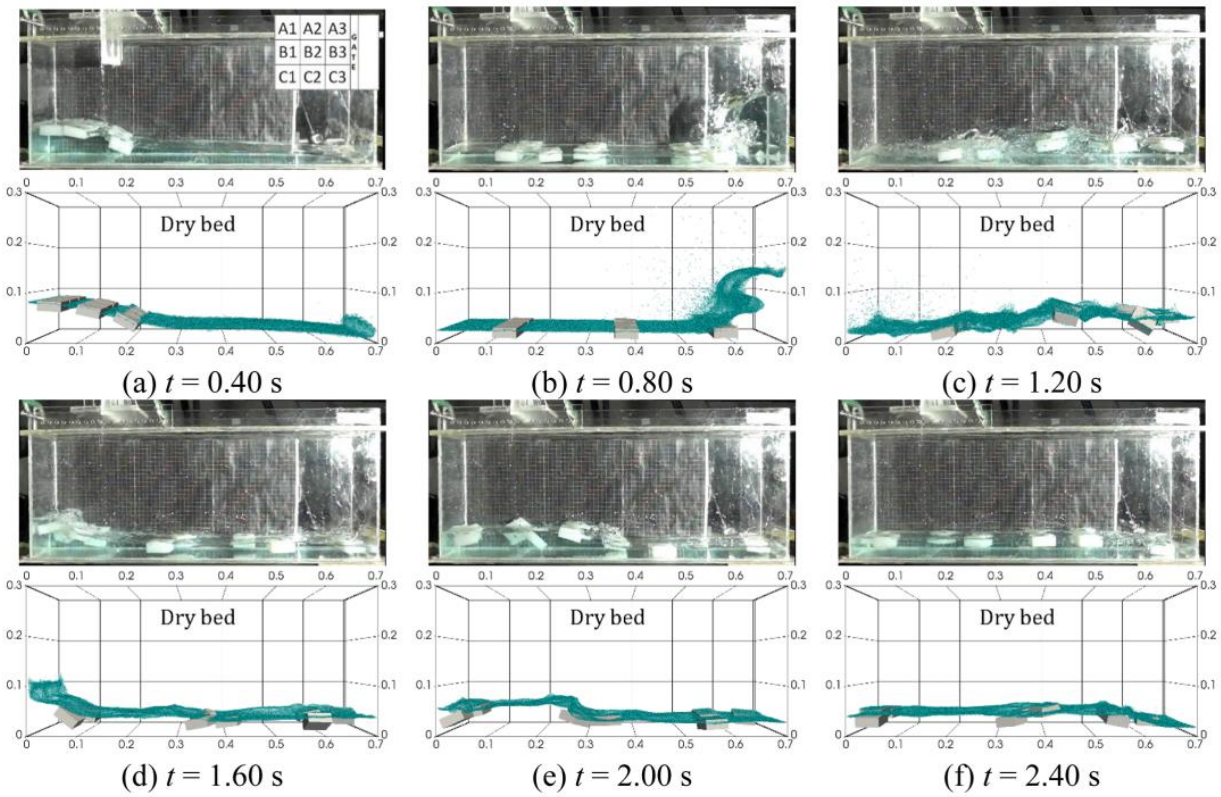

Fig. 17. Snapshots of the experimental and numerical dam breaking with 9 blocks and dry bed at the instants $t = 0.40$, 0.80, 1.20, 1.60, 2.00, 2.40 s (front view).

fluid, very good agreement was obtained between experimental and numerical solid positions.

In Fig. 9, experimental and numerical solid positions for the fluid layer of 2.5 cm present a good agreement until $t = 1.6$ s. Nevertheless, after $t = 2.0$ s, the blocks A2 and B2 are transported downstream in the experiment while very slow motions are numerically computed.

Finally, the dam breaking with the 5 cm depth fluid layer is illustrated in Fig. 10. A good agreement between experimental and numerical solid motions can be seen until the instant $t = 1.2$ s. After $t = 1.2$ s, where the blocks move upstream and collisions among the blocks occur, the computed positions of the blocks A1 and B1 remain close to the upstream wall of the tank in the numerical results while these blocks are carried by the flow in the experimental results. In summary, numerical and experimental solid motions show qualitatively identical features.

The longitudinal and vertical motions of each block have been plotted to quantify the comparisons. Fig. 11(a) and (b) show the experimental and numerical longitudinal motions X_{B1} and X_{B2} of blocks B1 and B2, respectively, for the dry bed case during the first 3 s after the gate removal. Here the three experimental repeats have been named EXP 1, EXP 2, and EXP 3. As Fig. 11(a) shows, the initial trajectory of block B1 obtained numerically follows the tendency of the experimental one, but eventually, the block is transported downstream faster numerically than experimentally. While the maximum distance reached by the block B1 at $t = 1.5$ s is about 0.18 m in the experiments, it was overestimated at a distance of 0.3 m in the numerical simulation. The main reason for this discrepancy might be the difficulty in setting the initial arrangement of the blocks in regular and equally spaced positions, which might lead to values different from those numerically computed. In addition to this, the variations in the gate removal process might also influence the motions. After $t = 1.5$ s, block B1 is carried by the reflected wavefront, and larger discrepancies between the numerical and experimental results occur. These discrepancies, which also occur between the experimental runs, are reasonable due to the chaotic nature at this stage, because of an intense splash with air-water mixture created by the fall of the vertical run-up jet onto the underlying fluid. In fact, the breaking processes (e.g., wave-splash, plunging jet penetration depth, and breaking wave) exhibit chaotic behaviors, as previously revealed by the extensive investigation of laboratory observations and numerical simulations in Wei et al. (2018). On the other hand, the longitudinal motions of the block B2 (Fig. 11(b)) are correctly reproduced by the numerical simulations until $t = 1.0$ s. After that, the computed motion presents the same tendency as the experimental ones.

As shown in Fig. 12, the measured vertical motions Y_{B1} and Y_{B2} of blocks B1 and B2, respectively, were accurately predicted by the numerical simulations, indicating that the buoyancy force is well reproduced by the numerical model.

Fig. 13 shows the experimental and numerical longitudinal motions X_{B1} and X_{B2} of blocks B1 and B2, respectively, in dam-break flows with downstream depths of $H_{do} = 1$, 2.5, and 5 cm. For the depth of $H_{do} = 1$ cm (Fig. 13(a_1)), the block B1 is transported downstream by the wave front, reaching a maximum distance between 0.20 and 0.26 m at around $t = 1.2$ s in the experiments, whereas in the numerical simulation block B1 moves slightly faster and reaches the maximum distance of 0.28 m at around $t = 1.1$ s. Subsequently, the block B1's experimental and numerical motions are in good agreement. After $t = 1.5$ s, chaotic features similar to the dry bed case occur due to the violent hydrodynamic impact followed by the wave breaking, and the computed motion matches the measured motions from the second experimental run only. As shown in Fig. 13(b_1), the measured motions of block B2 are very well predicted by the numerical model. For the depth of $H_{do} = 2.5$ cm (Fig. 13 (a_2)), a maximum distance between 0.18 and 0.26 m at around $t = 1.25$ s is reached by block B1 in the experiments, whereas block B1 moves

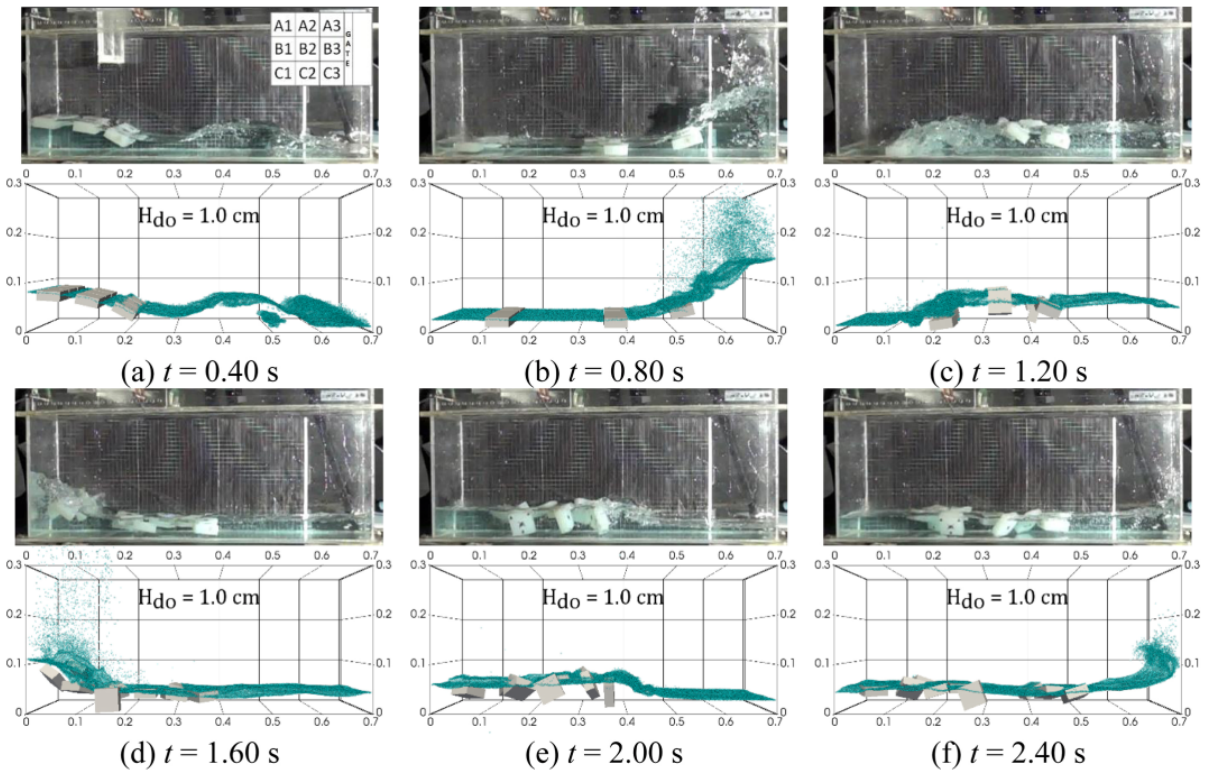

Fig. 18. Snapshots of the experimental and numerical dam breaking with 9 blocks and wet bed H_{do} = 1 cm at the instants t = 0.40, 0.80, 1.20, 1.60, 2.00, 2.40 s (front view).

slightly faster in the numerical simulation, reaching a maximum distance of 0.23 m at around t = 1.1 s. During the upstream return of block B1, the computed motion is in reasonable agreement with the experimental ones. Again, due to the chaotic features of the breaking wave process after t = 1.5 s, the experimental motions present distinct patterns between them, while a slower motion was numerically obtained, and the block remains almost in the same position. The measured and computed motions of block B2 are in very good agreement until t = 1.0 s, but, subsequently, the computed motion matches well the results from the first experiment while underestimating the results from the second and third experiments (Fig. 13(b_2)). Finally, for the higher bed depth H_{do} = 5 cm (Fig. 13(a_3)), the block B1's maximum displacements measured experimentally vary between 0.08 and 0.11 m while the computed maximum distance reaches 0.12 m, both occurring at around t = 0.8 s. When the block B1 moves back upstream, the computed motion is in reasonable agreement with the first experimental results. After t = 1.5 s, significant discrepancies between numerical and experimental motions of block B1 were obtained. The numerical and experimental results prior to t = 1.5 s show that the reflected wave transported the blocks A2 and B2 toward the blocks A1 and B1, which collide against the upstream wall. Afterwards, the block B1 was submerged into water and was transported by the wave. Nevertheless, in the experimental runs, the motion of block B1 is more affected by the thrust generated by the wave than in the numerical simulation. A good agreement is obtained between experimental and numerical motions for the block B2, despite the underestimation of the block's displacement in the numerical simulation after t = 1.9 s, as shown in Fig. 13(b_3).

The vertical motions Y_{B1} and Y_{B2} of blocks B1 and B2, respectively, are provided in Fig. 14(a_1)-(a_3) and (b_1)-(b_3). Although some minor discrepancies are observed, the trends of the computed vertical motions of both blocks agree well with the experimental ones.

The maximum longitudinal displacements $X_{A1,max}$, $X_{A2,max}$, $X_{B1,max}$ and $X_{B2,max}$ reached by the blocks A1, A2, B1, and B2, respectively, from the instant t = 0 to t = 1.5 s are illustrated in Fig. 15. Since the initial potential energy decreases with the increase of initial fluid depth in the bed (H_{do}) and the initial energy dissipation is higher for wet beds due to the plunging or collapse wave breaking caused by the hydraulic jump, it is expected that the increase of H_{do} will lead to a decrease of the wave front speed and, as a consequence, a decrease on the maximum distance reached by the blocks during the dam-break phase. However, the results provided by the experiments do not match exactly this behavior, and some variations can be observed between H_{do} = 0 and 1 cm for the blocks A1 and B1, initially placed closer to the upstream tank wall, as shown in Figs. 15(a) and (c). On the other hand, the numerical results for these blocks presented the anticipated behavior. The experimental and numerical results for the blocks A2 and B2 are in very good agreement with the expected behavior.

5.2. Dam breaking with 9 blocks

The free-surface profiles of the present model and experimental runs for the cases with 9 blocks in dry and wet beds are compared in Fig. 16. Again, the splash is not presented for the wave profiles, and the blocks are omitted. At the early stage, t = 0.41 s, the formation of the mushroom-like jet occurs when a downstream fluid layer is present (Fig. 16(b_1), (c_1) and (d_1)). Furthermore, as previously discussed for the cases with 4 blocks (see Fig. 6), at the instants t = 0.83 s and t = 1.50 s, the increase of the downstream fluid layer leads to slower wave propagation. In other words, the sequence of events such as wave impact and run-up happens later with the increase of the downstream depth. In

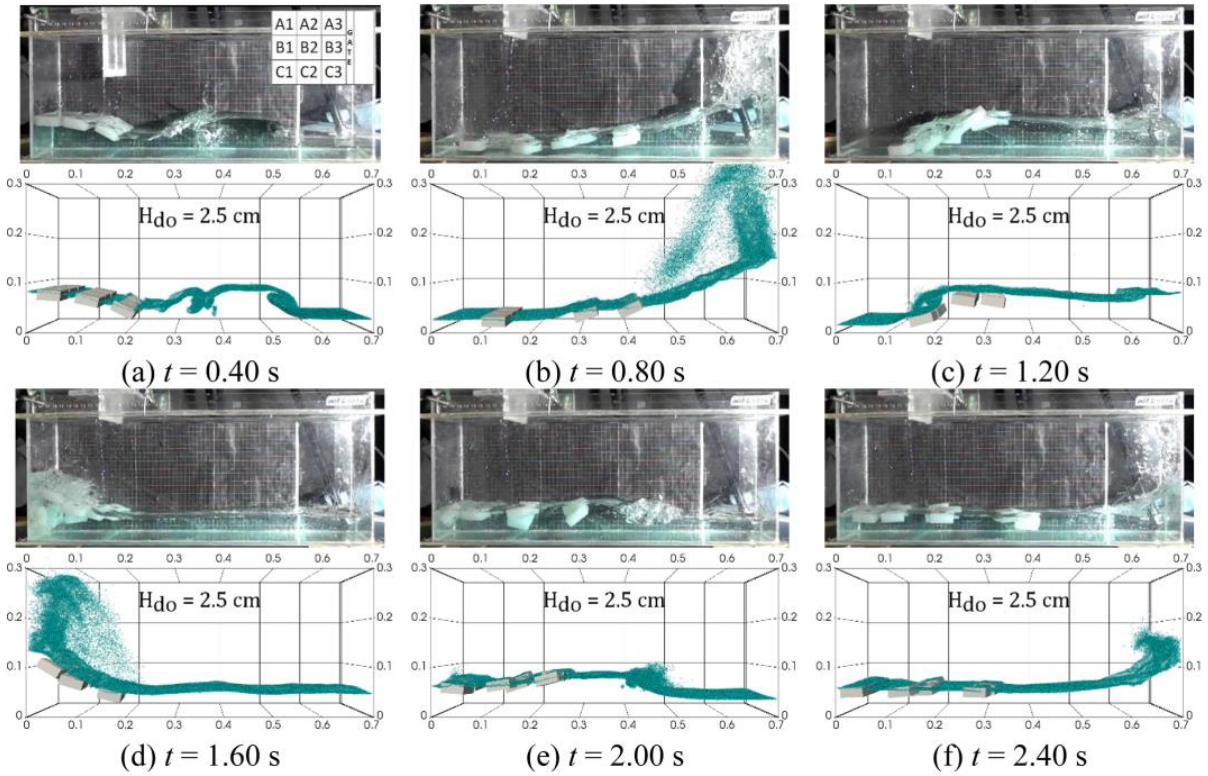

Fig. 19. Snapshots of the experimental and numerical dam breaking with 9 blocks and wet bed H_{do} = 2.5 cm at the instants t = 0.40, 0.80, 1.20, 1.60, 2.00, 2.40 s (front view).

general, as in the previous cases with 4 blocks, there is a satisfactory agreement between numerical and experimental free-surface profiles. By comparing the wave profiles of the 9 block case (Fig. 16) with those of the 4 block case (Fig. 6), the differences, despite being relatively small, are more evident in the later stage of the hydrodynamic process. Thus, the presence of the light-weight blocks is almost negligible in the initial gravity dominant dam-break event. However, the fluid-solid interaction is not negligible in the late hydrodynamic impact and wave breaking events. A detailed discussion about the effect of ice floes on the flow is presented in Appendix.

Figs. 17-20 (also see Video 2) show a sequence of frames of the dam breaking with 9 blocks from the experimental repeats and numerical simulations. The top view of the 9 blocks is highlighted at the top left. Fig. 17 shows a reasonable agreement between experimental and numerical block motions until t = 1.2 s. Afterwards, the merging of the collapsed upward water flow and reflected wave dramatically disturbs the water surface and, as a result, a more chaotic motion of the solids is generated, especially for the solids downstream. Consequently, the computed solid positions deviate from the experimental ones after t = 1.6 s. For the dam breaking scenario with H_{do} = 1 cm, experimental solid motions are well predicted by the numerical simulations until t = 1.2 s (Fig. 18). At the instant t = 1.6 s, the solid motions are disturbed by the combination of a reflected wave and the collapsed water flow. As a result, the computed solid motions deviate from the experimental ones, although the present model reproduced the main features of the solid trajectories. Figs. 19 and 20 depict the dam breaking with a fluid layer of 2.5 and 5 cm depth, respectively. The numerical predictions of the solid motions are in good agreement with the experimental ones through all of the 2.4 s considered in the analyses, although they do not match exactly. In general, the results indicated that the present model is able to predict the solid motions with satisfactory details.

Fig. 21 provides the experimental and numerical longitudinal motions X_{C1}, X_{C2}, and X_{C3} of blocks C1, C2, and C3, respectively. The large variability of the maximum displacement in the dam-break phase reached by block C1 in the experiments, ranging from 0.08 to 0.22 m, indicates that its motion is significantly affected by any initial experimental disturbance (Fig. 21(a)). Besides, the numerical motion agrees well with the third experiment but overestimates the results from the first and second experiments until t = 1.7 s, approximately. Subsequently, while in the experiments the block C1 hits the wall, collides with others, and is transported downstream, in the numerical simulations, the block only hits the wall and is transported downstream very slowly, almost remaining in the same position. In addition, as in the previous cases with 4 blocks, the fluid flow becomes chaotic at this stage, and the solid motions are influenced by many factors such as wave breakings and multiple solid collisions. According to the experimental results, the block C2 is transported downstream, reaching the maximum longitudinal motions between 0.33 and 0.43 at around t = 1.2 s, and then moves upstream until t = 1.8 s, approximately (Fig. 21(b)). After that, distinct patterns were obtained from the experimental repeats, and the computed motion presents a tendency similar to the first experiment. Fig. 21(c) shows that during the first 0.9 s, the numerical motions of block C3 match well the experimental motions from EXP 1 and EXP 3, but overestimate EXP 2. Subsequently, the computed motion is closer to the results from EXP 1 and EXP 3.

Fig. 22 compares the experimental and numerical vertical motions Y_{C1}, Y_{C2}, and Y_{C3} of blocks C1, C2, and C3, respectively. The overall trends of the computed vertical motions agree well with the experimental ones. However, as discussed in the previous section for 4 blocks, some local discrepancies are also present.

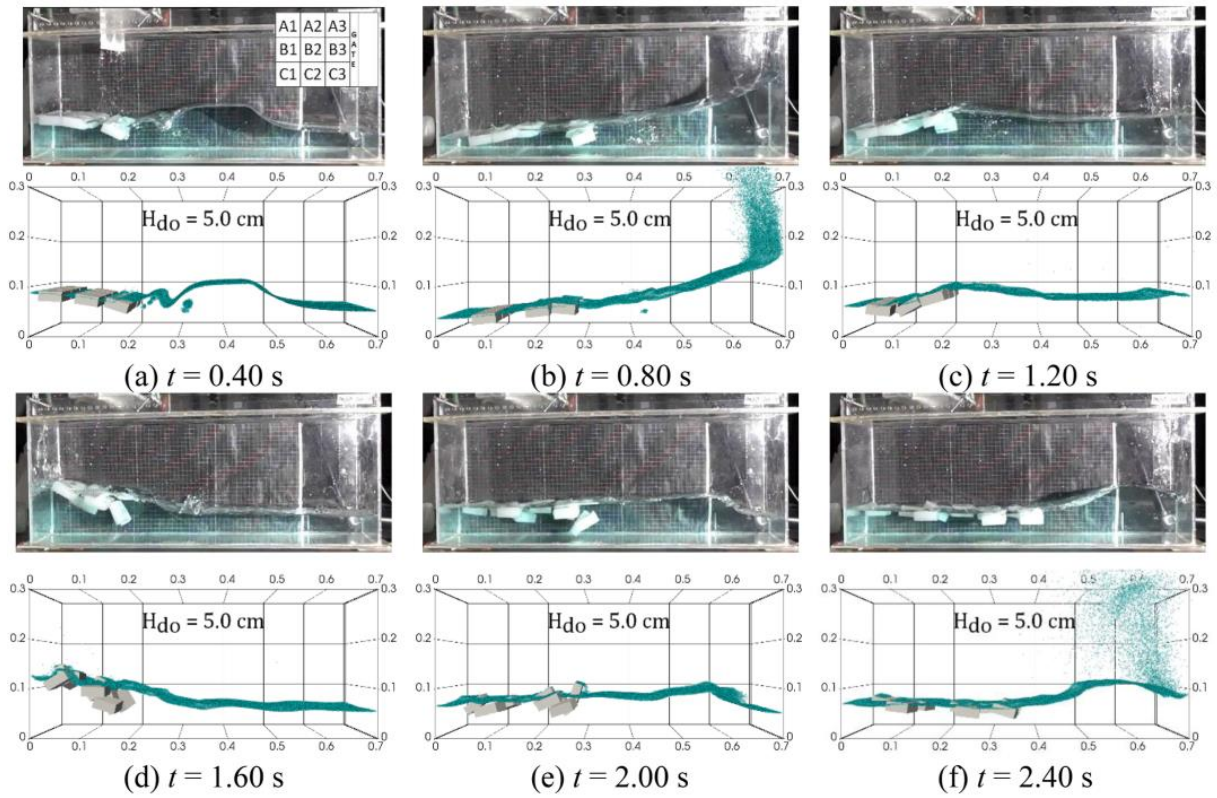

Fig. 20. Snapshots of the experimental and numerical dam breaking with 9 blocks and wet bed H_{do} = 5 cm at the instants t = 0.40, 0.80, 1.20, 1.60, 2.00, 2.40 s (front view).

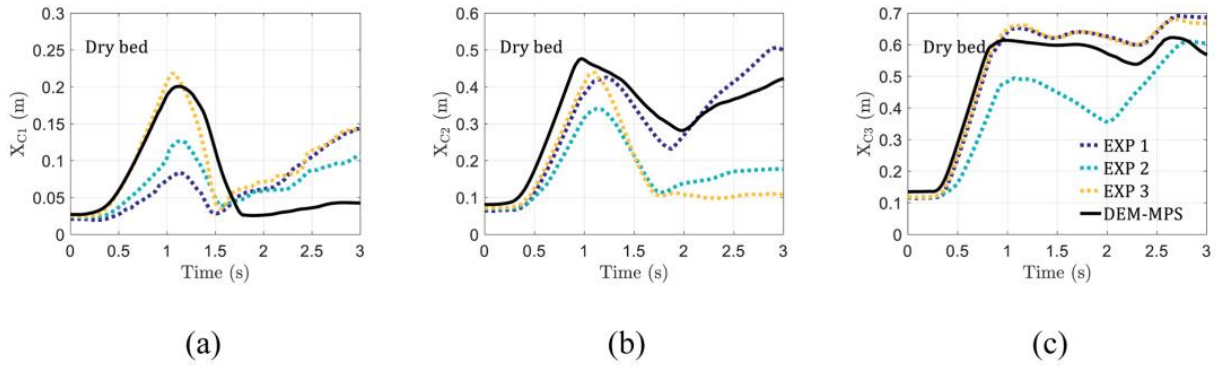

Fig. 21. Dam breaking with 9 blocks and dry bed. Experimental (dotted lines) and numerical (solid line) motions of the (a) block C1, (b) block C2 and (c) block C3 along the longitudinal direction.

In Fig. 23, the computed longitudinal motions X_{C1}, X_{C2}, and X_{C3} of blocks C1, C2, and C3, respectively, are compared against the experimental ones, considering the three downstream depths of H_{do} = 1, 2.5, and 5 cm. As in the previous cases with the dry bed, the experiments present a noticeable variation of the initial maximum distances reached by the block C1 for H_{do} = 1.0 and 2.5 cm (Fig. 23(a_1) and (a_2)). Besides, the computed motions for these two depths agree well with the experimental ones, although, for H_{do} = 1 cm, the block C1 moves faster and reaches a maximum distance of about 0.22 m, higher than the maximum distance around 0.18 m measured in the experiments. For H_{do} = 5 cm, the motion of block C1 is well reproduced by the numerical simulations during the first 1.5 s, and after, it matches only the third experiment but underestimates the values from the first and second ones (Fig. 23(a_3)).

A good agreement between numerical and experimental motions of block C2 for H_{do} = 1 and 2.5 cm during all intervals of 3 s is shown in Fig. 23(b_1) and (b_2). Furthermore, the computed motion is overestimated for H_{do} = 5 cm during the first 1.3 s, approximately, followed by a better agreement between t = 1.3 s and t = 3.0 s (Fig. 23(b_3)).

For all downstream depths, the motions of block C3 are well reproduced by the numerical simulations (Fig. 23(c_1)-(c_3)).

Fig. 24 shows the experimental and numerical vertical motions Y_{C1}, Y_{C2}, and Y_{C3} of blocks C1, C2, and C3, respectively. When compared

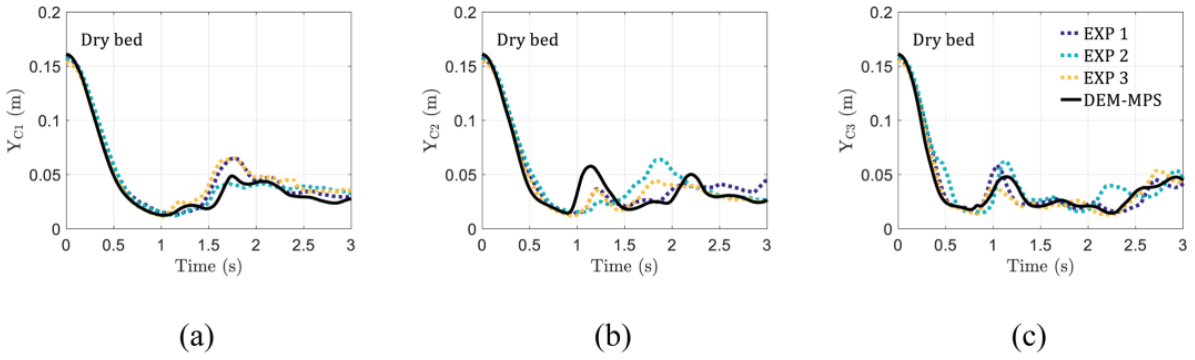

Fig. 22. Dam breaking with 9 blocks and dry bed. Experimental (dotted lines) and numerical (solid line) motions of the (a) block C1, (b) block C2 and (c) block C3 along the vertical direction.

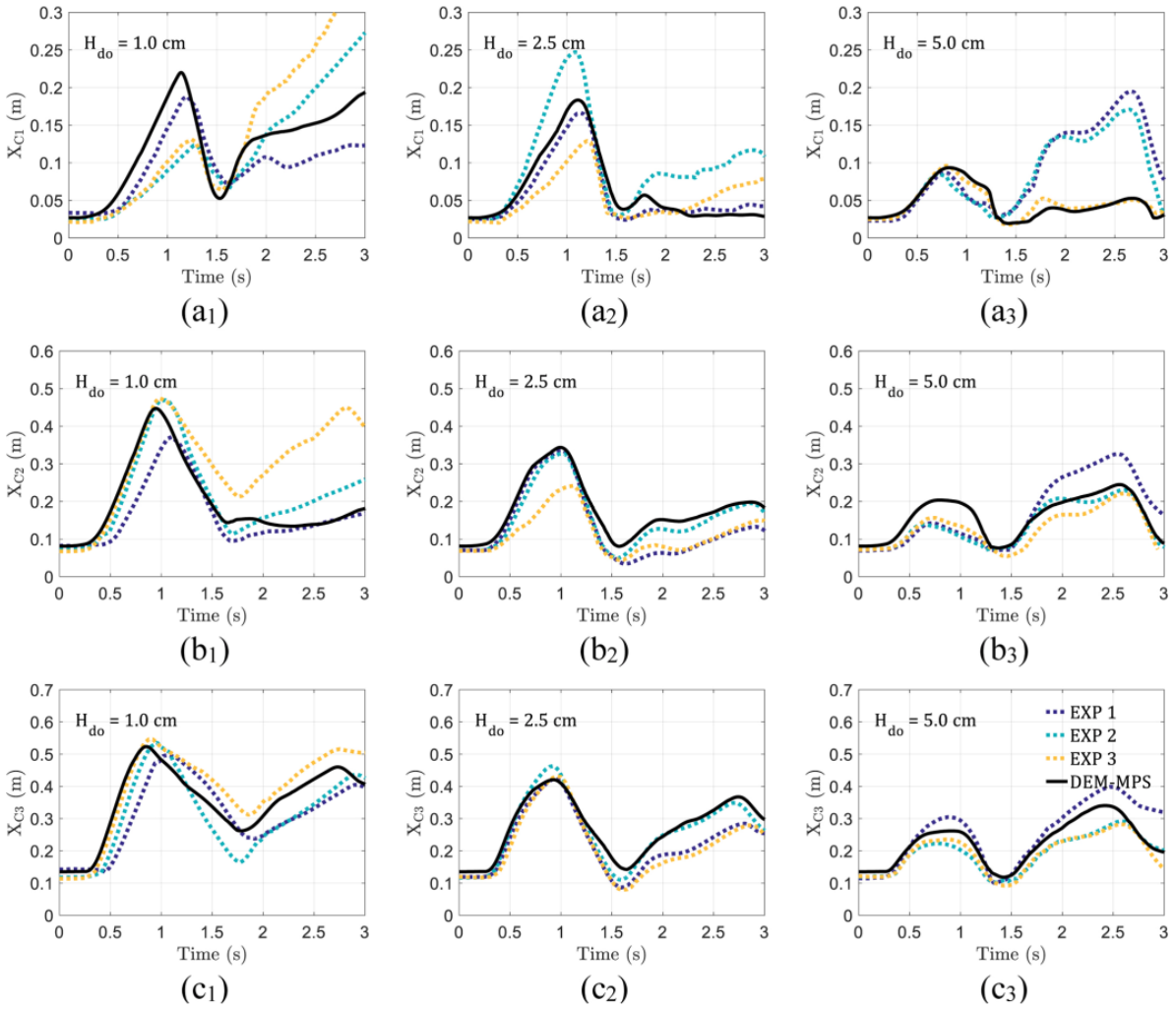

Fig. 23. Dam breaking with 9 blocks and wet beds: H_{do} = 1, 2.5, and 5 cm. Experimental (dotted lines) and numerical (solid line) motions of the (a_1, a_2, a_3) block C1, (b_1, b_2, b_3) block C2 and (c_1, c_2, c_3) block C3 along the longitudinal direction.

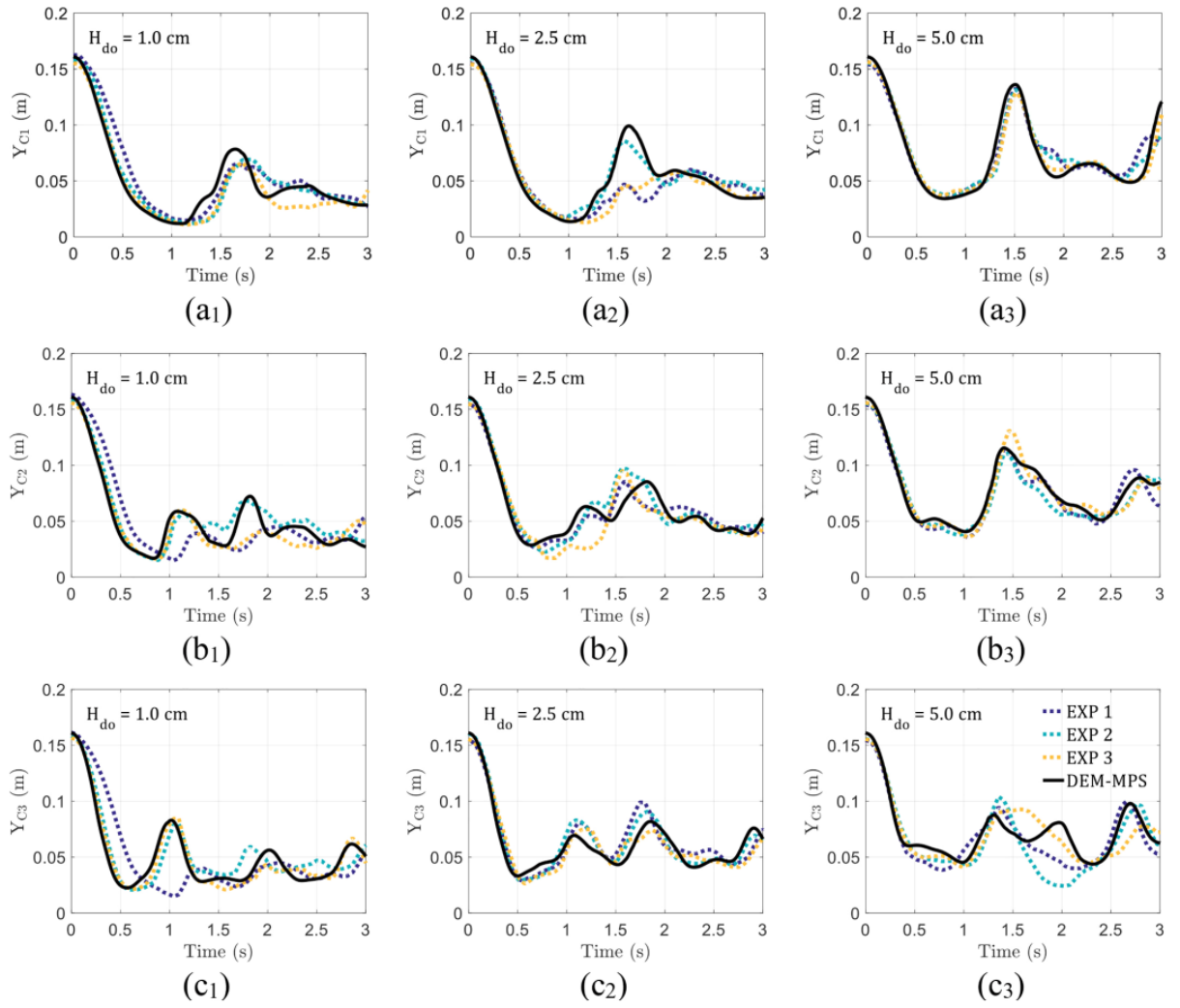

Fig. 24. Dam breaking with 9 blocks and wet beds: H_{do} = 1, 2.5 and 5 cm. Experimental (dotted lines) and numerical (solid line) motions of the (a_1, a_2, a_3) block C1, (b_1, b_2, b_3) block C2 and (c_1, c_2, c_3) block C3 along the vertical direction.

with experimental motions, all computed motions present some local discrepancies, but overall features of the experimental vertical motions are very well reproduced by the numerical model.

The overall good agreement between experimental and computed motions demonstrates that the proposed model is able to reproduce the main behaviors of the complex fluid-solid interaction phenomenon, suggesting that it can be extended for the simulation of real-scale ice-wave interaction problems, such as ice-jam formation and breakup and ice-structure interaction.

6. Concluding remarks

A 3D fully Lagrangian numerical model, based on a hybrid DEM-MPS technique, for modeling the complex dynamics of ice-wave interaction was developed and evaluated in the present work. A set of benchmark dam-break experiments with floating block floes over dry and wet beds, which representing a simplified form of a jam release, were designed and conducted. The experiments provided quality data for the numerical validation and investigation of the dynamic behavior of ice floes and complex hydrodynamics.

Both the obtained experimental and numerical results show that the increase of initial downstream fluid level leads to a decrease of the wave front speed and the generation of the mushroom-like jet. These features are consistent with previous works (Stansby et al., 1998; Jánosi et al., 2004). In most cases, the maximum distances reached by the blocks during the dam-break phase are smaller when the downstream fluid layer is higher. However, this behavior is not observed for the experimental results of the A1 and B1 blocks (i.e. the further upstream blocks) in the dam-break phase with 4 blocks over the dry and wet bed of 1 cm fluid layer. The main reason for this discrepancy could be the difficulty in spacing equally and regularly the blocks apart.

The agreements between the experimental and numerical wave profiles as well as the positions of the blocks are quite satisfactory, thus, showing the effectiveness of the present approach to reproduce the main features of the fluid-solid interaction phenomenon. Nevertheless, the differences between computed and measured solid motions are more evident after the merging of the collapsed upward water flow and reflected wave. It is reasonable since the blocks are subjected to a very complex and highly non-linear free-surface flow during this stage.

In addition to the above, the experimental results provide

comprehensive data for the validation and parametrization of theoretical/numerical models for modeling wave-ice floes interaction.

7. Future research

The results suggest that the present model can be extended to a parallelized solver able to handle simulations of real-scale ice dynamic problems with a large number of ice floes, such as ice-jam formation and breakup and ice floes interaction with hydraulic structures, and then supporting or even substituting laboratory experiments. Future extension of the model for the real-scale problems (with hundreds of floes) can be done using a massively parallel code (see Fernandes et al. (2015)), and by incorporating multi-resolution techniques (Shibata et al., 2017; Tanaka et al., 2018), in which high-resolution is used only near the local critical areas, while low-resolution is used in the far-field.

This study has been the first step toward developing a fully 3D Lagrangian model, for highly dynamic ice movements. The suggestion for future works will be to evaluate the model for test cases with real ice and extend the application of the model to study in-depth the physics of real-scale problems such as ice jam formation and breakup. Furthermore, a turbulent model is recommendable. Notwithstanding, one should keep in mind that the duration and effect of the shear forces near the tank bottom and lateral walls is attenuated when the upstream height H_{up} and the water bed H_{do} increase, as observed by Jánosi et al. (2004) from a series of experiments, and illustrated in Fig. 14 of the numerical study conducted by Khoshkonesh et al. (2019). Therefore, whereas the turbulence has an important effect in dry bed events, neglecting the turbulence does not imply considerable limitation of the proposed coupled model for some practical applications. Another limitation is the absence of a proper bed-to-ice friction model, which is very important near the wave front.

Since the dam breaking event is a gravity-driven phenomenon, the effects of the surface tension were neglected in numerical modeling. However, at the initial condition, the floating blocks, which have a large perimeter, were placed very close to each other, rendering the surface tension force strong enough to have relevant effects at the very beginning of the water column collapse, and possibly making it one of the causes of the chaotic nature of the experimental results.

The computed motions are well reproduced by the present model, but the computed forces are dependent on constants that require calibration, as the collision ratio and friction coefficient. In this sense, further effort is desirable to improve the model, such as the implementation of the solid-solid contact model based on the impulse method (Li et al., 2020), which requires less or no parameter tuning. Since shear forces would be very important in ice jam formation and release events, it is recommended to take into account fluid shear stress in close future works. Furthermore, a numerical model to simulate the internal ice stress and ice-breaking process, therefore suitable to reproduce drift ice dynamics, should also be considered in future studies.

Declaration of Competing Interest

The authors declare that they have no known competing financial interests or personal relationships that could have appeared to influence the work reported in this paper.

Acknowledgments

Authors would like to acknowledge the support of the Coordenação de Aperfeiçoamento de Pessoal de Nível Superior - Brasil (CAPES) Finance Code 001 and the Natural Sciences and Engineering Research Council of Canada (NSERC) for providing scholarship support for the first and second authors, respectively. This research was also partially supported by Canada Research Chair Program and Fonds de recherche du Québec – Nature et technologies (FRQNT). Authors would like to also thank Mr. Étienne Bélanger for his assistance in setting up the experiments. The first and fourth authors are also grateful to Petrobras for financial support on the development of the MPS/TPN-USP simulation system based on MPS method.

Appendix A. Calculation of shear forces and static friction coefficients

Table A1 shows the masses used for the calculation of shear forces and static friction coefficients between the blocks of polypropylene.

Table A1
Masses used to determine the coefficient of friction.

Try	Mass (g)	Shear force (g)	Coefficient of friction	Try	Mass (g)	Shear force (g)	Coefficient of friction
1	1702	675	0.397	10	2135	900	0.422
2	1702	700	0.411	11	2135	900	0.422
3	1702	675	0.397	12	2135	850	0.398
4	1702	650	0.382	13	2135	925	0.433
5	1702	750	0.441	14	2668	1050	0.394
6	2002.5	750	0.375	15	2668	1150	0.431
7	2002.5	825	0.412	16	2668	1225	0.459
8	2002.5	850	0.424	17	2668	1025	0.384
9	2002.5	900	0.449	18	2668	1100	0.412
Average				0.413			
Median				0.412			
Standard deviation				0.023			

Appendix B. DEM and MPS coupling algorithm

Schematic diagram of the DEM and MPS coupling algorithm is shown in Fig. B1.

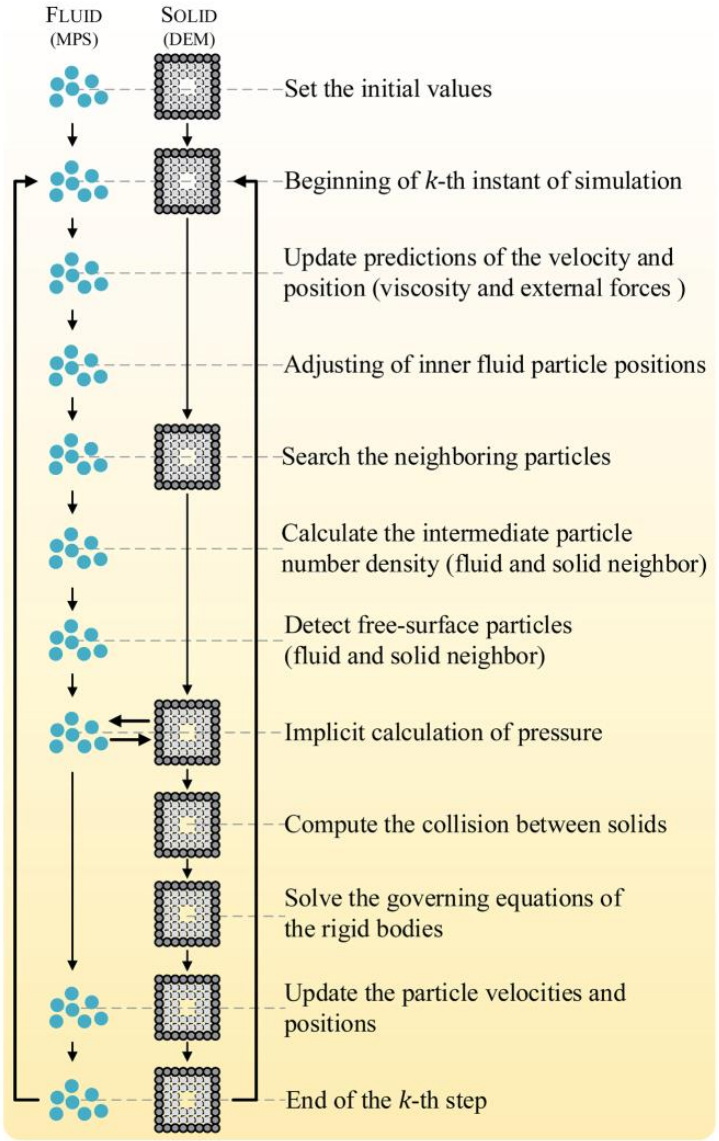

Fig. B1. Schematic diagram of the DEM and MPS coupling algorithm.

Appendix C. Flow simulations without blocks

In this appendix, a discussion of the effect of ice floes on the flow is outlined. For the sake of comparison, numerical simulations without blocks were also performed, and the computed wave profiles at selected instants are illustrated in Figs. C1–C4. As can be noticed, the computed wave profiles without solids are slightly different from those of 4 blocks (Figs. 7–10) and 9 blocks (Figs. 17–20), and these small differences are more evident in the late stage of the hydrodynamics process, i.e., $t \geq 1.6$ s. A closer look at Fig. 7(d), Fig. 17(d), and Fig. C1(d) reveals that for the simulations with a dry bed, a slightly higher splash occurs for the case without blocks at $t = 1.6$ s. By comparing Fig. 8(f), Fig. 18(f), and Fig. C2(f), a very small difference for the run-up occurs between the simulations without and with 4 blocks for filling depth $H_{do} = 1$ cm at $t = 2.4$ s. Comparing the results for $H_{do} = 2.5$ cm, Figs. 9(d) and (f), 19(d) and (f), and C3(d) and (f) show that distinct splashes occur for the simulations without and with blocks at the instants $t = 1.6$ s and $t = 2.4$ s despite with relatively small difference. Finally, the comparison between Fig. 10(d), Fig. 20(d), and Fig. C4(d) illustrates that a higher splash is computed for the case without blocks and $H_{do} = 5$ cm at $t = 1.6$ s. In summary, these results show that the presence of the light-weight blocks is almost negligible in the initial gravity-dominant dam-break event. However, the presence of the blocks is not negligible as time goes by, and the intensity as well as the sequence of events, like the wave impact, run-up, and splashing, are higher in the cases without the blocks.

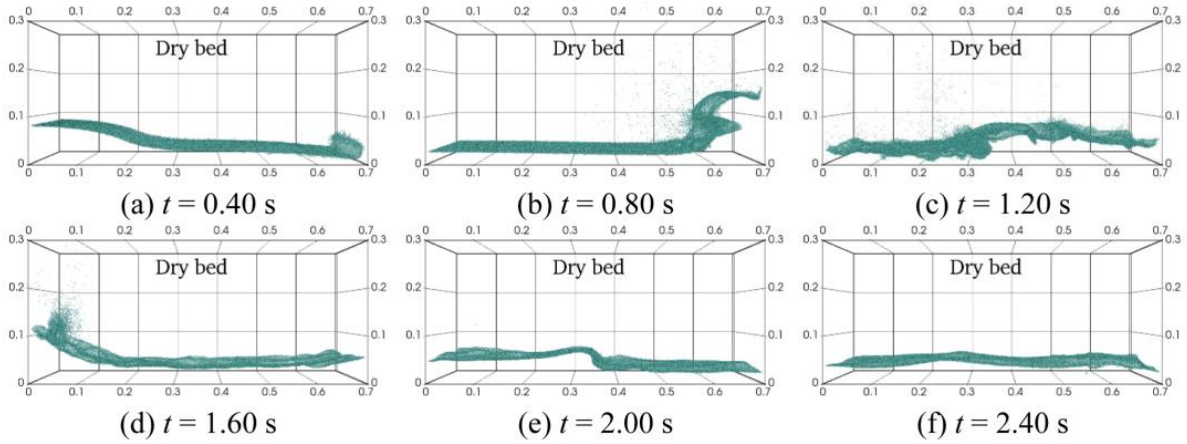

Fig. C1. Snapshots of the numerical dam breaking without blocks and dry bed at the instants t = 0.40, 0.80, 1.20, 1.60, 2.00, 2.40 s (front view).

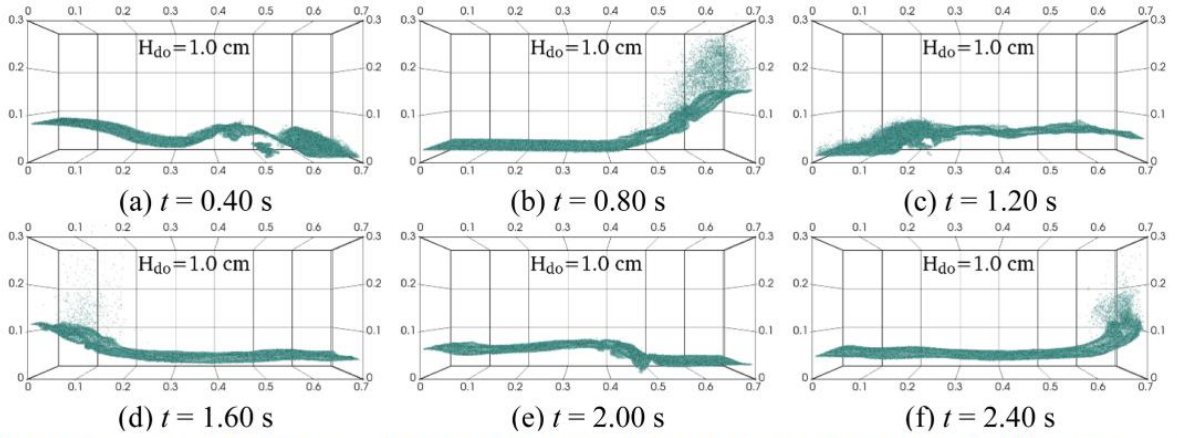

Fig. C2. Snapshots of the numerical dam breaking without blocks and wet bed H_{do} = 1.0 cm at the instants t = 0.40, 0.80, 1.20, 1.60, 2.00, 2.40 s (front view).

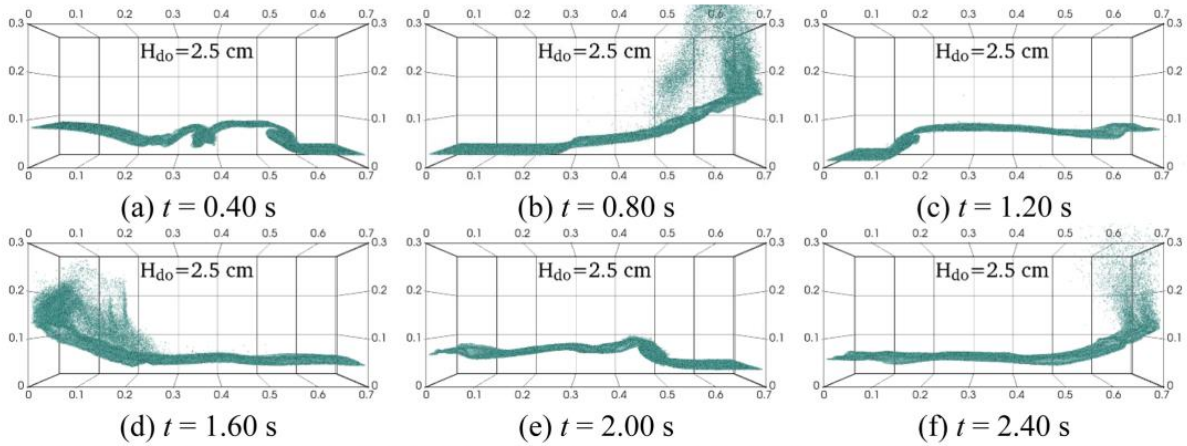

Fig. C3. Snapshots of the numerical dam breaking without blocks and wet bed H_{do} = 2.5 cm at the instants t = 0.40, 0.80, 1.20, 1.60, 2.00, 2.40 s (front view).

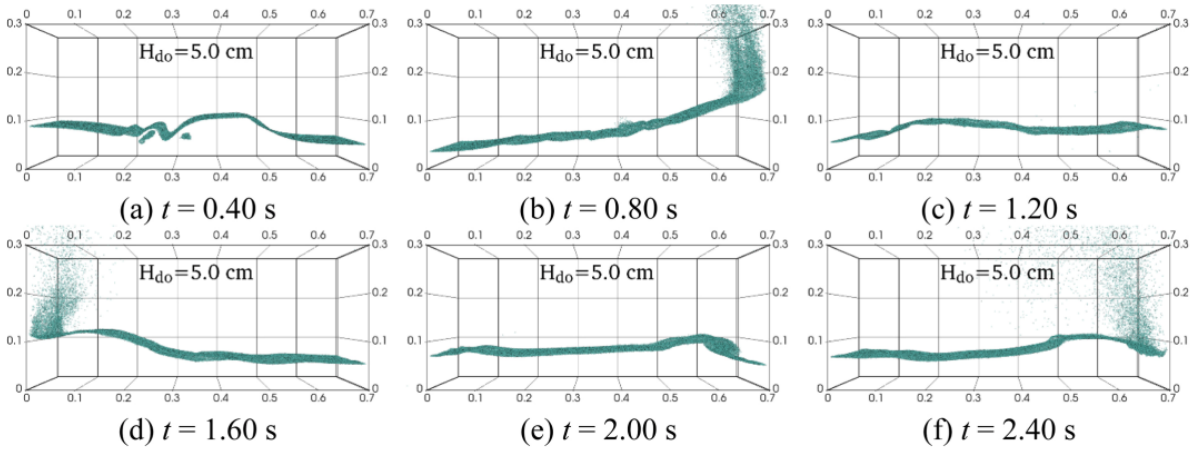

Fig. C4. Snapshots of the numerical dam breaking without blocks and wet bed H_{do} = 5.0 cm at the instants t = 0.40, 0.80, 1.20, 1.60, 2.00, 2.40 s (front view).

Appendix D. Supplementary data

Supplementary data to this article can be found online at https://doi.org/10.1016/j.coldregions.2021.103266.

References

Ahrens, J., Geveci, B., Law, C., 2005. ParaView: An End-User Tool for Large Data Visualization, Visualization Handbook. Elsevier.
Amaro Jr., R.A., Cheng, L.-Y., Osello, P.H.S., 2019. An improvement of rigid bodies contact for particle-based non-smooth walls modeling. Comput. Particle Mech. 6 (4), 561–580.
Bai, W., Zhang, T., McGovern, D.J., 2017. Response of small sea ice floes in regular waves: A comparison of numerical and experimental results. Ocean Eng. 129, 495–506.
Beltaos, S., 2007. River ice breakup processes: recent advances and future directions. Can. J. Civ. Eng. 34 (6), 703–716.
Beltaos, S., 2010. Assessing ice-jam flood risk: methodology and limitations. In: Proceedings of the 20th IAHR International Symposium on Ice.
Beltaos, S., Pomerleau, R., Halliday, R.A., 2000. Ice-Jam Effects on Red River Flooding and Possible Mitigation Methods.
Beltaos, S., Rowsell, R., Tang, P., 2011. Remote data collection on ice breakup dynamics: Saint John River case study author links open overlay panel. Cold Reg. Sci. Technol. 67 (3), 135–145.
Bennetts, L.G., Williams, T.D., 2015. Water wave transmission by an array of floating discs. Proc. Roy. Soc. A 471.
van den Berg, M., Lubbad, R., Løset, S., 2019. The effect of ice floe shape on the load experienced by vertical-sided structures interacting with a broken ice field. Mar. Struct. 65, 229–248.
Blackburn, J., She, Y., 2019. A comprehensive public-domain river ice process model and its application to a complex natural river. Cold Reg. Sci. Technol. 163, 44–58.
D. Brown, "Tracker," 2019. [Online]. Available: https://physlets.org/tracker/index.html. (Accessed on 02 01 2020).
Canelas, R.B., Crespo, A.J.C., Domínguez, J.M., Ferreira, R.M.L., 2016. SPH–DCDEM Model for Arbitrary Geometries in Free Surface Solid–Fluid Flows, vol. 202, pp. 131–140.
Courant, R., Friedrichs, K., Levy, H., 1967. On the Partial Difference Equations of Mathematical Physics. IBM J. Res. Dev. 11 (2), 215–234.
Crespo, A.J., Gómez-Gesteira, M., Dalrymple, R.A., 2008. Modeling dam break behavior over a wet bed by a SPH technique. J. Waterw. Port Coast. Ocean Eng. 134 (6), 313–320.
Cundall, P.A., Strack, O.D.L., 1979. A discrete numerical model for granular assemblies. Geotechnique 29 (1), 47–65.
Dagum, L., Menon, R., 1998. OpenMP: an industry standard API for shared-memory programming. IEEE Comput. Sci. Eng. 5 (1), 46–55.
Dai, M., Shen, H.H., Hopkins, M.A., Ackley, S.F., 2004. Wave rafting and the equilibrium pancake ice cover thickness. J. Geophys. Res. 109 (C7).
Daly, S.F., Hopkins, M.A., 2001. Estimating forces on an ice control structure using DEM. In: Proceedings of the 11th Workshop on the Hydraulics of Ice Covered Rivers. Calgary.
Duan, G., Yamaji, A., Koshizuka, S., Chen, B., 2019. The truncation and stabilization error in multiphase moving particle semi-implicit method based on corrective matrix: Which is dominant? Comput. Fluids 190, 254–273.
Ebert, E.E., Curry, J.A., 1993. An intermediate one-dimensional thermodynamic sea ice model for investigating ice-atmosphere interactions. J. Geophys. Res. 98 (C6), 10085–10109.
Farzin, S., Fatehi, R., Hassanzadeh, Y., 2019. Position explicit and iterative implicit consistent incompressible SPH methods for free surface flow. Comput. Fluids 179, 52–66.
Favier, J.F., Abbaspour-Fard, M.H., Kremmer, M., Raji, A.O., 1999. Shape representation of axi-symmetrical, non-spherical particles in discrete element simulation using multi-element model particles. Eng. Comput. 16 (4), 467–480.
Fernandes, D.T., Cheng, L.-Y., Favero, E.H., Nishimoto, K., 2015. A domain decomposition strategy for hybrid parallelization of moving particle semi-implicit (MPS) method for computer cluster. Clust. Comput. 18 (4), 1363–1377.
Gingold, R.A., Monagham, J.J., 1977. Smoothed particle hydrodynamics: theory and application to non-spherical stars. In: Monthly Notices of the Royal Astronomical Society, vol. 181, pp. 375–389.
Gong, H., Polojärvi, A., Tuhkuri, J., 2019. Discrete element simulation of the resistance of a ship in unconsolidated ridges. Cold Reg. Sci. Technol. 167.
Gropp, W., Lusk, E., Doss, N., Skjellum, A., 1996. A high-performance, portable implementation of the MPI message passing interface standard. Parallel Comput. 22 (6), 789–828.
Harada, E., Gotoh, H., Ikari, H., Khayyer, A., 2019. Numerical simulation for sediment transport using MPS-DEM coupling model. Adv. Water Resour. 129, 354–364.
Healy, D., Hicks, F., 2001. Experimental Observations on Ice Jam Shoving.
Herman, A., Cheng, S., Shen, H.H., 2019. Wave energy attenuation in fields of colliding ice floes - part 1: Discrete-element modelling of dissipation due to ice-water drag. Cryosphere 13 (11), 2887–2900.
Hicks, F., 2003. Modelling the interaction of climate, hydrology and river ice hydraulics, Mackenzie GEWEX Study (MAGS) Phase 2. In: Proceedings of the 8th Scientific Workshop. Jasper.
Hoomans, B., 2000. Granular Dynamics of Gas-Solid Two-Phase Flows.
Hopkins, M., 2004. A discrete element Lagrangian sea ice model. Eng. Comput. 21 (2/3/4), 409–421.
Hopkins, M., Daly, S.F., 2003. Recent advances in discrete element modeling of river ice. In: Proceedings of the 12th Workshop on the Hydraulics of Ice Covered Rivers. Edmonton.
Hopkins, M., Shen, H.H., 2001. Simulation of pancake-ice dynamics in a wave field. Ann. Glaciol. 33, 355–360.
Hopkins, M.A., Hibler, W.D., 1991. Numerical simulations of a compact convergent system of ice floes. Ann. Glaciol. 15, 26–30.
Hopkins, M.A., Tuthill, A.M., 2002. Ice boom simulations and experiments. J. Cold Reg. Eng. 16 (3), 138–155.
Hu, J., Zhou, L., 2015. Experimental and numerical study on ice resistance for icebreaking vessels. Int. J. Naval Archit. Ocean Eng. 7 (3), 626–639.
Ikeda, H., Koshizuka, S., Oka, Y., Park, H. Sun, Sugimoto, J., 2001. Numerical analysis of jet injection behavior for fuel-coolant interaction using particle method. J. Nucl. Sci. Technol. 38 (3), 174–182.
Jánosi, I.M., Jan, D., Szabó, K.G., Tél, T., 2004. Turbulent drag reduction in dam-break flows. Exp. Fluids 37 (2), 219–229.

Jasek, M., 2003. Ice jam release surges, ice runs, and breaking fronts: field measurements, physical descriptions, and research needs. Can. J. Civ. Eng. 30 (1), 113–127.
Ji, S., Di, S., Liu, S., 2015. Analysis of ice load on conical structure with discrete element method. Eng. Comput. 32 (4), 1121–1134.
Johnson, K.L., 1985. Contact Mechanics. Cambridge University Press, Cambridge.
Kawano, Y., Ohashi, T., 2015. Numerical study on c-axis orientations of sea ice surface grown under calm sea conditions using a particle method and Voronoi dynamics. Cold Reg. Sci. Technol. 112, 29–38.
Khoshkonesh, A., Nsom, B., Gohari, S., Banejad, H., 2019. A comprehensive study on dam-break flow over dry and wet beds. Ocean Eng. 188.
Koshizuka, S., Oka, Y., 1996. Moving-particle semi-implicit method for fragmentation of incompressible fluid. Nucl. Sci. Eng. 123 (3), 421–434.
Koshizuka, S., Nobe, A., Oka, Y., 1998. Numerical analysis of breaking waves using the moving particle semi-implicit method. Int. J. Numer. Methods Fluids 26 (7), 751–769.
Koshizuka, S., Ikeda, H., Oka, Y., 1999. Numerical analysis of fragmentation mechanisms in vapor explosions. Nucl. Eng. Des. 189 (1–3), 423–433.
Lauber, G., Hager, W.H., 1998. Experiments to Dam-break Wave: Horizontal channel. J. Hydraul. Res. 36 (3), 291–307.
Lee, B.-H., Park, J.-C., Kim, M.-H., Hwang, S.-C., 2011. Step-by-step improvement of MPS method in simulating violent free-surface motions and impact-loads. Comput. Methods Appl. Mech. Eng. 200 (9–12), 1113–1125.
Leppäranta, M., 2011. Free drift. In: The Drift of Sea Ice. Springer Praxis Books, Heidelberg.
Li, J.-J., Qiu, L.-C., Tian, L., Yang, Y.-S., Han, Y., 2019. Modeling 3D non-Newtonian solid–liquid flows with a free-surface using DEM-MPS. Eng. Anal. Bound. Elem. 105, 70–77.
Li, Y., Asai, M., Chandra, B., Isshiki, M., 2020. Energy-tracking impulse method for particle-discretized rigid-body simulations with frictional contact. Comput. Particle Mech. 8, 237–258.
Liu, L., Ji, S., 2018. Ice load on floating structure simulated with dilated polyhedral discrete element method in broken ice field. Appl. Ocean Res. 75, 53–65.
Løset, S., 1994. Discrete element modelling of a broken ice field - part I: model development. Cold Reg. Sci. Technol. 22 (4), 339–347.
Luo, W.-Z., Guo, C.-Y., Wu, T.-C., Su, Y.-M., 2018. Experimental research on resistance and motion attitude variation of ship–wave–ice interaction in marginal ice zones. Mar. Struct. 58, 399–415.
McGovern, D.J., Bai, W., 2014. Experimental study on kinematics of sea ice floes in regular waves. Cold Reg. Sci. Technol. 103, 15–30.
Metrikin, I., Løset, S., 2013. Nonsmooth 3d discrete element simulation of a drillship in discontinuous ice. In: Proceedings of the 22nd International Conference on Port and Ocean Engineering Under Arctic Conditions.
Morse, B., Burrell, B., Hilaire, A.S., Bergeron, N., Messier, D., Quasch, T., 1999. River ice processes in tidal rivers: research needs. In: Proceedings of the 10th Workshop on River Ice. Winnipeg.
Nafziger, J., She, Y., Hicks, F., 2016. Celerities of waves and ice runs from ice jam releases. Cold Reg. Sci. Technol. 123, 71–80.
Paavilainen, J., Tuhkuri, J., 2013. Pressure distributions and force chains during simulated ice rubbling against sloped structures. Cold Reg. Sci. Technol. 85, 157–174.
Ritter, A., 1892. Die Fortpflanzung de Wasserwellen. Zeitschrift Verein Deutscher Ingenieure 36 (33), 947–954.
Robb, D.M., Gaskin, S.J., Marongiu, J.C., 2016. SPH-DEM model for free-surface flows containing solids applied to river ice jams. J. Hydraul. Res. 544 (1), 27–40.
Robinson, M., Ramaioli, M., Luding, S., 2014. Fluid–particle flow simulations using two-way-coupled mesoscale SPH–DEM and validation. Int. J. Multiphase Flow 59, 121–134.
Sakai, M., Shigeto, Y., Sun, X., Aoki, T., Saito, T., Xiong, J., Koshizuka, S., 15 August 2012. Lagrangian–Lagrangian modeling for a solid–liquid flow in a cylindrical tank. Chem. Eng. J. 200–202, 663–672.
Sayeed, T., Colbourne, B., Molyneux, D., 2018. Experimental and numerical investigation of wave induced forces and motions of partially submerged bodies near a fixed structure in irregular waves. Ocean Eng. 163, 451–475.
Shakibaeinia, A., Jin, Y.-C., 2010. A weakly compressible MPS method for modeling of open-boundary free-surface flow. Int. J. Numer. Methods Fluids 63 (10), 1208–1232.
Shakibaeinia, A., Jin, Y.-C., 2012. MPS mesh-free particle method for multiphase flows. Comput. Methods Appl. Mech. Eng. 2229–2232, 13–26.
She, Y., Andrishak, R., Hicks, F., Morse, B., Stander, E., Krath, C., Keller, D., Abarca, N., Nolin, S., Tanekou, F.N., Mahabir, C., 2009. Athabasca River ice jam formation and release events in 2006 and 2007. Cold Reg. Sci. Technol. 55 (2), 249–261.
Shen, H.T., 2010. Mathematical modeling of river ice processes. Cold Reg. Sci. Technol. 62 (1), 3–13.
Shibata, K., Masaie, I., Kondo, M., Murotani, K., 2015. Improved pressure calculation for the moving particle semi-implicit method. Comput. Particle Mech. 2, 91–108.
Shibata, K., Koshizuka, S., Matsunaga, T., Massaie, I., 2017. The overlapping particle technique for multi-resolution simulation of particle methods. Comput. Methods Appl. Mech. Eng. 325, 434–462.
Soleimani, K., Ketabdari, M.J., 2020. Meshfree modeling of near field two-liquid mixing process in the presence of different obstacles. Ocean Eng. 213.
Squire, V.A., 2007. Of ocean waves and sea-ice revisited. Cold Reg. Sci. Technol. 49 (2), 110–133.
Squire, V.A., 2018. A fresh look at how ocean waves and sea ice interact. Phil. Trans. R. Soc. A 376 (2129).
Squire, V.A., 2020. Ocean Wave Interactions with Sea Ice: a Reappraisal. Annu. Rev. Fluid Mech. 52 (1), 37–60.
Stansby, P.K., Chegini, A., Barnes, T.C.D., 1998. The initial stages of dam-break flow. J. Fluid Mech. 374, 407–424.
Stockstill, R.L., Daly, S.F., Hopkins, M.A., 2009. Modeling floating objects at river structures. J. Hydraul. Eng. 135 (5), 403–414.
Tanaka, M., Cardoso, R., Bahai, H., 2018. Multi-resolution MPS method. J. Comput. Phys. 359, 106–136.
Timco, G.W., Frederking, R.M.W., 1996. A review of sea ice density. Cold Reg. Sci. Technol. 24 (1), 1–6.
Timco, G.W., Weeks, W., 2010. A review of the engineering properties of sea ice. Cold Reg. Sci. Technol. 60 (2), 107–129.
Tsukamoto, M.M., Cheng, L.-Y., Motezuki, F.K., 2016. Fluid interface detection technique based on neighborhood particles centroid deviation (NPCD) for particle methods. Int. J. Numer. Methods Fluids 82 (3), 148–168.
Tsukamoto, M.M., Cheng, L.-Y., Kobayakawa, H., Okada, T., Bellezi, C.A., 2020. A numerical study of the effects of bottom and sidewall stiffeners on sloshing behavior considering roll resonant motion. Mar. Struct. 72.
Tuhkuri, J., Polojärvi, A., 2018. A review of discrete element simulation of ice–structure interaction. 376: 20170335. Phil. Trans. R. Soc. A 376 (2129).
Vetsch, D., 2011. Numerical Simulation of Sediment Transport with Meshfree Methods.
Wang, C.D., Meylan, M.H., 2004. A higher-order-coupled boundary element and finite element method for the wave forcing of a floating elastic plate. J. Fluids Struct. 19 (4), 557–572.
Wang, L., Jiang, Q., Zhang, C., 2017. Improvement of moving particle semi-implicit method for simulation of progressive water waves. Int. J. Numer. Methods Fluids 85 (2), 69–89.
Wei, Z., Li, C., Dalrymple, R.A., Derakhti, M., Katz, J., 2018. Chaos in breaking waves. Coast. Eng. 140, 272–291.
Xue, Y., Liu, R., Li, Z., Han, D., 2020. A review for numerical simulation methods of ship–ice interaction. Ocean Eng. 215.
Ye, Y., Xu, T., Zhu, D.Z., 2020. Numerical analysis of dam-break waves propagating over dry and wet beds by the mesh-free method. Ocean Eng. 217.
Yiew, L.J., Bennetts, L.G., Meylan, M.H., Thomas, G.A., French, B.J., 2017. Wave-induced collisions of thin floating disks. Phys. Fluids 29 (12).
Yiew, L.Y., Bennetts, L.G., Meylan, M.H., French, B.J., Thomas, G.A., 2016. Hydrodynamic responses of a thin floating disk to regular waves. Ocean Model 97, 52–64.
Zhang, N., Zheng, X., Ma, Q., 2019. Study on wave-induced kinematic responses and flexures of ice floe by Smoothed Particle Hydrodynamics. Comput. Fluids 189, 46–59.

APPENDIX B EXPERIMENTAL EXTRA RESULTS

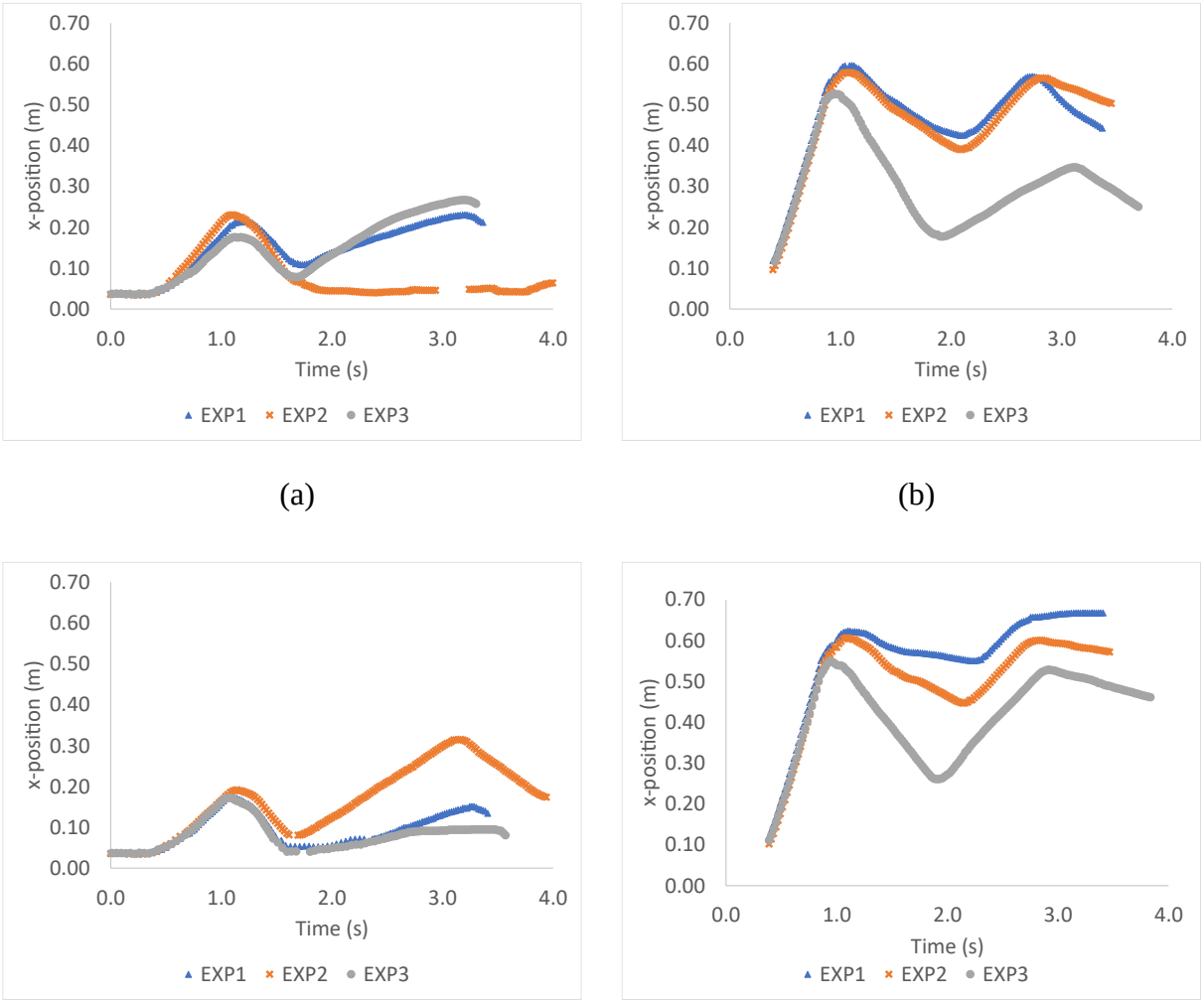

Figure B1 - Dam breaking with 4 blocks and dry bed. Experimental motions along the longitudinal direction of (a) Block A1 (b) A2 (c) B1 (d) B2.

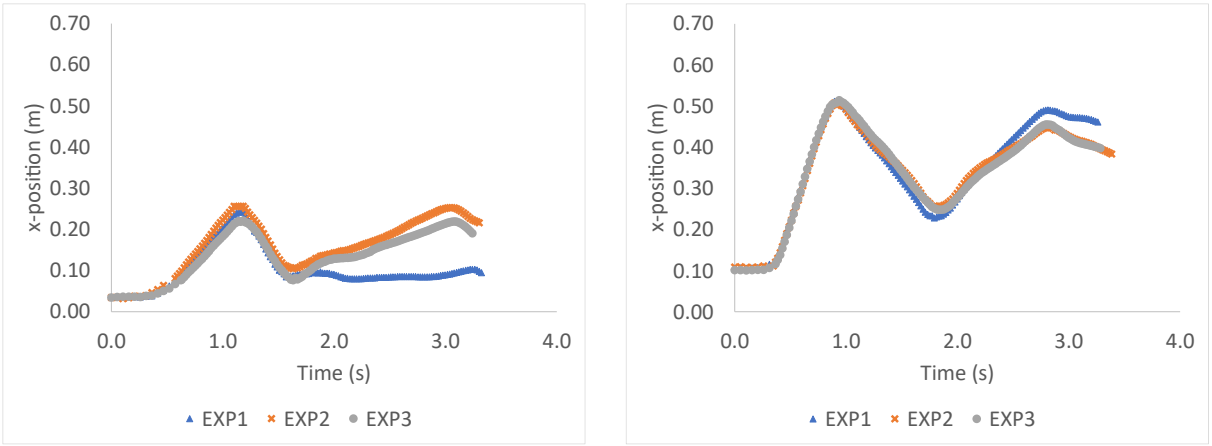

(a) (b)

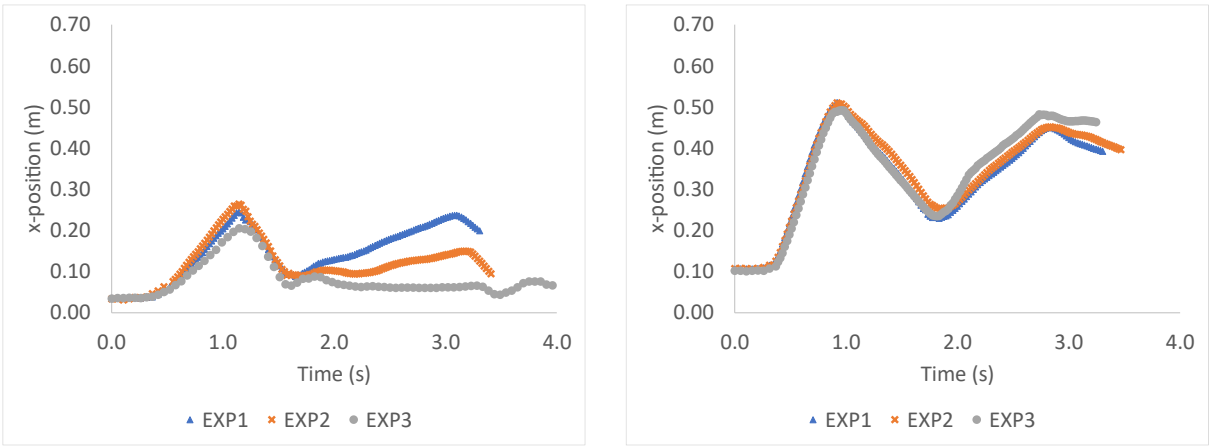

(c) (d)

Figure B2- Dam breaking with 4 blocks and H_{do}=1cm. Experimental motions along the longitudinal direction of (a) Block A1 (b) A2 (c) B1 (d) B2.

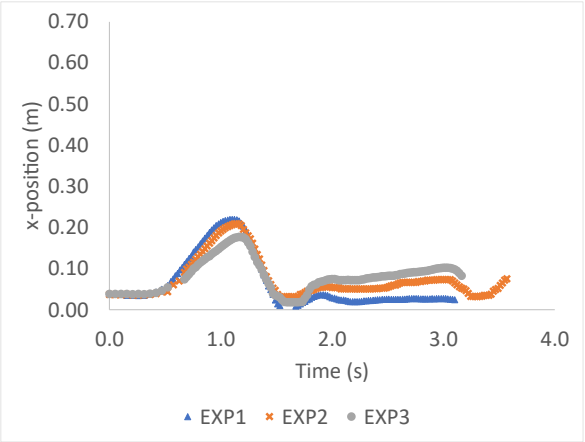

(a)

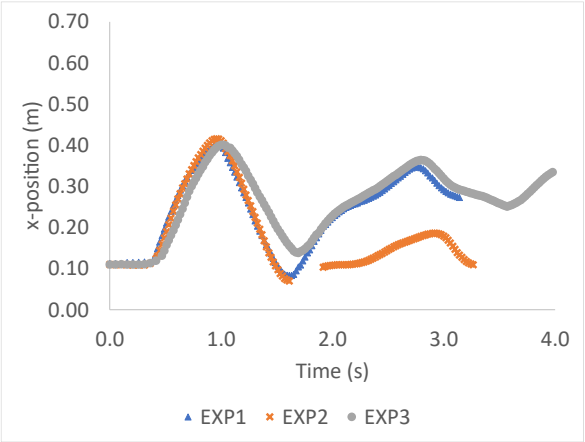

(b)

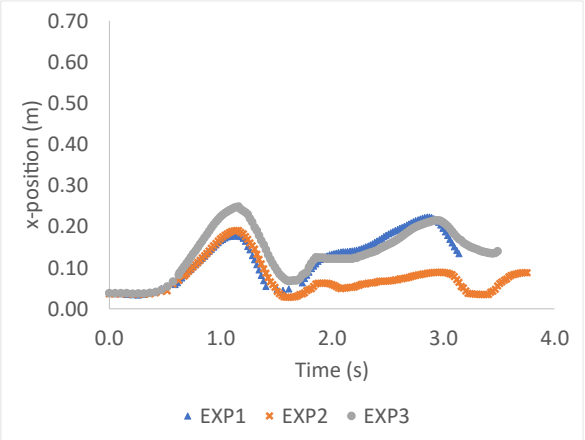

(c)

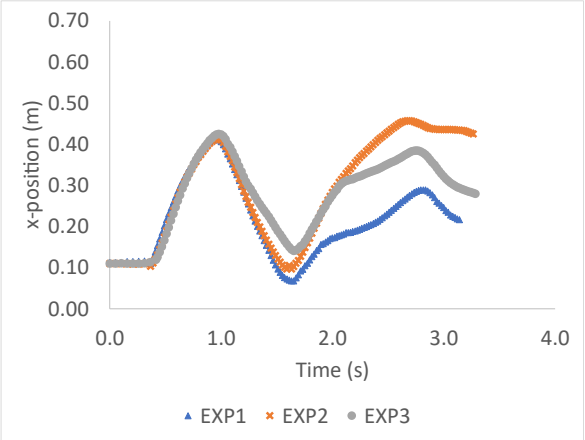

(d)

Figure B3 - Dam breaking with 4 blocks and Hdo=2.5cm. Experimental motions along the longitudinal direction of (a) Block A1 (b) A2 (c) B1 (d) B2.

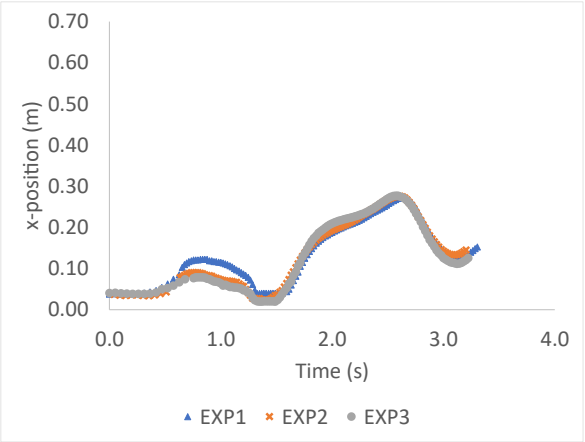

(a)

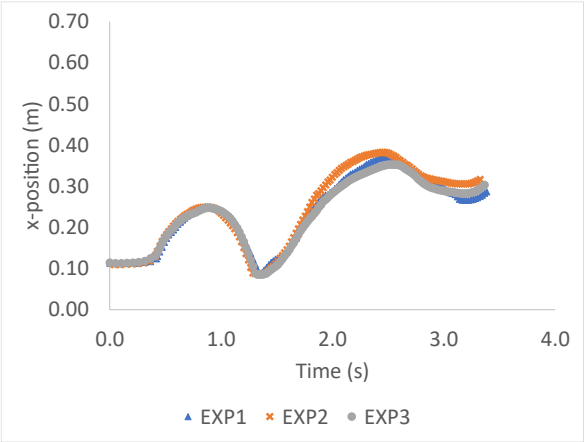

(b)

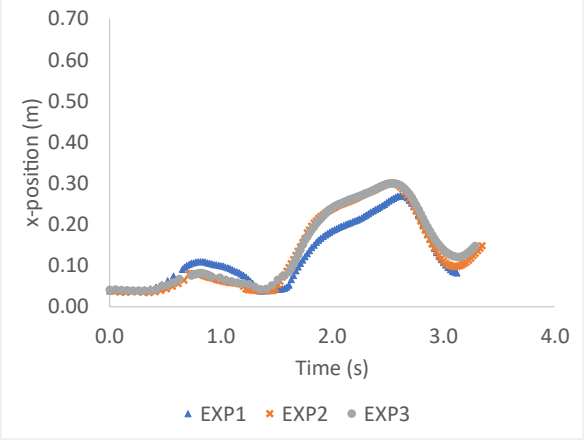

(c)

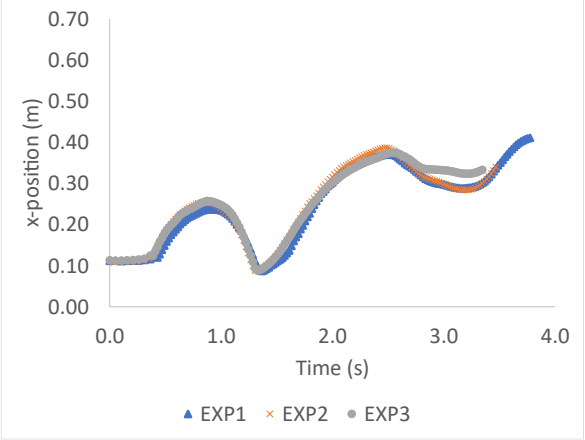

(d)

Figure B4 - Dam breaking with 4 blocks and Hdo=5 cm. Experimental motions of the four blocks along the longitudinal direction of (a) Block A1 (b) A2 (c) B1 (d) B2.

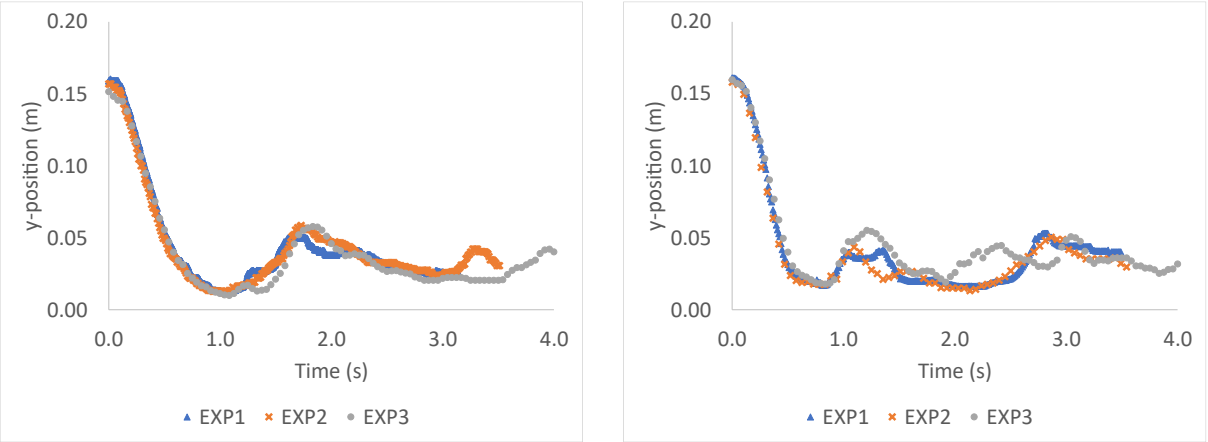

(a) (b)

Figure B5 - Dam breaking with 4 blocks and dry bed. Experimental motions along the vertical direction of (a) Block B1 (b) B2.

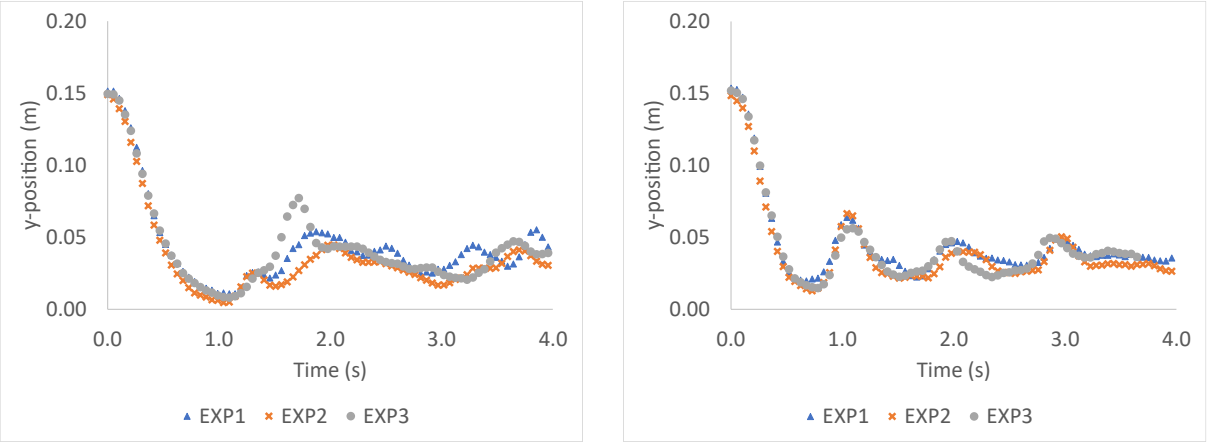

(a) (b)

Figure B6 - Dam breaking with 4 blocks and H_{do}=1cm. Experimental motions along the vertical direction of (a) Block B1 (b) B2.

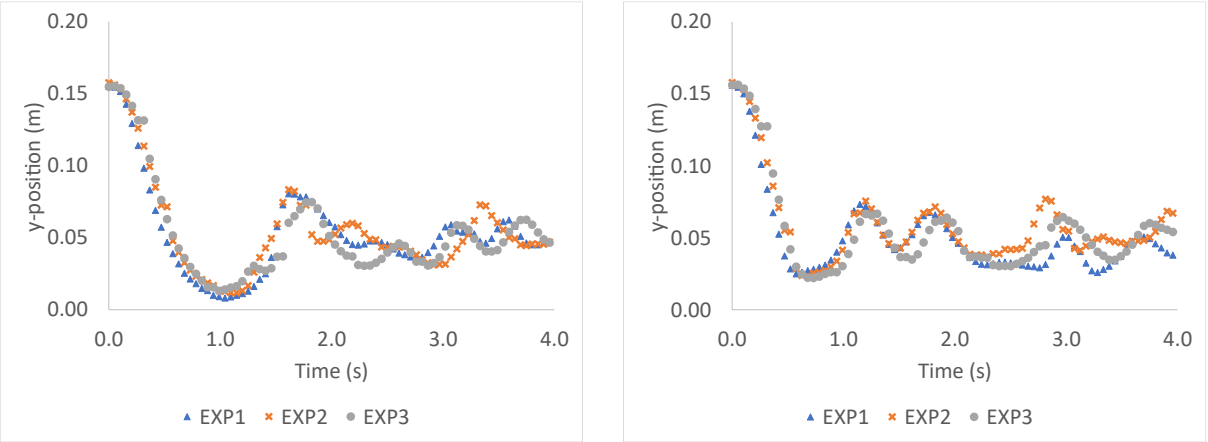

(a) (b)

Figure B7 - Dam breaking with 4 blocks and Hdo=2.5cm. Experimental motions along the vertical direction of (a) Block B1 (b) B2.

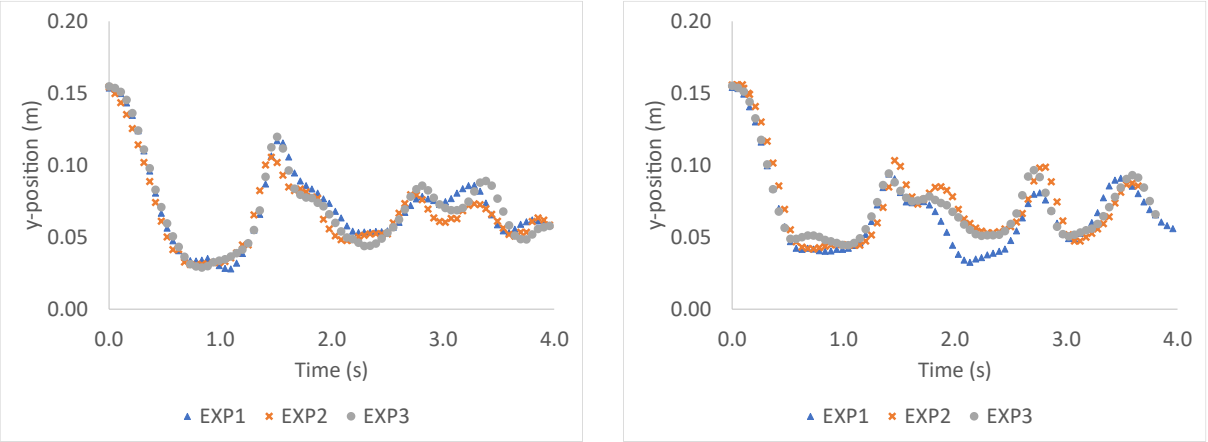

(a) (b)

Figure B8 - Dam breaking with 4 blocks and Hdo=5cm. Experimental motions along the vertical direction of (a) Block B1 (b) B2.

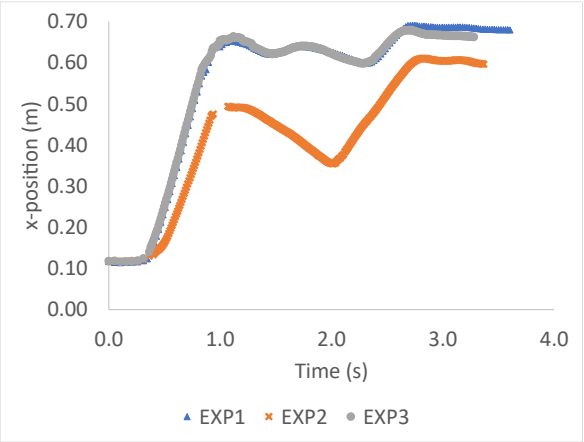

(a)

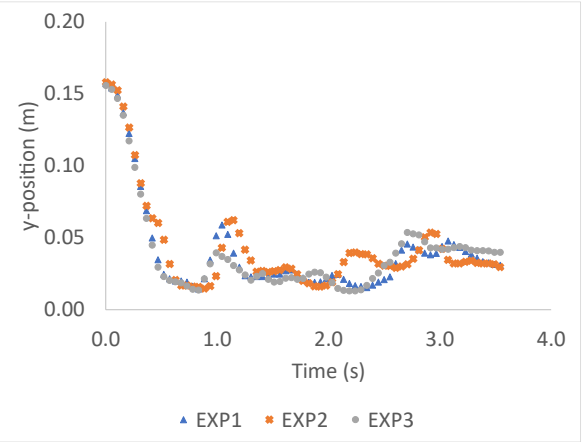

(b)

Figure B9 - Dam breaking with 9 blocks and dry bed. Experimental motions of block C1 in the (a) longitudinal and (b) vertical direction

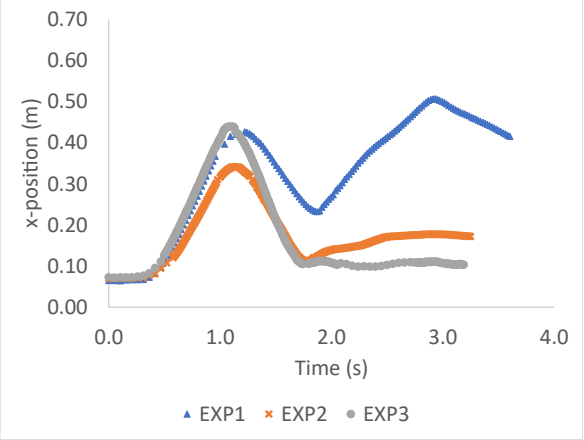

(c)

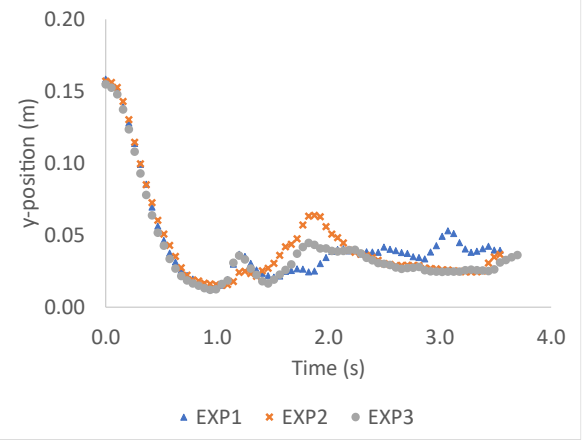

(d)

Figure B10 - Dam breaking with 9 blocks and dry bed. Experimental motions of block C2 in the (a) longitudinal and (b) vertical direction

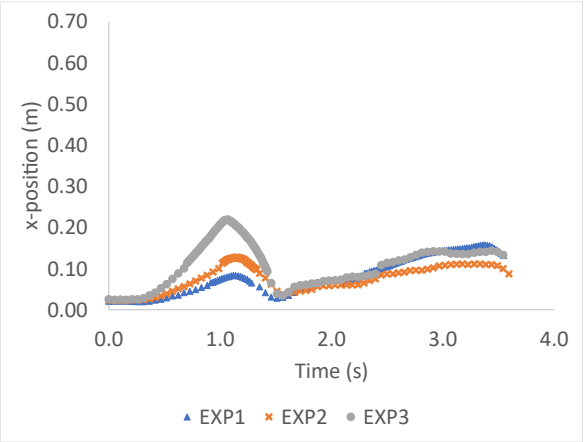

(a)

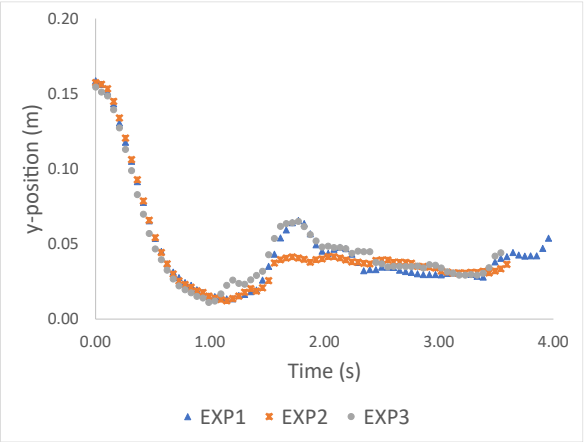

(b)

Figure B11 - Dam breaking with 9 blocks and dry bed. Experimental motions of block C3 in the (a) longitudinal and (b) vertical direction

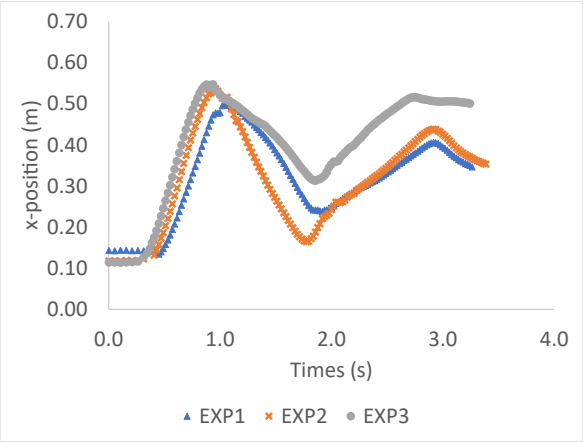

(a)

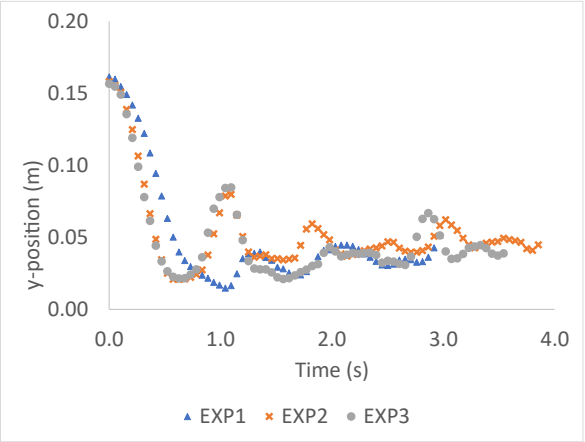

(b)

Figure B12 - Dam breaking with 9 blocks and H_{do}=1cm. Experimental motions of block C1 in the (a) longitudinal and (b) vertical direction

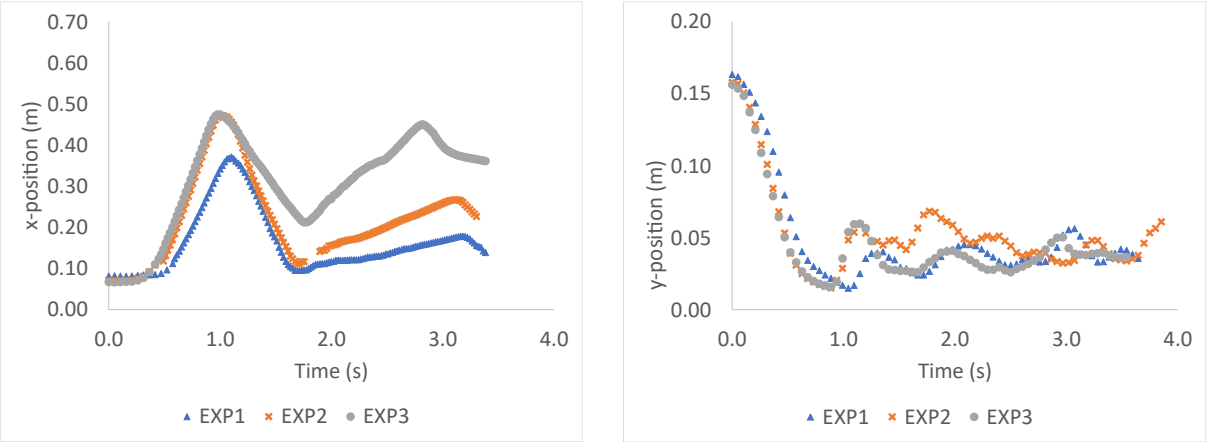

(a) (b)

Figure B13 - Dam breaking with 9 blocks and Hdo=1cm. Experimental motions of block C2 in the (a) longitudinal and (b) vertical direction

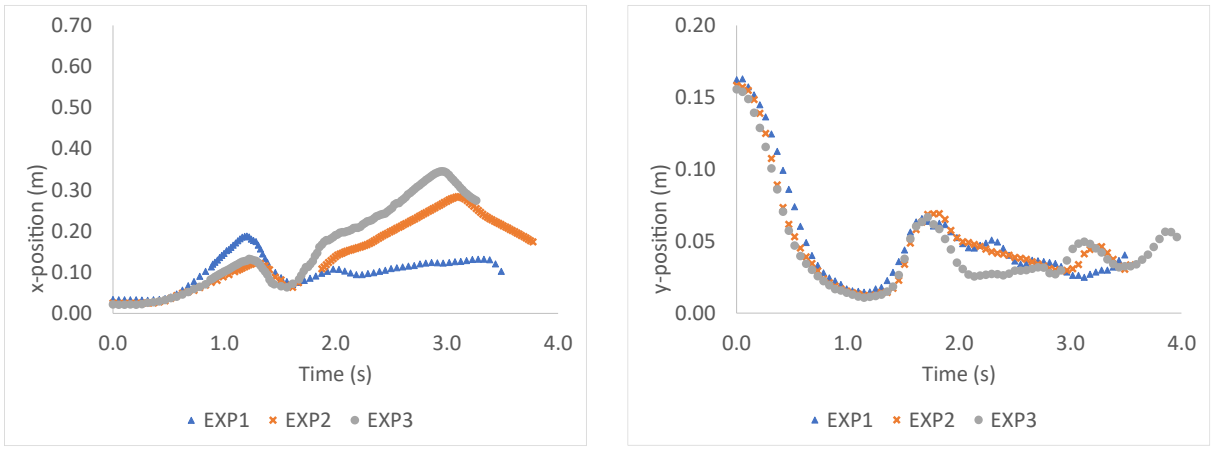

(a) (b)

Figure B14 - Dam breaking with 9 blocks and Hdo=1cm. Experimental motions of block C3 in the (a) longitudinal and (b) vertical direction

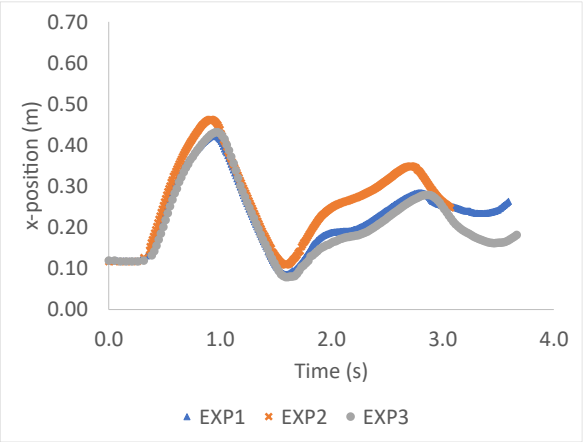

(a)

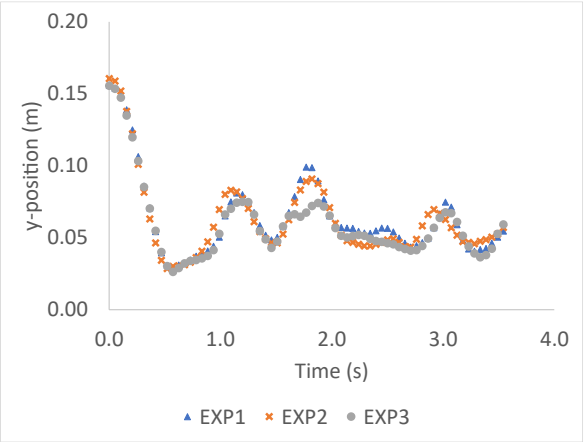

(b)

Figure B15 - Dam breaking with 9 blocks and H_{do}=2.5 cm. Experimental motions of block C1 in the (a) longitudinal and (b) vertical direction

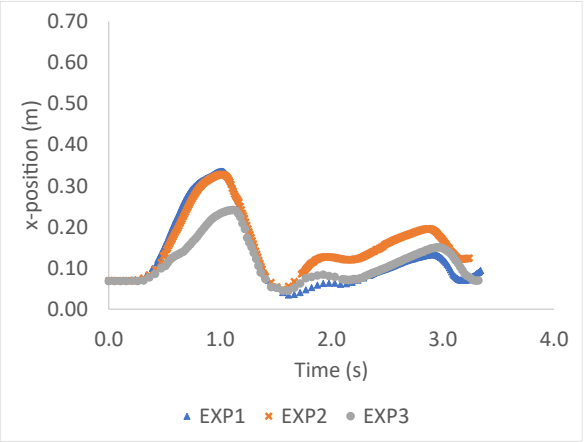

(a)

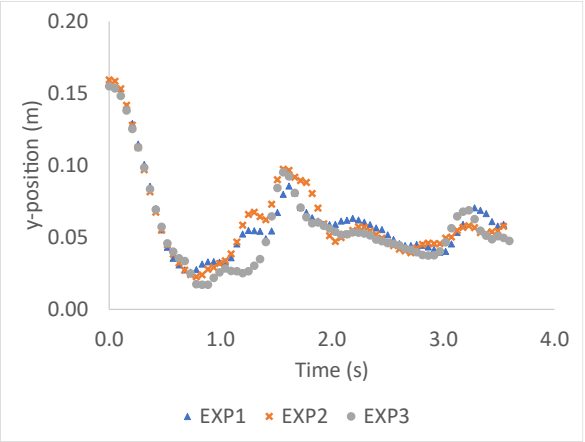

(b)

Figure B16 - Dam breaking with 9 blocks and Hdo=2.5 cm. Experimental motions of block C2 in the (a) longitudinal and (b) vertical direction

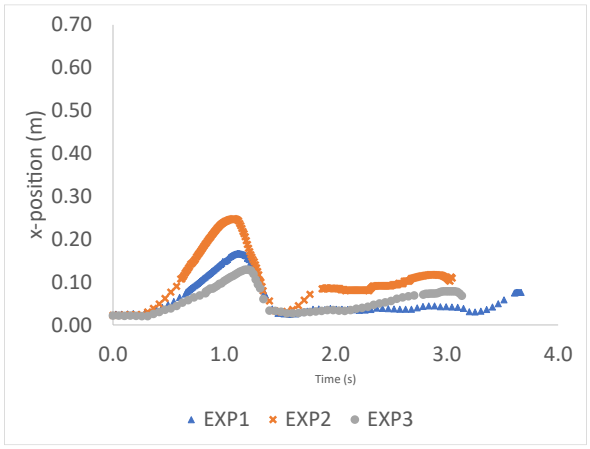

(a)

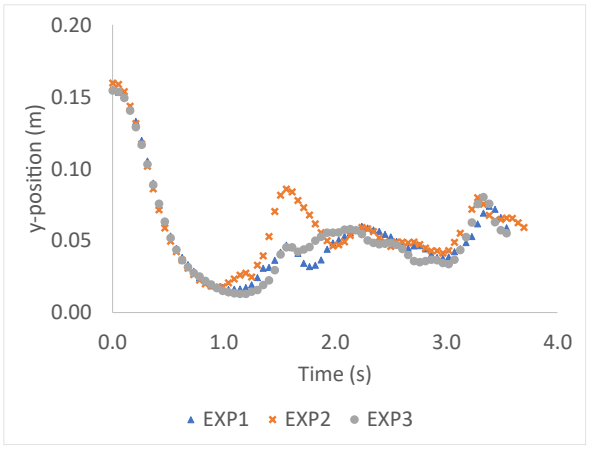

(b)

Figure B17 - Dam breaking with 9 blocks and Hdo=2.5 cm. Experimental motions of block C3 in the (a) longitudinal and (b) vertical direction

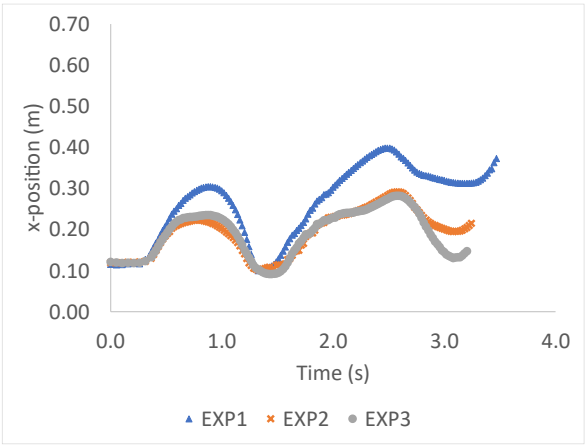

(a)

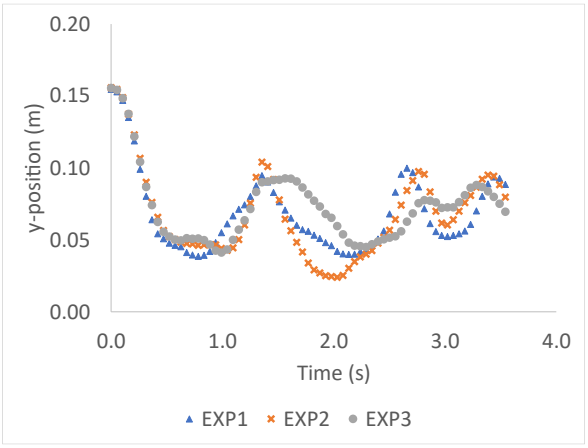

(b)

Figure B18 - Dam breaking with 9 blocks and H_{do}=5 cm. Experimental motions of block C1 in the (a) longitudinal and (b) vertical direction

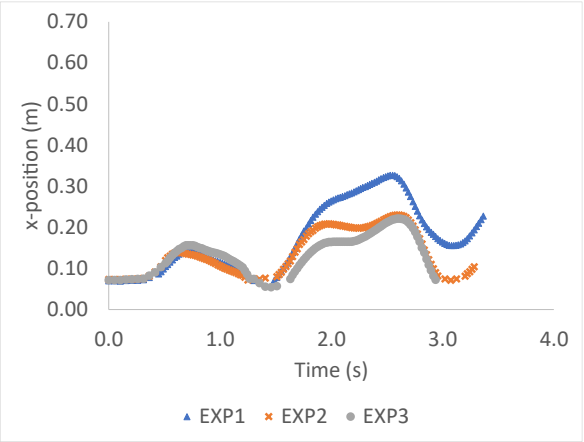

(a)

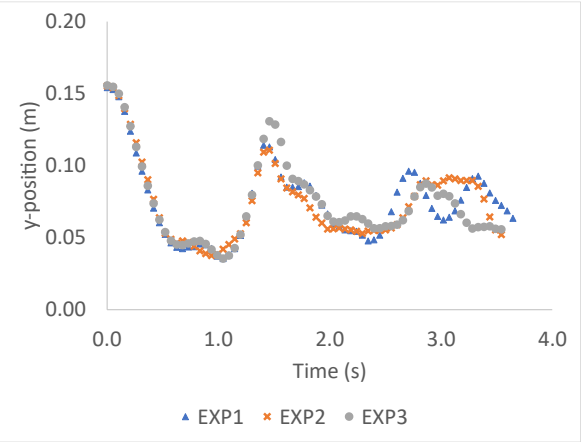

(b)

Figure B19 - Dam breaking with 9 blocks and Hdo=5 cm. Experimental motions of block C2 in the (a) longitudinal and (b) vertical direction

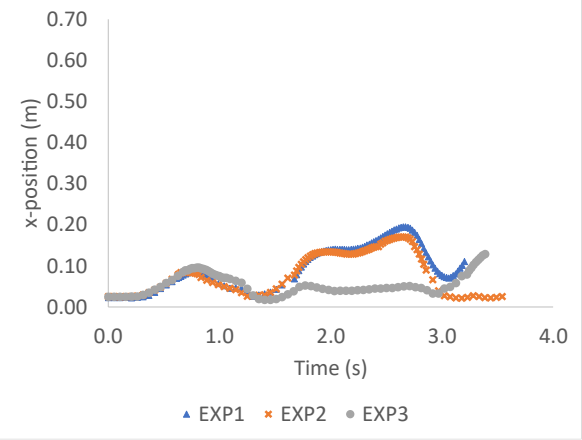

(a)

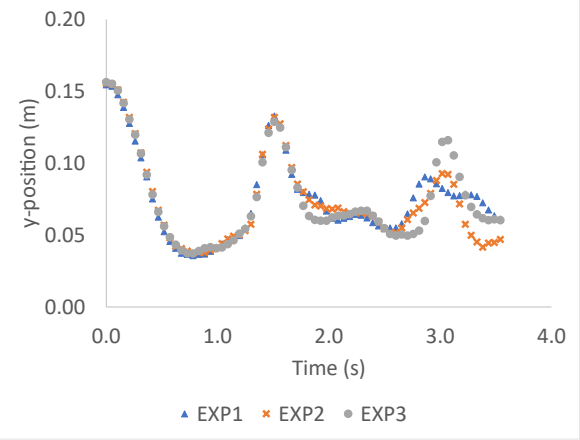

(b)

Figure B20 - Dam breaking with 9 blocks and Hdo =.5 cm. Experimental motions of block C3 in the (a) longitudinal and (b) vertical direction